Optical Characterisation of III-V Semiconductor Quantum Dots and Quantum Dot structures

Adam Dennis Ashmore

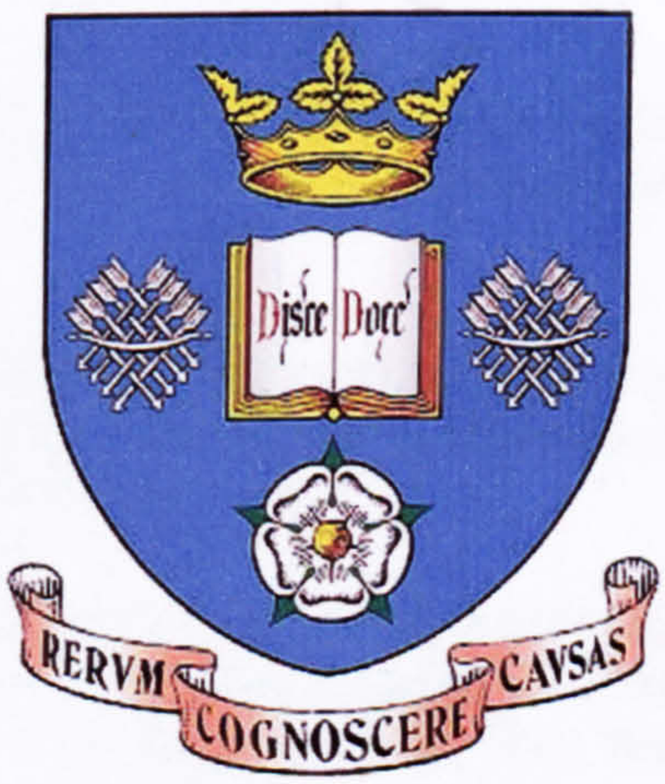

Department of Physics and Astronomy

Thesis submitted to the University of Sheffield for the Degree of

Doctor of Philosophy, September 2002.

Publications

'*Optical properties of single charge tuneable InGaAs quantum dots*.' A. D. Ashmore, J. J. Finley, R. Oulton, P. W. Fry, A. Lemaître, D. J. Mowbray, M. S. Skolnick, M. Hopkinson, P. D. Buckle and P. A. Maksym. Physica E: Low-dimensional Systems and Nanostructures, 13 127 (2002)

'*Manipulation of the homogeneous linewidth of an individual In(Ga)As quantum dot.*' R. Oulton, J. J. Finley JJ, A. D. Ashmore, I. S. Gregory, D. J. Mowbray, M. S. Skolnick, M. J. Steer, S. L. Liew, M. A. Migliorato, A. J. Cullis. Phys. Rev. B 66 5313 (2002)

'*Observation of multicharged excitons and biexcitons in a single InGaAs quantum dot*.' J. J. Finley, P. W. Fry, A. D. Ashmore, A. Lemaitre, A. I. Tartakovskii, R. Oulton, D. J. Mowbray, M. S. Skolnick, M. Hopkinson, P. D. Buckle, P. A. Maksym. Phys. Rev. B 63 1305 (2001)

'*Enhanced phonon-assisted absorption in single InAs/GaAs quantum dots*.' A. Lemaitre, A. D. Ashmore, J. J. Finley, D. J. Mowbray, M. S. Skolnick, M. Hopkinson, T. F. Krauss. Phys. Rev. B 63 1309 (2001)

'*Excitation and relaxation mechanisms in single In(Ga)As quantum dots*. ' J. J. Finley, A. Lemaitre, A. D. Ashmore, D. J. Mowbray, M. S. Skolnick, M. Hopkinson, T. F. Krauss. Phys. Stat. Sol. B 224 373 (2001)

'*Optical spectroscopic study of carrier processes in self-assembled In(Ga)As-Ga(Al)As quantum dot lasers*.' K. M. Groom, A. D. Ashmore, D. J. Mowbray, M. S. Skolnick, M. Hopkinson, G. Hill, J. Clark, P. M. Smowton. Phys. Stat. Sol. B 224 123 (2001)

'*Charged and neutral exciton complexes in individual self-assembled In(Ga)As quantum dots*.' J. J. Finley, A. D. Ashmore, A. Lemaitre, D. J. Mowbray, M. S. Skolnick, I. E. Itskevich, P. A. Maksym, M. Hopkinson, T. F. Krauss. Phys. Rev. B 63 3307 (2001)

'*Electronic properties of InAs/GaAs self-assembled quantum dot structures and devices studied by photocurrent spectroscopy*.' D. J. Mowbray, P.W. Fry, M. S. Skolnick, I. E. Itskevich, L. Harris, A. D. Ashmore, J. J. Finley, L. R. Wilson, K. L. Schumacher, J. A. Barker, E. P. O'Reill, M. Al-Khafaji, A. G. Cullis, M. Hopkinson, J. C. Clark, G. Hill. Acta Phys. Pol. A 98 279 (2000)

'*InAs-GaAs self-assembled quantum dot lasers: physical processes and device characteristics*.' D. J. Mowbray, L. Harris, P. W. Fry, A. D. Ashmore, S. R. Parnell, J. J. Finley, M. S. Skolnick, M. Hopkinson, G. Hill, J. Clark. Physica E 7 489 (2000)

'*Modal gain and lasing states in InAs/GaAs self-organized quantum dot lasers*.' P. W. Fry, L. Harris, S. R. Parnell, J. J. Finley, A. D. Ashmore, D. J. Mowbray, M. S. Skolnick, M. Hopkinson, G. Hill, J. C. Clark. J. Appl. Phys. 87 615 (2000)

'*Gain characteristics of InAs/GaAs self-organized quantum-dot lasers*.' L. Harris, A. D. Ashmore, D. J. Mowbray, M. S. Skolnick, M. Hopkinson, G. Hill, J. Clark. Appl. Phys. Lett. 75 3512 (1999)

Contents

Chapter 4: Photoluminescence Studies of Single Quantum Dots

Chapter 5: Absorption Processes and Carrier Relaxation in Single Quantum Dots

Chapter 6: Charge Tuneable Single Quantum Dots

Acknowledgements

There are many people who I would like to thank for the help they provided in the production of this thesis.

I would like to thank Dr. David Mowbray for his help and advice when compiling this thesis and for his guidance over my time at Sheffield. Thank you to my supervisor Dr. Mark Fox and the head of our research group Professor Maurice Skolnick for their patience in the production of this thesis.

This work owes much to Dr. John Finley who's continual development of ideas was an inspiration. I would also like to thank Dr. Aristide Lemaître for the enjoyable time spent working with him. And from the early days of my research I want to thank Lee Harris.

Thank you to Kris Groom and Ruth Oulton who came after me in Lasers and Single Dots respectively.

Most of this work would not have been possible with out the those who have aided in the growth and subsequent processing of the samples. Thanks to Mark Hopkinson of the EPSRC National Centre for III-V Technologies for the growth and involvement in improving and tailoring samples to our needs and for the insight into the dynamics of growth. I would also like to thank Dr. Geoff Hill for the processing of the laser samples and Professor Thomas Krauss from the University of St Andrews for the lithography of the single dot samples.

I would also like to thank Dr. Peter Maksym, University of Leicester, for his work on the theoretical side.

Last and certainly not least are all the other academics and students that I have worked (and played) with. Thanks to Luke Wilson, Paul Fry, Mohammed Emam-Ismael, Steve Parnell, Ruth Hollins (now Ashmore!), Matthew Steer, Adam Armitage, Max Migliorato, Jeremy Duck, Alan Bristow and all other members, past and present, of the Low Dimensional Structures & Devices research group at Sheffield University.

My thanks.

for Ruth

Optical Characterisation of III-V Semiconductor Quantum Dots and Quantum Dot Structures

Adam Dennis Ashmore

University of Sheffield

Abstract

This thesis describes an extensive study of the optical properties of In(Ga)As/Ga(Al)As quantum dots, both singularly and in laser devices. For the optical characterisation, the spectroscopic techniques of photoluminescence (PL), photoluminescence-excitation (PLE) and electroluminescence (EL) have been used. Additionally, for studying submicron structures, sophisticated micro-PL techniques allowed excitation, and detection, of a single quantum dot.

A variety of special growth and fabrication techniques were used to isolate a single quantum dot from the rest of the ensemble. Firstly, a submicron mesa that isolated a single quantum dot was fabricated using e-beam lithography and dry etching techniques. Excitation intensity and wavelength dependence of the emission provided information about the nature of the exciton complexes in the dot and the absorption and relaxation of carriers in the structure. The linewidth of the single exciton, and the variation with temperature, was measured. Secondly, samples consisting of a single layer of InGaAs quantum dots incorporated within the intrinsic region of a GaAs/AlGaAs Metal-Insulator-Semiconductor type Schottky structure allowed sequential dot charging via variation of the gate bias. Both n- and p- type samples, grown under similar conditions, were investigated. Single quantum dots were probed through submicron apertures opened in the top metal contact using electron beam lithography and dry etching. The emission undergoes several pronounced changes as additional carriers are sequentially loaded into the dot. The results reveal direct information regarding Coulomb interaction and correlation effects in dots containing a controlled number of excess electrons (up to four) or holes (up to two). Magneto-optical results reveal further information about the few-particle wave functions.

A detailed study of the device performance and physical processes in In(Ga)As-Ga(Al)As self-assembled quantum dot lasers showed that these lasers offer several potential advantages over conventional quantum well lasers including low threshold current density, temperature insensitive threshold current density and high differential gain. Device performance (threshold current density and its variation with temperature) has been studied as a function of a number of parameters, including dot density, dot composition and dot confinement potential. The application of large (<14T) magnetic fields has been used to study carrier transport and dot carrier capture effects. When applied along the growth axis, such fields result in an increase in the threshold current density and a decrease in the external quantum efficiency. These effects are attributed to inhibited inplane carrier transport resulting in an increase in the carrier capture efficiency by non-lasing dots. Spontaneously emitted light, recorded via small windows formed in the top metallic contact, has been studied as a function of injection current and temperature. Analysis of this data provides information on non-radiative loss mechanisms and dot carrier dynamics.

Chapter 1

III-V Semiconductor Self-Assembled Quantum Dots

1.1 Introduction

Over the last three decades low dimensional semiconductors have become of increasing interest. They have provided many opportunities to produce novel applications and have also allowed much fundamental research in the field. The first reduction in dimensionality, the Quantum Well (QW), is now fully integrated into our lives. For example QW lasers are used in telecommunications and also in our CD players to name but two uses. Now science is trying to reduce the dimensionality even further and achieve even more benefits. This has become possible due to improving growth and fabrication techniques.

This chapter will first introduce the thinking behind the reduced dimensionality and highlight the potential advantages of such systems. Secondly, various methods used to produce zero dimensional systems will be outlined. Finally, the growth and basic characterisation of Quantum Dots (QD) grown by Molecular Beam Epitaxy (MBE), the chosen method of this thesis, will be outlined. This will include the basic principles that are used in the later chapters. The effect of increasing the carrier occupation and also the basic considerations when producing a QD laser will be introduced.

1.2 Quantum Confinement

It is the small length scales involved in Quantum Dots (QD) that lead to the most interesting phenomena. To gain an idea of the regime that is being discussed in this thesis a simple picture of quantum mechanics should be built up. If we model the quantum dot as a particle in a box, with infinite potential barriers[1], we find that the solution to Schrödinger`s equation is

$$E = \frac{\hbar^2}{2m^*}\left(\frac{n\pi}{D}\right)^2 \qquad \textbf{Equation 1-1}$$

where E is the energy of the level, m* is the effective mass of the electron or hole, n is an integer quantum number and D is the size of the dot. The energy of the discrete level is inversely proportional to the square of the size of the well. So long as the size of the potential well results in the energy difference between the quantised levels being larger than the thermal energy of the system kT, then the carriers will be governed by quantum mechanics rather than bulk-like statistics. Considering an electron in an InAs Quantum Well (QW) the maximum width is 125nm at Helium temperatures and 15nm at room temperature.

The formation of such a potential well can be achieved by creating a double-heterojunction (DH). A double heterostructure is produced by sandwiching one semiconductor material between two layers of another. The sandwiched layer is a lower bandgap material than the outer layers. Thus any carrier located inside the QW is confined, but the probability of finding the particle outside the boundary is finite and this decreases exponentially with distance away from the well. DHs thin enough

to observe quantum effects were first fabricated in the 1960s using liquid-phase epitaxy (LPE). The control of the layer thickness improved in the1970s with the introduction of molecular-beam epitaxy (MBE) and it is now possible to control the layer thickness to a single atomic layer.

InAs and InGaAs QDs exist in the strong confinement regime. Indeed the size of the QDs is smaller than the Bohr exciton radius of the bulk material (12nm for InAs). This results in a system whose properties are affected far more by the size of each QD than the properties of the bulk material. If the QD was much larger than the Bohr radius then the dipole of the exciton would be reliant on the bulk Bohr radius[2]. In the strong confinement regime where the QD is smaller than the Bohr radius the exciton dipole will be greatly dependent on the size of the QD.

1.3 Confinement Nomenclature

In the literature the dimensionality is normally cited as 3D for bulk material, 2D for a QW, 1D for a quantum wire and 0D for a QD (all three dimensions have been confined, so there are no degrees of freedom for the translational motion). However occasionally a QD will be referred to as 3D confinement referring to the number of confined dimensions. This thesis will use the former nomenclature. The literature, especially early work, may refer to QDs as quantum boxes, again referring to the fact that all three dimensions have been confined. The term QD will be used here.

1.3.1 Density of States

The electronic and optical performance of a device is controlled by the density of states (DOS), which is defined as the number of available electronic states per unit volume per unit energy at an energy E. The three dimensional confinement of carriers in a QD provides an electronic density of states that is a series of delta functions at the discrete energies of the confinement states[3,4].

In a bulk material, where there is no confinement in any direction, the allowed states in **k**-space are contained in a sphere. Any extra states are placed on the surface of the sphere in a volume

$$4\pi k^2 dk \qquad \textbf{Equation 1-2}$$

In a sample of size L^3 Each point in **k**-space occupies a volume

$$\left(\frac{2\pi}{L}\right)^3 \qquad \textbf{Equation 1-3}$$

The number of **k** states within the range **k**→**k**+d**k** is therefore

$$\left(\frac{k^2}{2\pi^2}\right)Vdk \qquad \textbf{Equation 1-4}$$

where the volume

$$V = L^3 \qquad \textbf{Equation 1-5}$$

Each electronic state can have two spin orientations so the number of electronic states per unit volume in **k**-space is

$$g(k)dk = \frac{k^2}{\pi^2}dk$$ **Equation 1-6**

Converting this to an energy range of E→E+dE using $g(E)dE = g(k)dk$ and assuming that E(**k**) has the parabolic relation

$$E = \frac{\hbar^2 k^2}{2m^*}$$ **Equation 1-7**

the electronic density of states for a bulk material is

$$g(E) = \frac{1}{2\pi^2}\left(\frac{2m^*}{\hbar^2}\right)^{3/2} E^{1/2}$$ **Equation 1-8**

1.3.2 3D Density of States

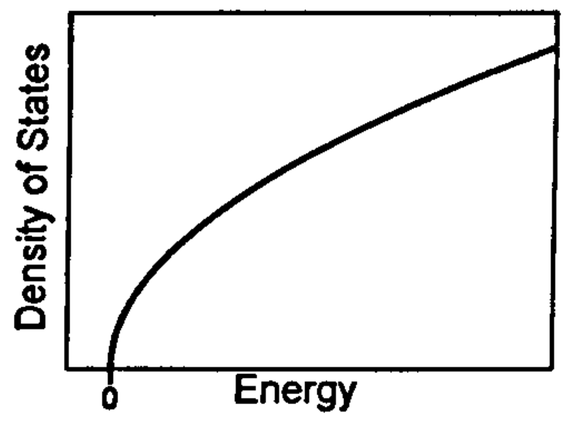

Figure 1.1 3D Density of States

The electronic properties of a semi-conductor are described by the DOS, the thermal energy in the system and also the Fermi level of the system. Electrons are fermions and by the Pauli exclusion principle cannot exist in identical energy states. So at absolute zero they occupy the lowest available energy states up to a maximum Fermi level. Carriers injected into the sample will relax to the lowest energy state available

that is defined by the DOS. At higher temperatures a certain fraction, characterised by the Fermi function, will exist above the Fermi level. This level is governed by Fermi-Dirac statistics and is a function of the temperature T. Both these effects contrive to produce broad emission spectra. Figure 1.2 shows the emission from bulk GaAs. The high power excitation and the thermal broadening have caused the emission to be very broad (~10meV). The recombination is not just occurring from states at the band gap but also from the higher energy states.

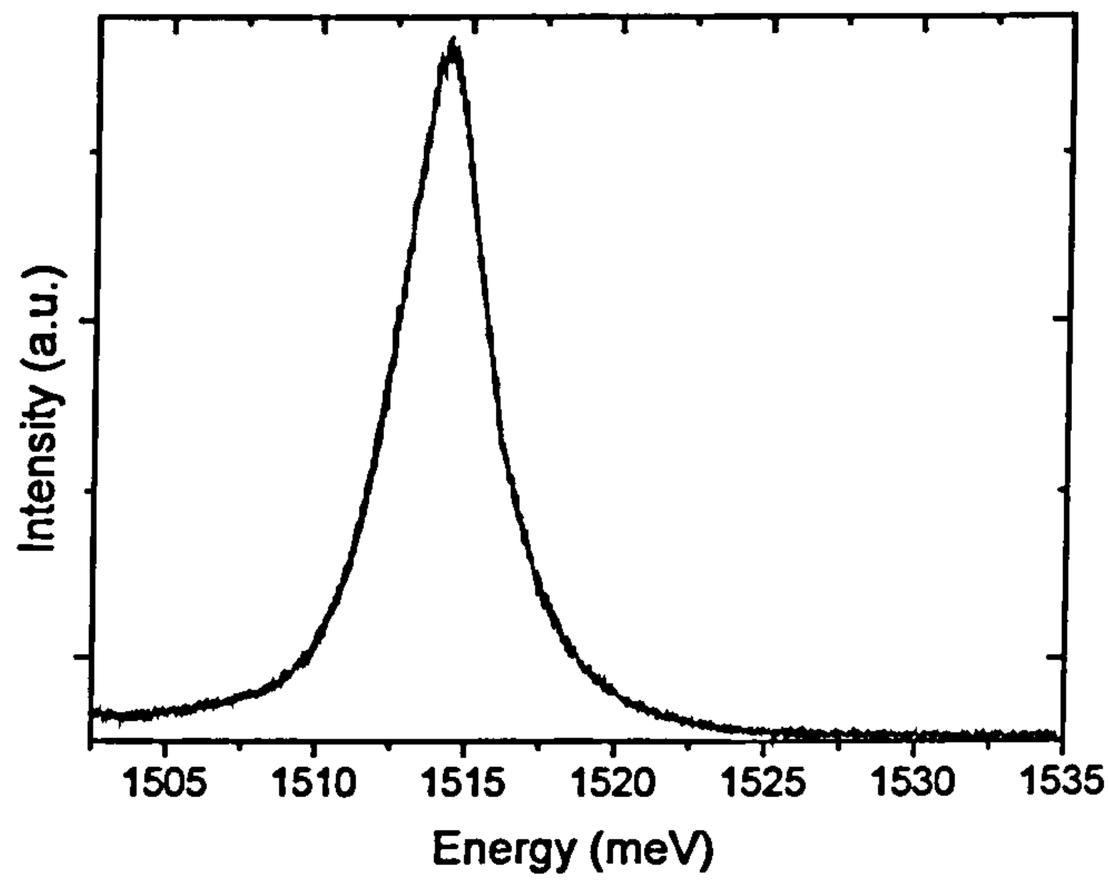

Figure 1.2 GaAs bulk emission. T=20K. Excitation energy 1.95eV.

1.3.3 2D Density of States

In the two dimensional case the density of states is derived from the assumption that the **k**-space states are confined to a circular area within the 2D plane as opposed to a spherical volume. Otherwise the derivation is similar and provides an electronic density of states that is constant with energy.

$$g(E)_{[2D]} = \frac{m^*}{\pi\hbar^2}$$ **Equation 1-9**

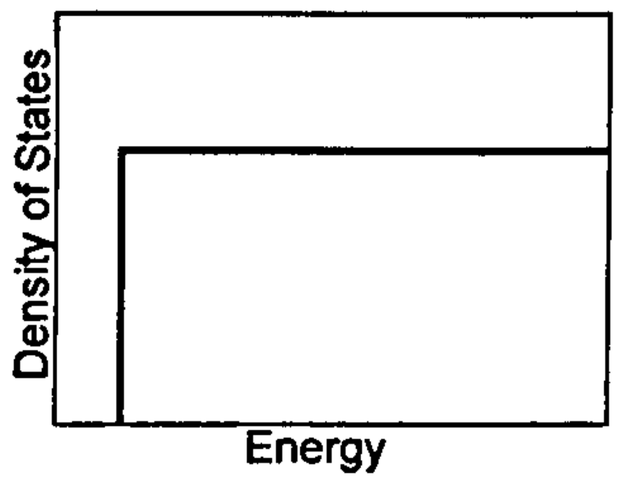

Figure 1.3 2D Density of States

In the early 1970s Henry predicted the advantages of using quantum wells[5] as the active layer in semiconductor lasers. The carrier confinement and nature of the electronic density of states should result in more efficient devices operating at lower threshold currents than lasers with "bulk" active layers. The first demonstration of a QW laser device was achieved by Van-der-Ziel et al. [6] in 1975. Although this first QW laser was much less efficient than a conventional laser, the situation was reversed through the use of new growth techniques like molecular beam expitaxy, and improvements in laser design[7]. An additional advantage of using a reduced dimensionality system is that the dependence of the energy levels on the quantum well width provides a means of "tuning" the resulting wavelength of the device.

1.3.4 1D Density of States

The one dimensional case is the quantum wire in which all the states lie on a straight line in **k**-space. When substituted into Equation 1.6 this results in a $E^{-1/2}$ dependence (Figure 1.1).

$$g(E)_{[1D]} = \frac{(2m^*)^{1/2}}{\pi\hbar^2} E^{-1/2} \qquad \textbf{Equation 1-10}$$

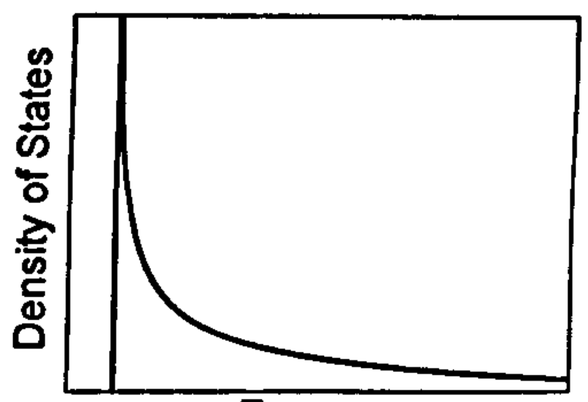

Figure 1.4 1D Density of States

Some work has been carried out on Quantum Wire systems, but generally they are more difficult than QDs to grow and do not offer the full benefits of a completely quantised system.

1.3.5 0D Density of States

In a zero dimensional quantum dot the density of states $g(E)_{[0D]}$ is effectively a δ-function (Figure 1.5). The electron is confined in all three dimensions and this leads to fully quantised energy levels. The electron can only have certain discrete energies in the quantum dot. The energy of the states and the number of states available depends on the shape and size of the dot potential.

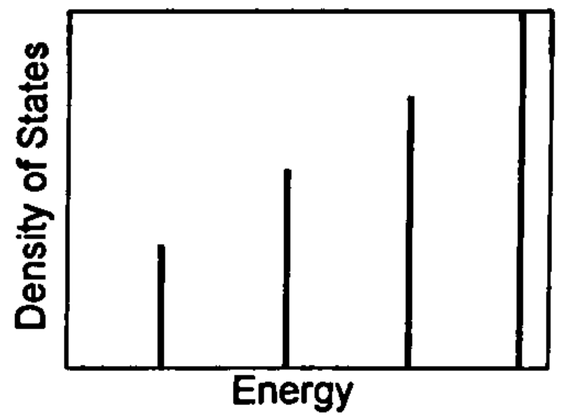

Figure 1.5 0D Density of States: Several levels are shown with an increasing, arbitrary degeneracy.

It has been shown that for a semiconductor laser the reduction in dimensionality should lead to an increase in efficiency, a decrease in the lasing threshold, less temperature dependence and narrower spectral lines[8]. In a quantum well only the electrons near the edge of the energy band will contribute directly to the gain at the lasing process. All the other electrons in the energy band are effectively wasted. In QDs at T=0 all the electrons are near the edge of the bands because the bands are extremely narrow (Figure 1.5) and therefore all the electrons can participate in the lasing process.

Energy levels are discrete in the [0D] case and can be considered atom-like. The degeneracy of the energy levels in a QD should follow a similar pattern to the atomic system, the lowest energy level being analogous to the s-shell and having a degeneracy of 2 (i.e. can contain a spin up and spin down carrier). Additionally any devices fabricated from such a material will have a temperature independent behaviour[8] as long as the sub level energy separations are much greater than kT.

1.4 Realisation of a 0D system

1.4.1 Precipitates in glass

The first 0D systems realised were fabricated from group II-VI materials in glass matrixes (Figure 1.6). Spherical clusters of CdSe or CdS could be formed in molten glass that were only a few tens of nm in diameter. In this system the glass is the barrier for the sandwiched II-VI material with the lower potential. CdSe in glass was the first development of nano-sized semiconductor crystals by Rocksby[9] in the 1930s. These have been commercially available for decades as colour filters. Quantum confinement effects were confirmed experimentally by Ekimov and Onushenko[10] in the 1980s. The electrically insulating glass matrix prohibits electric injection and hence has prevented their application in light-emitting divices.

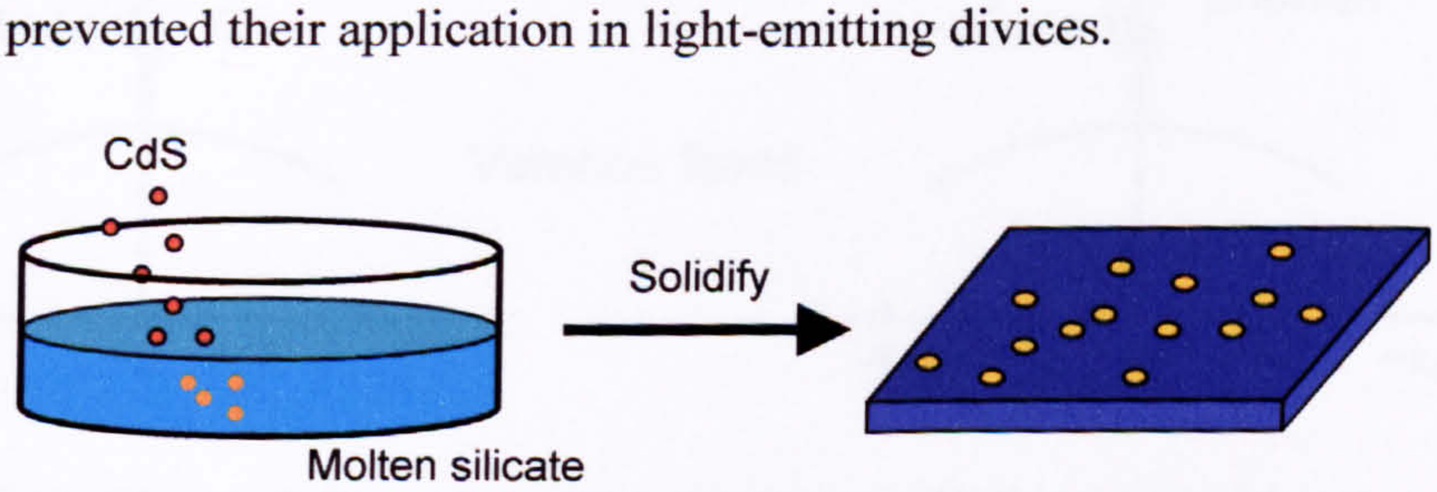

Figure 1.6 Precipitates in glass

1.4.2 III-V materials

The use of III-V materials has certain advantages over Silicon, especially in optoelectrical applications such as lasers. The relaxation of an electron in GaAs from the conduction band to the valence band is a direct transition involving only the emission of a photon (Figure 1.7). The conduction band minimum and the valence

band maximum occur at the same point in k-space allowing the emission of a photon to satisfy the conservation of both energy and momentum. However in Silicon the conduction band minimum does not coincide with the maximum in the valence band in k-space. The emitted photon has a very small momentum and can not provide the required momentum change to allow a transition. Consequently the simultaneous emission of a phonon is required to conserve momentum. This dual process is much slower than the single emission of a photon and hence indirect transitions are slower and become less likely in the presence of competing non-radiative processes.

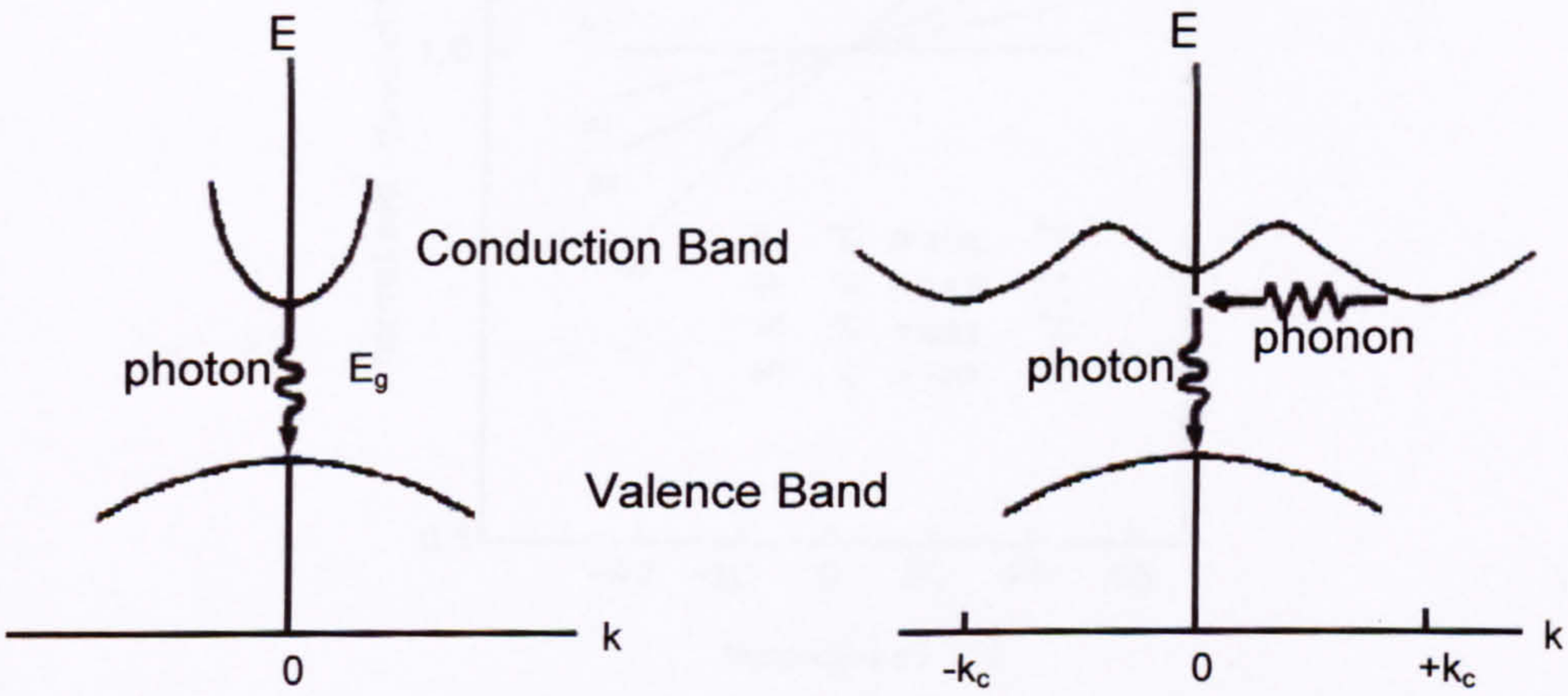

Figure 1.7 A Direct (left) and Indirect (right) radiative recombination process. The indirect transition is a two particle process and is slower than the one particle direct process.

1.4.3 Quantum Well in Magnetic Field

The first practical demonstration of the advantages of a system[11] that had less degrees of freedom than a QW was performed by Y.Arakawa and H.Sakaki. In this demonstration a large magnetic field was applied to a QW laser and the effect on the temperature dependence of its threshold current was investigated. An artificial 0D

system was created by confining the carriers in one dimension using the conventional QW and using the magnetic field to confine the carriers in the other two perpendicular directions. The authors showed theoretically and experimentally that a 0D laser should have temperature independent threshold current (Figure 1.8). The large magnetic field had the effect of confining the carriers in the two dimensions perpendicular to the QW confinement.

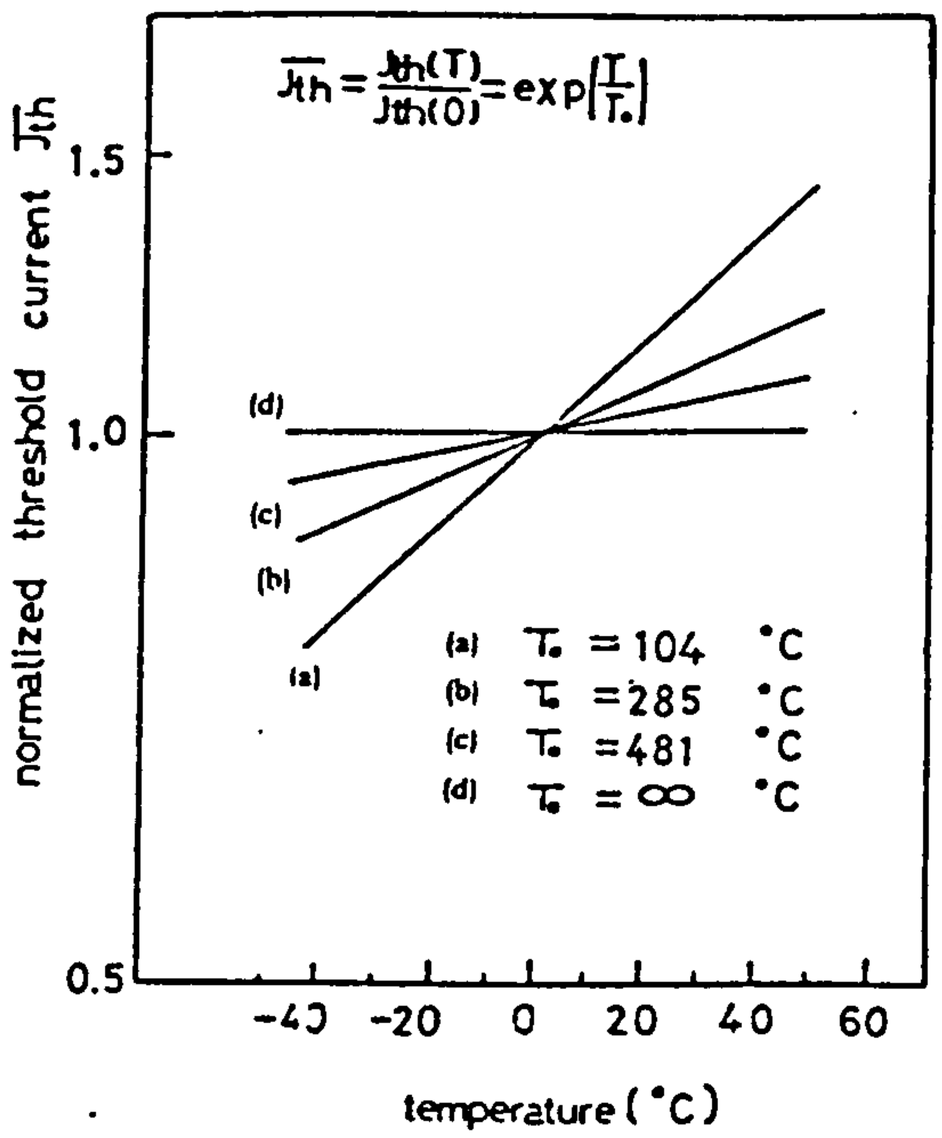

Figure 1.8 Numerical example of threshold current J_{th} calculated by extending the model of Lasher and Stern[12] for (a) 3D conventional lasers, (b) 2D QW lasers, (c) 1D Quantum Wire lasers, and (d) 0D QD lasers (From Ref. 8).

1.4.4 Fabrication of Quantum Dots from a Quantum Well

The first attempt to fabricate a QD device used a QW as the starting point. A 2D QW layer was grown and the extra confinement was achieved using post growth fabrication techniques. A sub micron pillar structure was defined using e-beam lithography and chemical etching[13]. In this case the vertical confinement was

provided by a DH and the two horizontal confinements were provided by the circumference of the pillar (Figure 1.9). This method has not however been very successful because of the damage caused by etching, which increases rapidly as the size of the structure is reduced causing the intensity of the emission to fall dramatically[14]. It is possible to fabricate QDs of a size down to ~10nm, but it has proved impossible to extract bright luminescence from the smallest structures.

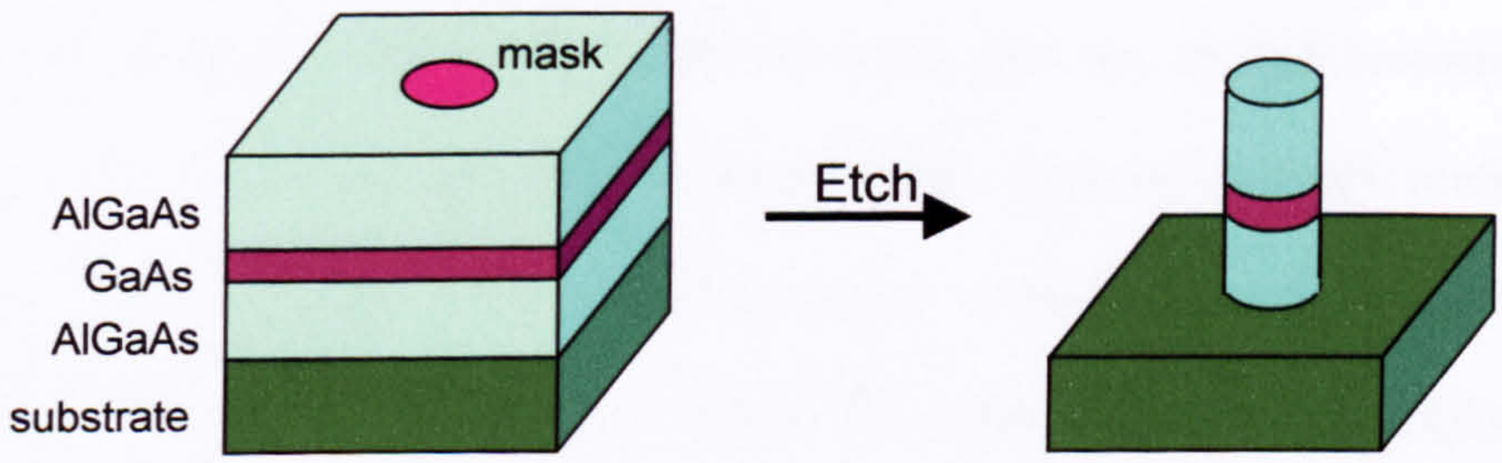

Figure 1.9 Fabrication of a GaAs/AlGaAs QW into a QD (2D-0D)

1.4.5 Self-assembled growth of 0D systems

Self-assembled QDs can form naturally when specific growth conditions are satisfied. The QDs discussed during this thesis are grown by Molecular Beam Epitaxy (MBE). In this technique differing semiconductor materials are deposited on a substrate and the sample is built up layer by layer (Figure 1.10). When growing a structure with different layers an important parameter to consider is the lattice constant. Each material has a different lattice spacing (Figure 1.11). When two layers of material are grown that have differing lattice constants, the second layer becomes extremely strained as it tries to adopt the lattice constant of the first layer. It is interesting to note that GaAs, $Ga_xAl_{1-x}As$ and AlAs all have a similar lattice constant and that growing alternating layers of these materials is easy, allowing simple structures to be grown. InAs and GaAs have a lattice constant difference (or lattice mismatch) of 7%.

This means that up to a critical thickness a perfect InAs QW (albeit highly strained) can be grown on a GaAs layer. However, above the critical layer thickness (approximately 1.8 to 2.4 monolayers) the strain energy becomes too great and is released by the formation of defects and dislocations or by the formation of nm sized islands (QDs) on the surface of the InAs QW (or the wetting layer, WL). This growth phenomenon (although not using MBE) was first investigated[15] in the 1930s and is called the Stranski-Krastanow (S-K) growth mode after the original researchers. By carefully controlling the growth conditions some material systems preferentially undergo island formation[16]. Generally this occurs when the thickness of the layer is only slightly larger than the critical thickness[17,18], in the case of In(Ga)As QDs usually between 1.7 and 2.4 monolayers. The precise details of the growth conditions used to form the dots studied in this work will be outlined in the experimental chapters.

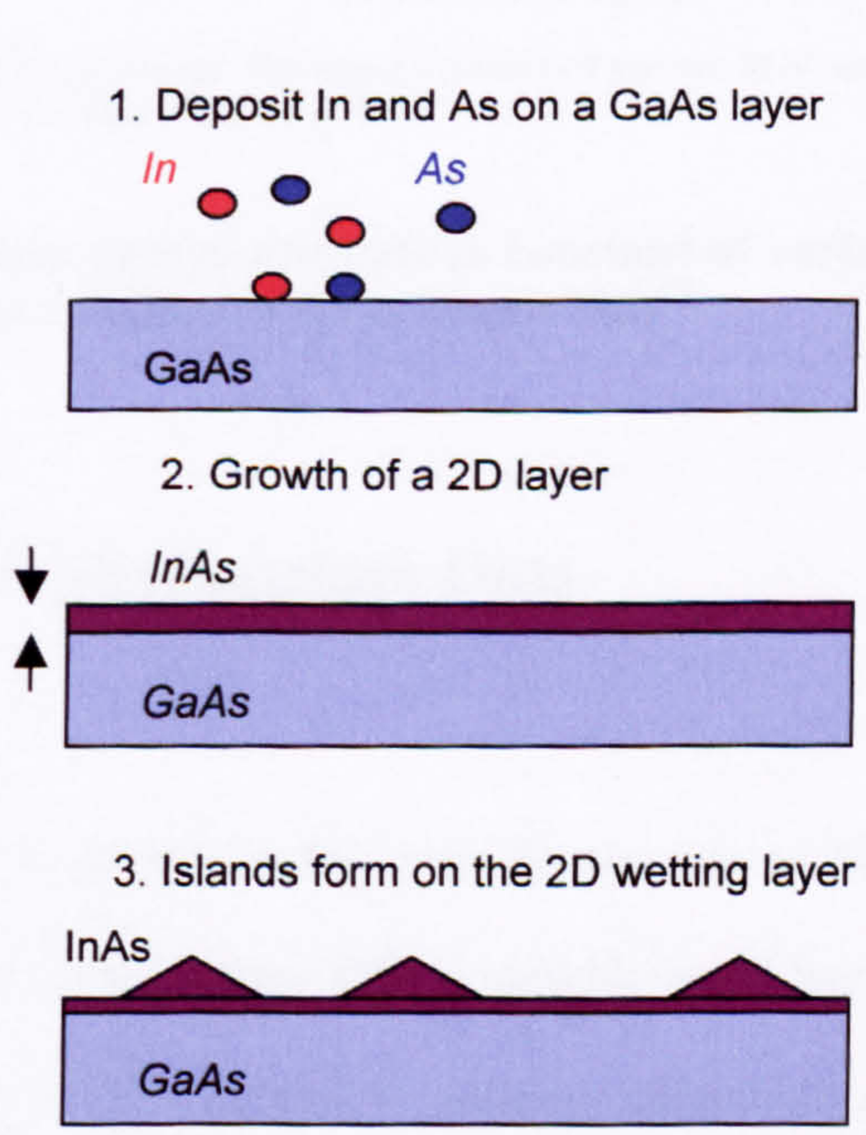

Figure 1.10 Schematic of S-K growth. 1. The thin layer of InAs is deposited on GaAs matrix. 2. This layer is built-up, growing a QW. 3. After a critical thickness is reached the layer undergoes a 2D to 0D transition, with InAs dots growing on a QW-like wetting layer.

The earliest attempts to grow QDs by the S-K growth mode were made by L. Goldstein et al. in the mid 1980s[19]. Using TEM imaging techniques they observed regular (self organised) island formation in an InAs/GaAs superlattice.

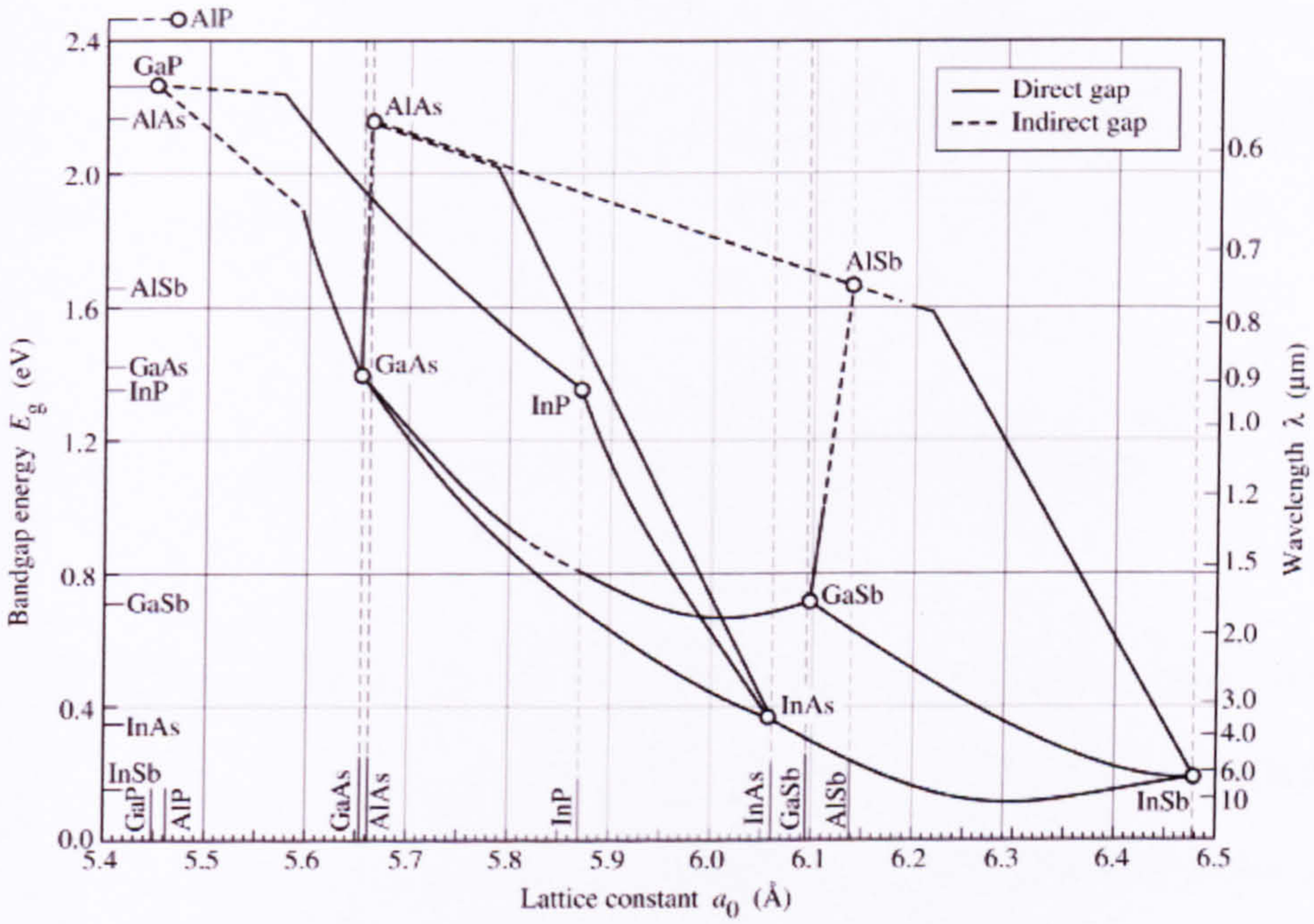

Fig. 7.6. Bandgap energy and lattice constant of various III-V semiconductors at room temperature (adopted from Tien, 1988).

Figure 1.11 Bandgap energy and lattice constant of various III-V semiconductors at room temperature (adapted from Tien 1988)[20]

1.5 Ensembles of Quantum Dots

An advantage of S-K growth is the large density (up to $10^{11}cm^{-2}$) of QDs produced during growth. This makes these QDs a suitable candidate for laser devices as there are a larger number of QDs present to undergo stimulated emission, which increases the gain that is available.

However, the mechanism behind the formation of these islands does not yield dots with a large degree of uniformity. The variation of the QD size produces inhomogeneous broadening of the emission of a self-assembled QD sample, with linewidths of tens of meV being typical (Figure 1.12 and Figure 1.13). The emission spectra is comprised of the emission of a very large number of QDs all with slightly different recombination energies.

1.5.1 Emission Spectra Dependence On Carrier Density

The following section will briefly discuss the changes that occur in the emission spectra as the QDs are loaded with more carriers. These will be discussed with reference to a simple p-i-n structure that is presented in more detail in Chapter 3. The QDs can be loaded with carriers electrically by the application of a bias across the sample. Figure 1.12 shows the change in the emission spectra as the current is increased and more carriers are loaded into the QDs. At low currents (low carrier densities) the spectra consist of two peaks. As the current increases the higher peak becomes dominant and extra peaks develop at higher energies. This corresponds to recombination from higher order states in the QDs analogous to the $n \geq 2$ transitions in the Helium atom.

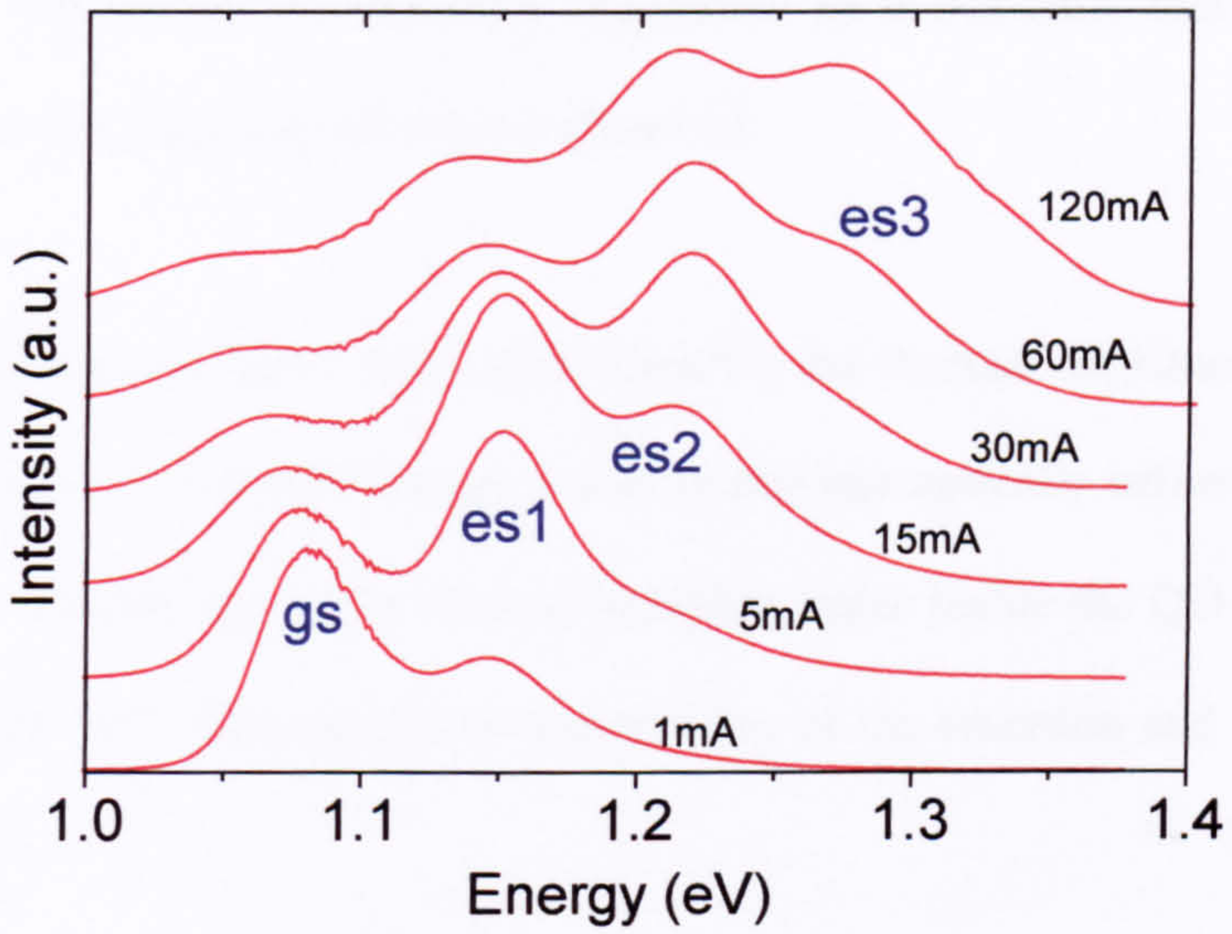

Figure 1.12 QD Ensemble emission from a mesa of diameter 400μm at T=80K. There is a slight shift to lower energy due to heating (§1.5.2) from the applied CW current.

1.5.2 Temperature dependence of PL emission.

The overall effect of temperature on the QD emission is shown in Figure 1.13. The overall shift of the QD emission to lower energies is caused by bandgap narrowing. The emission undergoes a slight enhancement in intensity along with a reduction of the inhomogeneous linewidth between 0K and 100K, followed by a broadening of the linewidth and decrease of intensity from 100K to 300K. The PL spectrum red-shifts faster than the band gap of the material (Figure 1.13)[21]. At low temperature (T<100K) the carriers are captured by all the QDs randomly. Once captured the carriers in the QDs cannot be thermally excited out (kT<9meV) so the emission reflects the natural distribution of the QD ensemble. As the temperature increases the narrowing of the linewidth is a result of carrier thermalisation increasing the mobility of the carriers in the 2D wetting layer. QDs are preferentially captured by larger QDs that have an increased confinement potential. As the carriers populate these QDs

more readily the energy of emission decreases, so a red-shift that is of greater magnitude than the bandgap red-shift is observed.

At higher temperatures, up to 300K (kT=25meV), the thermal distribution of carriers causes the higher excited state energy levels to become optically active and broadens the emission. Carriers are easily excited to higher states inside the QD and thermally ionised from the QD. This results in a quenching of the emission and a widening of the linewidth[22].

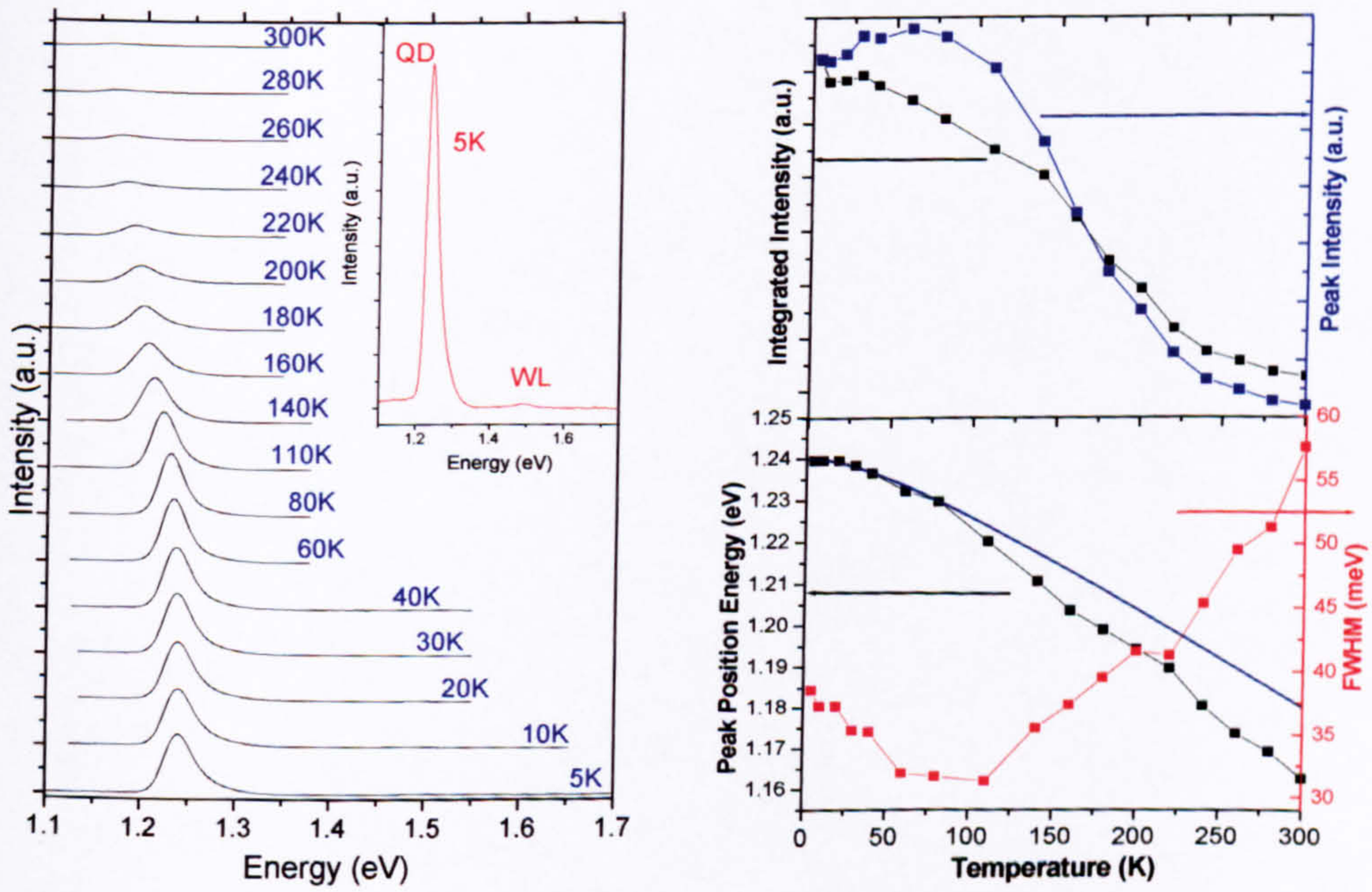

Figure 1.13 Left: Temperature dependence of the PL from a QD ensemble. Insert shows a close-up of the 5K spectra, showing the wetting layer position. Right: Temperature dependence of the intensity (both integrated and peak), the peak's energy and the full-width-half-maximum FWHM linewidth. The relative band gap shift of InAs is shown in dark blue for comparison.

1.6 Growth conditions

There are many parameters that can be altered during the growth and although it is not the scope of this thesis to investigate the exact nature of them all it is necessary to draw attention to their importance. In further chapters some of these parameters are exploited to manufacture QDs with the desired characteristics (i.e. improved uniformity, optimum density). The major parameters are V/III ratio, growth rate, temperature and the amount of material deposited (layer thickness). All of these can be used to control the shape, size, density, composition and uniformity of the QDs.

The layer thickness is extremely important because island formation only occurs immediately after the critical thickness has been surpassed. However this can be monitored in-situ during growth by studying the RHEED (Reflected High Energy Electron Diffraction) pattern. When the surface undergoes the transition from a flat QW layer to the QD layer after island formation, the diffracted e-beam pattern changes dramatically allowing easy identification of the onset of QD growth.

All the samples studied in this thesis were grown by M. Hopkinson at the EPSRC Central Facility for III-V Semiconductors located in the Electronic and Electrical Engineering Department, The University of Sheffield.

1.6.1 V-III Ratio Growth Parameter

An important growth parameter is the V/III flux ratio parameter. This is the ratio of the flux of Arsenic to Indium that is used to deposit the QD layer on the surface of the sample. In fact a change in most of the other parameters results in a change to the V/III flux ratio. The MBE machine used does not permit a change in the As_2 flux, so any change in growth rate is controlled by a change in the In flux. This has an effect on the V/III ratio. A high growth rate is considered to be $0.1MLs^{-1}$ and this has the corresponding ratio of $f_{As}/f_{In}=14$ where f is the flux rate of each element. A relatively slow growth rate of $0.01MLs^{-1}$ thus has a much larger ratio of $f_{As}/f_{In}=140$. An increase in temperature allows much larger mobility of the In during growth. This has the same effect as increasing the In flux. The main results are presented in Figure 1.14. Emission from both the QDs at approximately 1025nm and the underlying 2D WL at 875nm can be seen. Figure 1.14 shows that an increase in the As_2 flux relative to the In flux decreases the wetting layer emission with respect to the QD emission due to the increase in the density of the QDs formed. An increase in the V-III ratio also shifts the QD emission to longer wavelength, indicating a change in the QD size, shape and composition. For example an increase in the QD size would produce this effect. The emission becomes more complex and very broad for the highest ratio investigated, indicating poor growth. Figure 1.15 shows that the emission intensity increases as the V/III ratio is increased, indicating that a greater density of QDs have been produced.

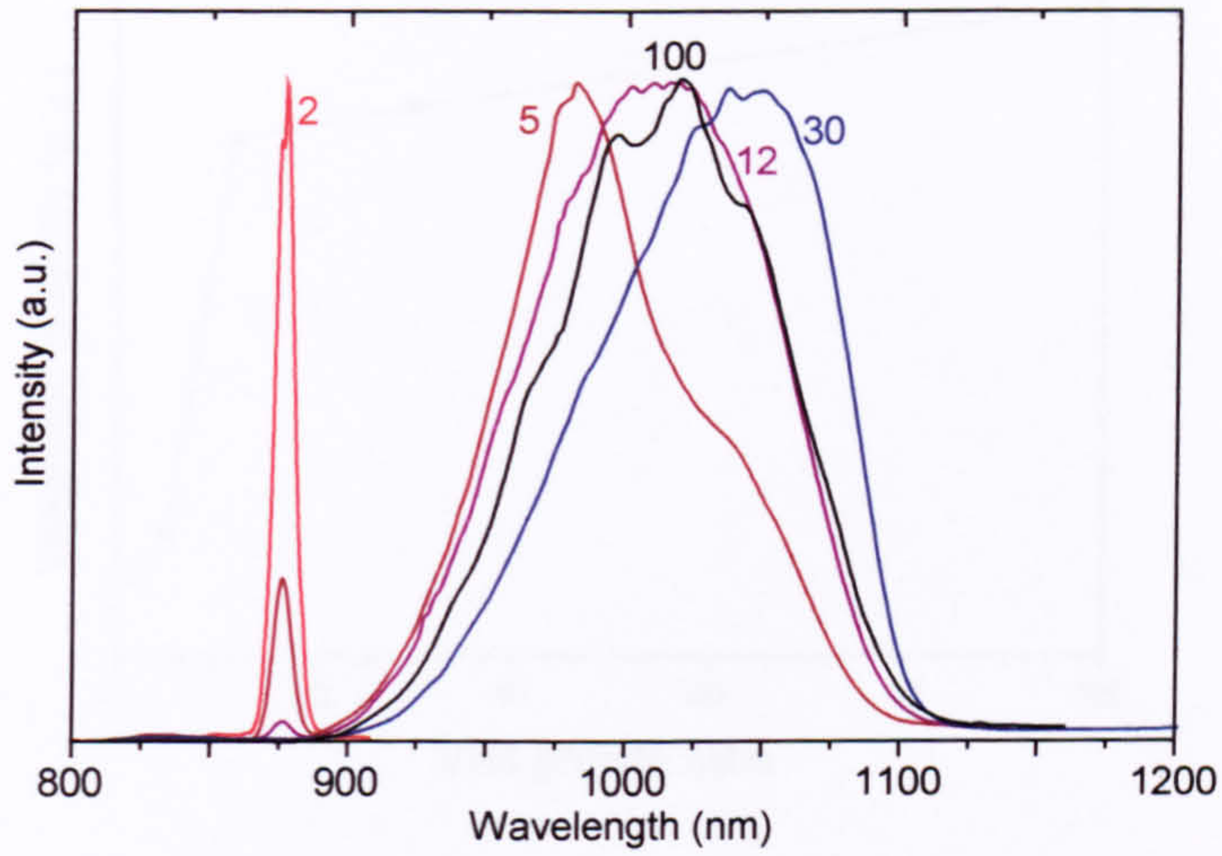

Figure 1.14 Normalised PL emission of samples grown with varying V/III ratio. Excitation is at 488nm T=10K. The emission from structures with As/In ratios of 2 (red), 5 (brown), 12 (purple), 30 (blue) and 100 (black) are plotted.

The threshold V/III ratio for dot formation is between 2 and 5. This is highlighted in Figure 1.16 where a shift of the main emission peak is observed, as the QD formation becomes dominant. The increase in QD density causes an increase of the integrated PL intensity of the sample. The V/III ratio also affects the emission wavelength of the QD ensemble with higher ratios resulting in emission at lower energies due to a change in the size, structure and composition of the QDs. A shift to lower energy indicates an increase in the size of the QDs. At very large V/III ratios we see that the emission becomes complex and shifts back to higher energies. At this high ratio the growth has become non-uniform and uncontrollable.

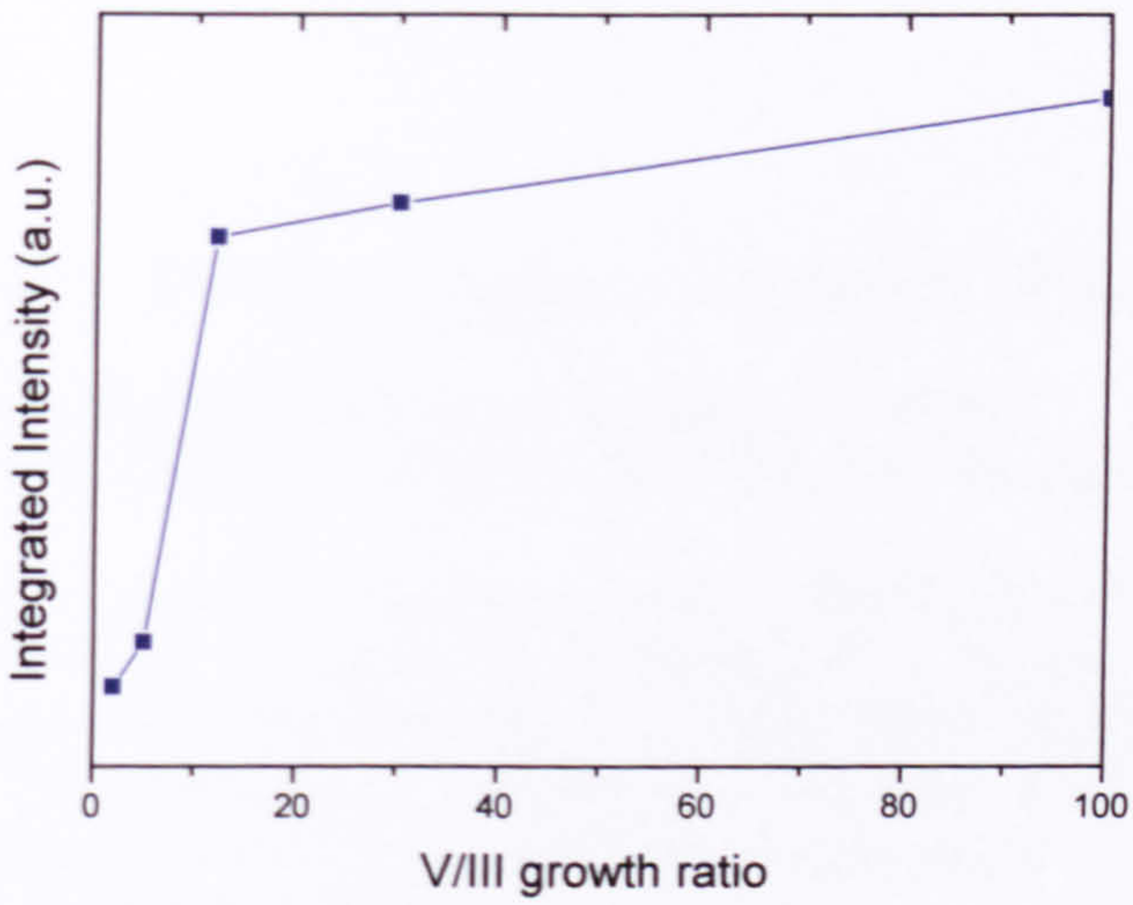

Figure 1.15 Variation of PL intensity with increasing V/III flux ratio.

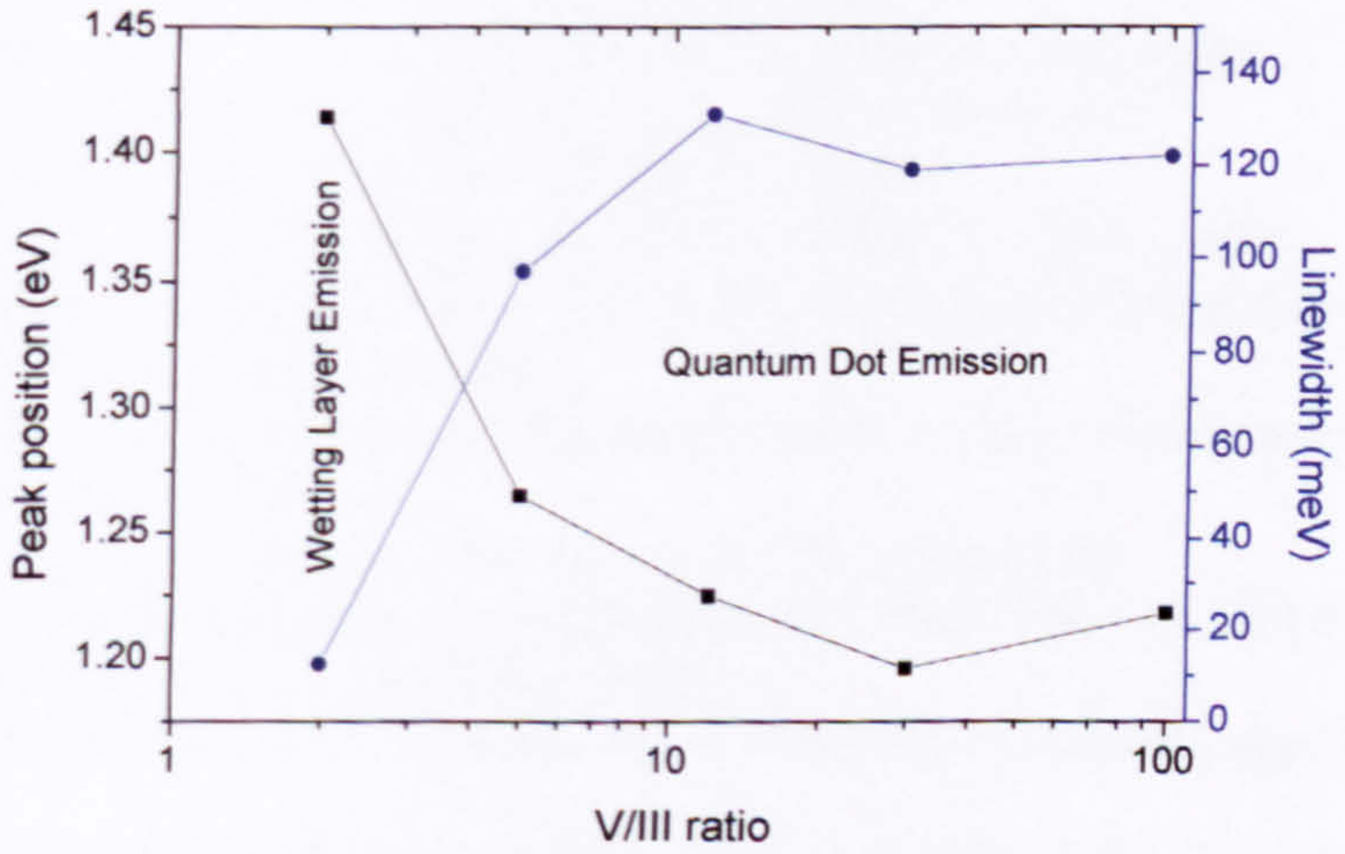

Figure 1.16 Variation of FWHM and PL peak position with increasing V/III flux ratio.

[1] A.P. French and E. F. Taylor, *Introduction to Quantum Physics*, Chapman & Hall (1994)
[2] C. F. Klingshirn, *Semicondutor Optics*, Springer p169 (1997)
[3] J. Y. Marzin, J. M. Gerard, A. Izrael, D. Barrier and G. Bastard, *Phys. Rev. Lett.*, **73**, 716 (1994)
[4] D. Bimberg, N. N. Ledentsov, M. Grundmann, N. Kirstaedter, O. G. Schmidt, M. H. Mao, V. M. Ustinov, A. Y. Egorov, A. E. Zhukov, P. S. Kopev, Z.I. Alferov, S. S. Ruvimov, U. Gosele and J. Heydenreich, *Jpn. J. Appl. Phys.*, **35**, 1311 (1996)
[5] R. Dingle, W. Wiegmann, and C. H. Henry *Phys. Rev. Lett.* **33** (14), 827 (1974)
[6] J. P. van der Ziel, R. Dingle, R. C. Miller, W. Wiegmann, and W. A. Nordland, Jr. *App. Phys. Lett.* **26** (8) 463-5 (1975)
[7] W. T. Tsang, *Appl. Phys. Lett.* **38**, 835 (1981)
[8] Y. Arakawa and H. Sakaki, Appl. Phys. Lett. **40**(11), 939 (1982)
[9] H.P Rocksby, *J. Soc. Glass Techn.* **16**, 171 (1932).
[10] A. I. Ekimov And A. A. Onushchenko Jetp Lett **40**(8) 1136 (1984)
[11] Y.Arakawa and H.Sakaki - App. Phys. Lett. **40**(11) 939 (1982)
[12] G. Lasher and F. Stern, *Phsy. Rev. A* **133** 553 (1964)
[13] A. Scherer and H. G. Craighead, *Appl Phys Lett* **49**(19) 1284 (1986)
[14] A. Forchel, H. Leier, B. E. Maile, and R. Germann *Festkorperprobleme (Advances in Solid State Physics)* **28**, 99 (1988)
[15] I. N. Stranski and L. Krastanow *Sitzungsberichte d. Akad. Wissenschaften in Wien, Abt. Iib, Band* **146**, 797 (1937)
[16] J. Tersoff and R. M. Tromp, *Phys. Rev. Lett.* **70**, 2782 (1993)
[17] S. Guha, A. Madhukar and K. C. Raijkumar, *Apl. Phys. Lett.*, **57**, 2110 (1990)
[18] J. Drucker, *Phys. Rev. B., **48**, 18203 (1993)*
[19] L. Goldstein, F. Glas, J. Y. Marzin, M. N. Charasse, G. Leroux, *Appl Phys Lett* **47**, 1099 (1985)
[20] L.A.Coldren and S.W.Corzine, *Diode Lasers and Photonic Integrated Circuits*, Wiley (1995)
[21] A. Patanè, M. G. Alessi, F. Intonti, A. Polimeni, M. Capizzi, F. Martelli, M. Geddo, A. Bosacchi and S. Franchi, *Phys. Status Solidi A* **164**, 493 (1997)
[22] Z. Y. Xu, Z. D. Lu, X. P. Yang, Z. L. Yuan, B. Z. Zheng, J. Z. Xu, W. K. Ge, Y. Wang and L. L. Chang, *Phys Rev. B* **54** 11528 (1996)

Chapter 2

Experimental Techniques

2.1 Introduction

This chapter will outline the standard experimental techniques used in the optical spectroscopy of III-V semiconductor materials. The finer points of both experimental techniques and also growth and fabrication techniques are outlined in the relevant chapters. This chapter's aim is to cover the procedures that form the basis of the more complex experiments, to avoid repetition and to allow more convenient discussion of the relevant aspects.

2.2 Experimental procedures

2.2.1 Photoluminescence (PL)

Photoluminescence (PL) experiments can reveal much about a sample and involve measuring the emission that has been excited by an external light source (usually a strong monochromatic source of light such as a laser). The excitation photons are absorbed by the material creating electron-hole pairs. These undergo relaxation in the sample and are emitted at a lower energy, usually the bandgap of the material under investigation. In the PL experiments undertaken in this thesis three different laser

sources where used. These were a Helium-Neon (HeNe) laser (emission wavelength=632.8nm), an Argon ion (Ar^+) laser (488.0nm) or a tuneable Titanium-Sapphire (Ti:Sapphire) laser (700-1100nm). The Ti:Sapphire laser could be computer controlled to allow Photoluminescent-excitation (PLE) spectra to be recorded. This technique requires the measurement of luminescence at a fixed energy while the excitation energy is varied (by altering the emission of the Ti:Sapphire laser) This technique will be discussed in greater detail in Chapter 5. Using sophisticated imaging techniques to allow the accurate positioning of the excitation laser spot and also the detection area allows sub-micron structures to be probed. This, so-called Micro-PL, technique will be outlined in more detail in Chapter 4 and is used in Chapters 4,5 and 6.

2.2.2 Electroluminescence (EL)

A current source is used to provide a forward bias to the pn junction. Either a constant current source or a pulsed source, which reduces heating in the sample, was used. Pulsed measurements were carried out with a lock-in, a duty cycle of 0.01% and a pulse width of 0.3μs. Current-Voltage (IV) measurements used a computer controlled voltage source. This had a compliance that was set to either 20mA or 100mA.

2.2.3 Detection

The optical studies of the samples required the detection of the emission. The type of detection falls under two distinct types, broad band or spectrally resolved.

Broad, multi-wavelength detection was used for the laser devices to study the lasing performance. The total emission from the sample was measured to determine the lasing threshold (§2.2.2). A photo-diode is used to record the emitted light and both CW and pulsed light verses current (LI) were recorded. These characteristics allow the threshold current of the device to be determined.

Spectroscopic measurements were performed using a double 0.85m spectrometer with 1200lines.mm^{-1} 700nm blazed gratings giving a resolution of 0.45nm.mm^{-1} slit width. This spectrometer provided excellent stray-light rejection qualities that made it ideal for the PLE experiments performed in Chapter 5.

Detection was performed by either a nitrogen cooled Germanium p-i-n photodiode (Chapter 3), an avalanche Silicon photodiode (Chapter 4-6) or a mutlichannel liquid nitorgen cooled Silicon Charge Coupled Device (CCD) array (Chapter 4-6). The Germanium detector was sensitive from 800nm-1700nm and used for the laser characterisation study. The Silicon based detectors were sensitive for wavelengths less than 900nm, but their high efficiency made them suitable for the single QD work performed in this thesis.

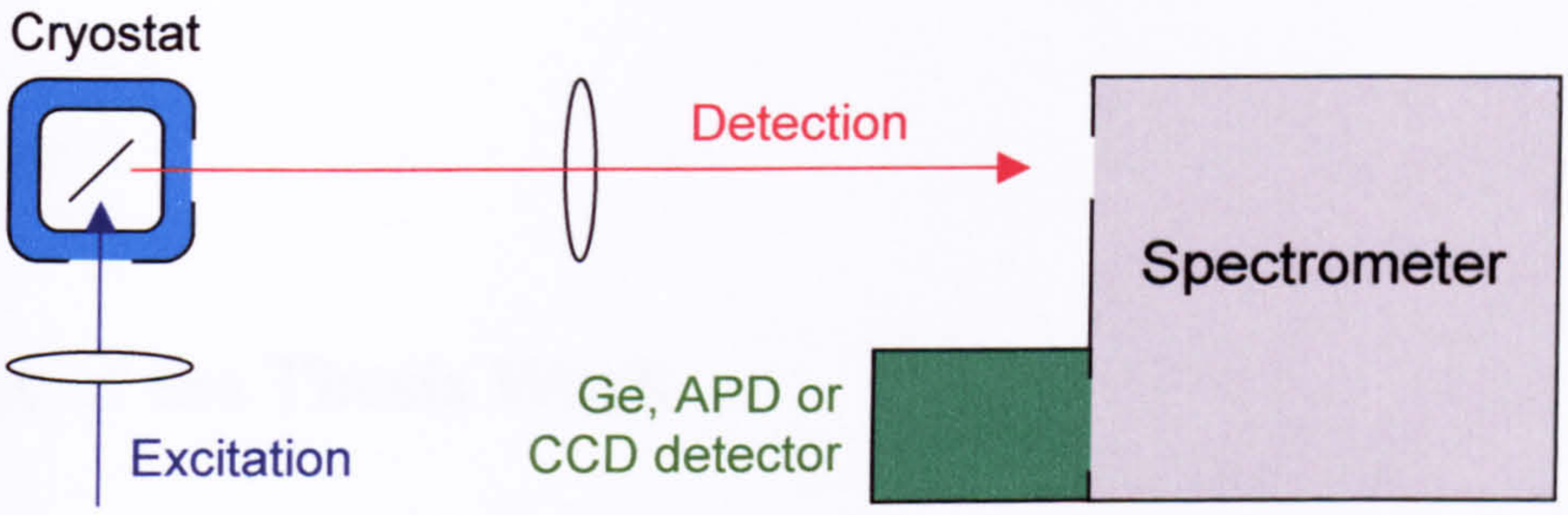

Figure 2.1 Schematic showing the basic PL and EL set-up.

2.2.4 Low temperature control

The temperature measurement range used in this thesis is from Helium temperatures (4.2K) to above room temperature 320K. The experiments were performed in an Oxford Instruments continuous flow Helium cryostat, a Nitrogen cryostat or a Helium cooled finger cryostat. An electrical heater was used to vary the sample temperature, and this was controllable to an accuracy of 0.1K

2.2.5 Magneto-optical investigations

Two superconducting magnets were used. Chapter 3 utilises an Oxford Instruments 14T vertical bore magnet. The magneto-optical results described in Chapters 4 –6 are performed using an Oxford instruments mini-magnet, which fits around a separate finger cryostat. All results were performed in the Faraday geometry.

Chapter 3

Outline of the Thesis Work

3.1 Introduction

The experimental work contained in this thesis concerns the optical properties of both single isolated QDs and QDs embedded in waveguide structures. The EPSRC Central Facility for III-V Semiconductors fabricated all the QD samples. This chapter consists of a brief outline of the experimental results in each chapter. The single QD investigations are in Chapters 4-6 and the QD laser device studies in Chapter 7.

3.2 Chapter 4: Photoluminescence Studies of Single Quantum Dots

In Chapter 4 several experimental techniques including μ-PL and μ-PLE are used to investigate the emission from a single QD isolated in a sub-micron mesa. The fabrication of the sample and the novel excitation and detection techniques used will be outlined. This includes a detailed description of the μ-PL set-up, which is utilised in chapters 4-6. Single QD emission is observed and the linewidth is found to be extremely narrow. Additionally, multi-particle complexes are identified and the many body interaction strengths are deduced. Finally the sample is placed in a magnetic field to aid further identification of the emission lines.

3.3 Chapter 5: Absorption Processes and Carrier Relaxation in Single Quantum Dots

Chapter 5 discusses carrier relaxation in a single QD by studying the photoluminescence excitation (PLE) of the same single QD as studied in Chapter 4. Particular attention is paid to the efficient carrier relaxation resulting from LO phonon emission. The results presented will show that LO phonon relaxation is possible because of the many phonon energies available and also due to LO+LA phonon coupling. It will also be shown, as expected, that the relaxation is greatly enhanced by the presence of a resonant state.

3.4 Chapter 6: Charge Tuneable Single Quantum Dots

Chapter 6 discusses the interactions between charged carriers in a QD by studying a single QD embedded in a Schottky structure. The details of this structure along with the mechanisms for loading the QD with single carriers are presented. Charged excitons with up to four excess electrons and up to two excess holes are observed. This enables direct measurement of the Coulomb and exchange interactions and provides evidence for the lifting of the p-shell degeneracy. Additionally Stark shift measurements reveal the nature of the electron and hole wavefunctions. Magneto-optical results show g-factors and diamagnetic shifts which are dependent upon the charge species present in the QD.

3.5 Chapter 7: Characterisation of Electrically Pumped In(Ga)As/GaAs Quantum Dot Lasers

In Chapter 7 work is presented on the characterisation of QD lasers including the threshold current and temperature dependence of the threshold current. A comparative study of various laser designs is presented. The effect of the number of layers, the QD density, the thickness between the layers and also the general design will be discussed. Simple Fabry-Perot devices were fabricated to allow easy comparison between samples. The work centres on achieving a truly temperature independent laser device with a low threshold current density and includes the realisation of room temperature operation.

The QD ensemble is comprised of many individual QDs and the interaction between these QDs is studied. Special QD laser devices were fabricated that contain a window in the top contact allowing the spontaneous emission to be studied above threshold. A direct measurement of QD transitions that do not undergo lasing revealed that there is no pinning of the Fermi level throughout the inhomogeneously broadened QD ensemble. Additional work will be presented on the effects that a high magnetic field (<14T) has on the performance of a QD laser.

Chapter 4

Photoluminescence Studies of Single Quantum Dots

4.1 Introduction

The emission from a single quantum dot (QD) is expected to be very sharp (<100μeV), being limited by homogeneous broadening. However, studies of QD ensembles, which may contain 10^7 QDs, reveal very broad emission (>20meV) as a result of inhomogeneous broadening caused by unavoidable fluctuations of QD size, shape and composition. Hence, to observe the homogeneously broadened linewidth it is necessary to isolate and study a single QD[1]. Studies of single QDs allow processes which occur on an energy scale much less than the inhomogeneous linewidth to be investigated. A good example of this, and the subject of this chapter, is the influence of many carrier interactions on the optical spectra. However, the utilisation of single QDs has a number of practical applications, including quantum computation, single electron transistors, photon turnstile and single photon sources and detection for quantum cryptography[2].

Further studies of single QDs concern the spin state of the confined carriers. This is of interest for fundamental physics, but may also have a number of applications. The rapidly expanding field of "spintronics" utilises spin instead of charge for applications

such as spin transistors and circularly polarised light emitting diodes. It has also been proposed that spin effects could be used in quantum computing. The recent observation of long spin-coherence times in semiconductor nanostructures suggests that control of the spin state of a carrier, in conjunction with confinement in a quantum dot, could be used to create a quantum entangled state, a process necessary for the creation of a "q-bit" in quantum computing[3].

In the present chapter it is shown that the homogeneous linewidth of a single QD occurs on a scale of a few tens of μeV. Although much larger than atomic emission lines (<1μeV)[4,5], such linewidths are extremely narrow for a semiconductor system. The only comparable linewidth in a semiconductor system is for donor or acceptor bound excitons in extremely pure bulk crystals[6]. The narrow linewidths obtained from a single QD allow the influence of many body effects on the emission spectra, arising as the QD is populated with two or more excitons, to be studied. Such effects occur on an energy scale of a few meV and hence are not observable in ensemble QD studies. Although in the present chapter, because the carriers are created optically, the QD is generally uncharged (containing an equal number of electrons and holes). However due to unequal electron and hole capture probabilities under certain excitation conditions it is also possible to observe single charged excitons. Further work presented in this chapter includes magneto-optical spectroscopy, where a diamagnetic shift and spin-splitting of the exciton states is observed.

4.2 Review of related, previously published work.

The influence of excess electron occupation on the optical properties of QDs has been reported for large ensembles, using conventional spectroscopic techniques[7,8]. Detailed interpretation was, however, complicated by inhomogeneous broadening (>20meV), which obscured the Coulomb effects involving energy shifts at the <1meV level. More recently, the development of spatially resolved spectroscopic techniques has circumvented these problems, enabling the investigation of individual dots for which the broadening is purely homogeneous in nature. Using such techniques, the effects of many body Coulomb interactions in charge neutral dots[9,10,11,12,13,14,15] have been studied. Single QDs with a net charge (unequal electron and hole number) have also been studied. Such QDs can be created in a number of ways: the carriers can be provided by modulation doping[16] (and photodepletion effects may be used to modify the QD carrier density) or the QDs may be incorporated into FET like structures allowing carriers to be loaded into the QD in a controlled way[17]. In addition, unequal electron and hole capture probabilities may allow simple optical excitation to result in a charged QD although this technique is somewhat uncontrollable.

Initial attempts at isolating a single QD both spatially and spectrally were performed by Gammon et al.[18]. In this work sub-micron apertures were formed in an opaque metal mask that was deposited on the sample surface. Apertures of sizes ranging from 25 μm to 0.5μm in diameter were formed using electron beam lithography in a 100 μm thick layer of Aluminium. For these samples the QDs were formed from well width

fluctuations in GaAs-AlGaAs quantum wells. These fluctuations provide in plane carrier confinement in addition to the vertical confinement provided by the quantum well.

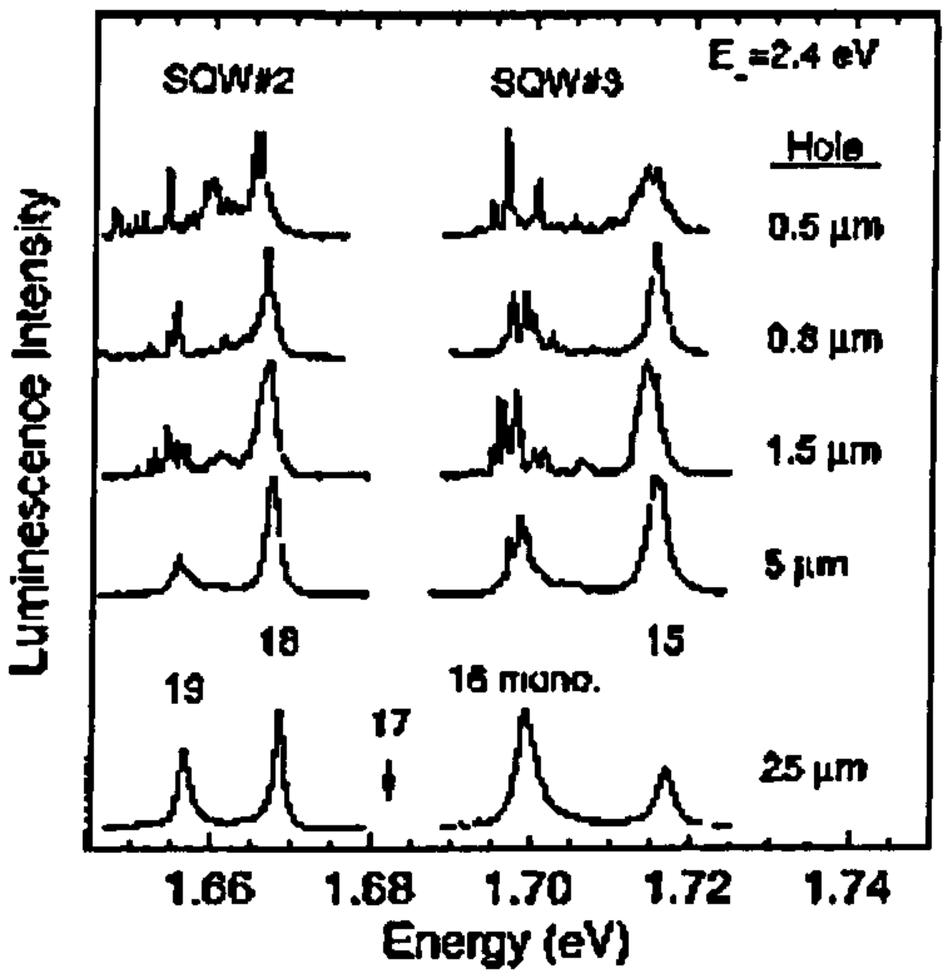

Figure 4.1 PL spectra from a range of small apertures formed in a metal mask deposited on the surface of a GaAs-AlGaAs QW structure. As the aperture size is reduced the effect of the inhomogenous broadening is lessened and individual QD emission lines become apparent. From Gammon et al.[18].

The effect of aperture size on the emission spectra is demonstrated in Figure 4.1 which shows the PL spectra for a range of aperture sizes. The PL from the 25µm aperture is clearly inhomogeneously broadened and is similar to that expected from a QW. The numbers (19,18,17,16) indicate the average QW width in monolayers. For any one sample two different emission lines are observed indicating monolayer QW width fluctuations on a large spatial scale. As the aperture size is reduced the peaks split up into a series of very sharp peaks, each of these new peaks represents the emission from one QD. With decreasing aperture size the number of these very sharp lines decreases, reflecting a decrease in the number of QDs probed. Under appropriate conditions (low

power and small aperture size) a single sharp line is observed, representing the recombination of a single exciton in a single QD.

The effect of changing the carrier occupation of a single state that is quantised in all three dimensions was first investigated by studying at the PL as the number of excitons in the structure was increased by increasing the laser excitation power. Brunner et al.[19], while studying island-like interface defects of a thin AlGaAs/GaAs quantum well, reported an increase of the exciton intensity (with excitation power) followed by a saturation, as the average QD exciton occupancy becomes >>1 (Figure 4.2). Biexciton emission was also observed with an onset at higher powers than for the exciton and a stronger dependence of intensity on incident power. A similar behaviour is observed for the QDs studied in this chapter.

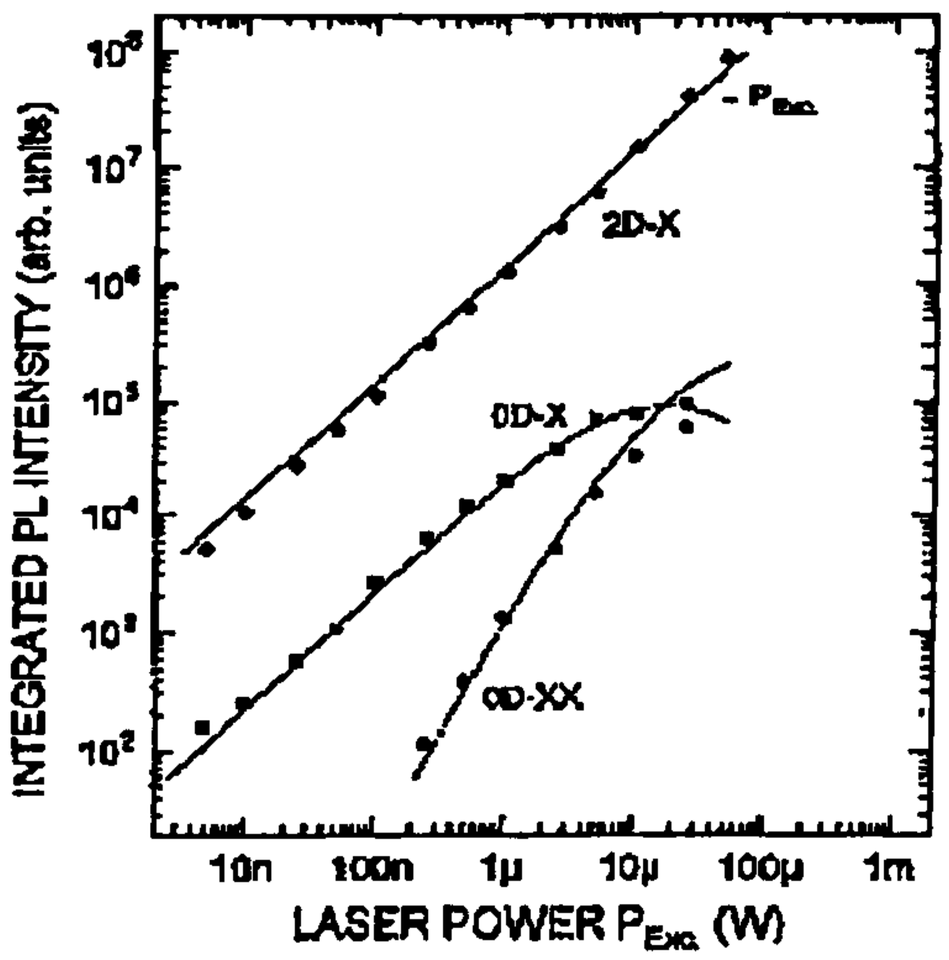

Figure 4.2 The excitation power dependence of the integrated PL intensity for the quantum well (2D-X), the QD exciton at (0D-X) and the QD biexciton line (0D-XX), which is situated 4meV below the 0D-X[19].

Bayer et al[20] studied multi-exciton complexes in single QDs formed by etching InGaAs/GaAs quantum wells. The binding energy of the biexciton was found to increase as the QD size was decreased and complexes containing upto four excitons were observed.

Studies of multi-exciton complexes in single self-assembled QDs were reported by a number of groups from 1998 onwards. Landin et al[12] observed a single narrow PL line for low power excitation, with three additional lines appearing for higher excitation powers. The initial line was attributed to the single exciton recombination with the additional lines attributed to the biexciton and negatively and positively charged excitons, the latter two resulting from unequal electron and hole capture by the QD.

Kuther et al[14] studied the magnetic field behaviour of the exciton and biexciton emission. Both lines exhibited identical diamagnetic shifts and spin splitting, indicating that the single particle states are not perturbed strongly in the biexciton.

Findeis et al.[21] studied both PL and PLE of single self-assembled QDs. In PL exciton (1X), biexciton (2X) and multi-exciton (3X and 4X) emission was observed, with the latter two processes resulting in lines from both the ground and the first excited states. In PLE a line attributed to GaAs LO-phonon assisted absorption was observed.

Hartmann et al[16] studied modulation doped QDs grown within tetrahedral shaped recesses formed on the initial substrate. Photodepletion was used to vary the electron occupation

from five to zero, allowing the observation of a single exciton recombination in the presence of up to five additional electrons. At high pump powers the QD is uncharged and 1X, 2X, 3X and 4X multi-exciton recombination was observed. The experimental behaviour was well described using a model involving the diagonalisation of the Hamiltonian matrix based on single particle states solved for a cylindrical confinement potential.

Dekel et al[9] studied the power dependent PL of a single self-assembled QD. As in other work an increasing number of emission lines was observed with increasing power, reflecting an increasing number of possible excitonic processes. However the specific form of the spectra are different in a number of ways to those reported by other workers and also presented in this thesis. Dekel et al.[9] modelled their experimental spectra by calculating the Coulomb interactions between the single particle wave functions calculated for an infinite depth parallelepipedal box.

In later work Dekel et. al.[13,22] developed a simple rate equation model that predicts the excitation power dependence of the multi-exciton intensities. This model will be used in understanding the power dependence of the single QD emission presented in this chapter. Dekel et al.[13,22] found a good agreement between their measured results and the predictions of their model (Figure 4.3), with the model accounting quantitatively for the dynamics of a small number of interacting electrons and holes confined within an optically excited semiconductor QD. This is discussed in more detail in §4.9.1.

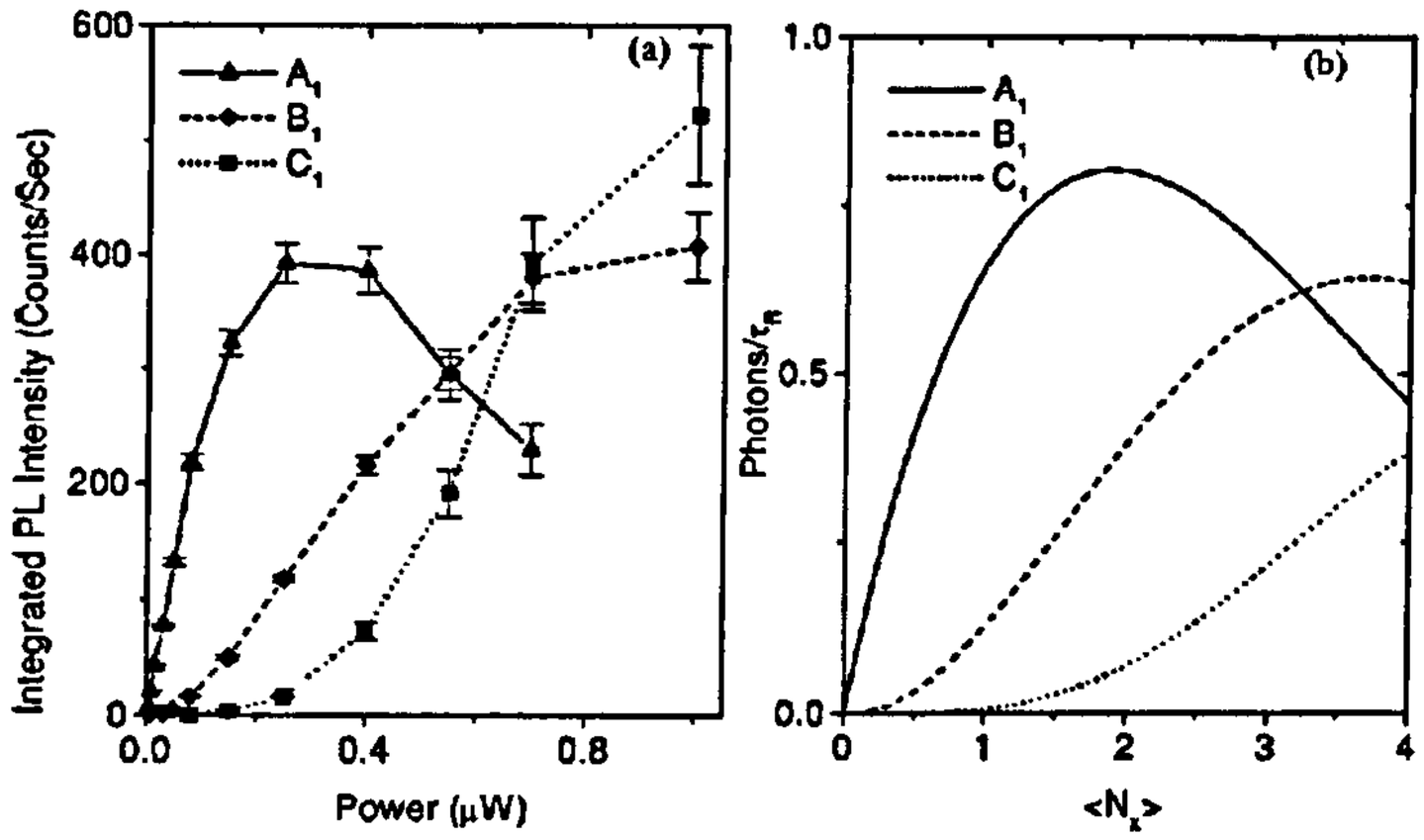

Figure 4.3 Measured (lhs) and calculated (rhs) spectrally integrated PL emission intensity as a function of CW excitation power (lhs) and steady-state number of photogenerated QD excitons (rhs) for various spectral lines. Line A_1 is the ground state single exciton line. Lines B_1 and C_1 are higher multi-excitonic state transitions[22].

The temporal dynamics of different QD recombination processes has been investigated by Thompson et. al.[23]. In this work time-resolved PL was performed for the neutral exciton (X^0), a singly charged exciton (X^*), the neutral biexciton ($2X^0$) and a charged biexciton ($2X^*$). Figure 4.4 shows PL decay curves for three different excitation powers. At the lowest excitation power only the exponential decay from the neutral exciton is present, with a lifetime of 1.36 ± 0.06 ns. At an intermediate power, the charged exciton and neutral biexciton are also observed. The lifetime of the charged exciton is similar to that of the neutral exciton (1.07 ± 0.02 ns). This similarity is expected, as there is only one recombination path for the singly charged exciton as it is impossible for one of the carriers to recombine without a spin-flip process. In contrast the biexciton has two recombination paths (either the spin up or spin down electron can recombine with the appropriate hole) leading to a lifetime for 2X which is half that of X (0.59 ± 0.02 ns

$\therefore t_{2X}=0.43t_X$). The highest power spectrum also contains the charged biexciton. At high powers the rise time of the exciton increases compared to the low power value. This occurs because the high QD carrier population permits the observation of the single exciton only after the biexciton recombination. Confirmation of this sequence of processes is provided by the shift of the maximum intensity for X of 0.61ns, almost identical to the 0.59±0.02ns decay time of 2X.

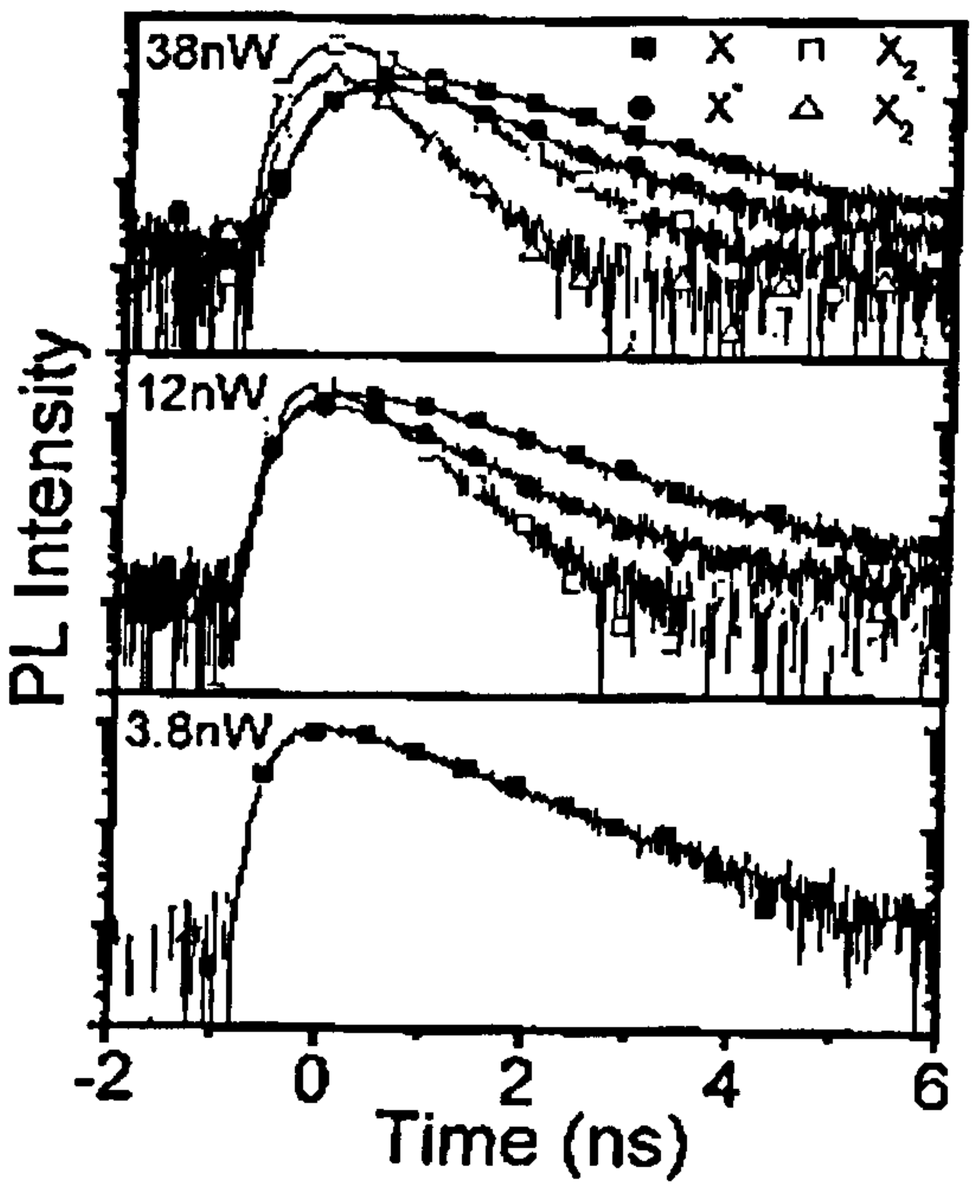

Figure 4.4 PL decay curves for three different excitation powers. Decay curves for the exciton and the negatively charged excitons are shown. At high powers the biexciton and charged exciton decays are also shown.

The majority of the studies of spin effects in semiconductor QDs has involved the application of a magnetic field to probe exciton Zeeman spin splitting, electron-hole exchange splitting, spin-dependent relaxation effects and excitonic "dark states"[24]. These studies have allowed the determination of carrier g factors[25,14,24], wavefunction spatial

extents and carrier effective masses. g-factors for carriers confined within a QD have been calculated by Kotlyar et. al.[26] as a function of the lateral and vertical size for QDs formed by etching InGaAs/GaAs QWs. The spin-splitting of the exciton is found to increase rapidly with decreasing QD diameter but with a more complicated behaviour (including a sign reversal) with dot height. For QD diameter below ~50nm the hole g-factor is larger than the electron g-factor.

Arkadiusz Wojs and Pawel Hawrylak[27] have calculated the effect of free carriers on the photoluminescence from modulation-doped, self-assembled QDs. Exact diagonalisation studies of up to eight electrons plus a single hole were performed, and Hartree-Fock calculations for up to 20 electrons were performed. The photoluminescence spectrum is simulated and the band-gap renormalisation in a zero-dimensional system is discussed. The tendency of electrons in degenerate, partially filled electronic shells to maximise their total spin leads to a strong dependence of the PL spectra on the number of electrons *N*, the magnetic field *B*, and the polarisation of the emitted light. Figure 4.5 shows simulated PL spectra from Ref 27 as a function of both magnetic field and dot electron occupancy (N). A non-zero temperature is assumed to allow the observation of recombination from excited states. For N=1 (uncharged dot) a single ground state line is observed (the exciton X) which undergoes a week diamagnetic shift in magnetic field. At higher energy the Zeeman splitting of an excited state is observed. As electrons are added to the dot many more emission lines occur, reflecting the different possible recombination processes.

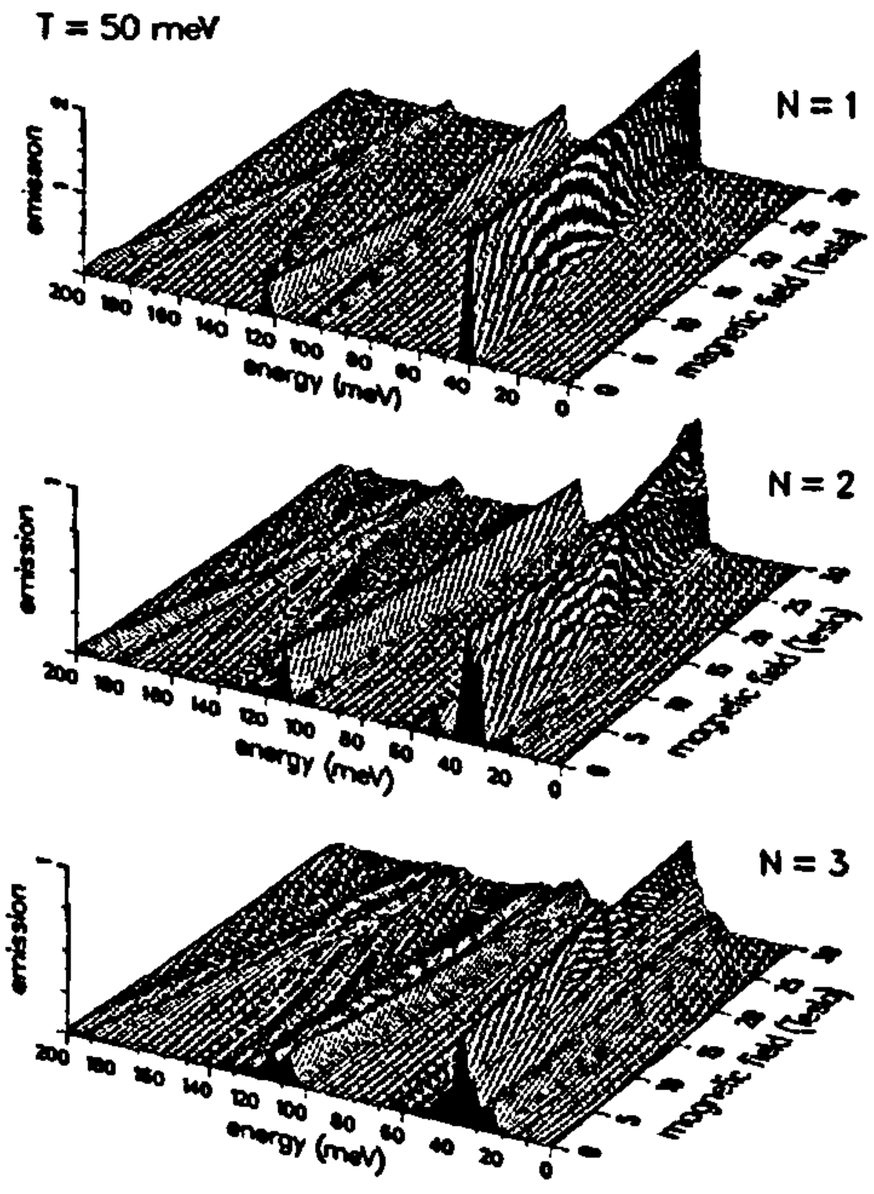

Figure 4.5 Magnetic-field evolution of the emission spectra for *N*=1-3 electrons in the initial state, assuming a Boltzmann distribution of initial states with an effective temperature *T*=50 meV [27].

4.3 Sample design

The sample studied in this chapter was grown by molecular beam epitaxy (MBE) on a [100]-orientated n+ doped GaAs substrate. The sample structure was relatively complex, consisting of the following layer sequence. After a 300nm thick $Al_{0.33}Ga_{0.67}As$ blocking barrier, a 175nm $Al_{0.13}Ga_{0.87}As$ cladding layer and 25nm GaAs layer were deposited. Next the QD layer was grown consisting of 2.4 monolayers (ML) of InAs grown at 500°C and 0.01MLs^{-1}. The QDs were formed by the Stranski-Krastanow process. Scanning tunnelling microscopy (STM) and transmission electron microscopy (TEM) of a similar, but uncapped sample, reveals a QD height of 5nm and a base width of 18nm

with a lens-like shape (Figure 4.6). The relatively slow growth rate results in a low areal QD density of ~$5x10^9cm^{-2}$. The structure was completed with 25nm of GaAs and a second 175nm thick $Al_{0.13}Ga_{0.87}As$ cladding layer. A schematic diagram of the sample band structure is shown in Figure 4.7.

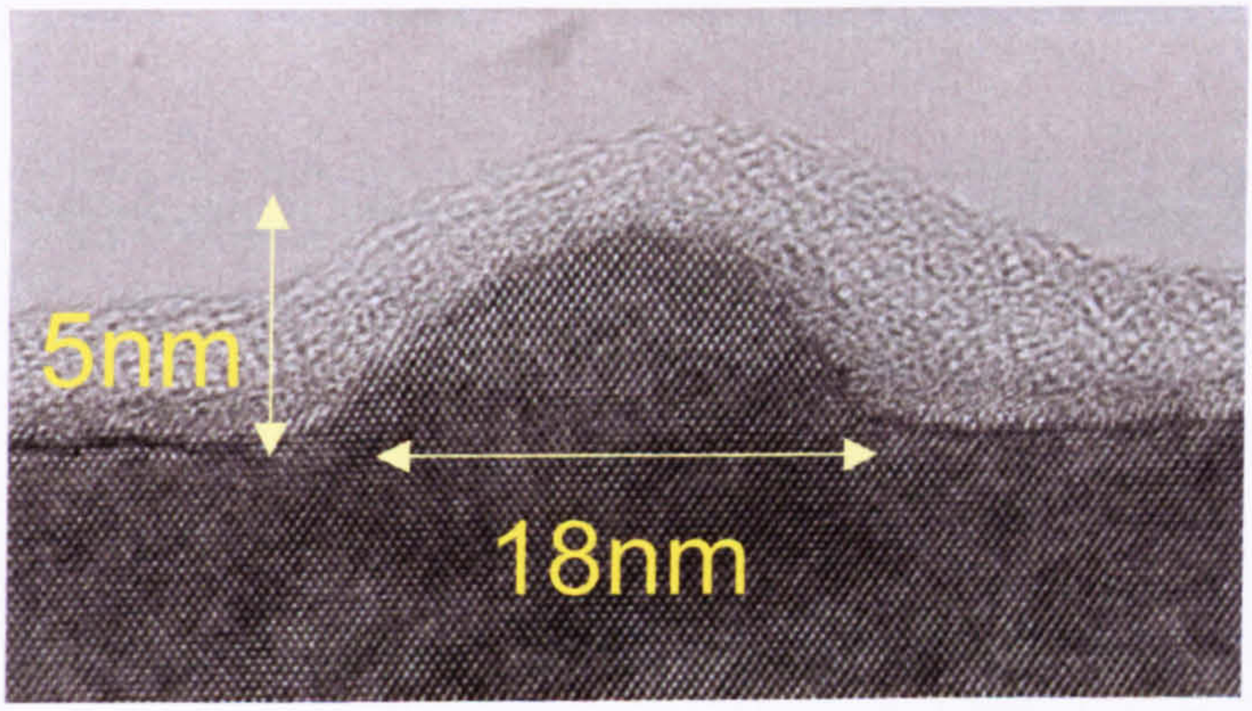

Figure 4.6 Cross sectional TEM micrograph of an uncapped InAs quantum dot. The QD was grown by MBE at the III-V Central Facility (Sheffield). Image provided by M.Al'khafaji.

The form of the sample allowed the creation of carriers either directly in the QD, in the GaAs close to the QD or throughout the AlGaAs cladding layer simply by changing the laser excitation energy.

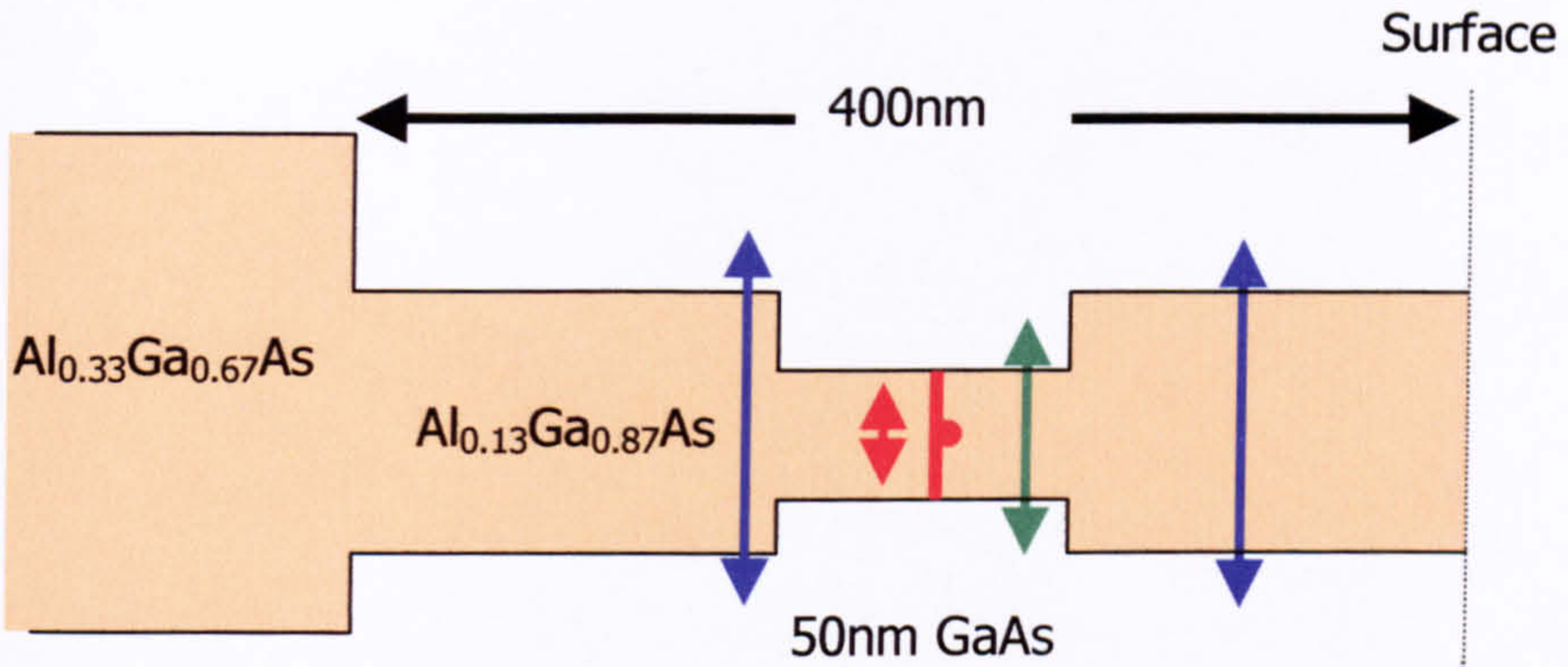

Figure 4.7 Schematic band structure of the sample studied in this chapter. Varying the excitation energy allows excitation in the $Al_{0.13}Ga_{0.87}As$ (blue arrows), the GaAs (green arrow) and the wetting layer or directly into the QDs (red arrow).

After growth, the sample was capped with Si_3N_4 and rapidly thermally annealed for 300s at 750°C to blue shift the low temperature QD emission[28] to 1330meV, where it is accessible to sensitive Si-based detectors. Following the annealing, the wetting layer emission was observed at 1460±5meV compared with a value of 1420meV before annealing (Figure 4.8). Following annealing, the inhomogeneously broadened QD ground state emission had a full width at half maximum (FWHM) of 50meV, centred at 1330meV. The effect of annealing is shown in Figure 4.9 and Figure 4.10, for a related sample but with a higher QD density. The dependence of the blueshift on temperature and anneal time is shown in Figure 4.10. The mechanism behind the blueshift is thought to be an intermixing of the QD with the surrounding GaAs matrix, resulting in changes of composition and size. This effect has been known for some years and provides an important tool for tuning the QD emission energy.

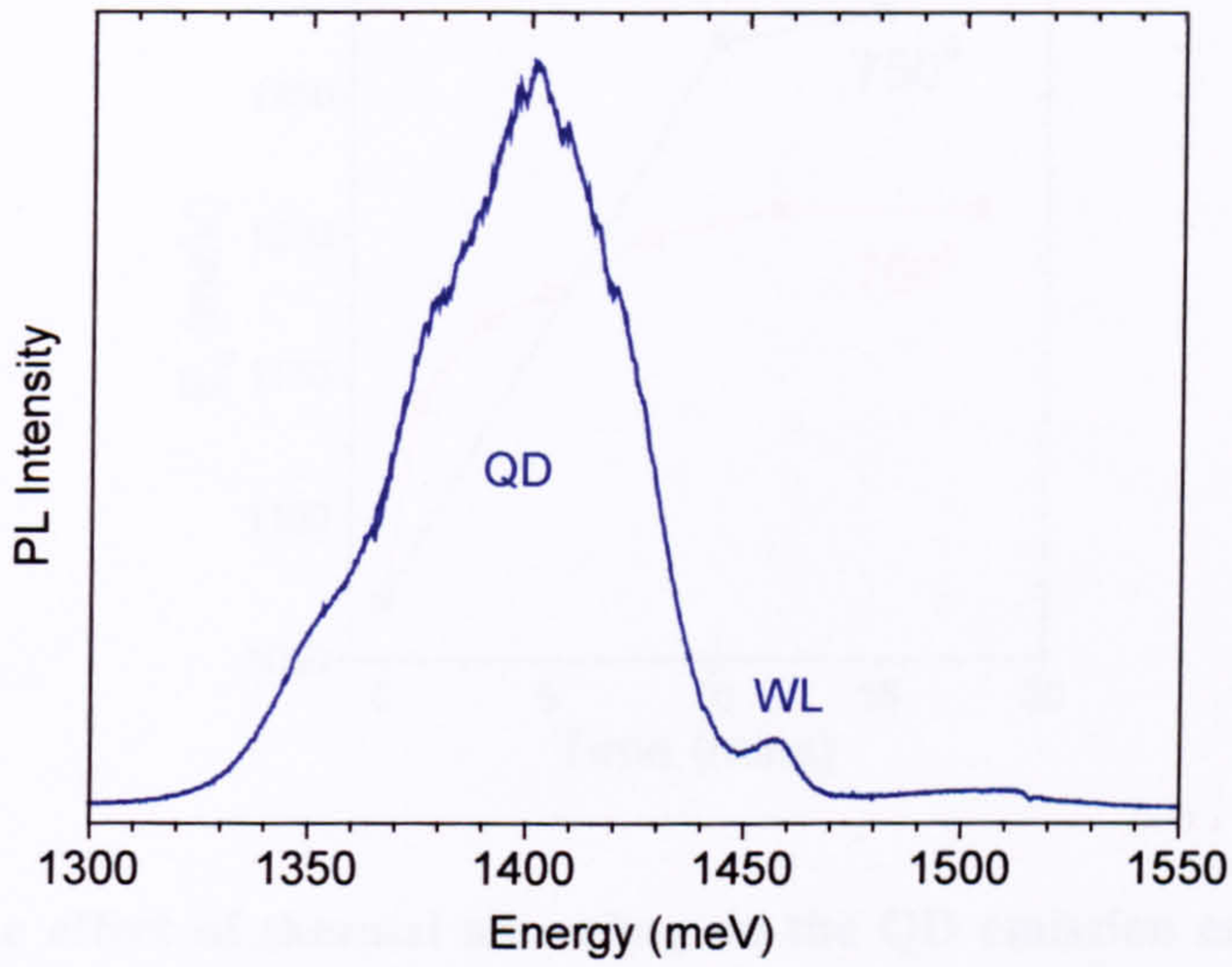

Figure 4.8 T=10K ensemble PL emission, following the thermal annealing. QD and WL refer to the quantum dot and wetting layer emission respectively.

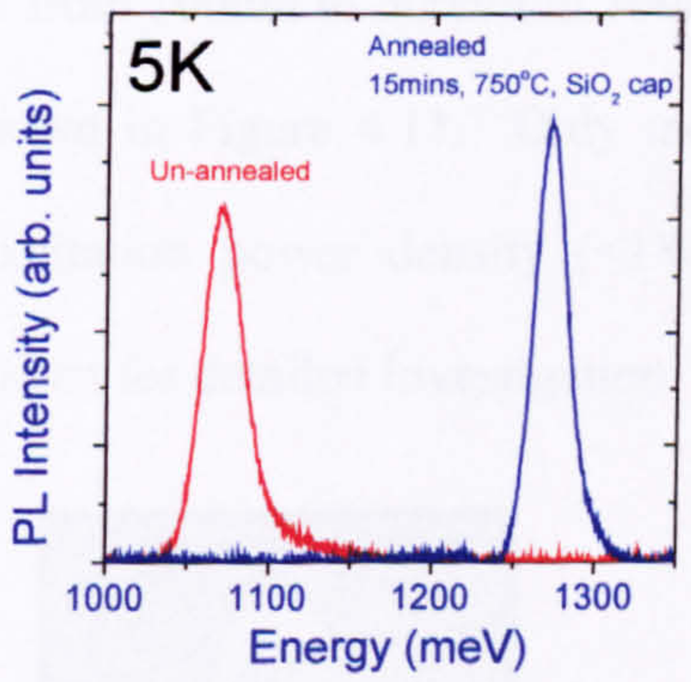

Figure 4.9 The effect of annealing an InAs QD sample at 750°C for 15 minutes on the low temperature emission spectrum.

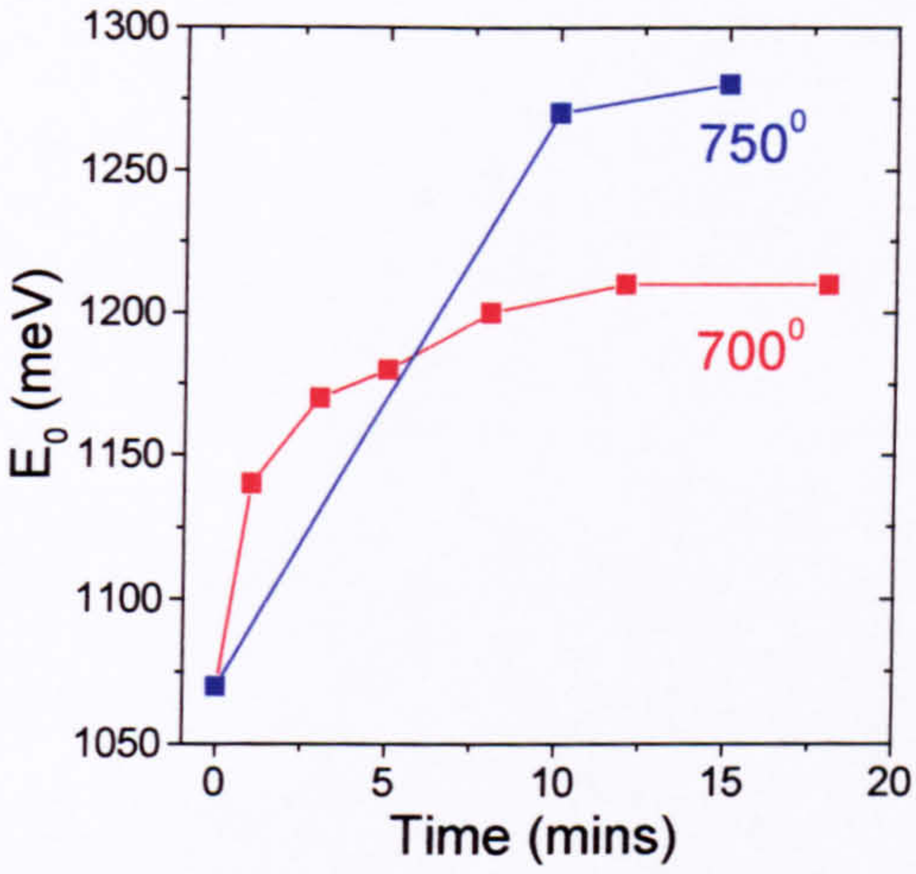

Figure 4.10 The effect of thermal annealing on the QD emission energy for a QD ensemble. The blue line indicates the shift due to annealing at 750°C, the red line indicates the shift due to annealing at 700°C. E_0 is the maximum of the ground state emission energy.

To isolate individual QDs for optical investigation, the annealed material was fabricated into an array of widely spaced mesas using e-beam lithography and plasma etching. The diameter of the mesas varied from 100nm to 500nm in 100nm steps. An SEM image of a 200nm diameter mesa is shown in Figure 4.11. Only mesas which exhibited a single emission line under low excitation power density (<1Wcm^{-2}), indicative of a single optically active QD, were chosen for detailed investigation.

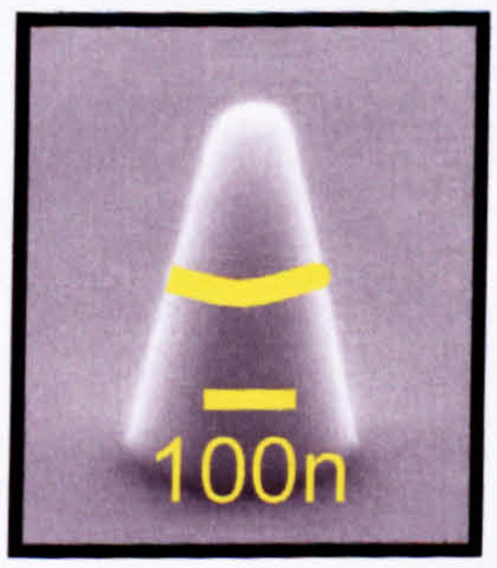

Figure 4.11 SEM of a sub micron mesa approximately 200nm in diameter. Fabricated by T. Krauss[29]

4.4 Experimental details

4.4.1 Experimental Apparatus

The measurements consisted of time integrated micro-PL spectra recorded mainly for a sample temperature of T=10K. A schematic diagram of the experimental set-up is shown in Figure 4.12. The sample is mounted in a cold finger, continuous flow cryostat with a base temperature ~10K. The cold finger is placed in the bore of a 5T superconducting magnet which allows the application of fields in the Faraday geometry. A microscope objective with a numerical aperture NA~0.6 provided a sub micron focused laser spot which could be accurately positioned on the sample using piezoactuators. The spot size was determined by scanning the laser spot over the edge of 50μm wide metallised stripes and measuring the transmitted power as a function of spot position. A square wave-like intensity profile is produced which can then be differentiated to give the spot size. This analysis, which neglects diffraction effects, indicates an approximate spot size of 600nm for 633nm light (Figure 4.13 and Figure 4.14). The maximum excitation power at the sample surface is 15μW. This is limited by the damage threshold of the pellicle beam splitter used to direct the incident laser beam into the objective. This power corresponds to an excitation density of approximately 1kWcm^{-2}.

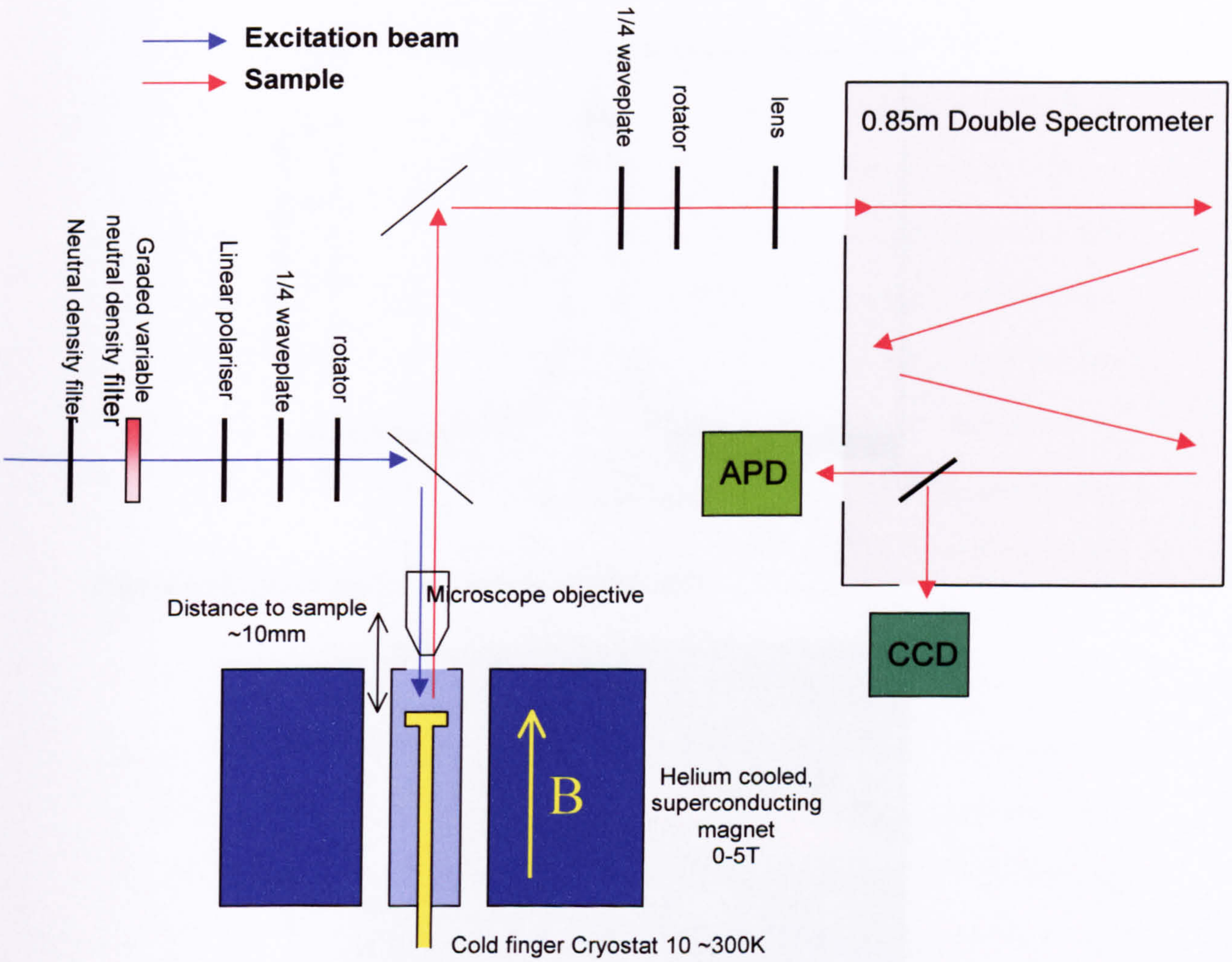

Figure 4.12 Schematic diagram of the experimental equipment used to study single QDs. The cold finger cryostat (light blue) is embedded inside a 0-5T superconducting magnet that produces a magnet field in the Faraday geometry.

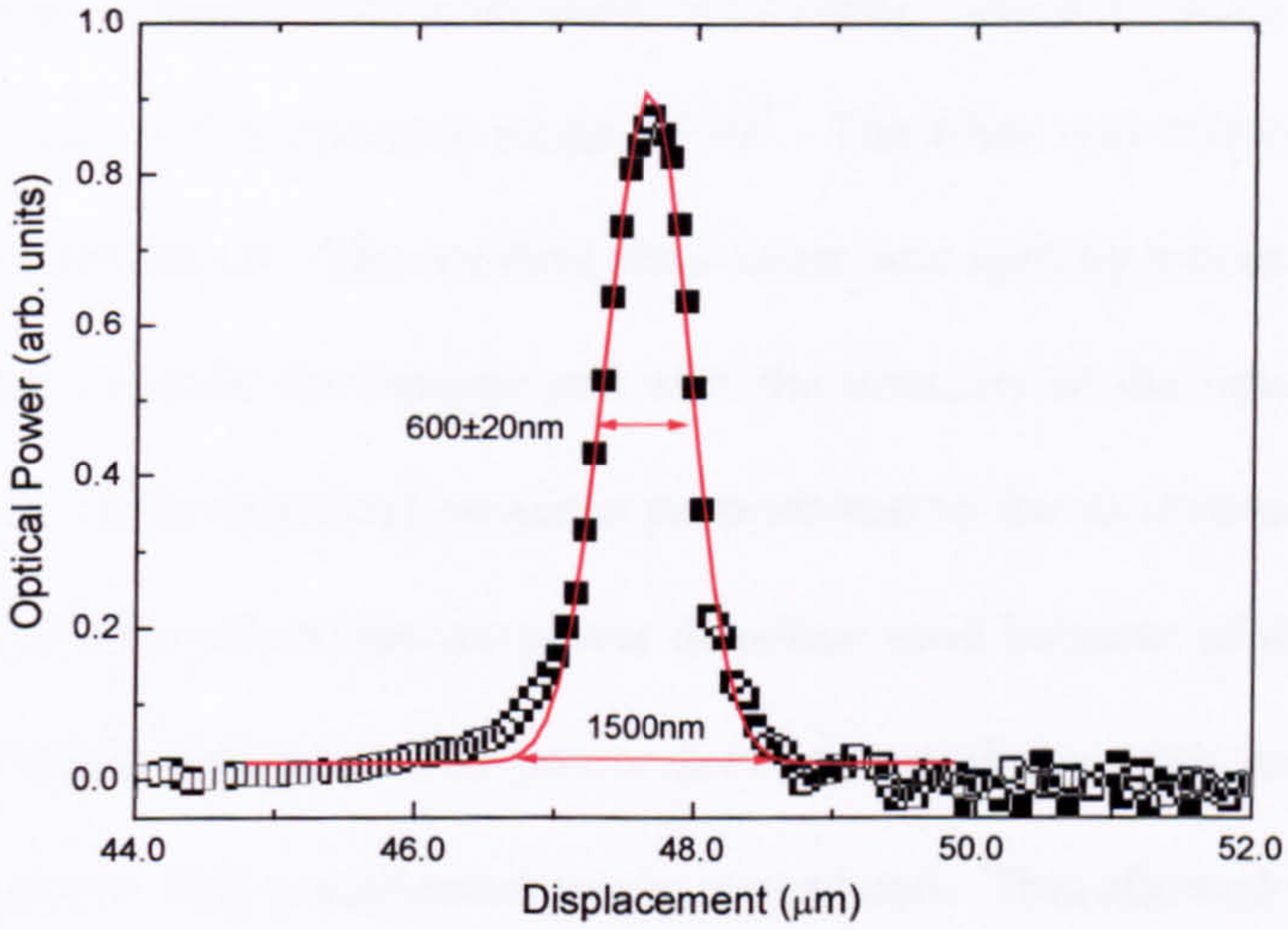

Figure 4.13 Spatial profile of the focused laser spot.

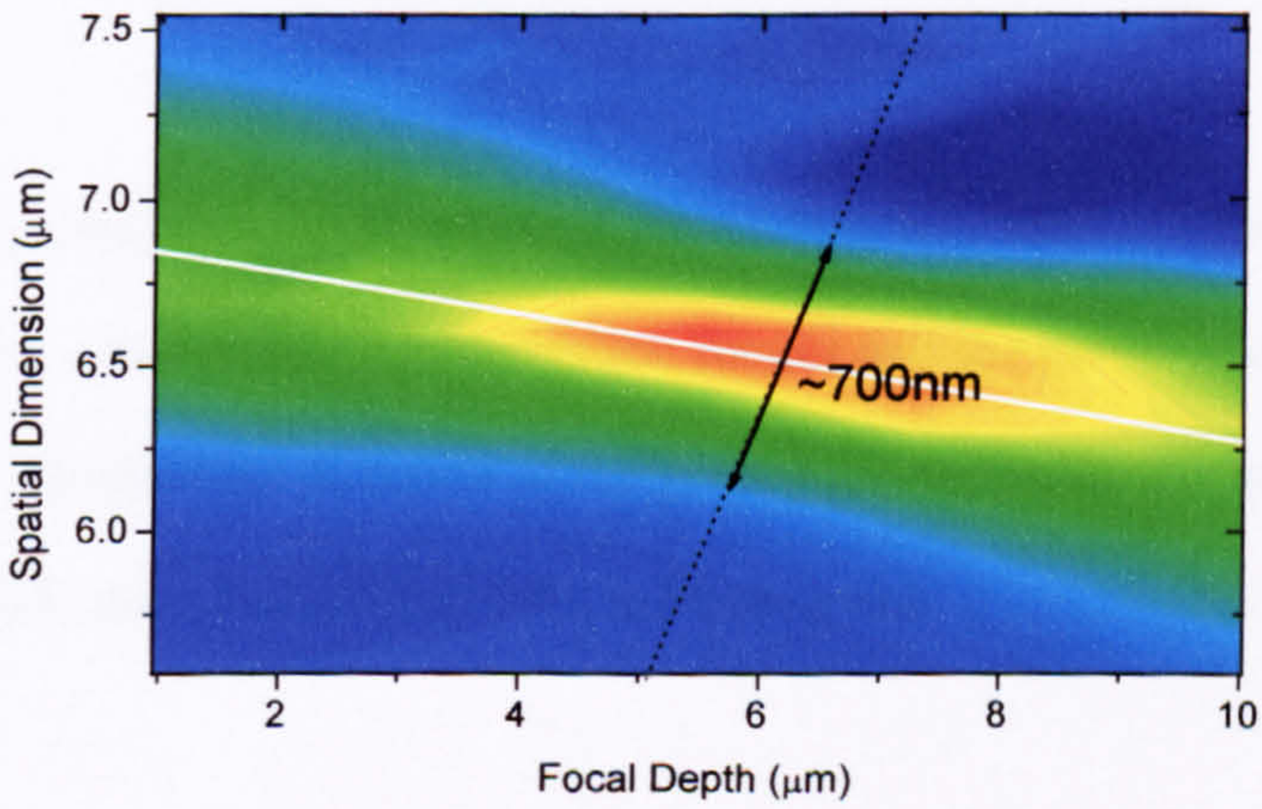

Figure 4.14 Spatial extent and focal depth of the focused laser spot size.

Excitation was provided by a tuneable Ti:Sapphire laser (E_{ex}=1250-1550meV) or by a HeNe laser (E_{ex}=1960meV). The PL was collected by the same microscope objective, dispersed by a 0.85m double monochromator (maximum resolution ~30μeV) and detected by a CCD camera or a single channel Si-avalanche photodiode (APD). Typical integration times for the CCD and APD were 30-300s and 1-20s respectively.

Power dependent measurements were performed using a circular graded, variable neutral density (ND) filter with a dynamic range of 10^3. The filter was rotated under computer control by a stepper motor. The incident laser beam was split by a beam splitter with one component used to excite the sample and with the intensity of the other being measured by a photodiode. This measured power is proportional to the excitation power density at the sample surface for all excitation power densities used because of the linear response of the pellicle beam splitter. The power incident on the sample was determined by replacing the sample with a calibrated power meter head. This allowed the determination of a calibration coefficient that gave the actual sample power in terms of the reference beam intensity.

To study the circularly polarised nature of the emitted luminescence the light was passed through a quarter wave plate. A polarisation rotator and the polarisation response of the spectrometer (a result of the direction of the grating grooves) allowed spectra for both left and right circularly polarised emitted light to be recorded.

4.4.2 Collection Efficiency of the Equipment

Assuming an average dot occupancy of one exciton and a radiative lifetime of 1ns a single quantum dot will emit a maximum of 10^9 photons per second. At a working distance of 10mm and a collection diameter of 4mm the microscope objective should collect approximately 1% of these photons. The intensity is further reduced by internal reflections inside the mesa that reduces the signal by ~50%, assuming the refractive index

of $Al_{0.13}Ga_{0.87}As$ is 3.23. At the wavelengths investigated the loss through the optics, including the beam splitters and spectrometer losses, were found to give a reduction of the signal by x0.01. The APD's quantum efficiency at the QD emission wavelength is 0.34 (Figure 4.15). These losses combined should result in a maximum measured intensity of approximately 10000 counts per second (cps), corresponding to a collection and detection efficiency of 10^{-5}. This compares well with the total measured intensity of 6000cps when the QD has an average occupancy of one exciton (Figure 4.23).

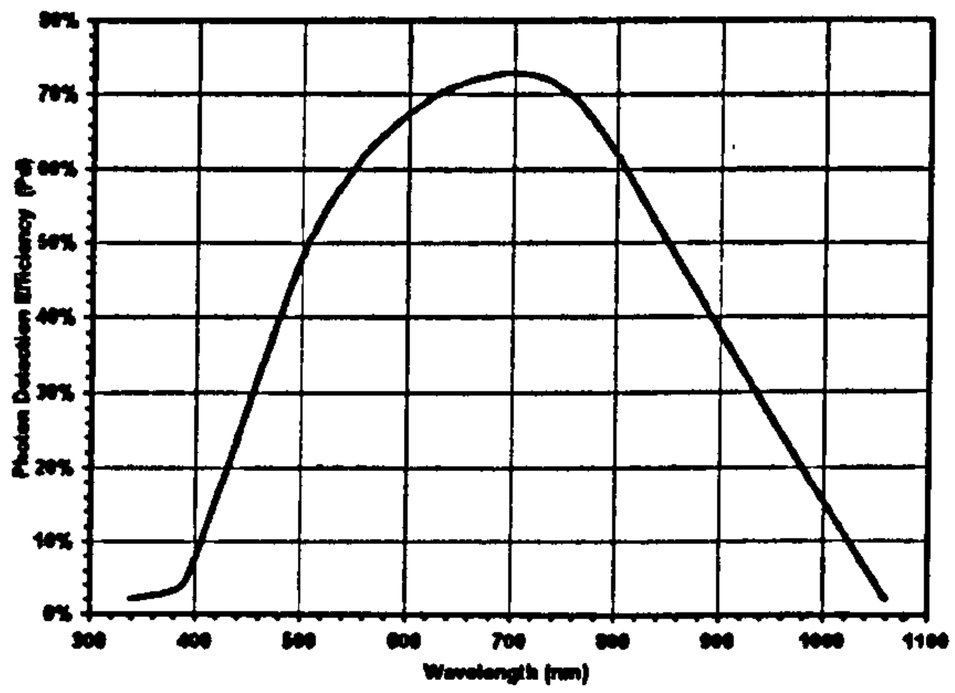

Figure 4.15 Response curve of the Silicon APD

4.5 Photoluminescence Spectra of Single Quantum Dots

PL spectra from a single dot are shown in Figure 4.16 as a function of excitation power and for an excitation energy of 1520meV, close to the GaAs band edge (the green arrow in Figure 4.7). The spectra consist of two groups of emission lines centred at ~1345meV and 1385meV. The latter group is only observed in the higher power spectra, which correspond to the case when the QD is occupied with a relatively large number of

excitons. This behaviour allows the lower energy group of lines to be attributed to recombination processes in the ground state of the QD (the s-shell) whereas the higher energy lines involve the recombination of excitons in the first excited state (the p-shell). The ground state emission is shown on an expanded scale in Figure 4.17. At the lowest excitation powers, a single narrow emission line is observed, labelled X in Figure 4.17. The full width at half maximum of this line is 40μeV, a value comparable to previous reports of single QD emission[1] and close to the resolution of the present measurement system (see §4.7). This emission line which, for the present QD, occurs at 1345meV (Figure 4.16 and Figure 4.17) arises from single neutral exciton recombination (X). For higher incident power the complexity of the emission increases, with two additional lines (X* and 2X) appearing, separated from X by +1.8 and -1.7meV, respectively. These lines are identified as arising from single charged exciton (X^*) and neutral biexciton (2X) recombination, respectively. At even higher power densities further lines appear to lower energy, labelled mX, which become increasingly dominant at higher powers. These features arise from multiexciton (m>3) recombination and span an energy band 5–7meV below X. Each line arises from recombination of an *s*-shell exciton, perturbed by the presence of the other s-shell exciton and also excitons occupying higher energy p or d states[15,30]. The larger linewidth of the mXs lines, relative to X, may arise from the greater multiplicity of initial- and final-state configurations. In addition lifetime broadening may be important since the final state containing one or more p-shell excitons but an unfilled s-shell is not a ground state of the system.

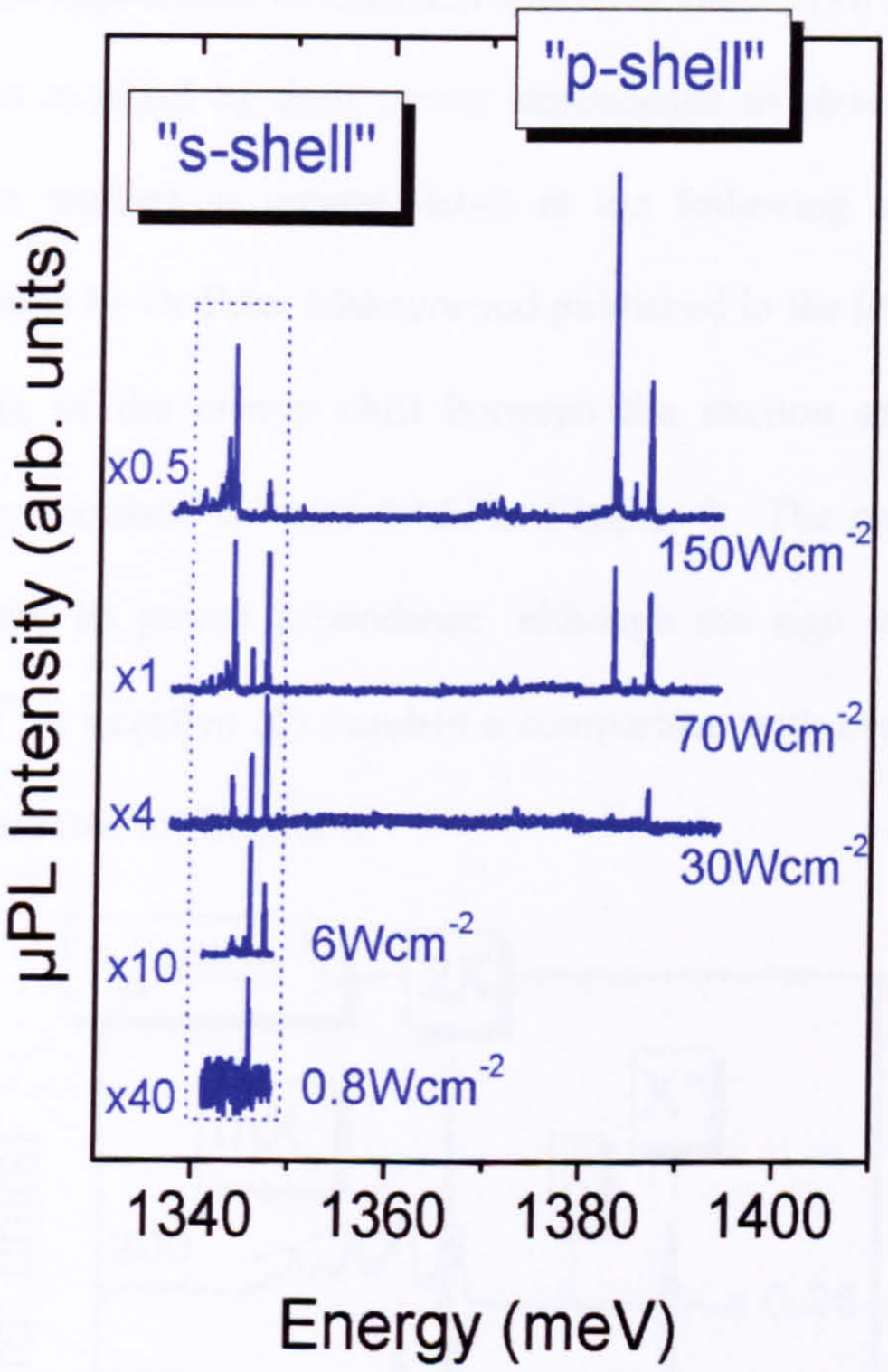

Figure 4.16 Low temperature (T=10K) μPL spectra obtained as a function of laser excitation power density (0.8-150Wcm^{-2}) for a single self-assembled quantum dot (dot-A). Ground state single and few-exciton complexes give rise to the group of ultra-narrow emission features around ~1340meV, whilst the peaks close to ~1385meV arise from p-shell recombination of higher order multi-exciton complexes. The excitation energy used was E_{ex}=1520meV

It is also of interest to note the simultaneous appearance of the p-shell emission and the biexciton ground state emission (Figure 4.16). The appearance of the latter indicates that the system has a finite probability of containing two excitons. At this point the second exciton may relax to the ground state if the spins of its electron and hole are anti-parallel to those of the first exciton. However for the case of parallel spins relaxation to the ground state is blocked by the Pauli principle and the second exciton remains in the p-

shell, resulting in the appearance of emission from that shell. The identification of the s-shell emission lines is aided by their power dependence as shown in Figure 4.16 and Figure 4.17 and as studied in greater detail in the following sections. In addition theoretical calculations by Dr Peter Maksym and published in the literature agree with the sign and magnitude of the energy shift between the exciton and biexciton. These calculations will be discussed in more detail in Chapter 6. The nature of the line X* is also determined from its power dependence, although the sign of this singly charged exciton (positive X^+ or negative X^-) requires a comparison with measurements of charge tuneable QDs as presented in Chapter 6.

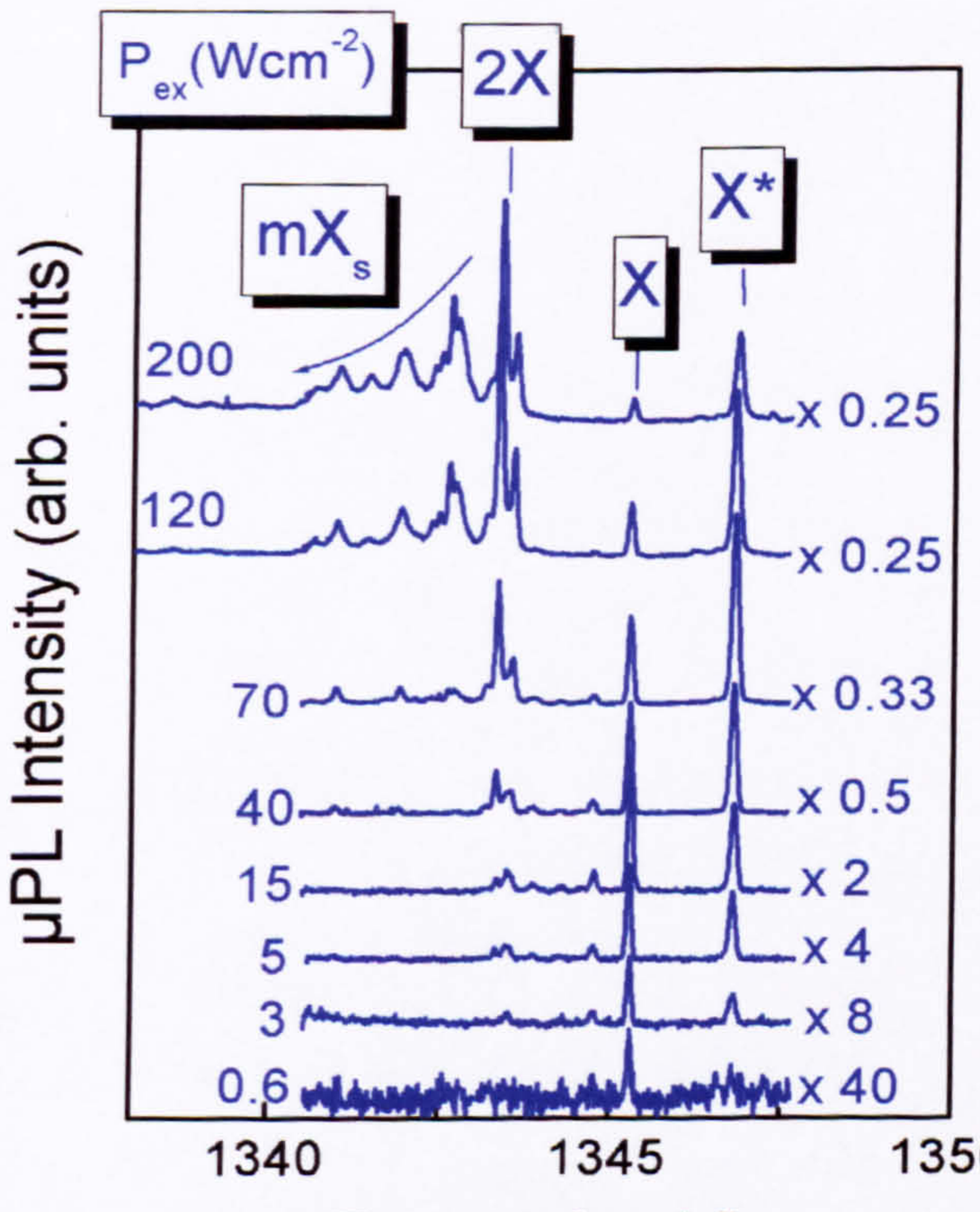

Figure 4.17 s-shell μPL spectra obtained from the ground state emission, illustrating the few and multi-exciton complexes on an expanded scale (from Figure 4.16).

4.6 Comparison of the Behaviour of Different Quantum Dots

Several mesas, each containing one optically active dot, were investigated and all were found to show very similar optical behaviour. Almost identical spectra were found for five different dots, demonstrating that the detailed form of the s-shell emission is determined by intrinsic QD effects, and not, for example, from perturbations due to ionised impurities or processing-induced defects. The results presented here are for two representative mesas. The PL spectra for the s-shell emission for the two mesas is shown in Figure 4.18 to illustrate the similarities of the spectra. The excitation conditions were identical for both spectra. Both QDs show single exciton (X), biexciton (2X) and charged exciton (X*) emission with a X-2X separation of –0.50 and –0.47meV and an X*-X separation of +1.49 and +1.44meV for QDs A and B respectively. These separations are very similar despite the absolute value of the single exciton emission differing by 14meV

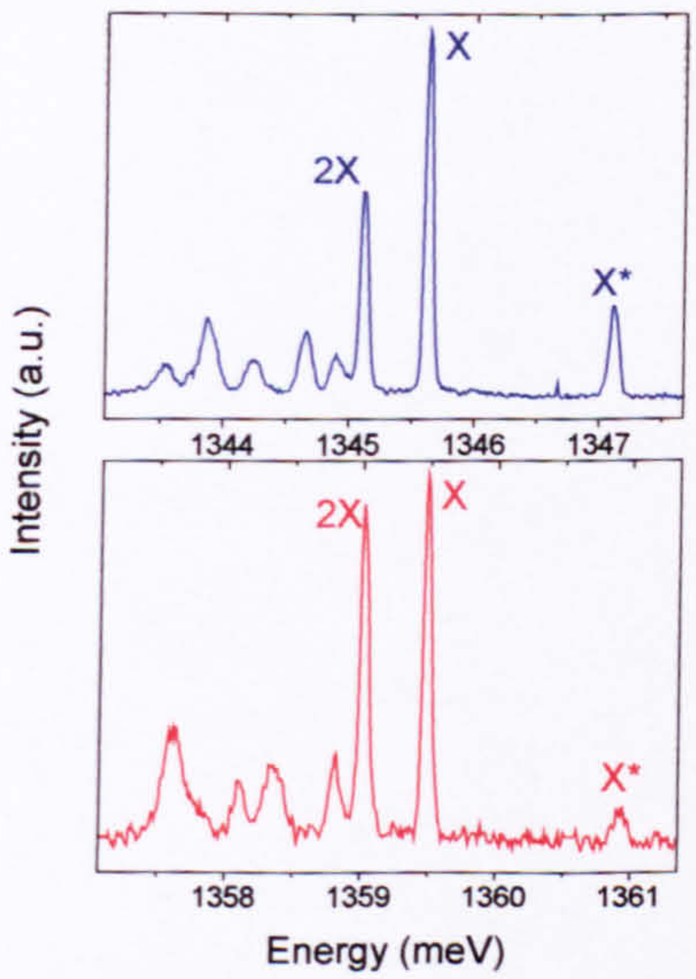

Figure 4.18 Comparison of the single QD emission spectra for QDs A (top) and B (bottom).

4.7 Linewidths of the Emission Lines

Figure 4.19 and Figure 4.20 show high resolution spectra of the single neutral exciton line (X) and the single charged exciton line (X*) respectively. Linewidths of 45μeV and 60μeV for X and X* respectively are measured, the former value being very close to the spectral resolution of the present experimental system (35μeV). Previous work has found similar linewidths[1]. In self-assembled QDs a typical value for the radiative lifetime is 1ns which corresponds to a broadening of <1μeV, much less than the present linewidths. Homogeneous linewidths have been measured directly using time resolved degenerate four wave mixing by Borri et al.[31] where a low temperature value of 2μeV is found. The relatively large linewidths found in the present measurements may be a consequence of the long integration time used to acquire the spectra and charge fluctuations near to the QD which perturb the QDs energy states. If such a mechanism is responsible for the observed broadening, the larger linewidth observed for X* than for X indicates that the former is more sensitive to these fluctuations.

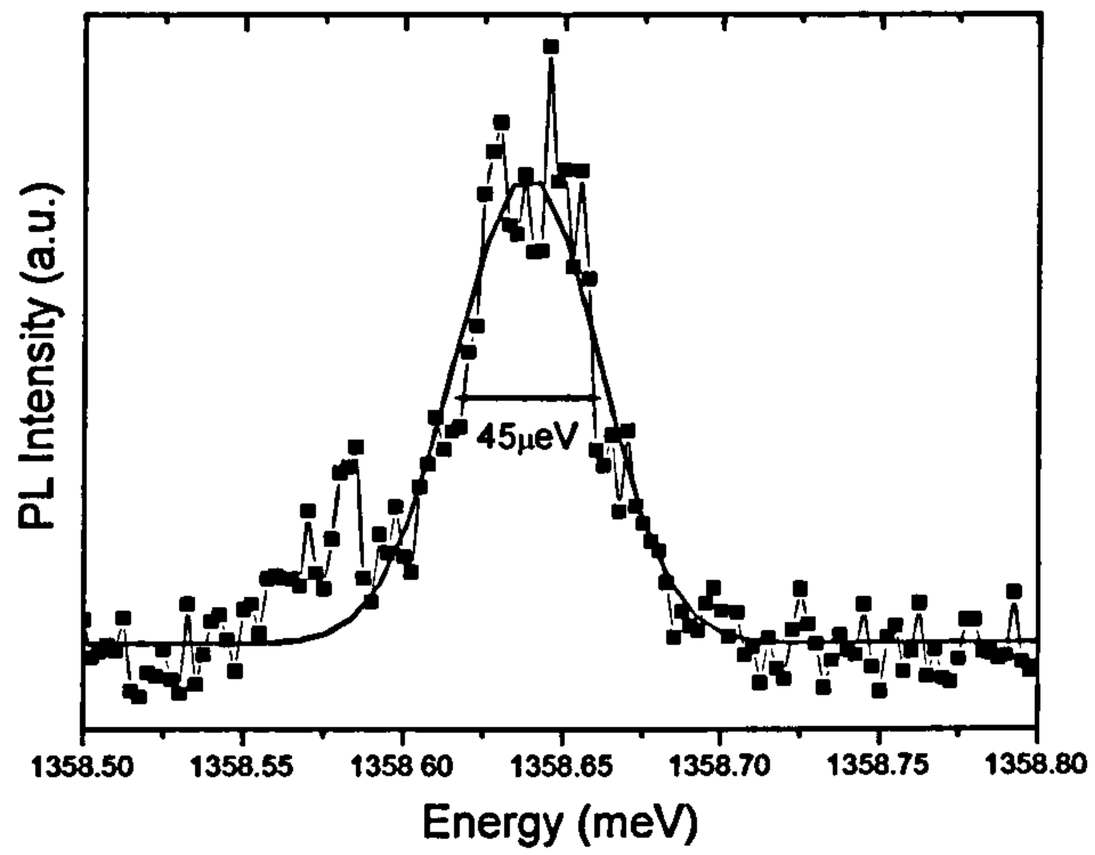

Figure 4.19 A high resolution spectrum of the single exciton emission from a single QD.

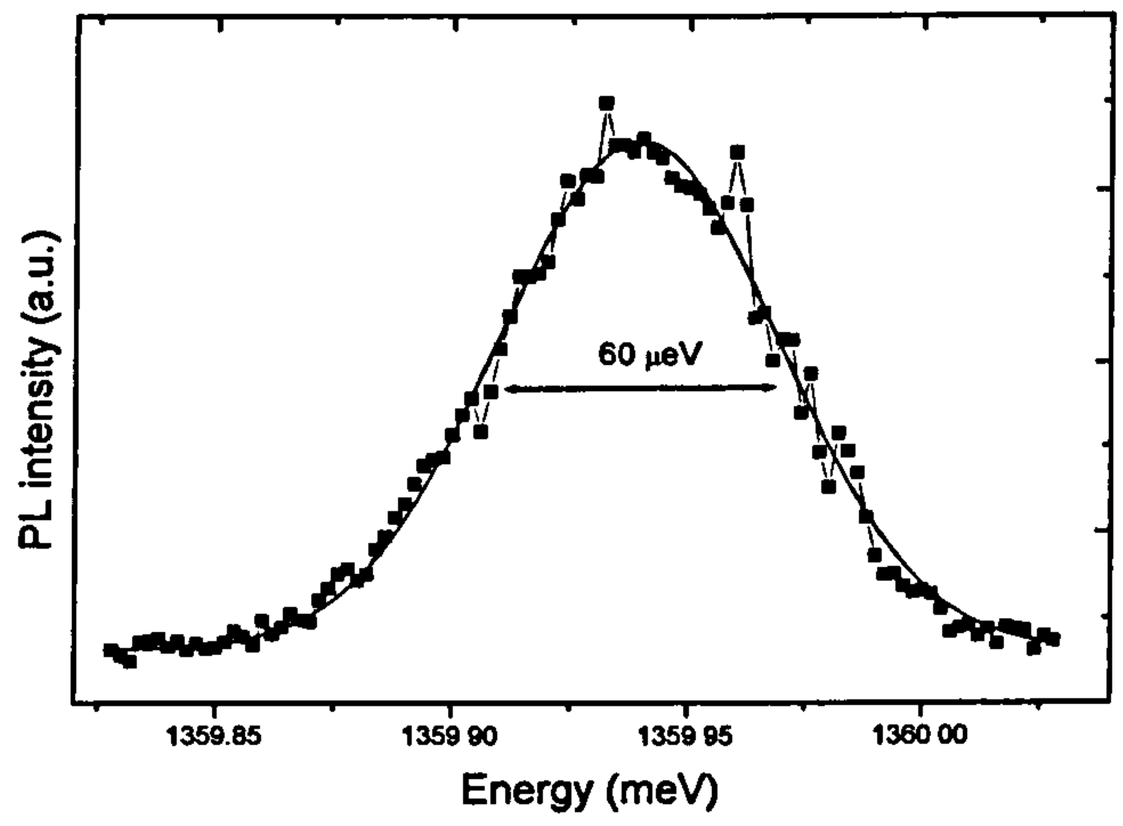

Figure 4.20 A high resolution spectrum of the X* exciton emission from a single QD.

4.8 Temperature Dependence of the Dot Emission.

The temperature shift of the QD emission approximately follows that of bulk the InAs, but with an offset due to the quantum confinement. An identical shift is found for

different QDs as shown in Figure 4.21. Lines A and B are both single exciton lines from dots in different mesas emitting at 1327meV and 1360meV respectively. The linewidth of the single dot emission is plotted as a function of temperature for two different dots in Figure 4.22. With increasing temperature the dot emission becomes weaker and an underlying background is observed, preventing linewidth measurements above ~80K.

At low temperature (<40K) only a very weak broadening of the X emission is observed (~0.4μeV.K^{-1}). Li and Arakawa[32] have calculated the optical linewidths for single QDs. A linear linewidth variation is predicted at low temperature with finite zero temperature broadening due to electron-phonon interactions involving low energy LA phonons. By fitting exponential functions to the data of Figure 4.22 energies of 1.0 and 1.4meV are extracted for dots A and B respectively, consistent with low energy acoustic phonon mediated broadening. Further studies of the interaction between acoustic phonons and electronic states are described in Chapter 5.

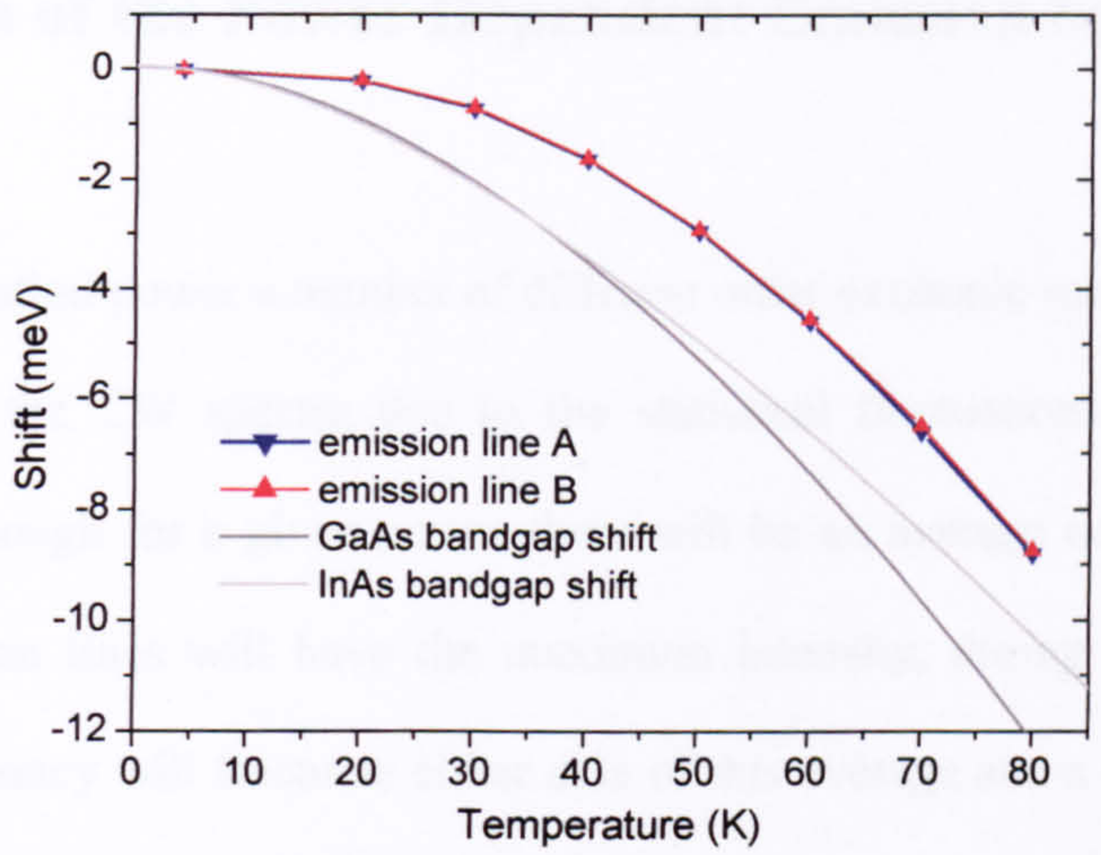

Figure 4.21 The temperature dependent shifts of the single exciton from two different dots. Emission line A occurred at 1345meV and B at 1360meV. The solid lines are the band gap shifts of bulk InAs and GaAs from reference[33]

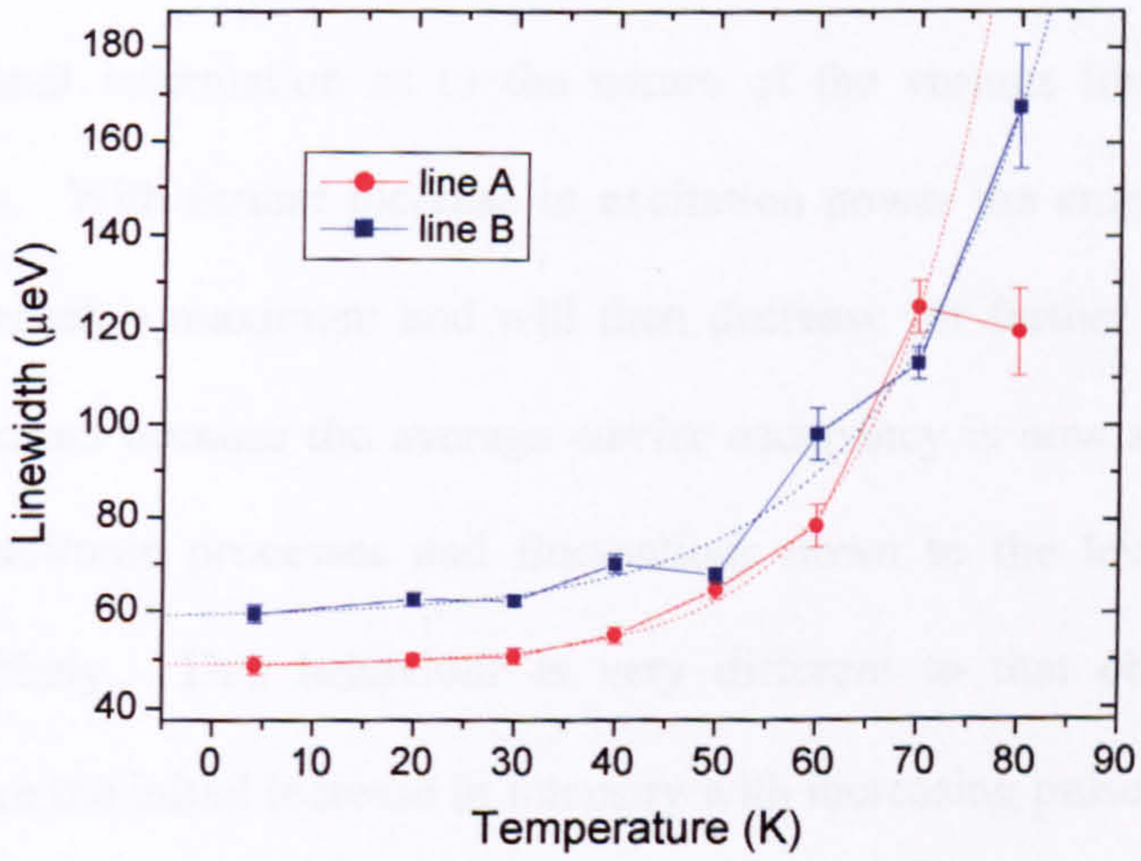

Figure 4.22 The temperature variation of the emission linewidths for two different single QDs. The dotted lines are exponential fits to the experimental data.

4.9 Analysis of the Power Dependent Emission Spectra

For a given excitation power a number of different order excitonic recombination features are observed in the CW spectra due to the statistical fluctuations of the QD carrier occupancy. Although for a given power there will be an average occupancy and hence one of the exciton lines will have the maximum intensity, during the time integrated spectra the occupancy will fluctuate either side of this average and a number of different excitonic features will be observed. With increase in excitation power a given order excitonic process will first increase in intensity, the functional dependence of the intensity on power being dependent on the order of the process; linearly for the single exciton, quadratic for the biexciton etc. As discussed below the power dependence provides additional information as to the nature of the various lines observed in the emission spectra. With further increase in excitation power the emission intensity of a given line will reach a maximum and will then decrease for further increase in power. This decrease occurs because the average carrier occupancy is now above that required for the given excitonic processes and fluctuations down to the level needed become increasingly unlikely. This behaviour is very different to that observed for pulsed excitation[34] where the initial increase in intensity with increasing pulse power is observed but not the high power decrease. This difference reflects the cascade-like process, which occurs for pulsed excitation where the laser pulse fills the QD up to a given occupancy. The excitons then recombine sequentially with all exciton orders less than and equal to the original QD occupancy being observed. Hence even if the QD is initially populated

with, for example, eight excitons, single exciton emission will be observed when the exciton number has decayed to one.

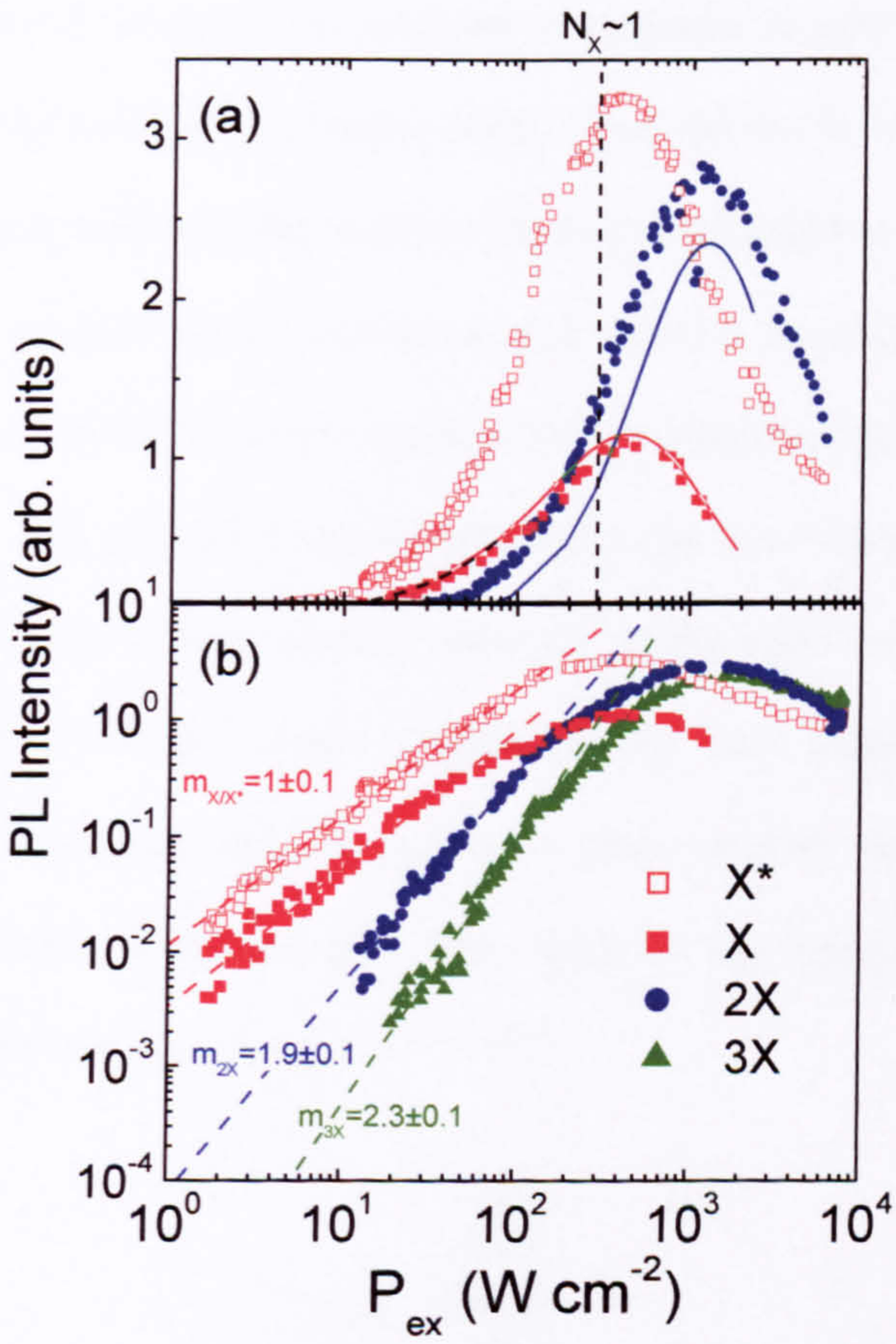

Figure 4.23 Detailed intensity variation of X, X*, 2X and 3X recorded as a function of excitation power density. The exponents of X and X* are m=0.98±0.1 and 1.02±0.1 respectively at low excitation power. For 2X and 3X, the low power exponent is m_{2X}=1.9±0.1 and m_{3X}=2.3±0.1 respectively.

4.9.1 Rate Equation Modelling of the Exciton Dynamics

In this section the rate equation used to model the exciton dynamics is described. This assumes equal capture of electrons and holes so that the QD is uncharged. As discussed

below there is evidence that unequal electron and hole capture may occur, giving rise to the creation of charged excitons. However this process does not invalidate the overall behaviour of the model. In the model excitons are captured into the QD from an external reservoir (barrier GaAs or the WL) and a steady state dot carrier occupation is formed, determined by the population of this reservoir (in turn determined by the laser power) and the time scales for exciton capture, relaxation and radiative recombination[1,9,19,35] (Figure 4.24). Non-radiative recombination is assumed to be negligible; a good approximation at low temperatures. The relaxation rate is assumed to be much faster than the radiative recombination rate (measured relaxation rates are of the order of a few picoseconds according to Sosnowski et al.[36] which is approximately three orders of magnitude less than the radiative relaxation time[23]) so that a given exciton relaxes to the lowest unoccupied state before recombining[13]. This leads to the sequential appearance of different exciton orders (X the 2X etc.)[9,10,11,13,14,15].

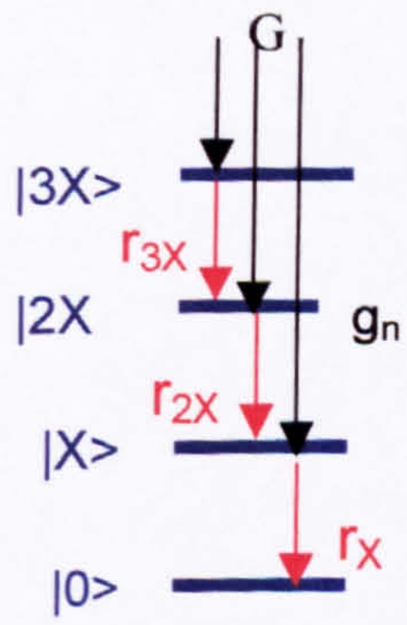

Figure 4.24 Exciton relaxation scheme. G is the overall photogeneration rate and g_n is the generation rate into the n_{th} level. The recombination rate of each level is denoted r_n.

The model considered in this work is based on the solution of coupled rate equations for X, 2X and six higher order complexes. A given state i can be created by excitonic capture directly into that state, given by the quantity g_i, which is directly proportional to the incident laser power. An exciton is lost from the state by radiative recombination at a rate $n_i r_i$ where n_i is the probability that the i^{th} state is occupied and r_i is the recombination rate for $n_i=1$. Recombination of an exciton in the next highest state i+1, occurring at a rate $n_{i+1}r_{i+1}$, provides an alternative mechanism for creating the i^{th} state. Finally the probability of the system being in the i^{th} state is decreased by the capture of excitons directly into the i+1 state at a rate g_{i+1}. For example the single exciton state X is destroyed if the QD captures a second exciton to form the biexciton state 2X. With these four creation and annihilation mechanisms the rate equation for the probability of the i^{th} state (n_i) is

$$\frac{dn_i}{dt} = g_i - n_i r_i + n_{i+1} r_{i+1} - g_{i+1} \qquad \textbf{Equation 4-1}$$

The generation rate of the i^{th} state g_i can be expressed in terms of the total generation rate in the reservoir, G, as:

$$g_i = G n_{i-1} \qquad \textbf{Equation 4-2}$$

where n_{i-1} is the probability that the next level is occupied and G is the total photogeneration rate. This result implies that carrier injection into the i^{th} state will not occur until the lower energy states are fully occupied. The total probability is normalised to unity, i.e.

$$\sum_{i=0}^{\infty} n_i = 1 \qquad \textbf{Equation 4-3}$$

Substituting 4.2 into 4.1

$$\frac{dn_i}{dt} = Gn_{i-1} - n_i r_i + n_{i+1} r_{i+1} - g_{i+1} \qquad \textbf{Equation 4-4}$$

For the time independent CW case

$$\frac{dn_i}{dt} = 0 \qquad \textbf{Equation 4-5}$$

for all i. Substituting this into equation 4.1 and solving analytically yields several coupled equations[37]. The solutions are of the form

$$n_i \propto G^i \prod_{j=1}^{i} \frac{1}{r_j} \qquad \textbf{Equation 4-6}$$

i.e. $n_1 \propto \frac{G}{r_1}$, $n_2 \propto \frac{G^2}{r_1 r_2}$, $n_3 \propto \frac{G^3}{r_1 r_2 r_3}$, etc.

The power dependence of the i^{th} order exciton will hence vary as G^i (i.e. linear for the exciton, quadratically for the biexciton etc...). Such a behaviour is observed experimentally for the lowest order exciton complexes as discussed in the next section. Deviation from the G^i trend, which are observed for higher i, may result from a variation of G as the dot occupancy increases.

4.9.2 Single Excitonic Emission

The power dependence of the intensity of the various s-shell emission lines (X, X*, 2X and mX in Figure 4.17) allows an unambiguous identification of their nature. Power-dependent emission measurements were performed using a continuously graded neutral

density filter and a single photon-counting detector. The emission intensities of the lines I_X, I_{X*}, I_{2X}, and I_{mX}) for excitation at 1520meV are presented in Figure 4.23a on log-linear and Figure 4.23b on log-log scales. These results are background-corrected because for large excitation powers a weak background of approximately 200cps is observed. This background is most likely due to scattered laser light. The form of the emission power dependencies was found to be very similar for two different dots.

Figure 4.23b shows that both I_X and I_{X*} increase linearly with excitation power, with an exponent $m_{X/X*}=1.05 \pm 0.1$, before simultaneously reaching a maximum intensity at 400Wcm^{-2} and decreasing for higher excitation powers. This linear behaviour confirms that both X and X* arise from single-exciton processes. However studies of the dependencies of X and X* on excitation energy (§4.10 and Chapter 5) show very different behaviour with X* not observed for direct excitation into the QD. This behaviour suggests that X is the uncharged exciton with X* a charged exciton produced by the unequal capture of electron and holes into the QD. This conclusion is supported by other experimental evidence. The X and X* lines do not exhibit any linear polarisation and hence it can be concluded that they do not arise from the splitting of the uncharged exciton by an asymmetric lateral confinement potential[13].

4.9.3 Power Dependent Multi-exciton emission

Figure 4.23 shows that the intensity of 2X increases approximately quadratically (exponent m=1.9± 0.1) with power. This behaviour confirms the identification of 2X as the biexciton.

The next line to appear at lower energy, 3X, has an exponent of m=2.3±0.1. This is significantly less than expected for the triexciton, which should scale m=3 with power. Assuming 3X is the tri-exciton line the weaker than expected power dependence suggests that the QD carrier capture efficiency decreases at high occupancies so that the QD carrier occupancy is no longer directly proportional to the incident laser power.

The solid lines in Figure 4.23 show the results of fitting the rate equation model to the experimental data. The overall agreement is very good. The fitting involves the solution of coupled rate equations for X, 2X and six higher order complexes. For the fitting of X and 2X the important input parameters are the ratio of the radiative rates for X and 2X, taken to be $r_x/r_{2x}=0.5$, and their relative formation rates, taken to be $f_x/f_{2x}=2$ [23]. The former ratio is assumed because the biexciton should have a recombination rate twice that of the single exciton, due to the biexciton having two recombination paths compared to one for the exciton. The power at which the single exciton lines (X and X*) have maximum intensity corresponds to an average QD exciton occupancy of unity. The excitation power axis (x-axis) of Figure 4.23 can also be considered as a measure of the average occupancy, $\overline{N}_X$. Average occupancy by a single exciton $\overline{N}_X = 1$ is indicated on

Figure 4.23, obtained from the fitting of the rate equation model. The power that corresponds to an occupancy of one agrees to within one order of magnitude of that calculated from the incident laser power, assuming a radiative lifetime of 1ns. Considering uncertainties in the true active area of the mesa this agreement is reasonable.

4.10 Resonant Excitation

All of the previous spectra were recorded for laser excitation energies above the InAs WL bandgap, resulting in the majority of e-h pairs being created in the GaAs. Figure 4.25 compares the single QD emission spectra recorded for a range of excitation energies, both above (blue spectra) and below (red spectra) the WL bandgap. In the latter case electrons and holes are directly created in the QD. For direct excitation into the QD a series of new lines (X_1, X_2 and X_3) are observed, all of which exhibit single exciton like behaviour. The properties and possible nature of these lines will be discussed in detail in Chapter 5.

Of importance to the present discussion is the behaviour of the lines X and X*. Both lines are observed for excitation above the wetting layer bandgap but for excitation directly into the QD only X is observed, although its intensity is reduced considerably due to the small absorption cross-section of a single QD. This behaviour confirms X* as being due to a charged single exciton, the formation of which requires the unequal capture of electron and holes by the QD. This is only possible when carriers are first excited into the GaAs and are subsequently captured by the QD. Direct excitation into the QD can only result in equal numbers of electrons and holes and hence X* cannot be

produced under these conditions. This behaviour is studied in more detail by the PLE measurements described in Chapter 5. Although the present results indicate that X* represents a single charged exciton, the nature of its charged state cannot be identified. However a comparison with results obtained from a structure where excess carriers of a known type can be controllably injected into a single QD (see Chapter 6) suggests that the blue spectral shift between X* and X arises from X* being positively charged (X^+, two holes plus one electron).

The mechanism via which unequal electron and hole capture occurs is unclear but may involve the electron being trapped by a defect or impurity state outside of the QD. These states could be formed on the surface of the sub-micron mesas, a fact supported by the absence of an X* line in structures where single QDs are isolated using sub-micron holes in a metal mask.

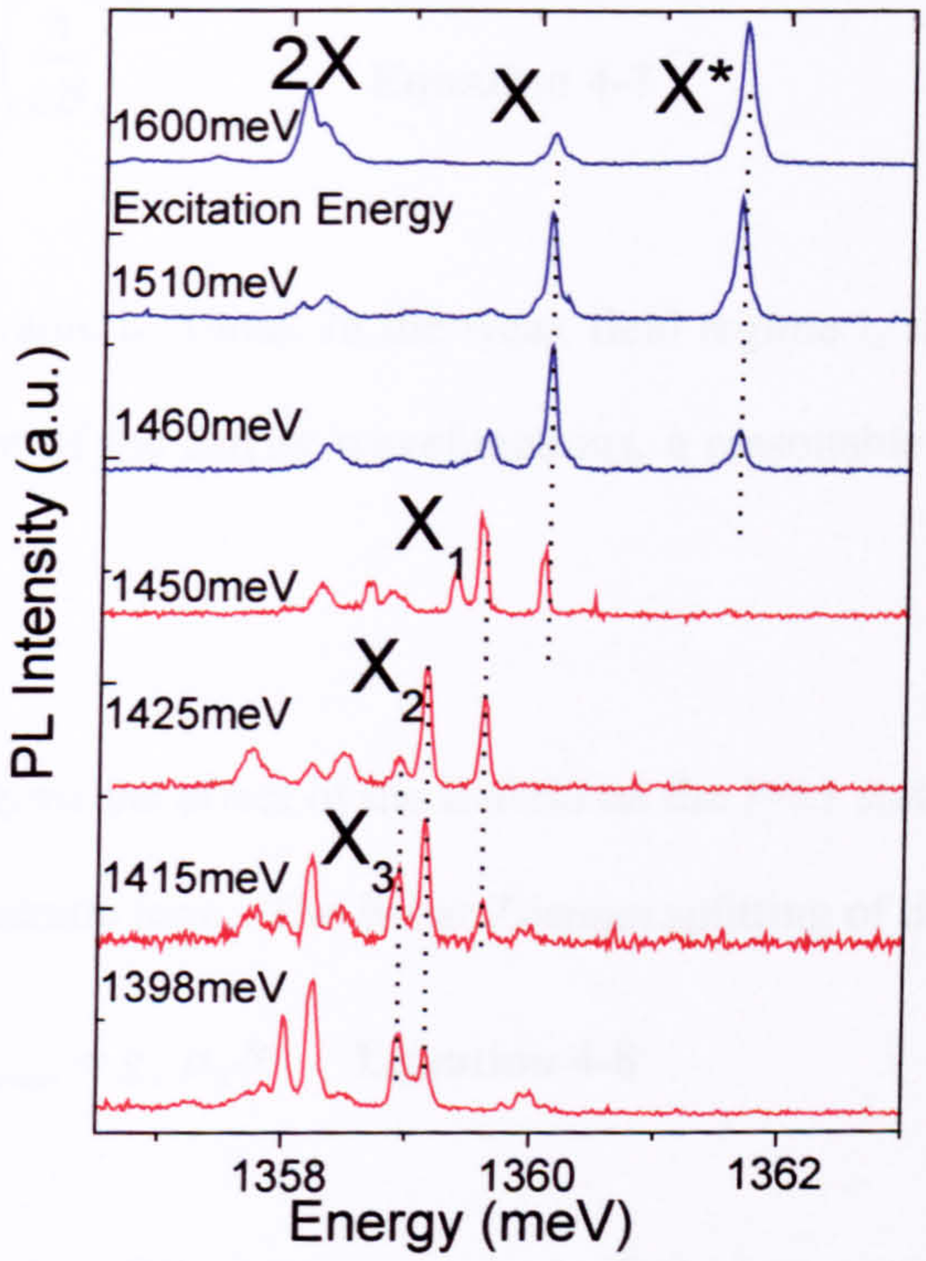

Figure 4.25 Ground state emission spectra for different excitation energies. As the excitation is tuned below the wetting layer band edge (~1460meV) three new peaks appear (X_{1-3}) to the low energy side of the original single exciton X. However X is still observable although its intensity is much weaker due to the reduced absorption. In contrast X* is only observed for excitation above the wetting layer bandgap. Blue spectra correspond to non-resonant and red spectra to resonant excitation.

4.11 Magneto-Optical Study of Single Quantum Dots

To study the nature of the QD wavefunctions magneto-optical measurements were performed with the magnetic field applied parallel to the growth axis (Faraday geometry) and fields in the range 0→5T. In the low field regime the magnetic energy is smaller than the exciton energy and hence the field can be treated as a weak perturbation. This regime can also be characterised by the magnetic field length

$$l_c = \left(\frac{\hbar}{eB}\right)^{1/2} \qquad \textbf{Equation 4-7}$$

which at 5T has a value l_c=10nm. In the weak field regime l_c should be greater than the typical spatial extent of the carrier wavefunctions, a reasonable approximation at a field of B=5T.

In the weak field regime the effect of the B-field on the J=±1 states of an exciton, consists of a linear and a quadratic term. The linear Zeeman splitting of the spin states is given by

$$\Delta E_{Zeeman} = g_X \mu_B B \qquad \textbf{Equation 4-8}$$

where g_X is the g factor of the exciton, μ_B is the Bohr magneton and B is the magnetic field. The quadratic diamagnetic shift increases the centre of gravity of the two spin split components

$$\Delta E_{dia} \approx \gamma_2 B^2 \qquad \textbf{Equation 4-9}$$

where γ_2 is the diamagnetic parameter for the exciton. For multiple excitons the difference between the magnetic interaction energy ($\Delta E_{Zeeman} + \Delta E_{dia}$) for the initial and final states will determine the overall behaviour of the exciton.

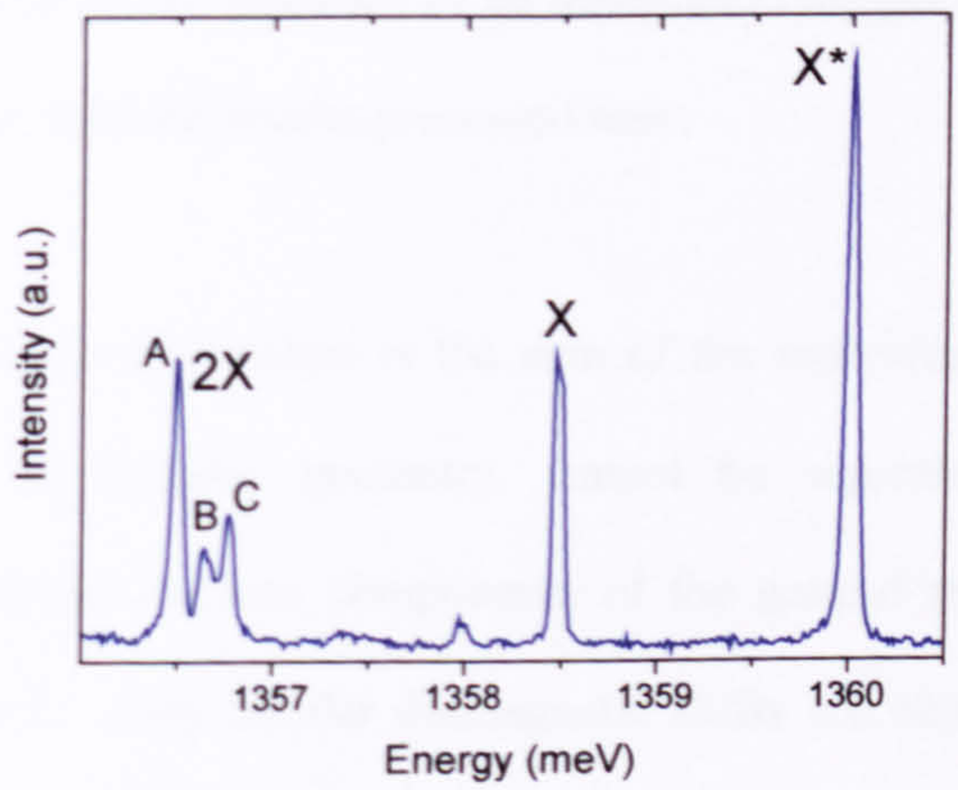

Figure 4.26 Ground state emission lines considered in the magneto-optical study. The sample is excited at 1480meV.

Figure 4.26 shows the s-shell emission lines under investigation in this section. X and X* are easily identified, but under closer scrutiny the biexciton line 2X appears to be comprised of three emission lines separated by less than 400μeV and labelled $2X_A$, $2X_B$ and $2X_C$. While the power dependence of these lines clearly indicated that they are biexcitonic in nature these measurements cannot identify their different origin. The comparison of the resonant and non-resonant emission spectra shows a modification of these emission lines, but it is ambiguous in nature. These lines are most likely to be comprised of the neutral biexciton (2X), the charged biexciton (2X*) and/or a higher order state. The perturbation caused by the extra carrier in the 2X* is expected to be small due to it being located in the p-shell. A reduction in the number of lines is observed, when resonant excitation is used, indicating that some of them are due to recombination of a charged species, but it is unclear which of these lines remains for resonant excitation. From studies of a charge tuneable sample (Chapter 6) it is clear that

the perturbation caused by the presence of an additional charged carrier (<1meV) on the biexciton is consistent with the results presented here.

The g-factor observed for an exciton is the sum of the individual electron and hole g-factors which, for the Faraday geometry, cannot be separately determined. The diamagnetic shift and the Zeeman components of the ground state emission lines are summarised in Table 1. Very similar diamagnetic shifts are observed for all the lines although there is a larger variation in g-factors.

Complex	g factor	Diamagnetic shift $\mu eV.T^{-2}$
X	0.466	15.7
X*	0.311	15.4
$2X_A$	0.342	15.3
$2X_B$	0.529	13.1
$2X_C$	0.218	15.1

Table 1 Diamagnetic and Zeeman components

Figure 4.27 shows the magneto-PL spectra for the single uncharged exciton as a function of magnetic field. The two different degrees of circular polarisations resulting from changes in the spin quantum number m_s of ± 1 are denoted by the red and blue lines. The spectra of Figure 4.27 show clearly the expected spin splitting and diamagnetic shift of the centre of gravity of the emission, the former gives a g factor of g_X=0.466. This g-factor is much smaller than measured in other work on single QDs. For example Kuther et al.[14] measure a value of g_X=3.02 for nominally $In_{0.6}Ga_{0.4}As$ QDs. This difference can be attributed to differences in the QD structure and composition. The g-factor for electrons in bulk InGaAs is known to be a strong function of the composition. Although

the QDs studied in this chapter are nominally InAs, the post growth annealing applied to increase the emission energy will result in a non-zero Ga composition. Even as grown InAs QDs are known to contain non-zero and non-uniform Ga composition[38]. Hence it is unsurprising that In(Ga)As QDs grown under different conditions, with different nominal compositions or subjected to different post-growth treatments will exhibit very different g-factors. In addition calculations by Kotlyar et al. [26] show that the g-factor is also dependent upon the size of the QD, providing further dependence on the structural properties of the QD.

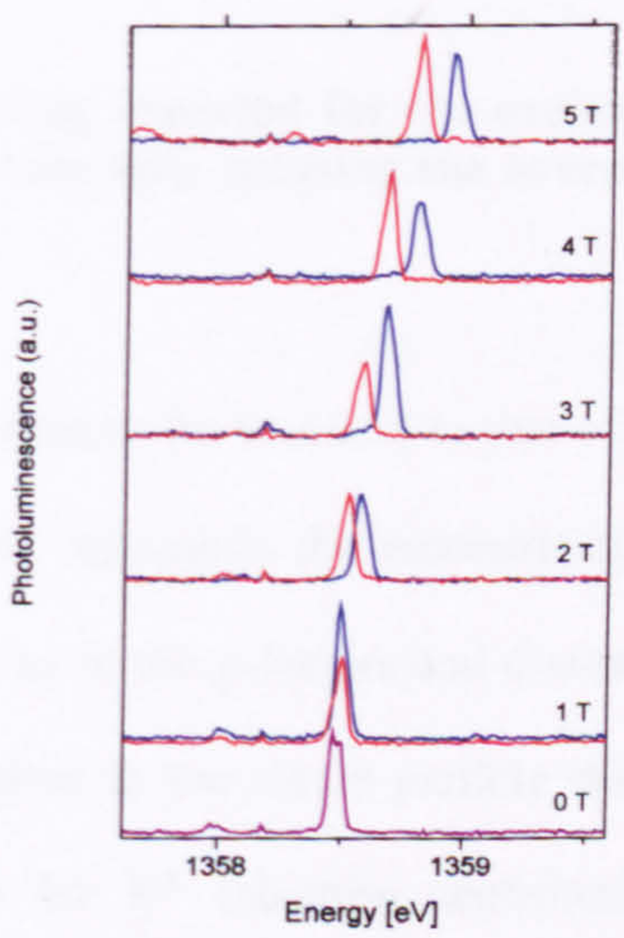

Figure 4.27 Exciton, X, emission line with increasing magnetic field.

Theoretically the exciton and biexciton should have identical g-factors and diamagnetic shift coefficients. The exciton has both the g-factors of the hole and electron contributing to its initial state, but no contribution to the final vacuum state. For the biexciton the antiparallel electrons and holes cancel in the initial state to give a zero total g-factor but there is a single exciton contribution in the final state (Figure 4.28).

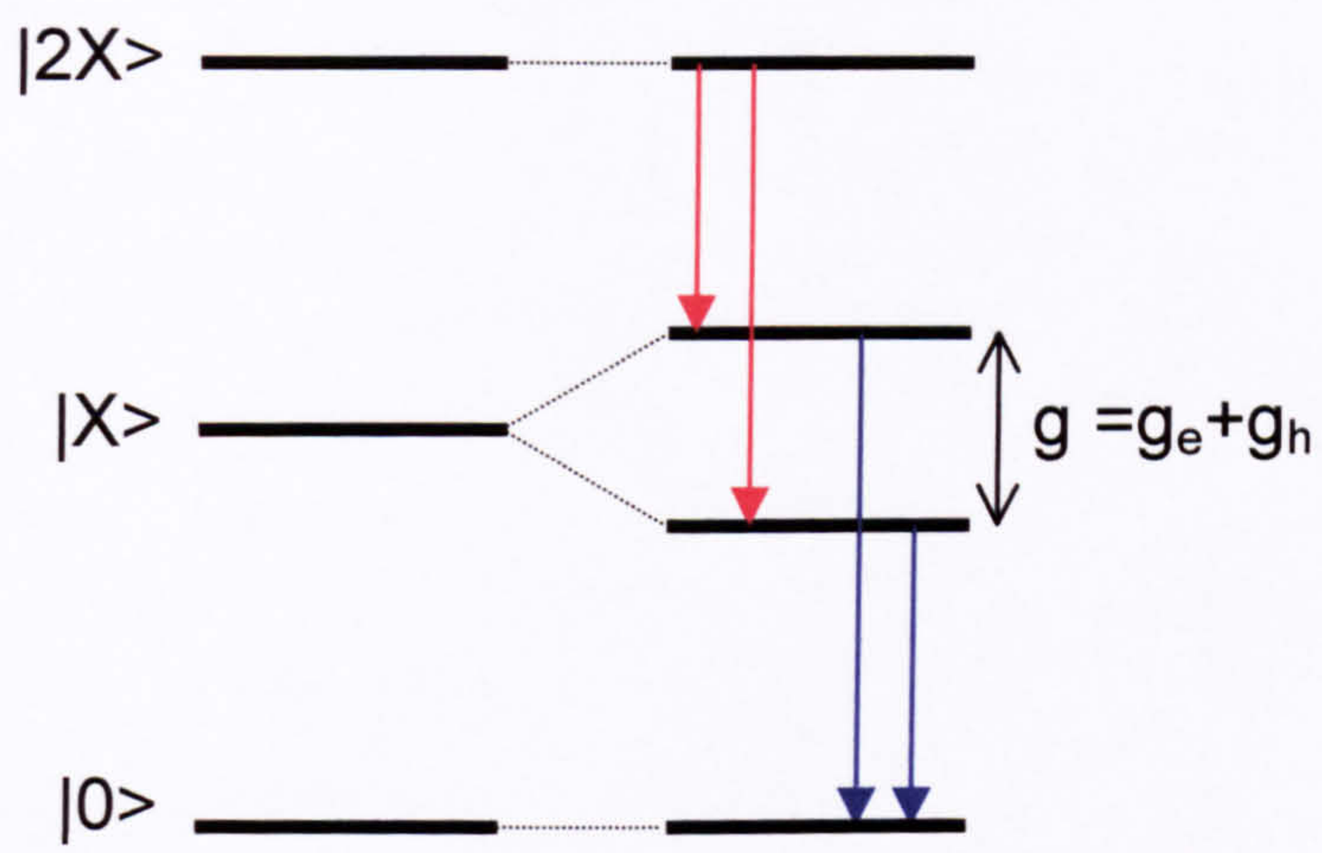

Figure 4.28 The spin splitting expected for the exciton and biexciton. Because the initial biexciton state has zero spin splitting the overall spin splitting of the exciton and biexciton is identical.

Although none of the 2X g-factors are identical to that of the exciton, the most similar is $2X_B$ suggesting that this line represents the recombination of the uncharged biexciton (Figure 4.29). The differences in the g-factors and diamagnetic shift coefficients for the lines may reflect a perturbation to the single particle states as a result of many-carrier interactions. This is seen for X* (electron contribution for the initial state, hole contribution to the final state for X^+ and vice versa for X^-) which should have the same g-factor and diamagnetic shift as X (Figure 4.30). Although the diamagnetic shifts are similar the g-factors are significantly different.

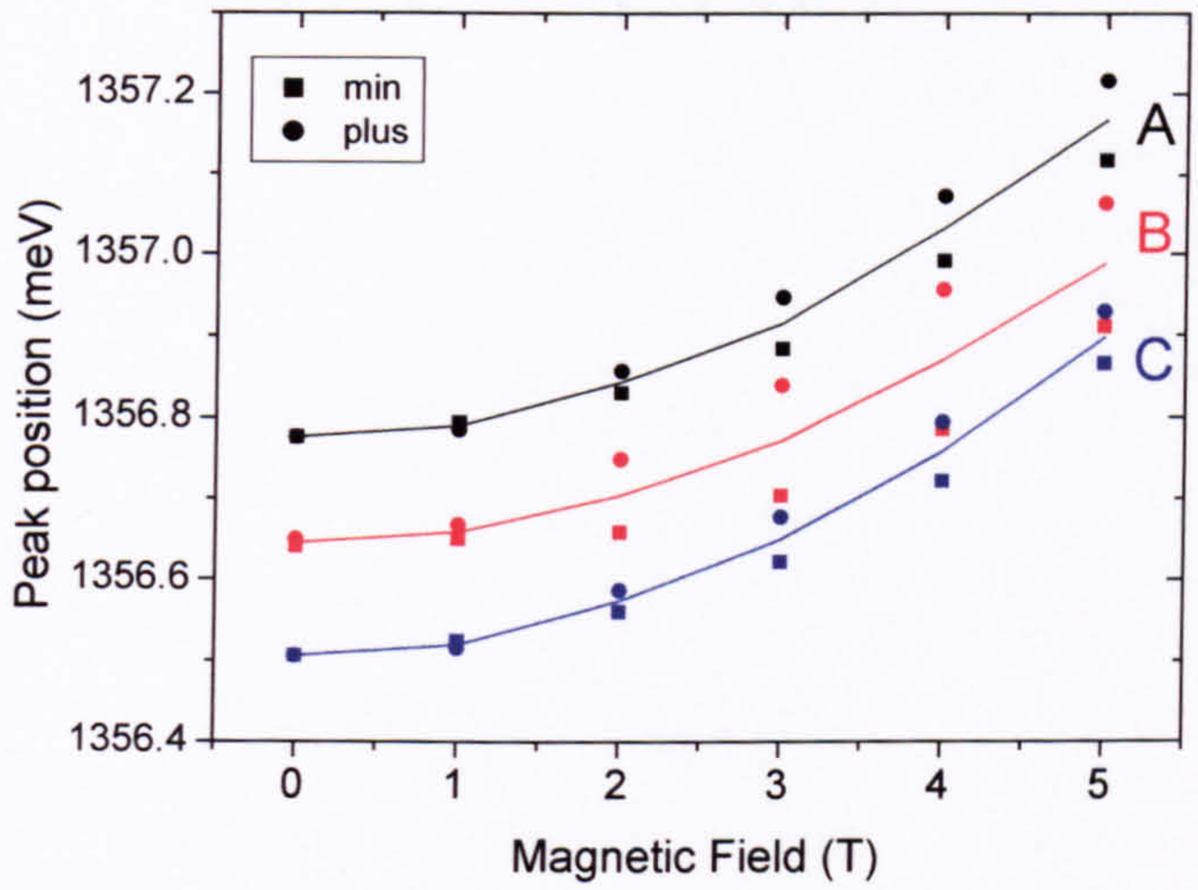

Figure 4.29 The peak positions of the three biexciton-like lines with magnetic field. The two different degrees of circular polarisations caused by the changes in the spin quantum number m_s of ±1 are plotted as circles and squares.

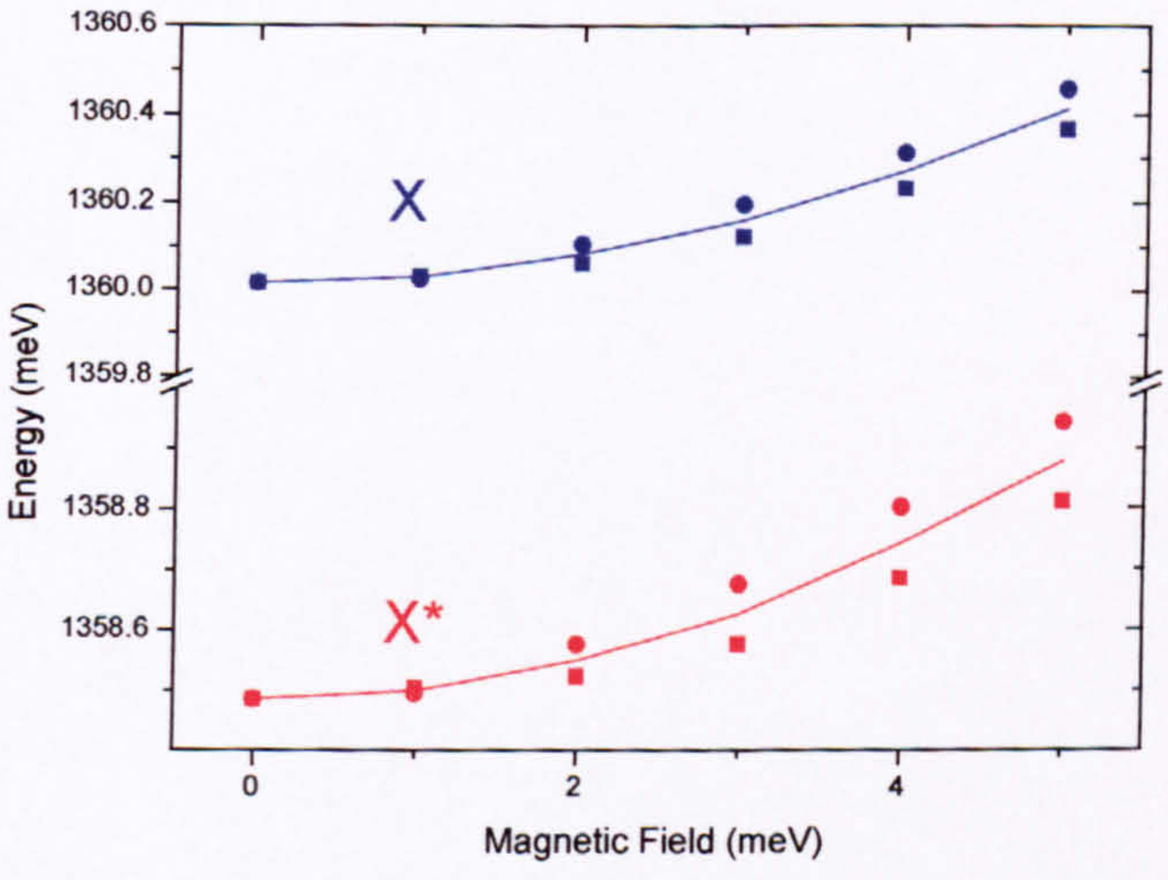

Figure 4.30 Peak positions of the two excitonic lines with magnetic field for the neutrally charged exciton emission line X and the charged exciton emission line X*. The two different degrees of circular polarisations caused by the changes in the spin quantum number m_s of ±1 are plotted as circles and squares.

Figure 4.31 shows the different magnetic field behaviour of X and $2X_B$. Their centre of gravities become closer together with increasing field and the smaller spin splitting of X is clearly seen. This results in the binding energy of the biexction being reduced with increasing magnetic field. This is clearly demonstrated in Figure 4.31 where the closest Zeeman spin split components of X and 2X become closer in absolute energy. The binding energy changes from 1.8meV at zero magnetic field to 1.5meV at 5T. Similar effects have been reported elsewhere[15].

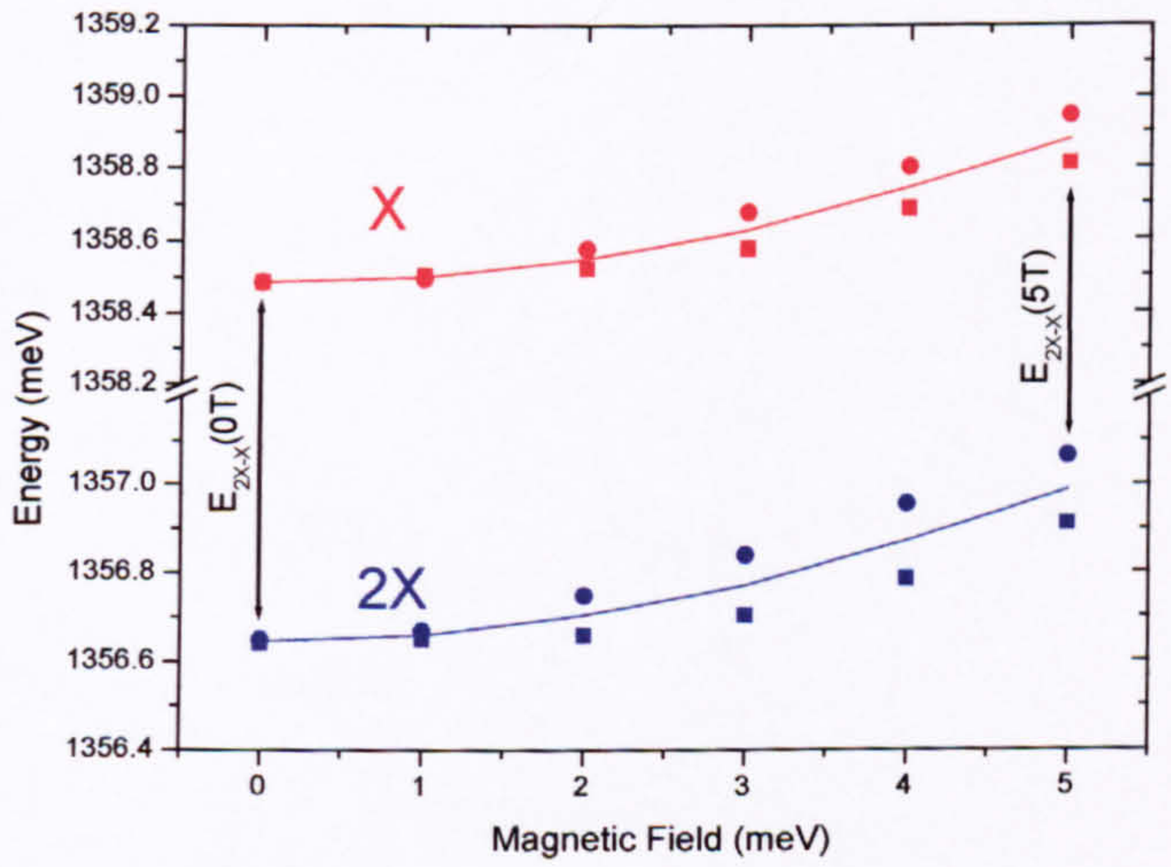

Figure 4.31 The peak positions of the excitonic (X) and a biexcitonic ($2X_B$) lines with magnetic field. The two different degrees of circular polarisations caused by the changes in the spin quantum number m_s of ±1 are plotted as circles and the squares.

4.11.1 The Spatial Extent of the Exciton Wavefunction

The centre of gravity of the exciton doublet shifts diamagnetically to higher energies with increasing field. For strong geometric confinement the single exciton diamagnetic shift can be approximated[39] by

$$\Delta E_{dia} = \frac{e^2}{8}\left(\frac{\langle r_e^2 \rangle}{m_e} + \frac{\langle r_h^2 \rangle}{m_h}\right)B^2 \qquad \textbf{Equation 4-10}$$

where $r_{e/h}$ is the mean square lateral extension of the electron/hole wavefunctions respectively. Assuming equal extensions then the diamagnetic shift is given by

$$\Delta E_{dia} = \frac{e^2\langle r^2 \rangle}{8}\left(\frac{1}{m_e} + \frac{1}{m_h}\right)B^2 \qquad \textbf{Equation 4-11}$$

The measured diamagnetic shift gives a value for $\sqrt{\langle r^2 \rangle}$ of 6.1nm, asuming bulk GaAs values for the carrier effective masses (m^*_e=0.067m_0 and m^*_h=0.25m_0). For an infinite depth well

$$\sqrt{\langle r^2 \rangle} = a\sqrt{\frac{1}{3} - \frac{1}{2n^2}} \approx 0.53a \qquad \textbf{Equation 4-12}$$

where a is the well width. Hence $\sqrt{\langle r^2 \rangle}$=6.1nm is consitent with a physicsal size of 11.5nm which is reasonably close to the dot base size of 18nm as determined by TEM (Figure 4.6).

4.12 Summary

The emission properties of a single self-assembled QD have been studied by isolating the dot in a 200nm diamter mesa. The mesa was fabricated using e-beam lithography followed by dry etching. For low excitation power a single, very sharp emission line is observed indicating the presence of only a single optically active dot displaying the expected δ-function like density of states. With increasing excitation power additional lines are observed reflecting the recombination of a single exciton in a dot that is occupied by additional electrons and/or holes. A binding energy for the biexciton (relative to the single exciton) of +1.7meV is measured. A charged exciton emission line is observed above the single charge neutral exciton line, reflecting unequal capture of electrons and holes into the dot. Comparison with results in Chapter 6 indicate that this line represents recombination of the positively charged exciton (X^+). Higher order uncharged excitonic recombination is also observed. For resonant excitation of the dot three new lines are observed, all exhibiting a single exciton nature. These features will be considered further in Chapter 5.

From laser power (or dot exciton occupation) dependent measurement of the emission intensities, the neutral exciton (X), the charged exciton (X*), the biexciton (2X) and the triexciton (3X) have all been conclusively identified. Both the neutral and charged excitons have intensity verses power exponents of 1.0 ± 0.1, the exponent for the biexciton is 1.9 ± 0.1, and for the triexciton 2.3 ± 0.1. The linear power dependence of the neutral and charged excitons is expected and demonstrates that the extra carrier in the

charged exciton has no effect on the carrier capture efficiency. The biexciton's behaviour is almost quadratic again as expected. The triexction does not have a cubic behaviour. This is attributed to a decrease of the carrier capture rate for highly occupied dots.

Magnetic field measurements have allowed the spatial extent of the confined wavefunction to be probed and have allowed the diamagnetic shifts and g-factors of the different excitonic complexes to be compared. The behaviour is complex and suggests significant departure from a single particle model.

[1] D. Bimberg, M. Grundmann, N.N.Ledentsov, *Quantum Dot Heterostructurs*, (Wiley) 1999)
[2] A.D.Yoffe. Advances in Physics 2001, **50** (1), 1 (2001)
[3] P. P. Paskov, P. O. Holtz, B. Monemar, J.M. Garcia, W. V. Schoenfeld, and P. M. Petroff, *Phys. Rev. B.* **62** 7344 (2000)
[4] T. P. Softley, *Atomic spectra*. Oxford University Press, (1994)
[5] I. I. Sobel'man, *Atomic spectra and radiative transitions - 2nd ed.*, Springer (1992).
[6] M. A. Gilleo, P.T. Bailey and D. E. Hill, *Phys. Rev.* **174**, 898 (1968)
[7] R. J. Warburton, C. S. Dürr, K. Karrai, J. P. Kotthaus, G.Medeiros-Ribeiro, and P. M. Petroff, *Phys. Rev. Lett.* **79**, 5282 (1997).
[8] K. H. Schmidt, G. Medeiros-Ribeiro, and P. M. Petroff, *Phys.Rev. B* **58**, 3597 (1998)
[9] E. Dekel, D. Gershoni, E. Ehrenfreund, D. Spektor, J. M. Garcia, and P. M. Petroff, *Phys. Rev. Lett.* **80**, 4991 (1998)
[10] F. Findeis, A. Zrenner, G. Böhm, and G. Abstreiter, *Solid State Commun.* **114**, 227 (2000)
[11] L. Landin, M. E. Pistol, C. Pryor, M Persson, L. Samuelson, and M. Miller, *Phys. Rev. B* **60**, 16 640 (1999)
[12] L. Landin, M. S. Miller, M. E. Pistol, C. E. Pryor, and L. Samuelson., *Science* **280**, 262 (1998)
[13] E. Dekel, D. Gershoni, E. Ehrenfreund, J. M. Garcia, and P. M. Petroff, *Phys. Rev. B* **61**, 11 009 (2000)
[14] A. Kuther, M. Bayer, A. Forchel, A. Gorbunov, V. B. Timofeev, F. Schäfler, and J. P. Reithmaier, *Phys. Rev. B* **58**, R7508 (1998)
[15] M. Bayer, O. Stern, P. Hawrylak, S. Fafard, and A. Forchel, *Nature* **405**, 923 (2000)
[16] A. Hartmann, Y. Ducommun, E. Kapon, U. Hohenester, and E.Molinari, *Phys. Rev. Lett.* **84**, 5648 (2000)
[17] R. J. Warburton, C. Schäflein, F. Haft, F. Bickel, A. Lorke, K.Karrai, J. M. Garcia, W. Schänfeld, and P. M. Petroff, *Nature* **405**, 926 (2000)
[18] D. Gammon, E. S. Snow and D. S. Katzer. *Appl. Phys. Lett.* **67**, 2391 (1995)
[19] K. Brunner, G. Abstreiter, G. Böhm, G. Tränkle, and G. Weimann. *Phys. Rev. Lett.* **73**, 1183 (1994)
[20] M Bayer T. Gutbrod, A. Forchel, V. D. Kulakovskii, A. Gorbunov, M. Michel, R. Steffan and K. H. Wang *Phys. Rev B* **58** 5740 (1998)
[21] F. Findeis, A. Zrenner, M. Markmann, G. Böhm and G. Abstreiter *Physica E* **7** 354 (2000)
[22] E. Dekel, D. V. Regelman, D. Gershoni, and E. Ehrenfreund W. V. Schoenfeld and P. M. Petroff, *Phys. Rev. B* **62** 11 038 (2000)
[23] R. M. Thompson, R. M. Stevenson, A. J. Shields, I. Farrer, C. J. Lobo, D. A. Ritchie, M. L. Leadbeater, and M. Pepper, *Phys. Rev. B*, **64** 201302R (2001)
[24] M. Bayer, O. Stern, A. Kuther, A. Forchel,. *Phys. Rev. B.* **61** 7273 (2000)
[25] M. Bayer, A. Kuther, A. Forchel, A. Gorbunov, V. B. Timofeev, F. Schäfer, J. P. Reithmaier, T. L. Reinecke, and S.N. Walck. *Phys. Rev. Lett.* **82** 1748 (1999)

[26] R. Kotlyar, T. L. Reinecke, M. Bayer, A. Forchel. *Phys. Rev. B.* **63** (2001)
[27] A. Wojs and P. Hawrylak *Phys. Rev. B* **55** 13 066 (1997)
[28] S. Malik, C. Roberts, R. Murray and M. Pate., *Appl. Phys. Lett.* **71**, 1987 (1997)
[29] T. Krass, University of St. Andrews.
[30] P. Hawrylak, *Phys. Rev. B* **60**, 5597 (1991)
[31] P. Borri, W. Langbein, J. M. Hvam, and F. Martelli, *Phys. Rev. B*, **59**, 2215 (1999)
[32] X. Q. Li and Y. Arakawa, *Phys. Rev B*, **60**, 1915 (1999)
[33] Landolt-Börnstein, *Numerical Data and Functional Relationships in Science and Technology,* **22a**, 83
[34] D. V. Regelman, E. Dekel, D. Gershoni, W.V. Scoenfeld, P. M. Petroff *Phys. Stat. Sol. B* **224** 343 (2001)
[35] M. Grundmann and D. Bimberg, *Phys. Rev. B* **55**, 9740 (1997)
[36] T. S. Sosnowski, T. B. Norris H. Jiang, J. Singh, K. Kamath, and P. Bhattacharya, *Phys. Rev. B* **57** R9423 (1998)
[37] E. Dekel, D. V. Regelman, D. Gershoni, and E. Ehrenfreund W. V. Schoenfeld and P. M. Petroff PRB **62** (16) 11038 (2000)
[38] P.W. Fry, I. E. Itskevich, D. J. Mowbray, M. S. Skolnick, J. J. Finley, J. A. Barker, E. P. O'Reilly, L. R. Wilson, I. A. Larkin, P. A. Maksym, M. Hopkinson, M. Al-Khafaji, J. P. R. David, A. G. Cullis, G. Hill, and J. C. Clark *Phys. Rev. Lett.* **84** 733 (2000)
[39] S.N.Walck and T.L.Reinecke, Phys. Rev. B **57**, 9088 (1998)

Chapter 5

Absorption Processes and Carrier Relaxation in Single Quantum Dots

5.1 Introduction

The coupling of excitons to longitudinal optical (LO) phonons in polar semiconductors arises from the polarisation of the lattice by the spatial difference of the electron and hole (e,h) charge distributions; the dipole moment of the exciton. This coupling has been analysed theoretically for bulk[1], quantum well[2] and quantum dot (QD) structures[3,4]. The strength of the coupling is very sensitive to the forms of the electron and hole wavefunctions and should vanish for identical distributions as, for example, might be expected in strongly confined QDs.

A measure of the strength of the exciton-LO-phonon coupling is provided by the ratio of the intensity of the phonon satellite observed in emission to that of the no-phonon line. The former involves the emission of both a photon and phonon whilst in the latter process only a photon is created. This intensity ratio gives the Huang-Rhys parameter, S, which describes the strength of the exciton-LO-phonon interaction. Recent studies of MBE grown InAs/GaAs self-assembled QDs have found significant, non-zero values for S, e.g. 0.03 [5], 0.01–0.5 [6], and 0.5 [7]. Bissiri et al[6] investigated the change of the electron-phonon

interaction with QD emission energy and found that the parameter S could vary over nearly two orders of magnitude. These values for S are comparable to, or exceed, values found for InGaAs-InP QWs (~0.003 [8]).

The high S values for self-assembled QDs could be due to a spatial separation of the electron and hole wave functions as a result of an asymmetric dot shape[5], the presence of piezoelectric fields[7] or the breakdown of the adiabatic approximation usually employed to treat exciton-LO phonon coupling[9]. Extrinsic effects such as the presence of charged point defects[4] may also lead to a polarisation of the exciton charge distribution and, as a result, enhanced LO phonon coupling. The study of the coupling between excitons and LO phonons in QDs is of both intrinsic interest and because the results may provide information concerning the nature of the electron and hole wavefunctions. In addition the LO-phonon-exciton coupling strength is important when considering carrier relaxation mechanisms, particularly in the present systems with discrete energy levels.

In the present chapter a range of single QD spectroscopic techniques are applied to study single QDs in the same InAs/GaAs sample as in Chapter 4. Single dot spectroscopy allows the detailed study of exciton LO phonon interactions which would otherwise be obscured by the strong inhomogeneous broadening present in ensemble studies – this broadening can be comparable to the phonon energy. Microphotoluminescence (μPL) is applied to search for phonon satellites at energies below the ground state emission and μPL excitation (μPLE) is applied to study exciton-LO-phonon processes in absorption and carrier relaxation mechanisms. The results reveal a very small S value for the

intrinsic emission spectra. However, in absorption very strong LO phonon features are observed for detection on the exciton, X emission. This contrasting behaviour between emission and absorption is attributed to the occurrence of a resonant mixing in absorption between the ground plus one 1LO phonon state and similar energy excited states, resulting in a breakdown of the adiabatic approximation. In addition it is found that for resonant QD excitation (below the energy of the wetting layer) several additional single exciton-like lines are observed in emission, which eventually dominate the spectra for low-energy excitation. In PLE these new lines exhibit strongly enhanced phonon coupling relative to X, and are attributed to single exciton transitions perturbed by charged defects in the mesa which contains the QD. However, as is the case for X, phonon satellites are absent in emission, indicating a weak intrinsic value for S.

5.1.1 Phonon-Carrier Coupling Mechanisms

In semiconductors carrier relaxation occurs primarily by the emission of phonons (lattice vibrations), although in 0D systems with discrete energy levels this might be forbidden by the phonon bottleneck (see Chapter 1). In this section a brief outline of carrier-phonon coupling mechanisms will be given, a more detailed discussion can be found in the article by Devresse[10]. All types of phonons can couple to charge carriers via the deformation potential mechanism. This mechanism arises due to the modulation of the local atomic spacing by a phonon, which in turn produces a modulation of the electronic band structure. However in III-V semiconductors the strongest phonon-electron coupling occurs for LO phonons due to the Fröhlich interaction. Although III-V semiconductors

have predominantly covalent bonds there is a small fraction of ionic bonding which results in small, but non-zero, equal and opposite charges on the group III and group V atoms. For low k optical phonons, alternate atoms vibrate in anti-phase and, for the LO phonons, this results in a macroscopic electric field which couples to the charge carriers. For an exciton the degree of coupling by this Fröhlich mechanism is dependent on the difference in the spatial extents of the electron and hole wavefunctions, for a QD this will be related to the dipole moment of the exciton. It is unclear how reducing the dimensionality of a semiconductor structure will affect the strength of the Fröhlich coupling. Generally it thought that a reduced dimensionality would lead to a decrease in the coupling strength[11]. The scattering of electrons by phonons is only possible when both energy and momentum are conserved and a reduced dimensionality limits the range of available states that satisfy these requirements. However the experimental results presented in this Chapter and previously published results[12] provide evidence for strong Fröhlich coupling in In(Ga)As-GaAs self-assembled QDs.

The interaction between LA phonons and carriers occurs via the deformation potential and also via the piezoelectric field produced by the LA phonons. It has been predicted by Inoshita et al.[13] that efficient carrier relaxation in QDs may occur via the joint emission of LO+LA phonons. It should be noted that if the phonon bottleneck does prevent efficient carrier relaxation by the emission of one or more phonons then Auger processes may may provide an alternative relaxation mechanism[14].

5.1.2 Phonon bottleneck

It has long been hypothesised that the discrete density of states inhibits LO phonon relaxation in QDs (Figure 5.1). Unless the energy separation of two states (ΔE) is equal to the LO phonon energy then relaxation is forbidden.

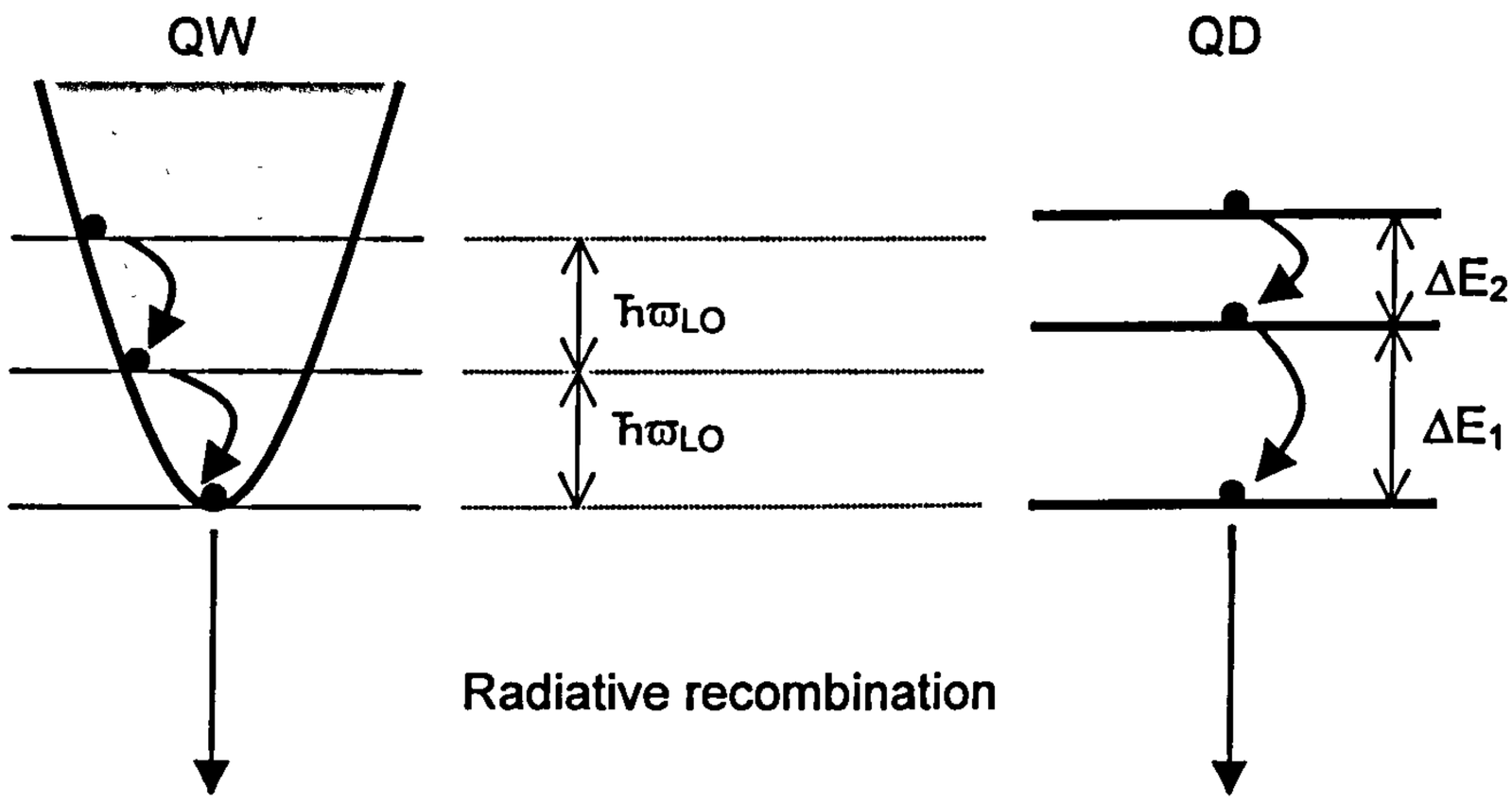

Figure 5.1 LO phonon relaxation in a QW (left) and a QD (right)

The results presented in the present chapter will show that LO phonon relaxation is possible because of the many phonon energies available and also due to LO+LA phonon coupling. It will also be shown, as expected, that the relaxation is greatly enhanced by the presence of a higher energy state.

5.2 Review of Relevant Published Work

Although there have been numerous studies of the optical spectroscopy of single QDs (see Chapter 4), there have been very few reports concerning phonon effects. Toda et al.[15] performed PLE measurements on single InGaAs-GaAs self-assembled QDs using a near field scanning optical microscope (SNOM). Above an energy ≈50meV from the detection energy (the single exciton line) a rising continuum was observed which eventually merges into the WL. In addition a series of sharp features were observed around 65meV, approximately equal to twice the LO phonon frequencies. These features were attributed to 2LO phonon resonant Raman lines, their strength possibly being enhanced by an underlying electronic state. The mechanism for this process is shown schematically in Figure 5.2(a). The phonons were assumed to be localised QD phonons, with their energies varying slightly from dot-to-dot. From their PLE results Toda et al[15] proposed a mechanism for the efficient relaxation of carriers within the dot (Figure 5.2(b)). Following excitation into the wetting layer initial relaxation occurs via the continuum states. Once the bottom of this continuum is reached further relaxation to the ground state occurs via the emission of localised phonons.

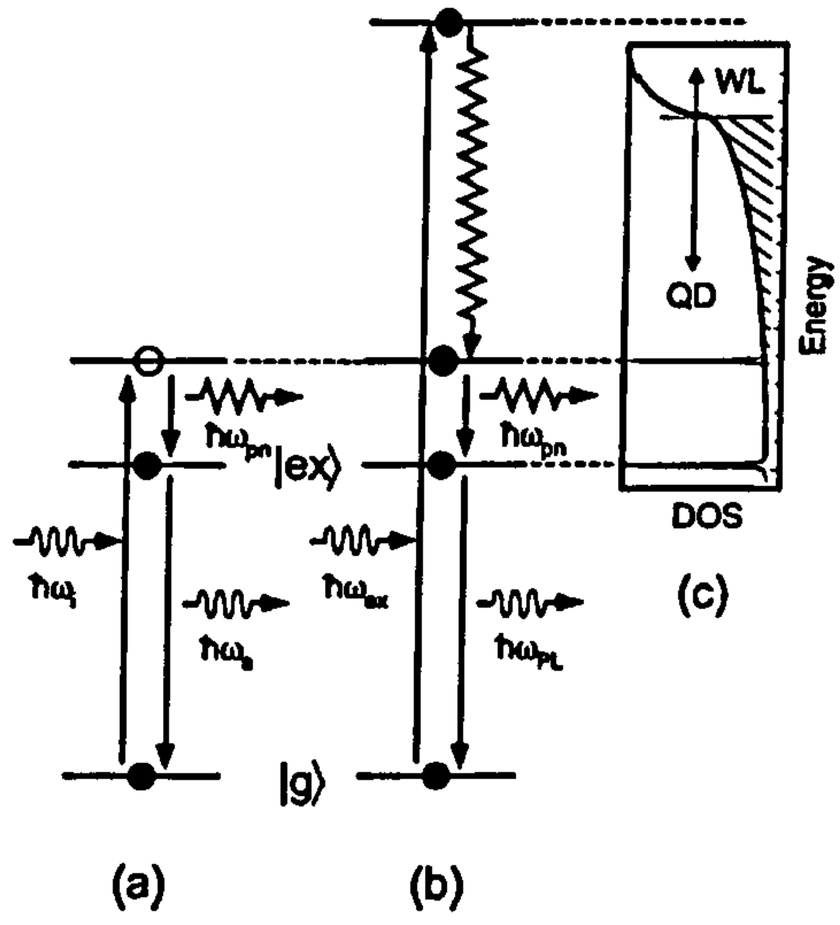

Figure 5.2 (a) Schematic diagram of a resonant Raman process showing incident (ϖ_i) and emitted ϖ_s photons and an optical phonon (ϖ_{pn}). (b) Carrier relaxation mechanism under nonresonant conditions showing exciting (ϖ_{ex}) and emitted ϖ_{PL} photons. (c) Schematic diagram of the DOS with a phonon feature (grey line). $|g\rangle$ and $|ex\rangle$ label the vacuum ground state and excitonic ground state, respectively. From Toda et al[15].

Findeis et al[16] also studied the PLE of a single QD. Phonon resonances were observed at 32 and 36meV and are attributed to InAs and GaAs LO-phonons respectively. In addition similar resonances were observed for detection on the biexciton emission. Creation of the biexciton by resonant excitation into the discrete QD states is unexpected as absorption of the first photon and the creation of an exciton renormalises the transition energy. This destroys the resonance with the incident laser energy, hence preventing the absorption of a second photon. Findeis et al[16] explained their observation of resonant biexciton creation using a mechanism that involves the initial creation of an exciton plus 1LO phonon and the subsequent relaxation of the exciton to its ground state followed by a second exciton plus 1LO phonon creation. However the second exciton creation occurs for a slightly different LO phonon energy to maintain the resonant condition. The PLE

spectra from Findeis et al.[16] is shown in Figure 5.3. As a real exciton must be created in the QD to initiate this process, Raman scattering is ruled out as an explanation for the phonon lines as Raman scattering produces only virtual excitons. Hence there is disagreement between the work of Toda et al[15] and Findeis et al[16] as to the nature of the lines observed in the PLE spectra of single QDs which occur at the LO phonon energies or integer multiples of these energies.

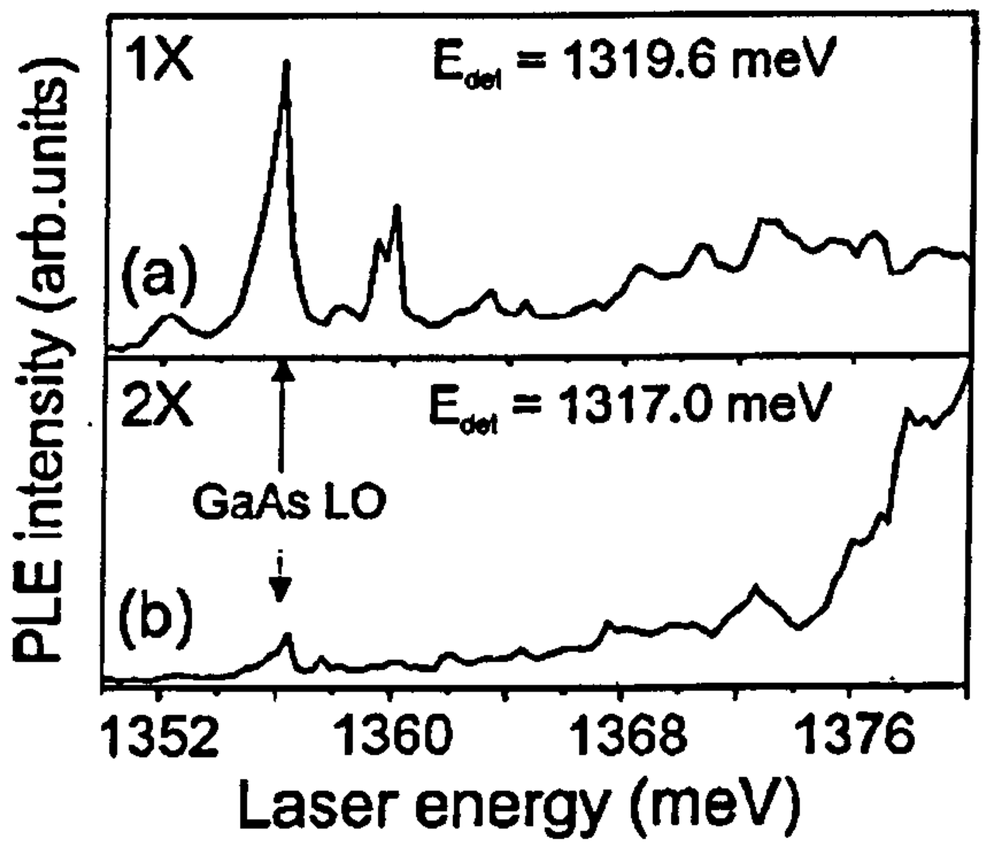

Figure 5.3 PLE spectra for detection on the exciton, X, and biexciton, 2X, line. Reproduced from Findeis et al.[16]

5.3 Experimental Details

PLE spectra were excited by a tuneable Ar^+ pumped Titanium-Sapphire laser, the emission of which is tuneable over the range 1700meV-1200meV. The intra cavity birefringence filter was controlled by a stepper motor under computer control. The spectral resolution of the measurements is limited by the linewidth of the laser, which is

<10μeV. The remaining experimental equipment has been described in §4.3. A power stabiliser was used to keep the laser output power constant over the spectral tuning range. This removed the need to correct the spectra for variations in laser power and prevented the distortion of the spectra by any non-linear effects.

5.4 PLE Spectroscopy of the Single Exciton Lines

5.4.1 Neutral and Charged Excitons

In order to substantiate the attributions of X and X*, made in the previous chapter, as neutral and charged single exciton complexes respectively, μPL-excitation (μPLE) spectroscopy was performed for detection on both of the emission lines. Such measurements reveal information concerning the charge status of the underlying excitons since charged complexes, which have unequal numbers of electrons and holes, cannot be created by resonant optical excitation of the QD (Figure 5.4). Thus, X* should exhibit no μPLE signal for excitation below the wetting layer, whilst X should give a non-zero signal with features which reflect both the absorption spectrum and available carrier relaxation channels[15,17,18].

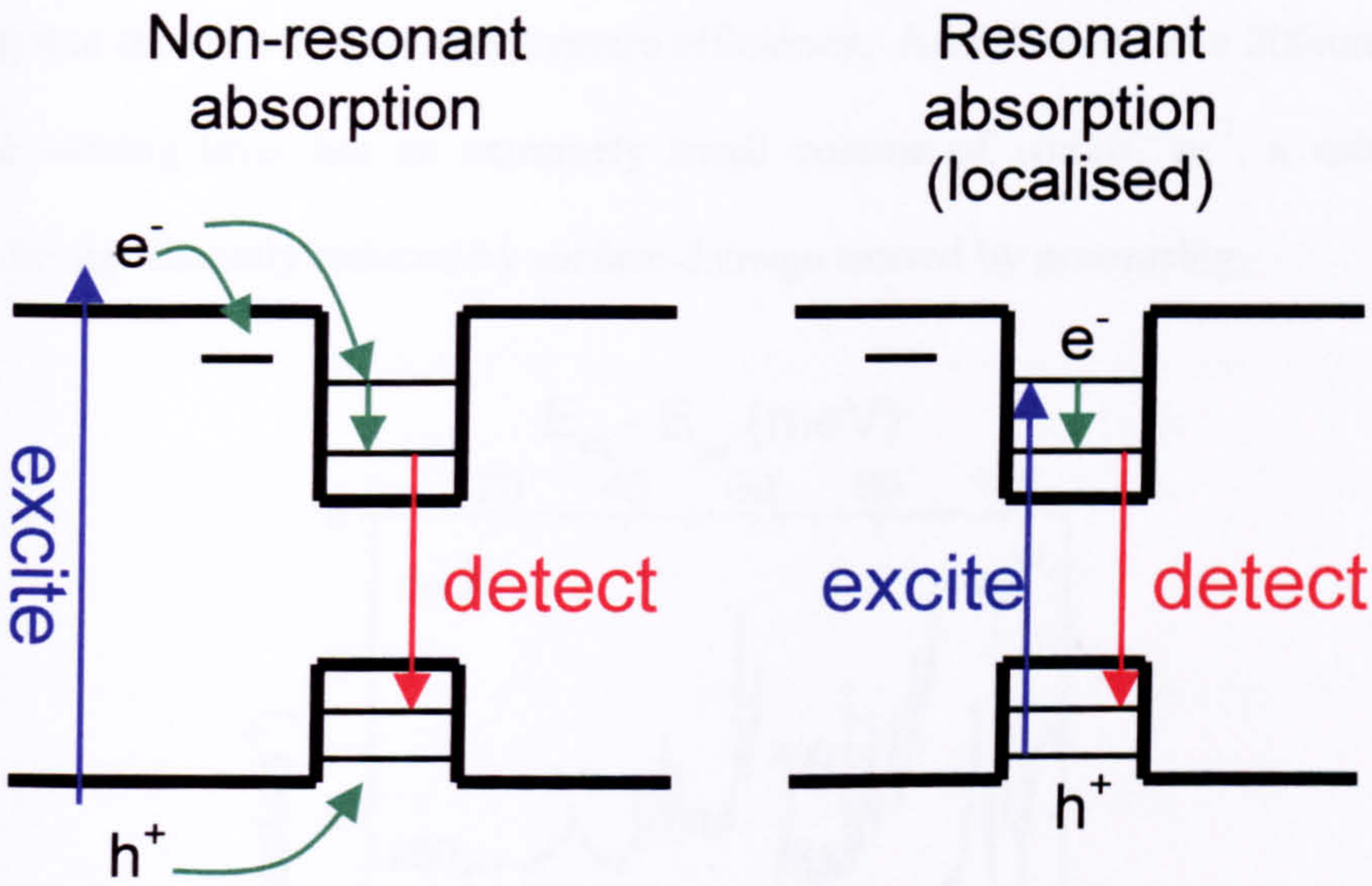

Figure 5.4 For non-resonant excitation (left) it is possible to produce an unequal (or equal) number of electrons or holes in the QD due to different electron and hole capture efficiencies. In the resonant (right) case the loss of one of the carriers from the QD is extremely unlikely and thus there are always an equal number of electrons and holes in the QD.

Figure 5.5 shows μPLE spectra detecting on X (E_{det}=1360.0meV, top panel) and X* (E_{det}= 1361.5meV, bottom panel) respectively. All the μPLE results presented in this Chapter were obtained using a very high laser excitation intensity of P_{ex}~500Wcm^{-2}, such that detectable emission could be observed for resonant excitation of a single quantum dot. However because of the low absorption of a single QD the carrier occupancy is still very low (<<1) under resonant excitation conditions. For X*, the μPLE spectrum exhibits a broad resonance centred at 1460meV which corresponds to the direct excitation of carriers into the wetting layer. For the present annealed quantum dot material, the wetting layer photoluminescence is observed at ~1450meV from an unpatterned region under conditions of very high excitation (see Chapter 4). Wetting layer emission is not observed for the sub-micron mesa structures for any excitation intensity investigated,

revealing that the QDs have a high capture efficiency. Additionally, in a 200nm diameter mesa the wetting layer has an extremely small volume of ~$3x10^{-21}m^{-3}$, a value that is likely to be significantly reduced by surface damage caused by processing.

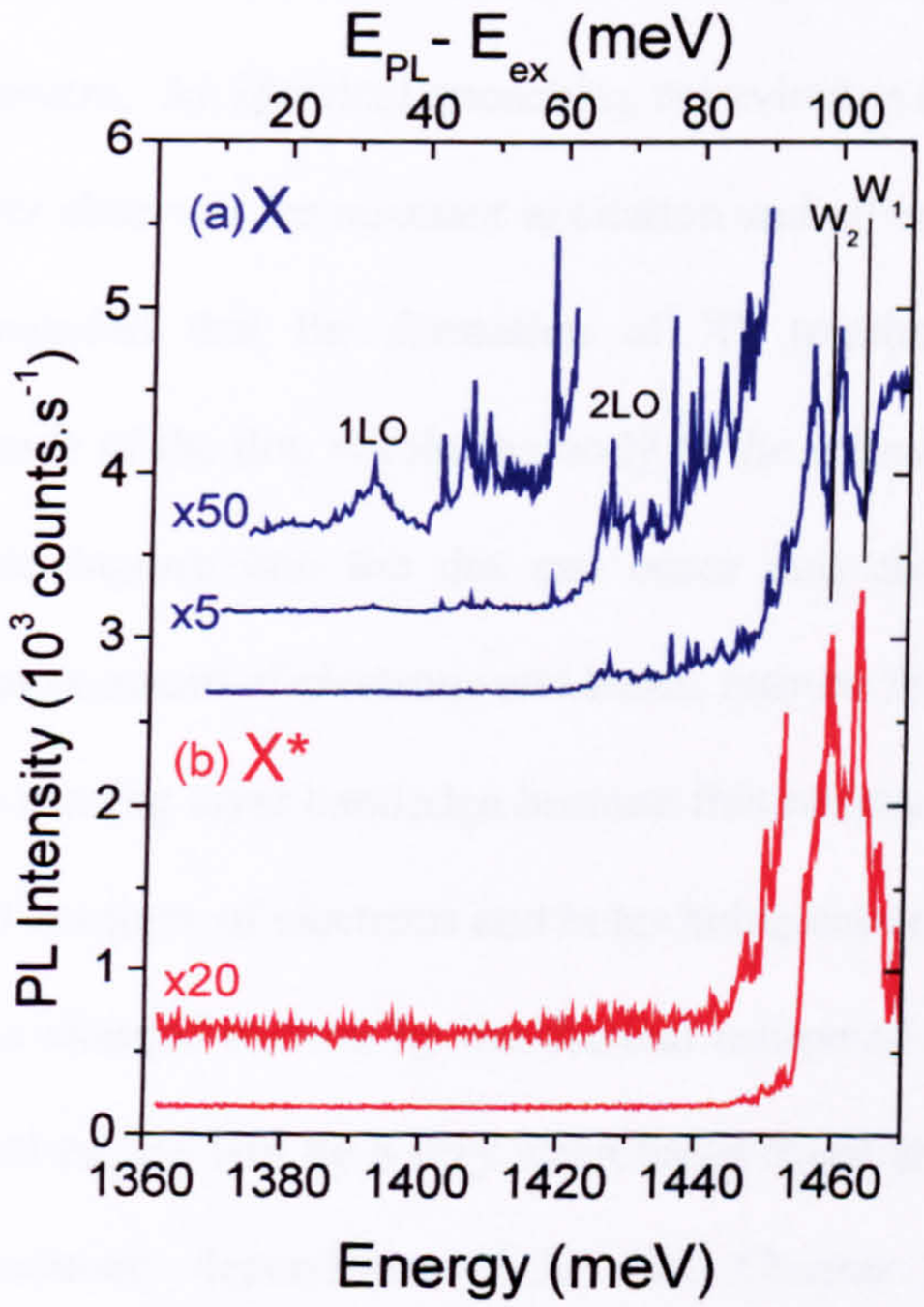

Figure 5.5 μPLE spectra detecting on the charged (X*) and neutral (X) single exciton emission lines. The X* μPLE spectrum illustrates the complete quenching of X* for resonant excitation, consistent with its identification as a charged complex. For X, magnified (x5 and x50) spectra are plotted revealing pronounced sharp electronic resonances arising from direct excitation of single particle states. In addition, broader single and multiple phonon related features (1LO, 2LO) are observed 32meV and 64meV above E_{det}.

As E_{ex} is tuned below ~1450meV, the μPLE signal obtained for X^* quenches completely, as can be clearly observed in the x20 expanded region in Figure 5.5. This quenching behaviour, which was found to be independent of the laser excitation intensity up to

~5.10^3 Wcm^{-2}, confirms the attribution of X* as arising from a charged exciton. This power independence of the quenching rules out X* as being due to a biexciton complex. In fact the biexciton is observed at energies lower than X in non-resonantly excited spectra (see Chapter 4) and may also be observed for high excitation power densities in resonantly excited spectra. An identical quenching behaviour is observed in all other dots studied with X* never observed for resonant excitation and all excitation intensities used. It can thus be concluded that the formation of X* requires the photocreation of excitons/carriers outside of the dot, within the body of the submicron mesa. In this case, unequal electron-hole capture into the dot can occur and charged excitonic species, consisting of different numbers of electrons and holes, may be formed. In contrast X can be formed below the wetting layer bandedge because this resonant excitation into the dot states results in equal numbers of electrons and holes being created in the QD. The initial resonant creation of a charged exciton by the thermal escape of one carrier is extremely unlikely, since thermal escape will be a very improbable event at low temperatures. The single exciton-like intensity dependence of X* (see Chapter 4), combined with the absence of a PLE signal for direct excitation of the dot, thus provides strong evidence that this emission line arises from the recombination of a charged single exciton.

The form of the μPLE spectra obtained for detection on X contrasts strongly with that discussed above for X*. The form of the PL spectrum for excitation directly in to the QDs is discussed in detail later (§5.5). Detecting on X a strong μPLE signal is observed for E_{ex}>1450meV, corresponding to direct excitation of electron-hole pairs into the wetting layer. Superimposed onto this broad resonance are a pair of pronounced peaks

labelled W_1 and W_2, at 1462±1meV and 1456±1meV respectively (Figure 5.5). These peaks exhibit pronounced anti-resonances with related features observed in the μPLE spectrum for detection on X*. This observation demonstrates that the formation of charged and neutral single exciton complexes for non-resonant excitation are competing processes, i.e. for a specific E_{ex} which may facilitate efficient charge separation we observe a reduction in the X formation efficiency and a corresponding enhancement of X*. The precise form of the X/X* anti-resonances were found to be sensitive to the excitation intensity used and differed from dot to dot. The wetting layer absorption structure is likely to be strongly influenced by mesoscopic fluctuations in the potential of the etched wetting layer and hence charge separation may be resonantly enhanced or inhibited for specific excitation energies. As the excitation energy is reduced below the wetting layer at 1450meV, a broad background is observed for the μPLE spectrum of X. This extends ~50meV below the wetting layer and is in strong contrast to the zero PLE intensity observed for X*.

It is possible that X* appears as a consequence of the mesa geometry utilised in the present experiment. Under conditions of weak excitation, charge trapping and subsequent separation may occur, involving detect states on the mesa surface. This effect would result in a build up of charge in the body of the mesa and a shift in the statistical carrier occupation of the dot towards charged species for few-exciton complexes. Tuning E_{ex} above the bandgap of the $Al_{0.13}Ga_{0.87}As$ barrier material increases the non-local excitation and effects due to the physical environment of the mesa are likely to become more important. In the present case non-local excitation above the

$Al_{0.13}Ga_{0.87}As$ bandgap increases the surface-volume ratio by a factor of ~8 and hence may be expected to enhance the prevalence of charged exciton species in the PL spectra. Figure 5.6 compares the μPLE spectra for both local (E_{ex}<1693meV) and non-local (E_{ex}>1693meV) excitation (i.e. below and above the $Al_{0.13}Ga_{0.87}As$ barrier) for both X and X*. For non-local excitation X* is much more intense than X, in contrast with the result for local excitation of the mesa. This behaviour provides confirmation of the above association between the appearance of charged species and the possibility for charge trapping by the mesa surface. Indeed, in the low power limit X* appears before X for non-local excitation and vice versa for local excitation. These observations suggest that carriers can become trapped in defect states that are produced during the formation of the mesa. These effects should not occur in an ensemble sample. However this does not preclude carrier trapping by intrinsic defects and previous reports[19] have attributed the observation of charged complexes in unprocessed material to background residual charge in the material.

With only the present results it is impossible to ascribe X* definitively to X^+ or X^-, i.e., X plus an excess hole or an excess electron respectively. In Chapter 6, measurements where carriers of a definite type can be injected electrically into a QD show that X^- occurs to lower energy than X, whilst X^+ occurs to higher energy. This finding is in agreement with previously published work[20,21] and is expected theoretically due to a larger hole-hole than electron-electron Coloumb interaction, a result of the more localised hole states due to their larger effective mass. Hence it can be concluded that X* results from the recombination of a positively charged exciton created for non-resonant excitation.

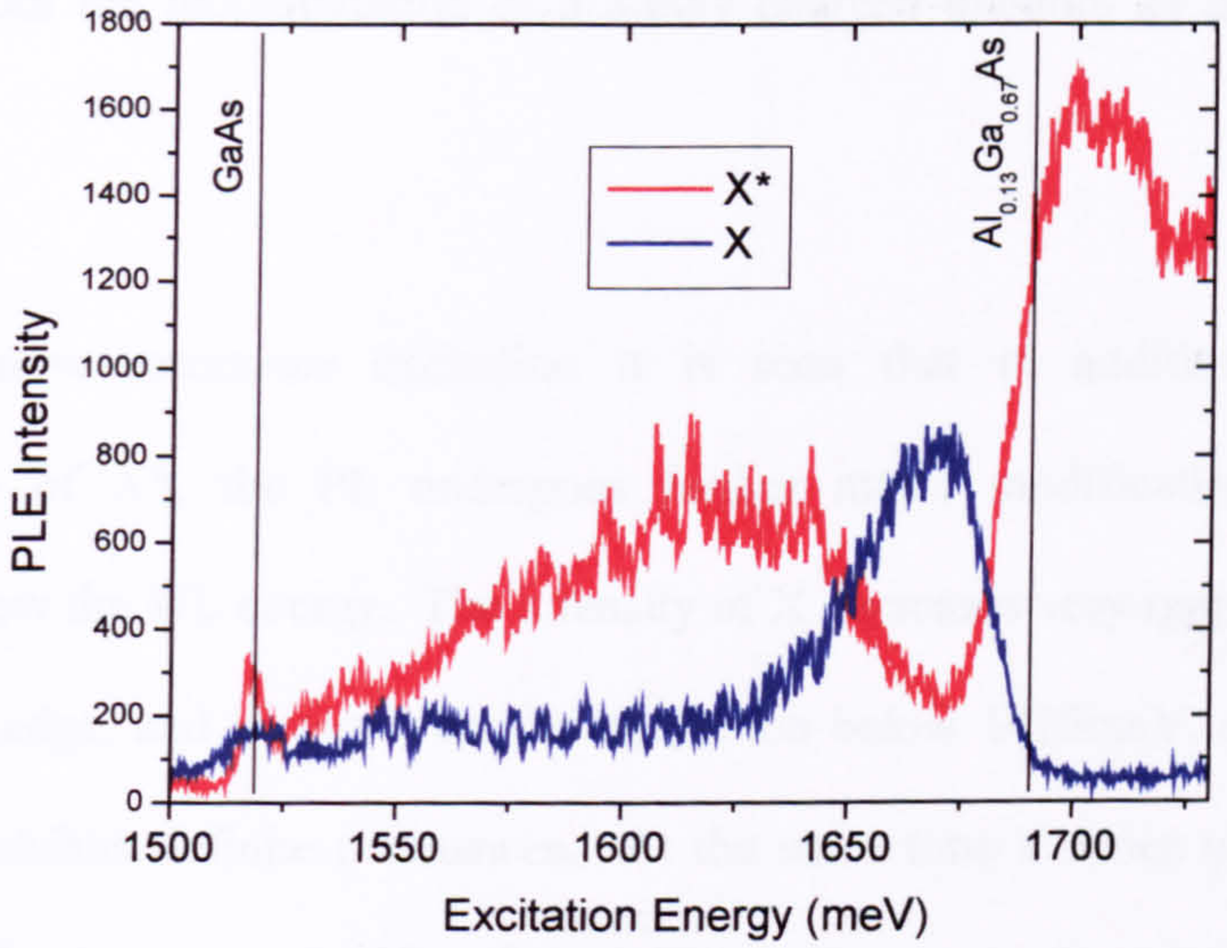

Figure 5.6. μPLE spectra for the emission lines X and X* and non resonant excitation at energies that extend from just below the GaAs band gap to well above the $Al_{0.13}Ga_{0.87}As$ bandedge.

5.5 Single Exciton Lines Observed Under Resonant Excitation

The form of the s-shell, ground state excitonic emission as a function of excitation energy (E_{exc}) has been presented previously (Figure 4.23) and the main behaviour is briefly summarised here. When carriers are created in the GaAs layers surrounding the dot (E_{exc}=1510meV), the emission consists of three lines separated by less than 2meV, for excitation powers (P_{exc}) such that the dot is occupied by on average approximately one electron-hole pair. A detailed study of the power dependence of these three lines shows that the central peak arises from the recombination of a single neutral electron-hole pair, X. The lower energy peak 2X, 2meV below X, arises from biexcitonic recombination, as confirmed by its quadratic dependence on P_{exc} (see Chapter 4)[22]. The highest energy line,

X*, arises from the recombination of a singly charged exciton, as discussed in detail above.

Considering now resonance excitation it is seen that in addition to the sudden disappearance of X*, the PL undergoes further major modifications when E_{exc} is decreased below the WL energy. The intensity of X decreases very rapidly for E_{exc} below the WL band edge, and is very weak for excitation below 1415meV, although it is still present and exhibits definite resonances. At the same time a series of new peaks (X_n) emerges on the low energy side of X. These lines gain in relative intensity and successively dominate the spectra as E_{exc} is reduced. A very similar behaviour has been observed for different single dots from the same wafer. PL spectra obtained for E_{exc}=1460 and 1415meV are shown in

Figure 5.7. The relative intensities of the X_n lines are very sensitive to E_{exc} but are independent of P_{exc}, consistent with a common order of excitonic process. The intensities of the X_n features are found to vary linearly with P_{exc}, indicating that they are associated with single exciton complexes[5].

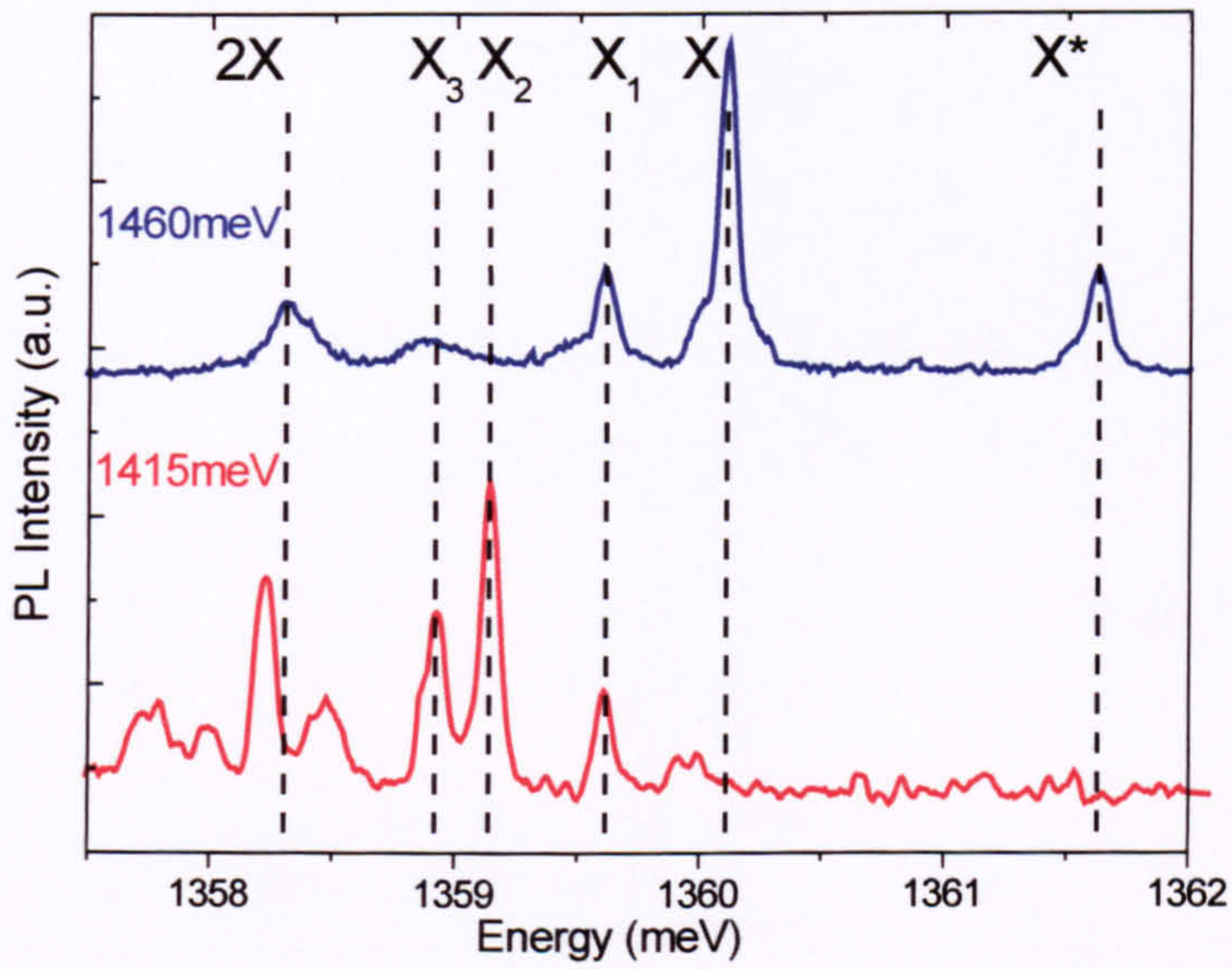

Figure 5.7 Ground state μPL emission for excitation slightly above and at the wetting layer bandedge. New, single exciton-like features (X_n) are observed at energies below X, which dominate the spectra for resonant excitation of the dot.

5.6 PLE Studies of the X_n Lines

PLE spectra for detection on each of the four emission lines X, X_1, X_2 and X_3 are presented in Figure 5.8a along with a non-resonant, high power PL spectrum to indicate the approximate energies of any excited state transitions, Figure 5.8b. The PL and PLE spectra are plotted as a function of absolute photon energy with the top axis of Figure 5.8 giving the approximate energy relative to the PLE detection energy.

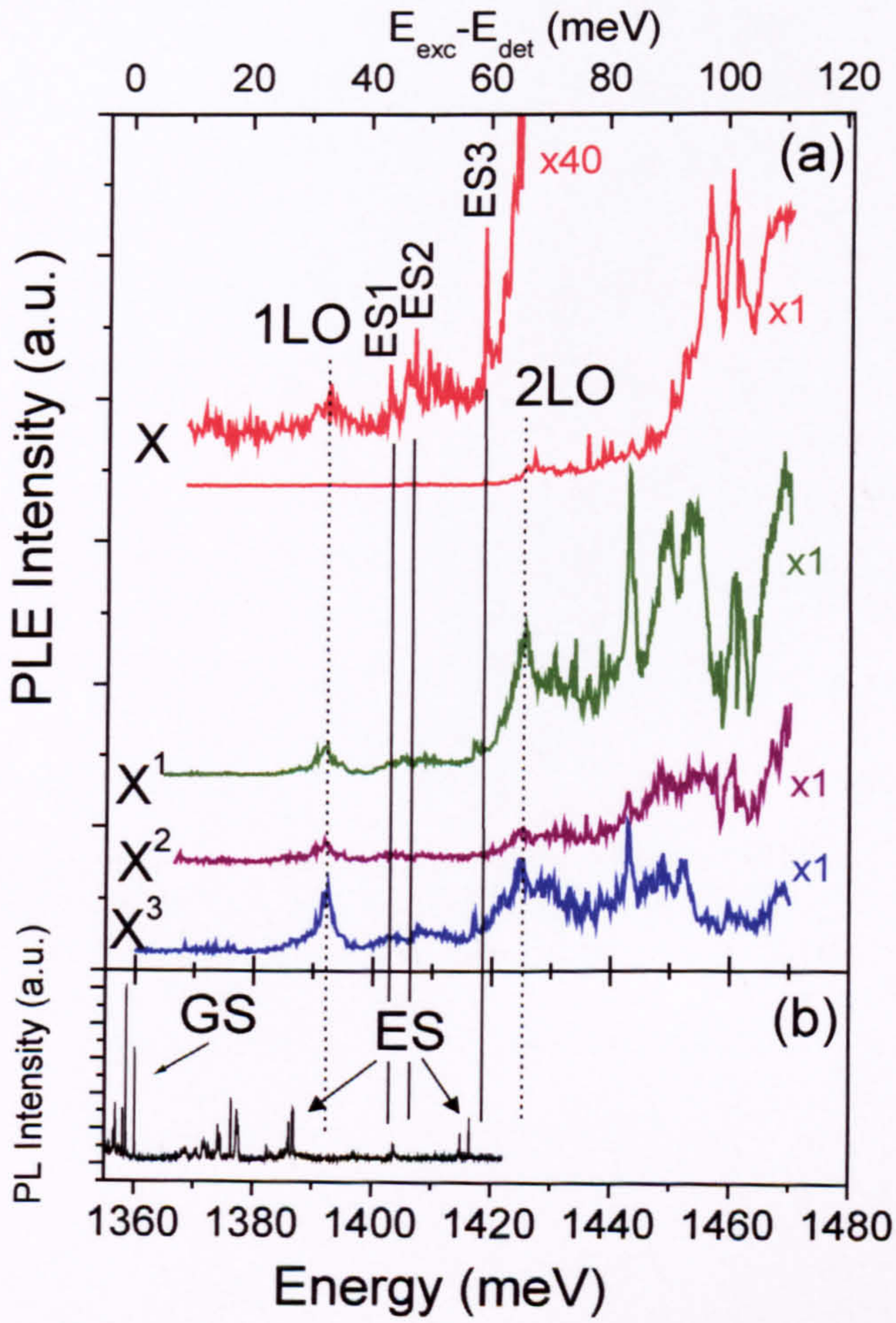

Figure 5.8 (a) PLE spectra for detection at the energies of the X and X_n lines observed in PL for the single QD of Figure 5.7. (b) High-power non-resonant PL spectrum showing the emission from excited states of the same single QD.

For detection on all of the emission lines, a series of ultra-narrow resonances (FWHM~100μeV) are observed in the PLE spectra over the range $\Delta E=E_{ex}-E_{det}$~60-80meV with, in addition, a continuum-like background for $\Delta E \geq 60$meV. At lower ΔE, a series of sharp but weak resonances, labelled ES1, ES2 and ES3, are observed ($\Delta E=43.1\pm0.1$, 47 ± 0.1 and 58.2 ± 0.1meV) which are very similar in energy to features

observed in the high power emission spectrum (indicated by the vertical full lines). The linewidth of these PLE resonances is extremely narrow (Figure 5.9) being comparable to the emission linewidth of 45μeV (§4.7). The close proximity between the emission and the ES1, ES2 and ES3 absorption features identifies the latter as arising from absorption into excited single particle states of the quantum dot (Figure 5.10a), the energy shift between emission and absorption arising from the effect of many body Coulomb interactions. Emission from excited states represents the situation where the QD is occupied by many carriers, whereas PLE occurs into an unoccupied QD and hence gives the true single particle state energy. Therefore the energy of the emission in the high power PL spectrum is that of the single particle states perturbed by many carrier interactions.

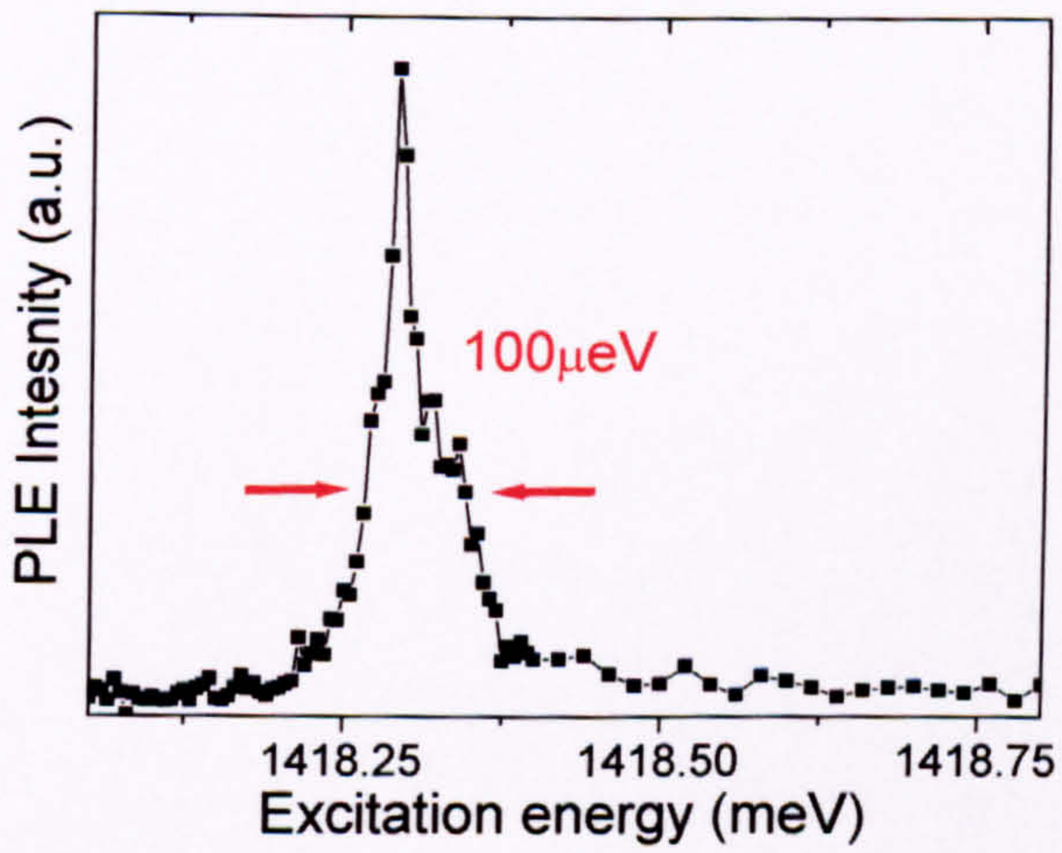

Figure 5.9 High resolution PLE spectrum of the ES3 electronic transition. The linewidth of this feature is similar to that of the single exciton line as observed in emission (~50 μeV).

In addition to the spectrally sharp, purely electronic features observed in the PLE spectra, two much broader peaks, labelled LO1 and LO2, occur at ΔE=+31±2meV and

+62±3meV respectively (indicated by the vertical dotted lines). The larger linewidths and relative energies of these features, and the fact that related features are not observed in emission, suggest that they represent LO-phonon-assisted excitation of the dot. These features have a relatively large linewidth of 3meV compared with the much narrower linewidths observed for the electronic transition, of <100μeV. The relative energies of these features at 31 and 62meV correspond closely to expected one and two LO-phonon energies, as reported in the literature for similar dots[12,23]. Their relatively large width may result from the coupling to a range of different phonons whose energies are modified by the effects of confinement and strain. This is discussed in more detail below.

The form of the PLE spectra for detection on X and the lines X_n exhibit a very contrasting behaviour. The intensity of the X PLE decreases very strongly, but not completely, for E_{ex}<1460meV (the wetting layer bandgap) with the intensity for excitation at the phonon features (1LO and 2LO) being more than two orders of magnitude weaker than for excitation above 1460meV. This strong decrease reflects the decrease in the absorption cross-section for resonant excitation. In strong contrast the PLE for detection on the X_n lines has approximately the same intensity for excitation at the wetting layer as for resonant excitation at the phonon energies. Another notable difference is the relative strength of the phonon and electronic features. For X the electronic features (ES1, S2 and ES3) are of a comparable intensity to the phonon features (LO1 and LO2), but for X_n the electronic features are much weaker. These observations indicate that X and the X_n series couple very differently to LO phonons and that they arise from two distinct types of excitonic species.

LO-phonon features may, in principle, arise in the PLE spectra of QDs as a result of several distinct processes, which are summarised schematically in Figure 5.10. The first mechanism is phonon-assisted absorption (Figure 5.10b)[16]. Here a photon is absorbed into the state GS+nLO (where n is an integer) followed by the creation of an exciton in the ground state (GS) and the simultaneous emission of nLO phonons. As will be discussed below this mechanism is likely to be strongly dependent upon the proximity of any electronic states to GS+nLO. The second mechanism (Figure 5.10c) involves absorption into a continuum of states, as postulated by Toda et al.[15], followed by fast relaxation by LO-phonon emission to the GS. This mechanism is similar to that observed in low quality quantum wells where only at energies nLO above the detection energy is relaxation sufficiently fast to lead to PL in the presence of competing non-radiative processes[24]. In such QWs the 2LO peak is much stronger than the 1LO peak due to the increased opportunity for conserving momentum. However the presence of a continuum of states is difficult to reconcile with the fully quantised energy levels expected for a QD. For an ensemble of QDs a range of excited state energies are possible due to QD size, shape and compositional inhomogeneity. In this case QDs appear to be selected whose excited-ground state energy separation is close to $n\hbar\varpi_{LO}$[23], resulting in features in the PLE spectra at integer multiples of the LO phonon energy. In studies of single QDs this selection process is not possible. However similar phonon features have been observed in many different single QDs, emitting at different energies and hence with a range of ground-state-excited-state energy separations. Nevertheless, despite the discrete energy level structure expected for a QD, PLE spectra (Figure 5.8) exhibit a broad, rising background for energies ≥60meV above the detection energy, suggesting the presence of

a high energy continuum. A similar feature is also present in the spectra of Toda et al[15]. Although the nature of this possible continuum is unclear (Toda et al[15] suggest that it may, in part, arise from tail states of the wetting layer) it does not appear to extend to low enough energies to account for the 1LO feature, and possibly even the 2LO feature. In addition no 3LO feature is observed even though the continuum is very strong at this energy. It can therefore be concluded that absorption into a continuum of states followed by the emission of multiple LO phonons is unlikely to be the reason for the form of the present single QD PLE spectra.

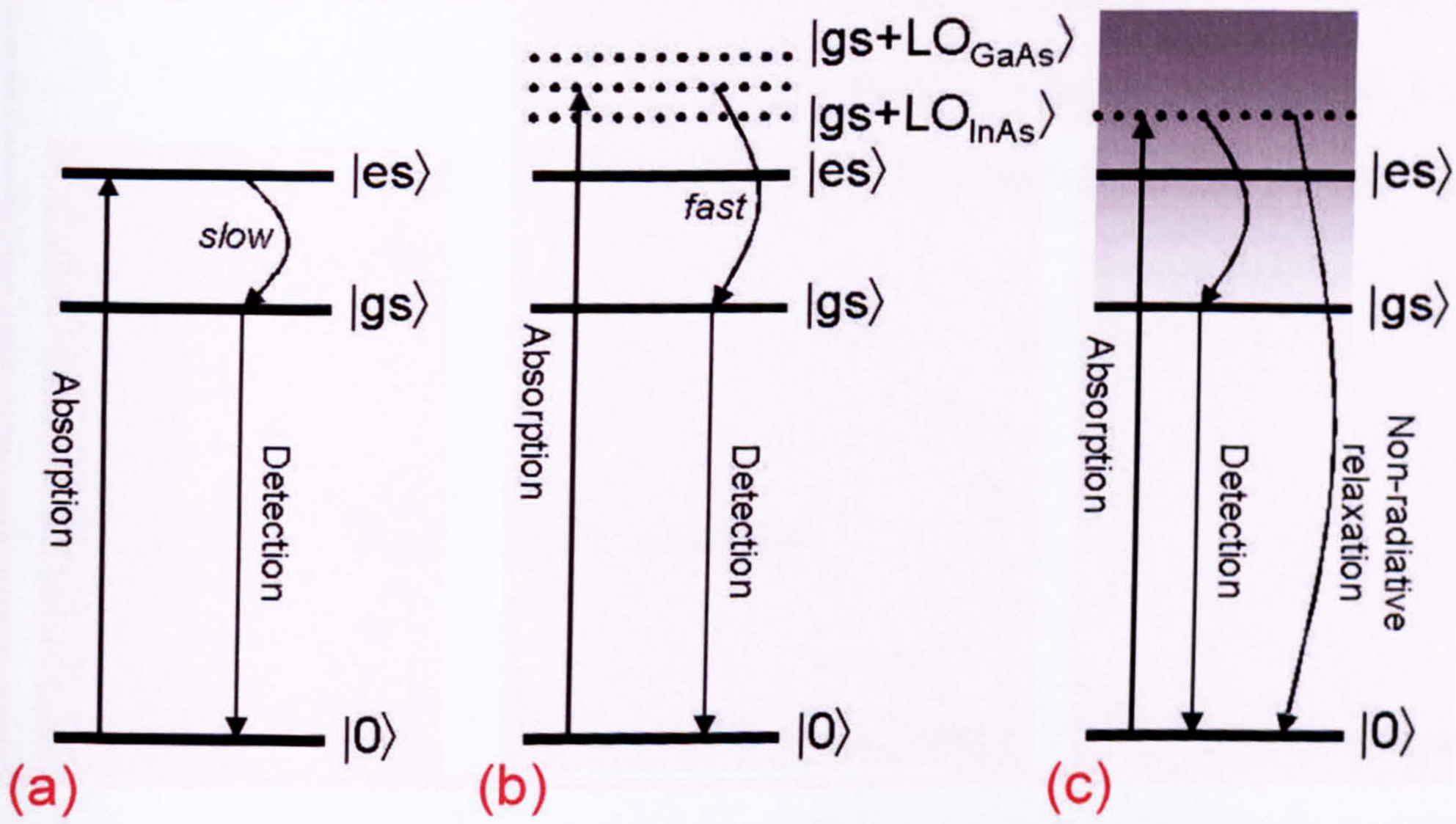

Figure 5.10 Possible mechanisms to explain the presence of LO phonon features in PLE. a) Absorption into a discrete energy state b) Phonon-assisted absorption c) Absorption into a continuum of electronic states and fast relaxation to the ground state.

The third mechanism is Raman scattering. This process is very similar in nature to the first mechanism but is coherent and is therefore expected to lead to a polarisation

memory between the incident and emitted photons. Such a polarisation memory is not found for the present QDs for excitation at the 1LO and 2LO energies, arguing against a Raman process.

It hence appears that the most probable mechanism to explain the 1LO and 2LO resonances observed in the PLE spectra is phonon-assisted absorption (case b in Figure 5.10). It is important to note that the 1LO features lies within a few meV of an excited state transition, as observed in the high excitation power PL (Figure 5.8), and thus the transition probability will be enhanced by resonant coupling with a real state. Unfortunately it is not possible to excite the QDs sufficiently hard to observe if there are any transitions close to 2LO.

5.6.1 Phonon resonance sub structure

The substructure of the 1LO phonon feature as observed in PLE is presented in Figure 5.11 and is seen to exhibit three distinct resonances, all with approximately a 3meV linewidth. The resonances are centred at approximately 27meV, 31meV and 35meV above the detection energy. This observation suggests that there are three distinct LO phonons to which carriers confined in the QD may couple.

Heitz et al.[5] identified two resonances centred at 32.3 and 35.7meV in the 1LO phonon emission satellite observed for an ensemble of self-assembled InAs QDs. In PLE studies of dot ensembles the same authors observed phonons of energies 29.6, 31.9, 35.0 and 36.6meV at multiples of 1, 2 and 3[25]. These four phonons were attributed to LO phonons from the wetting layer, the QD dots, an interface phonon and the bulk GaAs respectively. A comparison with the present results hence suggests that the features at 27, 31 and 35meV are due to wetting layer, quantum dot and interface phonons respectively. The precise energies of these phonons will depend on the composition of the dot which is sensitive to the growth conditions employed.

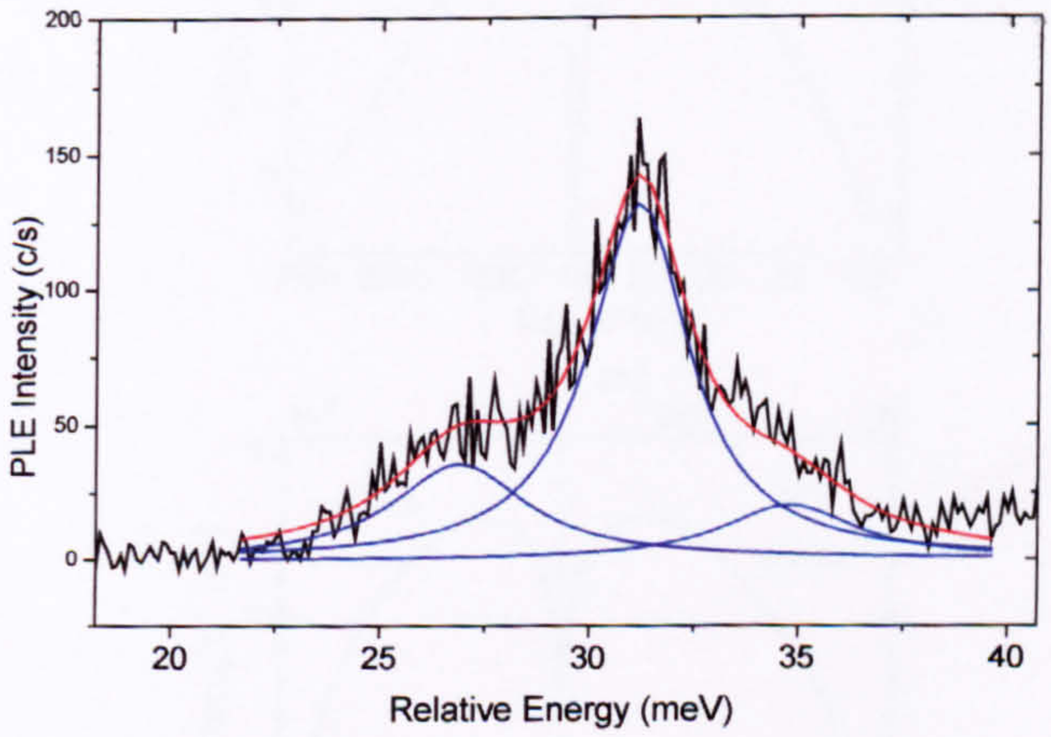

Figure 5.11 Sub structure of the 1LO phonon resonance for detection on X_1. Three Gaussians are used to model the experimental data, each with the same FWHM of approximately 3meV. The peaks are centred on approximately 27meV, 31meV and 35meV. The energy scale is relative to the detection energy of X_1.

The broadening of the LO phonon spectral features could be the result of a number of mechanisms. The phonon energies may vary spatially within the QD and surrounding matrix material due to inhomogeneities of the strain and/or composition. In addition the zero-dimensional confinement of the electrons and phonons may break the selection rule

which, for higher dimensionality systems, allows coupling only to small k-vector phonons. In this case coupling may occur to phonons across a significant fraction of their dispersion curve, resulting in an energy broadening in the spectra. Finally, calculations by Inoshita et al.[13] show that carriers can relax by emitting both an LO phonon and a low energy LA phonon; as long as the LA phonon energy is only a few meV then this process can occur very rapidly. This process, calculations of which are reproduced in Figure 5.12, would result in a broadening of the phonon features of order a few meV.

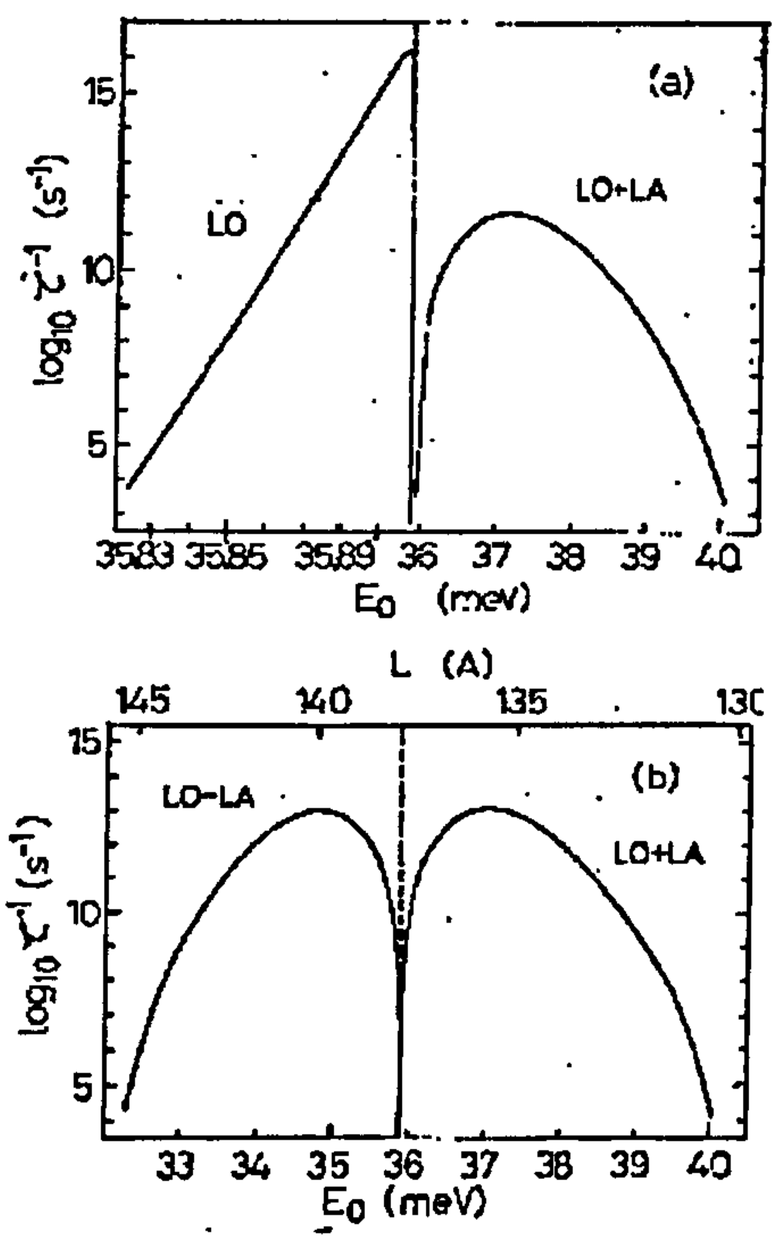

Figure 5.12 Calculated electron relaxation rate $^1/_\tau$ for energies E_0, in the vicinity of $\hbar\omega_{LO}$ due to the emission of an LO phonon or an LO phonon plus the emission or absorption of an LA phonon (a) T=0K; (b) T=300K. The results for only an LO phonon emission are not shown in (b), since they are nearly identical to (a). In (a), the abscissa is different above and below $\hbar\omega_{LO}$, which is indicated by the vertical dashed lines[13].

5.6.2 Carrier-Phonon Coupling in Emission

Even though strong LO phonon features are observed in PLE, the intrinsic LO-phonon coupling in the present dots appears to be very weak. This is concluded by examination of the PL spectrum in the energy range ~20-40meV below the X and X_n lines, which is shown in Figure 5.13 for excitation into the wetting layer at 1.46eV. In the energy range where LO phonon features are expected (30–36meV), no features are observed to within the noise level of the present measurements. This allows an upper limit of $2x10^{-4}$ to be set for the ratio of the intensity of the first LO phonon satellite of X to the intensity of X itself. The features observed ~20meV below the single exciton lines may arise from shake-up processes involving the excitation of an additional carrier to an excited state during excitonic recombination. An energy of 20meV corresponds reasonably well to the energy between the ground state X lines and the first excited state transition as observed in high power PL spectra.

The, at best, very weak exciton-LO-phonon coupling observed in the emission spectra of the present QDs is in strong contrast to the strong phonon features observed in absorption and also those reported in emission studies of QD ensembles, where Huang-Rhys parameters between 0.001 and 0.5 have been observed[5,6,7]. In the PLE spectra of the present dots a 1LO feature is observed for detection on X, with an intensity >1/400 that of the WL absorption. This significant intensity of the 1LO feature in absorption (PLE) but not in emission suggests the existence of a resonant enhancement of the phonon-

assisted process in absorption by mixing with a nearby electronic state. Such resonant mixing cannot occur in emission since there are no real states below the zero phonon energy.

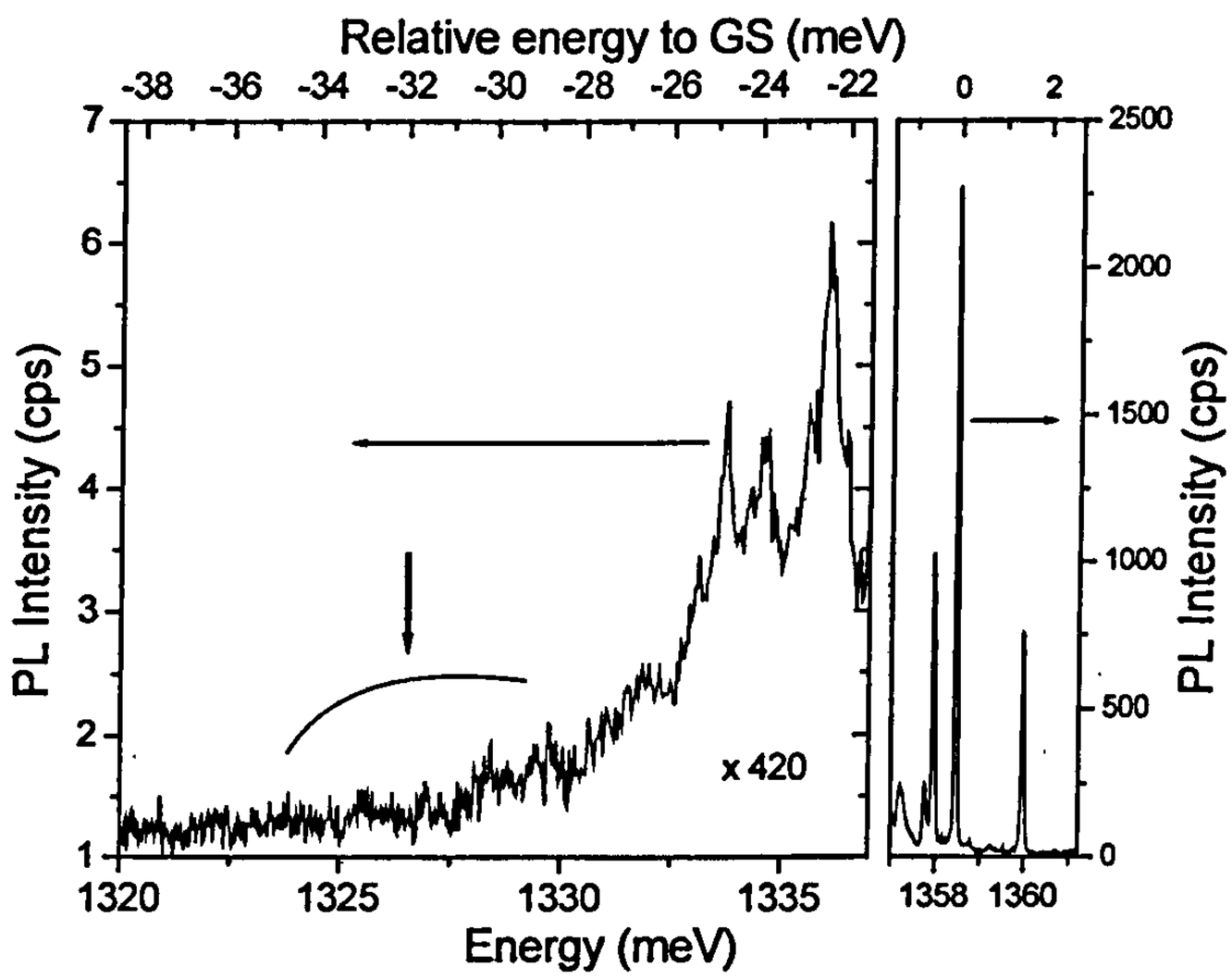

Figure 5.13 PL spectrum recorded on the low-energy side of the ground-state emission for a typical QD. No indication is found for LO-phonon satellite emission, expected in the energy range 30–40 meV below the ground-state emission, to within a factor of 5000 of the intensity of the zero phonon lines. The noise level in the 1320–1330 meV region is 0.0001 of the X signal.

The LO phonon features in the $X_{1,2,3}$ PLE spectra are much more intense still with x0.1~1 of the intensity of the WL features. In the introduction to this Chapter it was explained that the strength of the exciton-LO phonon coupling is determined by the dipole moment of the one exciton state of the system. In studies of the Stark effect[26] of large QD ensembles it was found that shape asymmetries, compositional non-uniformities and piezoelectric fields all act to reduce the electron-hole wavefunction overlap and hence to

enhance the dipole moment. The magnitude of the dipole moment will in turn strongly affect the degree of exciton-phonon coupling (§5.1.1). A possible explanation for the X_n lines is that they arise from exciton recombination perturbed by charged defects in or around the dot. This leads to a polarisation of the electron-hole charge distributions, an enhanced dipole, and hence to enhanced carrier LO phonon coupling. The presence of charged defects would further explain the appearance of new emission lines, $X_{1\text{-}3}$, below X as a result of Stark shifts by the electric fields produced by these charged defects. A single point charge situated 20nm from the dot would subject the dot to an electric field of 2.5 $kVcm^{-1}$. This would shift the exciton line by 0.2–1meV (depending upon the band structure) and is consistent with the experimental observations. The presence of several distinct X_n lines could arise from the time varying occupation of different defects, each individual defect, when occupied, giving rise to an individual X_n line. Such defects are likely to be neutralised by the high exciton densities in the GaAs matrix which occur for above gap excitation hence explaining the absence of the X_n lines for non-resonant excitation. However for resonant excitation, where carrier creation in the GaAs is very low, fluctuations in the occupancies of the defects is likely to be significant[27].

In all previously published studies of single, self-assembled QDs there has been no observation of the multiple single exciton lines (X_n) observed in the present QDs. Only singly charged excitons resulting from unequal electron and hole capture have been reported[21]. However in many cases the spectral resolution used may not have been sufficient to resolve the presence of additional lines slightly below X. In addition the present technique used to fabricate and isolate the single dots may be important. The

defects which produce the X_n lines may result from the annealing process employed to blueshift the QD emission energy to ~1.3eV (into the range of sensitive Si-based detectors) or alternatively may form during the fabrication of the sub-micron mesas. This conclusion is supported by results obtained from as-grown InGaAs dots, which emit in the 1.3eV spectral region without the need for annealing and are isolated with sub-micron holes formed in a metal mask, which removes the etching step. These QDs exhibit only a single X emission line for all excitation energies and incident laser powers. The results for these QDs are presented in Chapter 6.

5.7 Theoretical Studies of Exciton-Phonon Coupling Mechanisms in Quantum Dots

A theoretical model to describe exciton-phonon interactions in QDs has been developed by S. N. Balaban et al.[28]. For simplicity their model is based on a cylindrical shaped QD of size similar to the real QDs studied experimentally in this Chapter. Although it is a relatively simple model, it reveals information concerning normally dark states and the energies of these states in comparison to the phonon energies of the system. Significantly the model indicates that phonon-electron coupling is extremely likely.

The energy states and optical transition energies of cylindrical QDs with height h=5nm and radii R=8nm (Figure 5.14a), 9nm (Figure 5.14b) and 10nm (Figure 5.14c) have been calculated by Balaban et al.[28] and are shown in the appropriate figures. The confined

states in these QDs can be determined analytically if the electron-hole attraction and the degeneracy of the valence band is neglected. The effective masses of the electron and light hole are much smaller than that of the heavy hole in such a system and hence the lowest energy levels of the system correspond to excited states of the heavy hole, with the electron in its ground state. In addition, because the height of the QDs is much smaller than their diameter, the z-quantisation (the quantisation of the motion along the growth direction of the QD) is much stronger than the radial and angular quantisation. Hence, the first excited energy level for z-quantisation lies far above the excited energy levels resulting from the radial and angular motion. In Figure 5.14 a-c the lowest energy levels are plotted for an electron-hole pair with the electron in its lowest state and with the heavy hole in the lowest z-quantisation state and a range of different radial and angular states.

In the upper panels of the three figures, the intensities of the allowed transitions are plotted. The positions of the forbidden transitions are shown in the lower panels by black dashed lines. Red and green dashed lines indicate the energies of an exciton plus one LO phonon and of an exciton plus two LO phonons, respectively.

When considering non-resonantly excited photoluminescence, the strongest transitions shown in the upper panels of Figure 5.14a,b & c figures are due to a high probability of electron-hole recombination and this may be able to compete with the intra-level, non-radiative carrier relaxation. It is worth noting that for the interval R=8nm to 10nm, the calculated energy of the second allowed transition (the second most intense line in the

upper panels) is separated by less than one phonon energy from the ground state. This is consistent with the experimental data, where a number of sharp electronic features occur in the PL spectra below that of the one phonon peak (Figure 5.8).

Multiple phonon energies (nLO) which are added to the allowed transition energies are also plotted in the bottom panels of the figures. It can be seen that a number of purely electronic transitions exist in close proximity to these mixed electronic-phonon states. For the present range of QD size parameters there is always an optically forbidden transition close to GS+1LO. Mixing with the underlying states will make this normally forbidden transition allowed and it may therefore become observable in absorption. For GS+2LO there are a fairly large number of purely electronic transitions with similar energy which may explain why the 2LO feature is more intense in the PLE spectra than the 1LO feature. Although the model of Balaban et al.[28] does not calculate the degree of coupling between the electron and phonon and the purely electronic states it does predict the close proximity that is needed for strong coupling to occur.

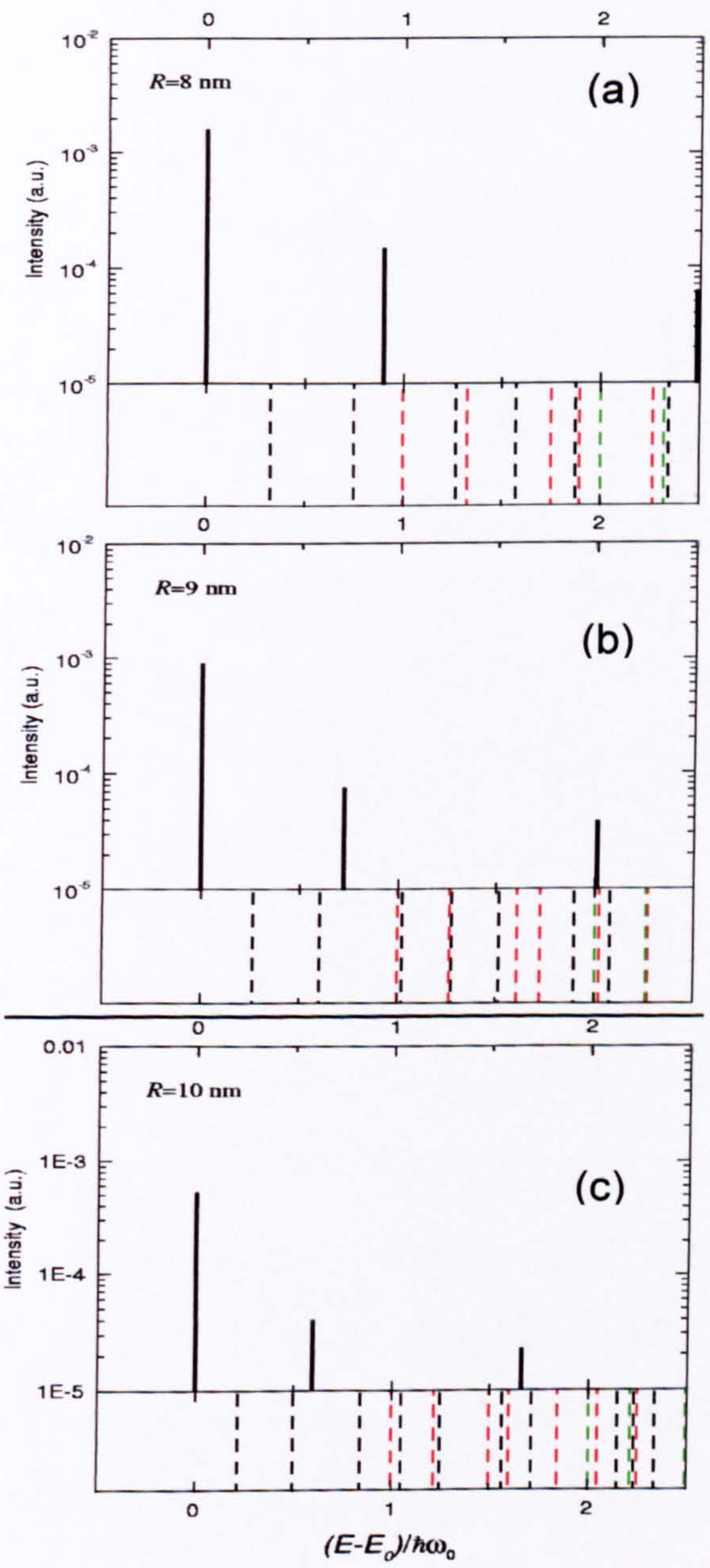

Figure 5.14 In the upper panels of all the figures, the intensities of allowed transitions are plotted. The positions of optically forbidden transitions are shown in the lower panels by black dashed lines. Red and green dashed lines indicate the energy levels of an exciton plus one LO phonon and of an exciton + two LO phonons, respectively. E_0 is the lowest transition energy and $\hbar\varpi_o$ is the phonon energy.

5.8 Magneto-Photoluminescence-Excitation

To further investigate the nature of the phonon resonances observed in absorption magneto-PLE has been measured for the dot in the Faraday geometry. For each applied field two spectra were recorded, corresponding to the two orthogonal circularly polarised senses of the detected light. The incident light for all spectra was unpolarised and the detection was centred on X_1. Figure 5.15 shows spectra recorded between 0 and 5T for the two detection polarisations. The form of the spectra is very sensitive to the field strength with new features appearing and disappearing as the field is varied. Although the intensities of the features change with field, their energies appear to be constant, consistent with a phonon nature. The application of the magnetic field therefore appears to alter the strength of the electron-phonon interaction for a given phonon with different phonons dominating the spectra at different fields. It seems likely that this behaviour results from a modification of the energy separation between the ground and excited electronic states by the magnetic field. Such a modification will occur if the excited state has a different orbital angular momentum in comparison to the ground state. As the relative energy of the excited state is varied by the field it will resonate with different phonons resulting in the observed changes in the form of the spectra.

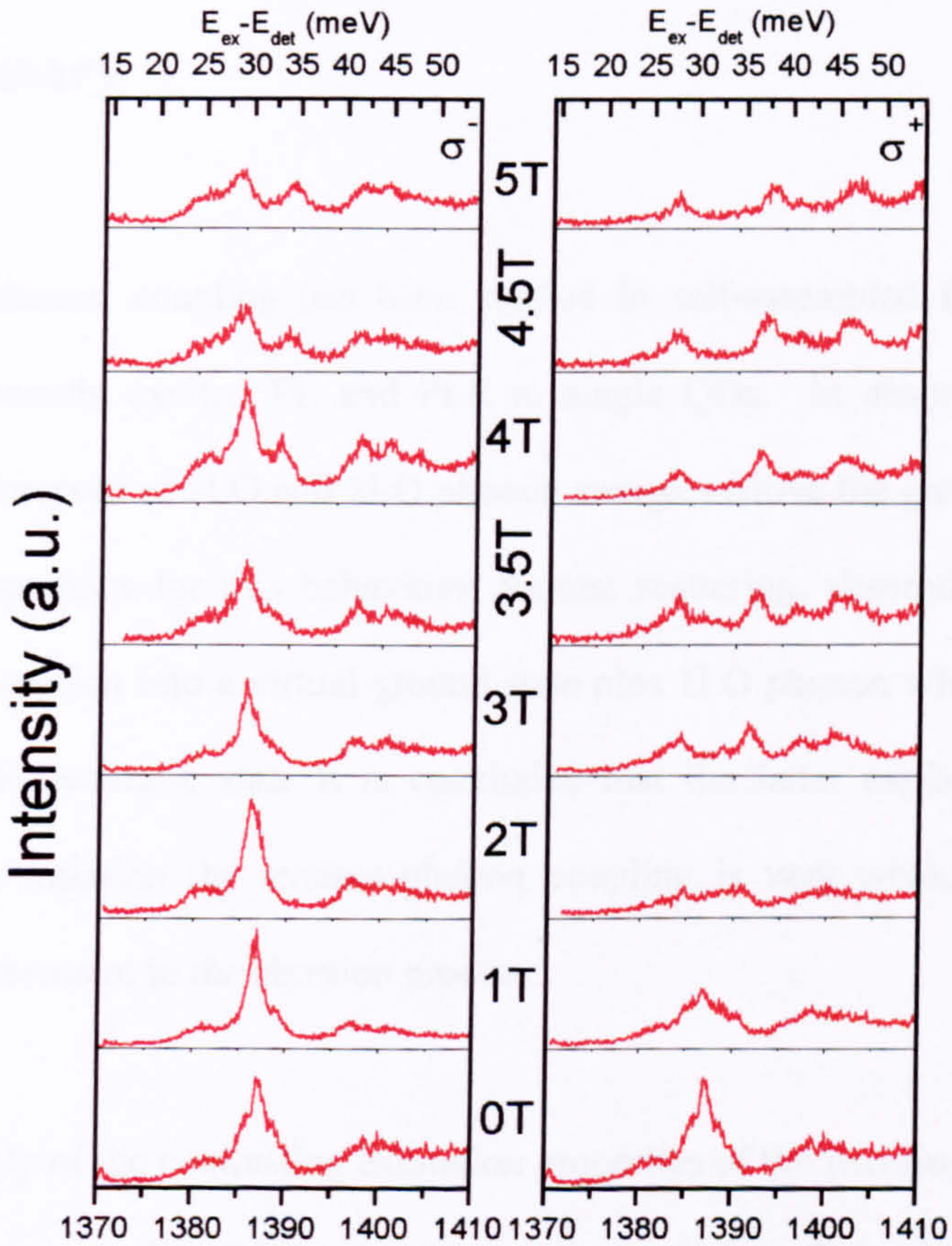

Figure 5.15 Magneto-PLE spectra recorded in the Faraday geometry for a single QD. The detection line is the single exciton X_1. The left panel corresponds to left-hand circularly polarised detection the right hand panel to right hand detection.

5.9 Summary

Exciton-LO-phonon coupling has been studied in self-assembled InAs/GaAs QDs by applying resonantly excited PL and PLE to single QDs. In absorption (PLE) strong features are observed at 1LO and 2LO phonon energies above the ground state. Of three possible explanations for this behaviour: Raman scattering, absorption into continuum states and absorption into a virtual ground state plus 1LO phonon with enhanced mixing with a nearby electronic state it is concluded that the latter explanation is the most probable. In emission the exciton-phonon coupling is very weak, consistent with a resonant enhancement in the abortion process.

A detailed study of the contrasting excitation properties of the two single exciton lines, X and X*, has been made. Whilst the neutral single exciton X is observed for resonant excitation of the dot, X* is absent. However the X* emission is enhanced for non-local excitation of the dot and the PLE spectra for detection on X and X* exhibit anti-correlated features. This behaviour indicates that X* results from the recombination of a single charge exciton which is created as a result of unequal electron and hole capture by the dot.

For resonant excitation of the QD a series of new emission lines are observed in the energy range ≤1-5meV below X. These lines are found to have a single exciton character and are attributed to a perturbation of X by charged defects situated near to the QD. Fluctuation of the charge of these defects results in the multiplicity of lines observed in

the time integrated spectra. These new lines display enhanced LO phonon features in PLE which probably arises from an enhanced exciton dipole as a result of a perturbation of the dot electron and hole charge distribution by the charged defects. The defects are believed to arise either during the annealing process used to shift the QD emission to a convenient spectral region or during the etching of the sub-micron mesas used to isolated the single QDs. Similar features are not observed in samples for which these two processing steps are not applied.

The experimental results are compared to the prediction of a simple theoretical model which suggests that significant exciton-LO phonon coupling is likely to occur in absorption due to mixing between the electronic ground state plus 1LO phonon and nearby optical transitions. Finally preliminary magneto-PLE measurements have been performed on the phonon features which are observed for detection on the single, uncharged and unperturbed exciton. The results indicate that the exciton-phonon coupling is strongly dependent on the relative energy of the excited state transition with respect to the phonon energy. Altering the excited state energy with respect to the ground state energy by means of the applied field results in coupling to different phonon modes.

[1] J. J. Hopfield, J. Phys. *Chem. Solids* **10**, 110 (1959)
[2] K. J. Nash, M. S. Skolnick, P. A. Claxton, and J. S. Roberts, *Phys. Rev. B* **39**, 5558 (1989)
[3] S. Schmitt-Rink, D. A. B. Miller, and D. S. Chemla, *Phys. Rev. B* **35**, 8113 (1987)
[4] S. Nomura and T. Kobayashi, *Phys. Rev. B* **45**, 1305 (1992)
[5] R. Heitz, I. Mukhametzhanov, O. Stier, A. Madhukar, and D. Bimberg., *Phys. Rev. Lett.* **83**, 4654 (1999)
[6] M. Bissiri G. Baldassarri Höger von Högersthal, A. S. Bhatti, M. Capizzi, and A. Frova P. Frigeri and S. Franchi., *Phys. Rev. B* **62**, 4642 (2000)
[7] A. Garcia-Cristobal, A. W. E. Minnaert, V. M. Fomin, J. T. Devreese, A. Y. Silov, J. E. M. Haverkort, J. H. Wolter, *Phys. Status Solidi B* **215**, 331 (1999)
[8] K J Nash and D J Mowbray, *J. Luminescence* **44** 315 (1989)
[9] V. M. Fomin V. N. Gladilin, J. T. Devreese, E. P. Pokatilov, S. N. Balaban, and S. N. Klimin., *Phys. Rev. B* **57**, 2415 (1998)
[10] J.T. Devreese, *Encyclopedia of Appl. Phys.* **14**, 383 (1996).
[11] S. Schmitt-Rink, D.A.B. Miller and D.S.Chembla, *Phys. Rev. B* **35**, 8113 (1987)
[12] R. Heitz, M. Veit, N.N. Ledentsov, A. Hoffmann, D. Bimberg, V.M. Ustinov, P.S. Kop'ev, and Zh.I. Alferov, *Phys. Rev. B* **56**, 10435 (1997).
[13] T.Inoshita and H. Sakaki. *Phys. Rev. B*, **46** 7260 (1992)
[14] B. Ohnesorge, M. Albrecht, J. Oshinowo, A. Forchel, and Y. Arakawa, *Phys. Rev. B* **54**, 11532 (1996).
[15] Y. Toda, O. Moriwaki, M. Nishioka and Y. Arakawa. *Phys. Rev. Lett.* **82**, 4114, (1999)
[16] F. Findeis, A. Zrenner, G. Böhm, and G. Abstreiter *Phys. Rev B* **61** R10 579 (2000) (2000)
[17] A. Zrenner, M. Markmann, A. Paassen, A.L. Efros, M. Bichler, W. Wegscheider, G. Böhm and G. Abstreiter, *Physica B* **256-258**, 300, (1998)
[18] F. Findeis, A. Zrenner, G. Böhm and G. Abstreiter, *Solid State Commun.* **114**(4), 227, (2000)
[19] M. Bayer, O. Stern, P. Hawrylak, S. Fafard, and A. Forchel, *Nature* **405**, 923 (2000)
[20] A. Hartmann, Y. Ducommun, E. Kapon, U. Hohenester, and E. Molinari, *Phys. Rev. Lett.* **84**, 5648 (2000)
[21] R. J. Warburton, C. Schäflein, F. Haft, F. Bickel, A. Lorke, K. Karrai, J. M. Garcia, W. Schönfeld, and P. M. Petroff, *Nature* **405**, 926 (2000)
[22] J. J. Finley, A. D. Ashmore, A. Lemaître, D. J. Mowbray, M. S. Skolnick, I. E. Itskevich, P. A. Maksym, M. Hopkinson, and T. F. Krauss., *Phys. Rev. B* **63**, 073307 (2001)
[23] M.J. Steer, D.J. Mowbray, W.R. Tribe, M.S. Skolnick, M.D. Sturge, M. Hopkinson, A.G. Cullis, C.R. Whitehouse, and R. Murray, *Phys. Rev. B* **54**, 17738 (1996)
[24] A. Chomette, B. Lambert, B. Clerjaud, F. Clerot, H. W. Liu and A. Regreny., *Semicond. Sci. Technol.* **3**, 351 (1988)

[25] R. Heitz, M. Grundmann, N. N. Ledentsov, L. Eckey,M. Veit, D. Bimberg, V. M. Ustinov, A. Yu. Egorov, A. E.Zhukov, P. S. Kop'ev, and Zh. I. Alferov, *Appl. Phys. Lett.* **68**, 361 (1996)
[26] P.W. Fry, I. E. Itskevich, D. J. Mowbray, M. S. Skolnick, J. J. Finley, J. A. Barker, E. P. O'Reilly, L. R. Wilson, I. A. Larkin, P. A. Maksym, M. Hopkinson, M. Al-Khafaji, J. P. R. David, A. G. Cullis, G. Hill, and J. C. Clark *Phys. Rev. Lett.* **84** 733 (2000)
[27] D. Robinson and B. B. Goldberg, *Phys. Rev. B* **61**, R5086 (2000)
[28] S. N. Balaban, V. N. Gladilin, V. M. Fomin, J. T. Devreese : *private communication.*

Chapter 6

Charge Tuneable Single Quantum Dots

6.1 Introduction

The work described in previous chapters has been concerned with the study of multiple-exciton complexes in single quantum dots. As a by product of this, charged exciton complexes were also identified and studied, although because these complexes were formed by the random nature of the dot carrier capture, their precise form (positive or negative) could not be determined. In addition it does not seem possible to produce multiple charged excitons using this method.

In the present chapter metal-insulator-semiconductor field effect transistor (MISFET) structures containing a single QD are used to produce and study multiply charged excitons. With these structures it is possible to produce single exciton complexes with up to four additional electrons or two additional holes. Charged biexciton complexes are also observed. The energetics of these complexes are studied in detail and their response to a magnetic field applied in the Faraday configuration investigated.

6.2 Review of Relevant Published Work

The effect of excess electrons in QDs has been investigated with some success in ensembles using normal experimental techniques that do not involve spatially resolving individual QDs[1,2]. While these studies do provide some useful information on the perturbations due to excess charge carriers, the findings are compromised by the large inhomogeneous nature of the system. The linewidths of ensembles are tens of meV, an order of magnitude larger than the predicted perturbations. Unambiguous results can only be obtained from investigations of a single QD where the homogeneous linewidth is just tens of μeV.

Warburton et al.[1] demonstrated the loading of electrons into a Schottky-type structure that contained quantum rings in the active region. Quantum rings are produced in a manner similar to the QD growth presented in the present work; utilising the Stranski-Krastanow growth mode, but introducing an annealing step after dot formation. Initially InAs quantum dots are grown followed by a GaAs capping layer. The growth is then paused, during which the dots become thinner in the growth direction and spread out in the growth plane, producing a donut ring-like structure. The quantum rings can be loaded sequentially with electrons and effects such as Coulomb blockade are observed. Features were observed in the Capacitance-Voltage characteristics when the rings are injected with one or two electrons. Further evidence suggests the possibility to inject up to six electrons into the rings before the injected electrons start to populate the wetting layer (Figure 6.1).

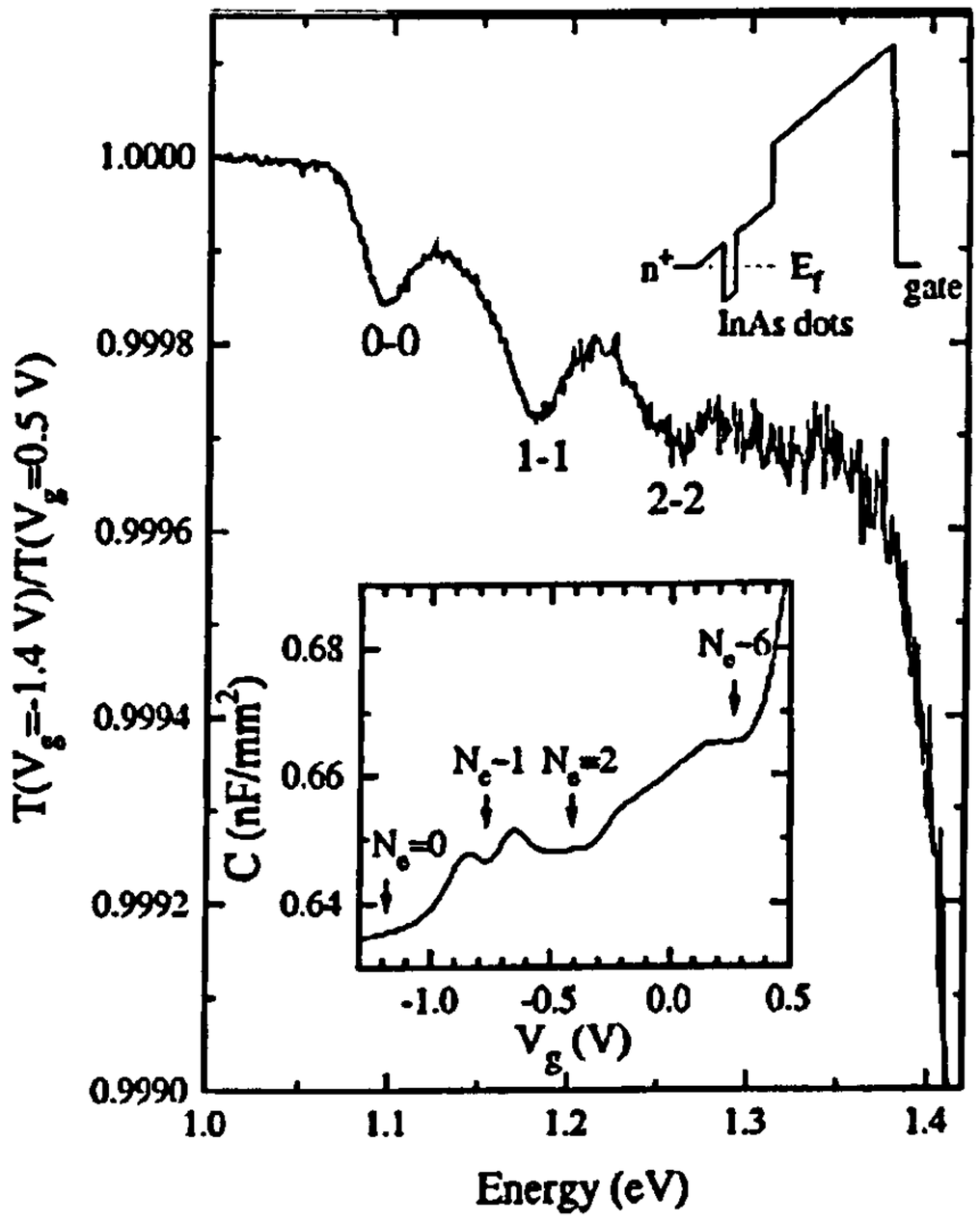

Figure 6.1 The upper inset shows the conduction band profile of the device along the growth direction, with Fermi energy, E_f. The capacitance, *C*, of the device at 4.2 K against gate voltage, *Vg*, is shown in the lower inset. Charging of the electron levels in the dots corresponds to peaks in the capacitance enabling the electron occupancy per dot, *Ne*, to be determined. The main figure shows the ratio of the transmission spectrum at *Vg* - 1.4 V to the spectrum at 0.5 V, also at 4.2 K.

Similar studies to those presented in this work have been reported by Zrenner et al. [3,4]. These works studied the emission spectra from just a single QD by using a metal mask with a sub micron sized hole. Charging with up to two extra electrons (N_e=2) was observed in the emission spectra (Figure 6.2). Each sequential injection of an extra electron caused a perturbation of the emission. Further charging resulted in broad emission attributed to the WL. However, the results presented below (§6.5.3) suggest that this broad emission may be attributed to X^{3-} (or 3 excess electrons). In the present work the emission from X^{3-} is much narrower, being comparable to the other charged states. However, the broad wetting layer emission observed by Zrenner

et al.[3,4] emerges at the same energy as the X^{3-} complex observed in this chapter, suggesting that in Zrenner et al.[3,4] the X^{3-} is partially unbound. Studies presented in this chapter on charge tuneable p-type structures has not been previously reported in the literature.

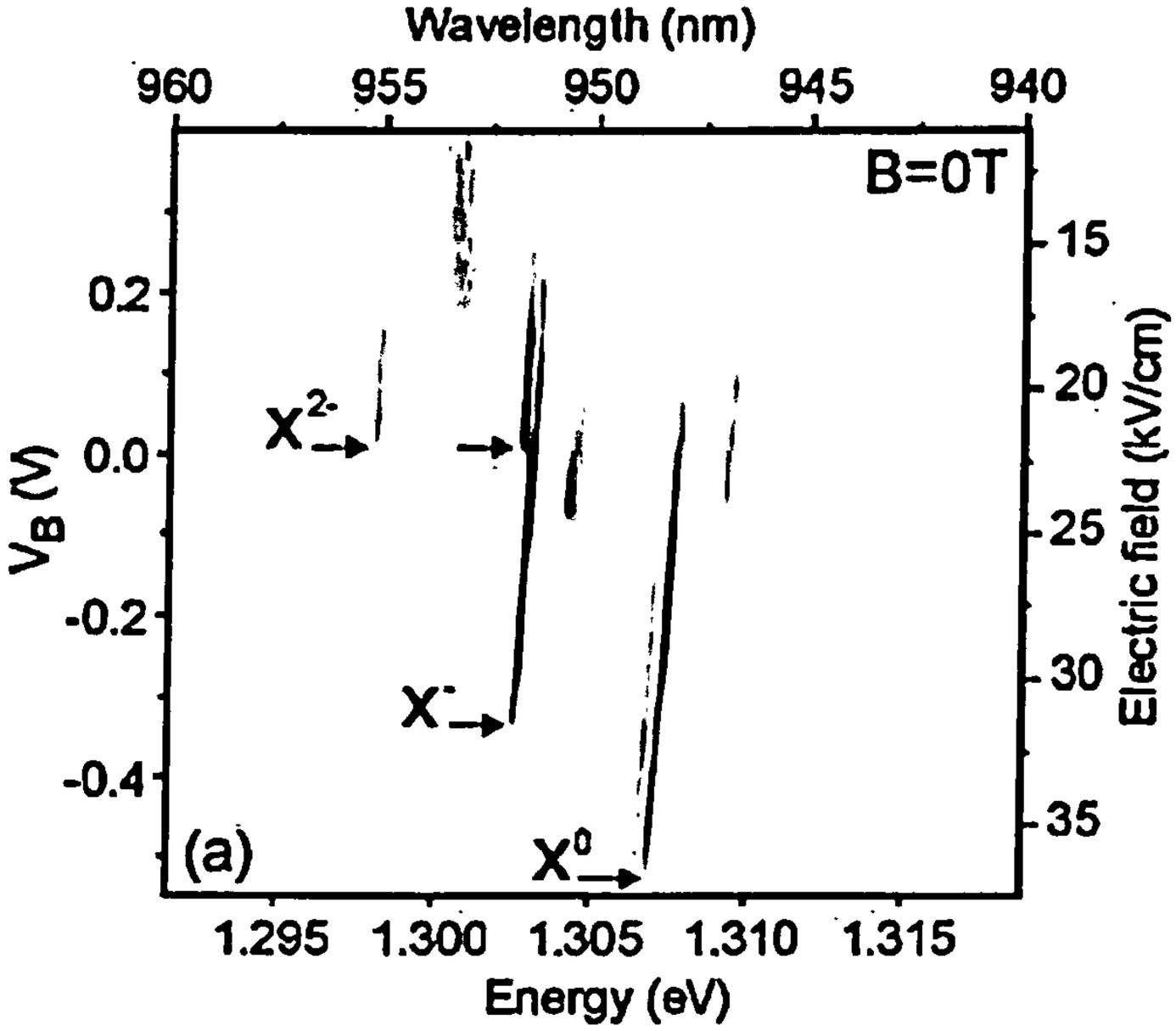

Figure 6.2 Grey scale plot of the PL intensity as a function of the PL energy and gate bias V_B. The series of lines can be assigned to emissions from s-shell transitions of X^0, X^{2-}, and X^+. From Zrenner et al. [3].

Further work on charge tunable structures has been carried out by Warburton et al.[11], however in this case the zero dimensional confining potential was provided by quantum rings. Single quantum rings were isolated using metal masks with submicron apertures. These results show many similarities to those of single QDs (Figure 6.3). A number of charging thresholds are observed (up to N_e=5) and for some charged states multiple emission lines occur, representing different spin configurations.

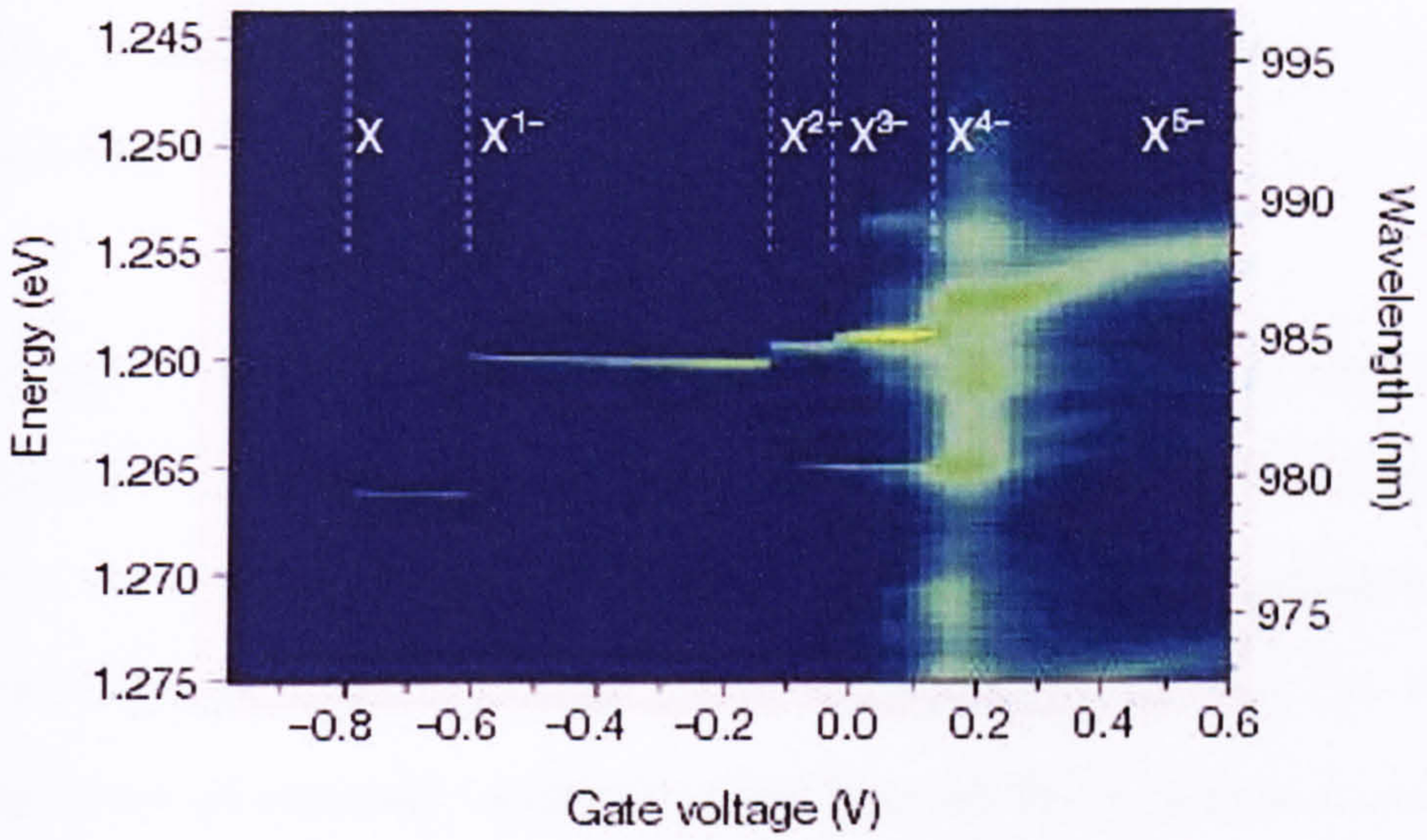

Figure 6.3 A colour-scale plot of the PL versus gate voltage at for a single quantum ring 4.2 K. Here dark blue, green and yellow correspond to low, medium and high signals, respectively. The pump power was kept below 1mW in order to populate the rings with no more than one exciton at a given time. The main features are from a single ring although the PL at 1.265eV, present around 0.0V, arises from a second ring.

Charged excitons have also been studied in modulation doped quantum dots[5]. n-type doping loads the dot with excess electrons. Photo-excitation can then be used to create extra electron and hole pairs. Excitation above the barrier band gap results in a different dot capture rate for electrons than holes, the rate being faster for minority holes due to the attractive Coulomb force. These holes recombine with the electrons allowing the electron number to be decreased by raising the excitation power. Many charge states have been observed and by applying both types of doping exciton complexes with up to three excess electrons and two excess holes are seen with perturbations of a similar order to those found in the present work.

Detailed theoretical calculations of the charged states of self-assembled QDs have been performed, the majority before spatially resolved spectroscopy was applied to

the study of single QDs. These studies show that the form of the emission spectrum is strongly dependent upon the number and configuration of electrons and is confined within the dot[4].

Knowledge of the form of the wavefunctions is needed to fully understand the results presented in this chapter and recently some experimental work has been performed to map the wavefunctions in the growth plane[6]. Magneto-tunnelling spectroscopy is used for electrons tunnelling through a QD. Wavefunctions with s, p and d like configurations are observed. Evidence is also observed for an in-plane anisotropy with a biaxial symmetry[7].

6.3 Device Structure

In the devices studied in this chapter QDs have been incorporated within the intrinsic region of a Metal-Insulator-Semiconductor Field Effect Transistor (MISFET) structure. This device consists of a top Schottky gate contact, a large bandgap blocking layer, the QDs grown within an intrinsic region and a doped region which provides a charge reservoir. Schematic band diagrams of the structure of n- and p-type devices are shown in Figure 6.4 and Figure 6.19 respectively. The samples were grown by MBE on semi-insulating [001] GaAs substrates. The growth of the structure commenced with a 200nm buffer layer followed by a 50nm n-type Si doped layer ($N=4.0\times10^{18}cm^{-3}$) or a p-type Be doped layer ($N=4.0\times10^{18}cm^{-3}$). Next a 25nm undoped GaAs spacer layer, and the QDs, formed by depositing 6ML of $In_{0.5}Ga_{0.5}As$ at 515°C were grown. Atomic force microscopy performed on identically grown, but

uncapped dots revealed approximately lens shaped dots with lateral (vertical) dimensions of 23±7nm (2.5±1nm) and a density of ~$5x10^{10}$ cm^{-2}. The QD layer was capped with 15nm GaAs, a 75nm thick $Al_{0.33}Ga_{0.33}As$ blocking barrier and a 5nm GaAs cap. After growth, room temperature PL of the wafers gave a peak emission of 1.29eV for the n-type sample, with an inhomogeneous broadening of 69meV. For the p-type sample emission occurred at 1.17eV with a linewidth of 60meV. These results indicate that the QD size, shape and composition are very similar for the two samples. Ohmic contacts were formed to the doped layer and a 70nm thick titanium Schottky gate was evaporated on the sample surface. Large area devices were used for capacitance-voltage characterisation. Devices containing a single dot were fabricated as described below.

6.3.1 Device Operation

For the initial device considered the doped region is n-type which provides a reservoir of electrons. Variation of the Schottky gate potential (V_g) allows the tuning of the Fermi level relative to the QD states, permitting the sequential charging of the dots as electrons tunnel from the reservoir into the QD states. For increasing V_g, QD energy levels are moved below the Fermi Energy of the n-doped region. Initially, the bias brings the first s-shell energy level below the Fermi energy, allowing the first electron to tunnel in from the n-doped region. The bias that allows a second electron to tunnel into the s-shell (the s-shell is doubly degenerate) is significantly different to the first tunnelling bias due to the additional Coulomb charging energy of a few tens of meV [8]. In the present experiments the direct effect of Coulomb charging is not observed for the s-shell because the first electron arises from the photocurrent exciton that is

required to probe the system. However Coulomb charging effects are observed for the injection of electrons into the p-shell where distinct charging thresholds for three, four, and five electrons are observed.

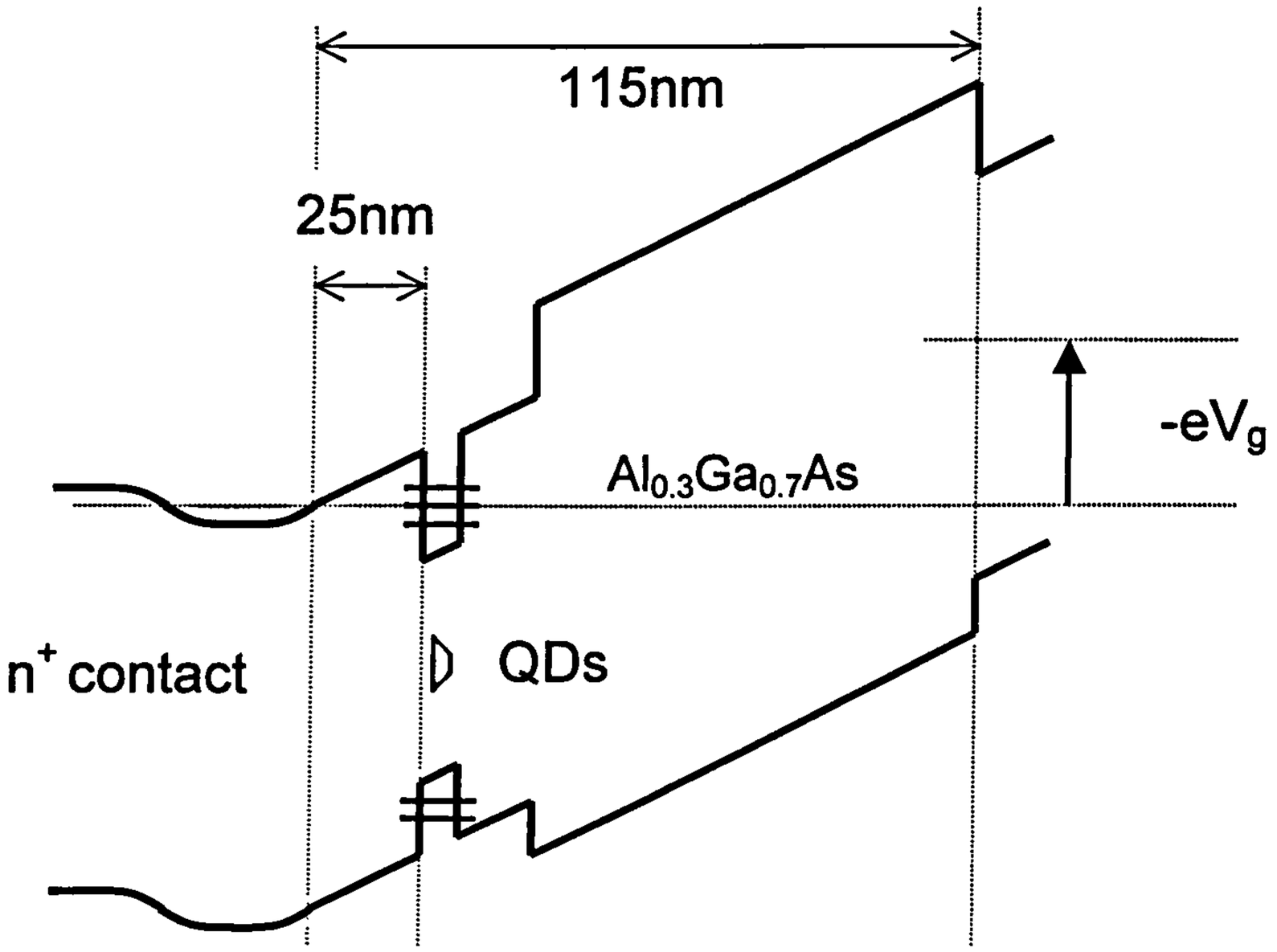

Figure 6.4 Schematic band diagram of an n-type MISMET device. The growth sequence is from left to right.

In addition to controlling carrier injection into the dots the gate potential also produces an electric field which affects carrier tunnelling and also the dot optical properties via the Quantum Confined Stark Effect (QCSE). The electric field, F, in the device is calculated using the following expression

$$F = \frac{(V_g + V_b)}{L} \qquad \textbf{Equation 6-1}$$

where V_b is the built in potential and L is approximately the thickness of the intrinsic region. The built in potential is given by half the GaAs band gap and can be determined from the current-voltage characteristics of the devices (Figure 6.5). This

gives a value of V_b= -0.75V in agreement with the bandgap of GaAs at 10K of 1.519eV [9]. Flat band conditions hence occur for V_g=0.75V. Figure 6.5 shows that the device exhibits excellent reverse breakdown characteristics.

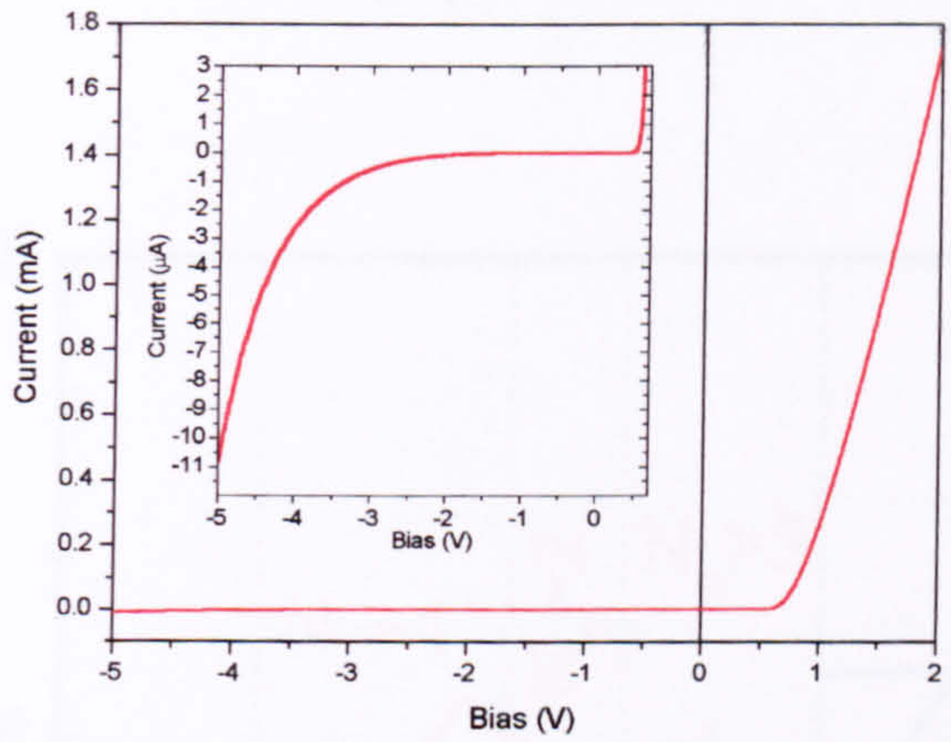

Figure 6.5 Current-voltage characteristic of a large area n-type device. Turn on occurs for V_g=0.75V.

6.3.2 Capacitance-Voltage characteristics

The capacitance-voltage characteristics of a 200μm diameter device containing approximately $6x10^7$ QDs is presented in Figure 6.6. The data was recorded under weak optical excitation (~0.1W.cm^{-2}), tuned to the peak of the ground state emission (~1.29eV). Using such excitation is found to result in clearer characteristics. For $V_g \leq$-1V the capacitance shows a smooth variation with V_g due to the depletion of the n^- doped region, with the QDs uncharged. As V_g is decreased in magnitude towards flat band conditions, pronounced features due to the charging of the QD states are observed. A peak at V_g=-0.75V and two minima (highlighted by dotted lines in Figure 6.6) at V_g=-0.63V and –0.48V are a clear fingerprint of Coulomb blockade.

The dotted lines separate the charge regimes of the device. Charging with up to three electrons is clearly observed (N_e is the number of electrons that have been injected into the dot by the gate voltage). For $V_g \geq -0.2V$ the capacitance increases rapidly. This increase is attributed to the charging of the two dimensional wetting layer states.

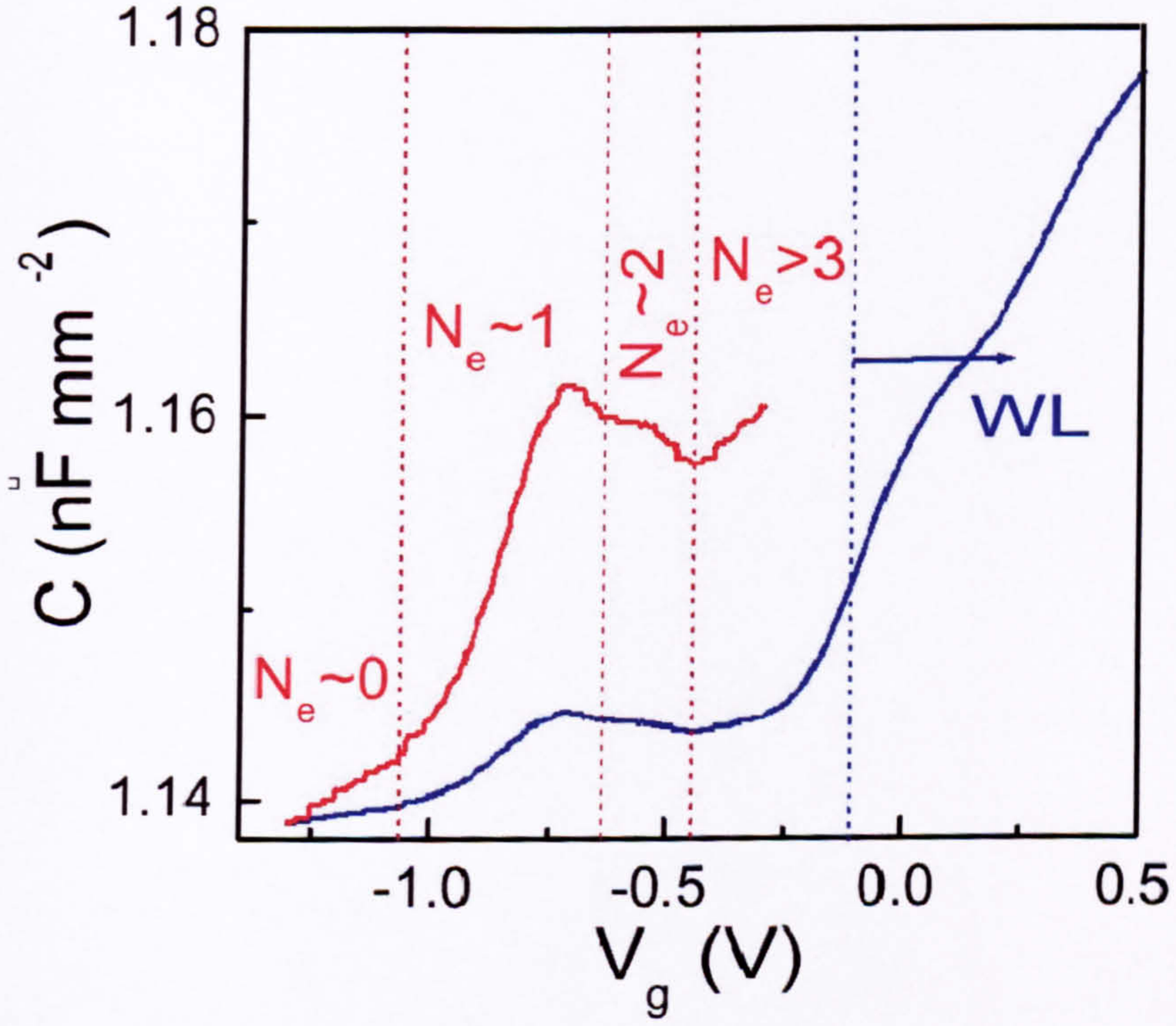

Figure 6.6 Capacitance-Voltage characteristics of an n-type device at T=4.2K. The dotted lines define the excess charge regions.

6.4 Experimental Details

The spectroscopic study of single QDs is performed using micro-photoluminescence (μPL) techniques, via nano-apertures formed in the Schottky gate contact. The apertures, with sizes ranging from 100 to 500nm, were formed using electron beam lithography and dry etching. Apertures exhibiting photoluminescence (PL) from only a single QD were selected for detailed study. The measurements were carried out at T~10K with a range of excitation wavelengths provided by a HeNe laser emitting at 1.96eV, and a tuneable Titanium-Sapphire laser with an emission energy range of 1.75eV to 0.9eV. The luminescence was dispersed by a 0.85m double grating monochromator (~35μeV resolution) and detected with a cooled CCD detector (Figure 5.3). For the majority of the measurements the incident laser power was kept sufficiently low such that single exciton processes dominated the emission spectra.

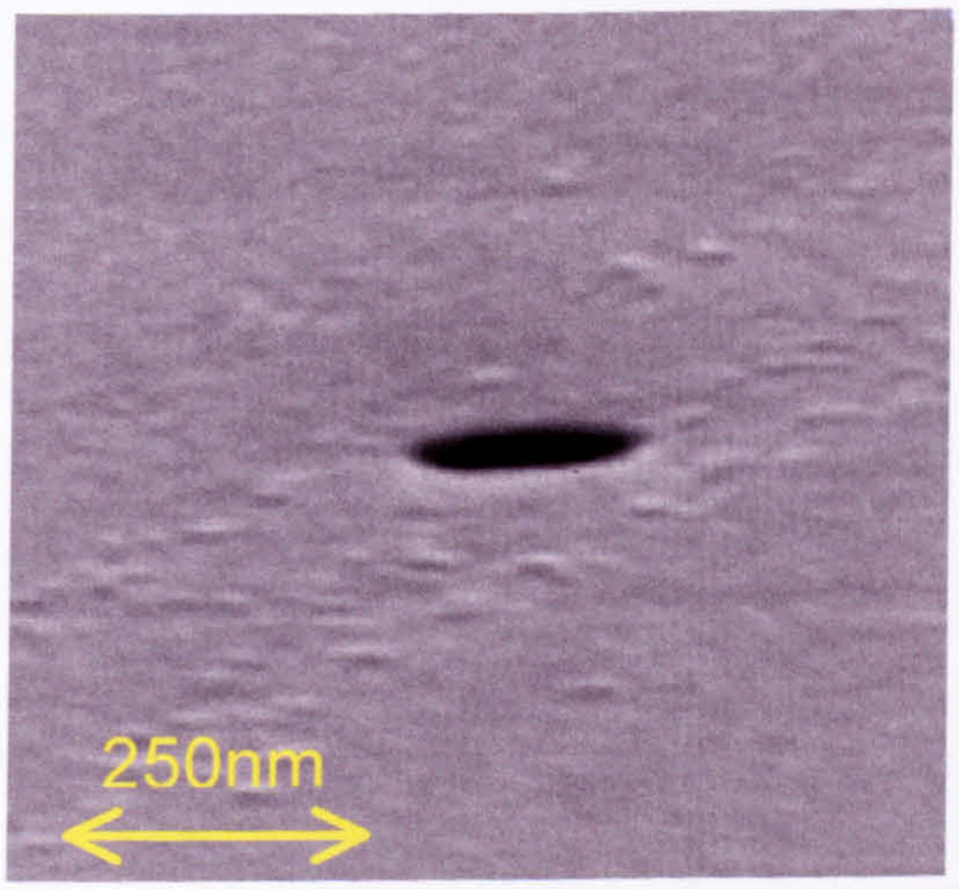

Figure 6.7 Aperture fabricated by e-beam lithography and dry etching techniques.

6.5 Sequential Quantum Dot Charging with Excess Electrons

The evolution of the ground state (s-shell) emission from a single dot with V_g (N_e), for an n-type sample, is summarised by the greyscale image of Figure 6.8. Spectra obtained for specific N_e are also shown in Figure 6.8 for comparison. The four horizontal red lines indicate charging thresholds determined from both the form of the spectra of Figure 6.8 and also from the capacitance voltage measurements of large area devices (Figure 6.6). For large negative V_g, the dot is uncharged and recombination due to the charge neutral exciton (X^0) is observed (~40μeV FWHM). As V_g is reduced, electrons are sequentially loaded into the dot and the form of the PL emission undergoes a series of pronounced transformations that reflect controlled modifications of the configuration and number of particles in the dot.

For large reverse bias and low excitation power only a single emission line is observed. This corresponds to the situation where the Fermi energy is below the first energy level in the QD and no excess electrons (N_e=0) are able to tunnel from the reservoir into the QD. In the emission spectra, only the recombination of a single neutral electron and hole pair, the single neutral exciton (X^0), is observed (a weaker biexciton line, $2X^0$, is observed to lower energy, reflecting the statistical nature of the dot carrier capture). Complementary photocurrent measurements performed for V_g<-1V support the identification of X^0, revealing a single absorption feature which evolves with decreasing V_g into X^0, as observed in PL (§ 6.7). As V_g is reduced further, the PL spectrum undergoes a pronounced transformation as a single additional electron (N_e=1) is added to the dot. X^0 is quenched (V_g=-1.175V) and is replaced by the negatively charged exciton (X^-), which is red-shifted from X^0 by -5.5±0.7meV

(Figure 6.9). The sign and magnitude of this shift remains approximately constant for different dots across the inhomogeneous distribution and is consistent with many body calculations performed using scaled harmonic oscillator-like basis states[10,11] (§ 6.6). These calculations reproduce the $X^0 \rightarrow X^-$ shift, the sign of which primarily arises because the lateral electron wave function is smaller than that of the hole. In this case, electron-hole attraction dominates over electron-electron repulsion in X^- and a red shift results[11,12,13]. These calculations are described in more detail below.

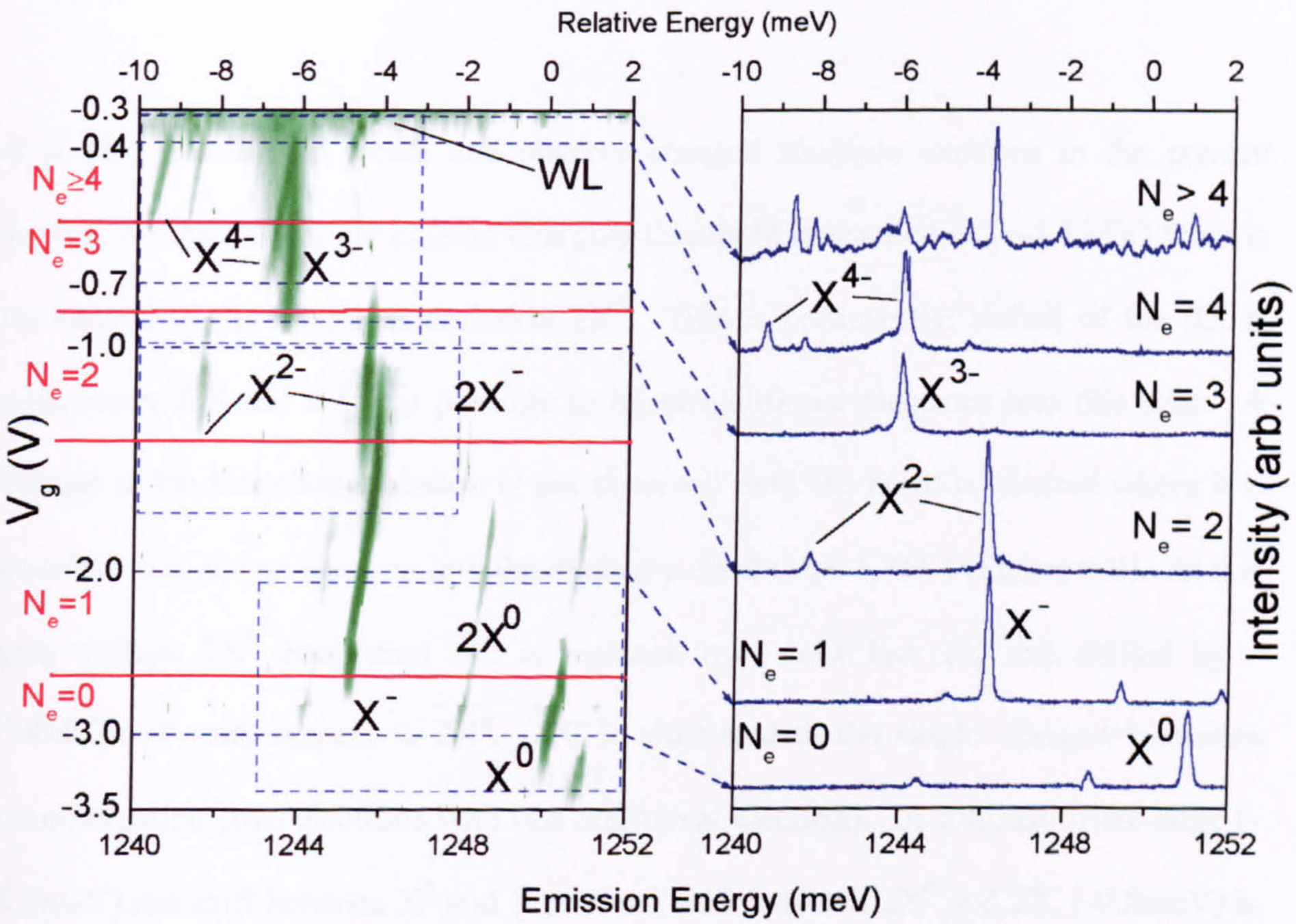

Figure 6.8 Low temperature (T=10K) single dot ground state (s-shell) PL as a function of gate potential. Horizontal red lines indicate charging thresholds. The boxed areas refer to regions of the characteristics which are shown in more detail in Figure 6.9, Figure 6.10 and Figure 6.12

For large reverse biases an additional very weak feature is evident at an energy 0.7meV higher than X^0. This feature is attributed to X^+ and arises when the electron from the photocreated exciton tunnels out of the QD, leaving just the photoexcited

hole. This occurs at high electric fields where the electron tunnelling rate becomes comparable to the exciton radiative recombination rate (the electron tunnelling rate exceeds the hole tunnelling rate due to the smaller effective mass of the former particle). Subsequently another photocreated exciton is captured into the QD and recombines in the presence of the additional hole.

6.5.1 Multi-Excitonic Complexes

It is also possible to create and observe charged multiple excitons in the present device. As the first single exciton charging threshold is reached (V_g=-1.175V) there is no change in the biexciton emission $2X^0$. This is because the s-shell of the dot is completely full and it is not possible to inject additional electrons into this state. A change in the biexciton emission is not observed until the point is reached where it is possible to inject an electron into the excited p-shell ($V_g \approx$-1.75V) (Figure 6.8). At this gate voltage $2X^0$ disappears and is replaced by a new line $2X^-$ red shifted by –0.8±0.2meV with respect to $2X^0$. $2X^-$ is attributed to the single charged biexciton recombination (two electrons with one additional electron). In contrast to the large (-5.5meV) red shift between X^0 and X^-, the red shift between $2X^0$ and $2X^-$ (-0.8meV) is much smaller. This observation, which is reproduced by many body calculations, arises because of the filled s-shell configuration of $2X^0$ and is a direct manifestation of shell filling effects in quantum dots.

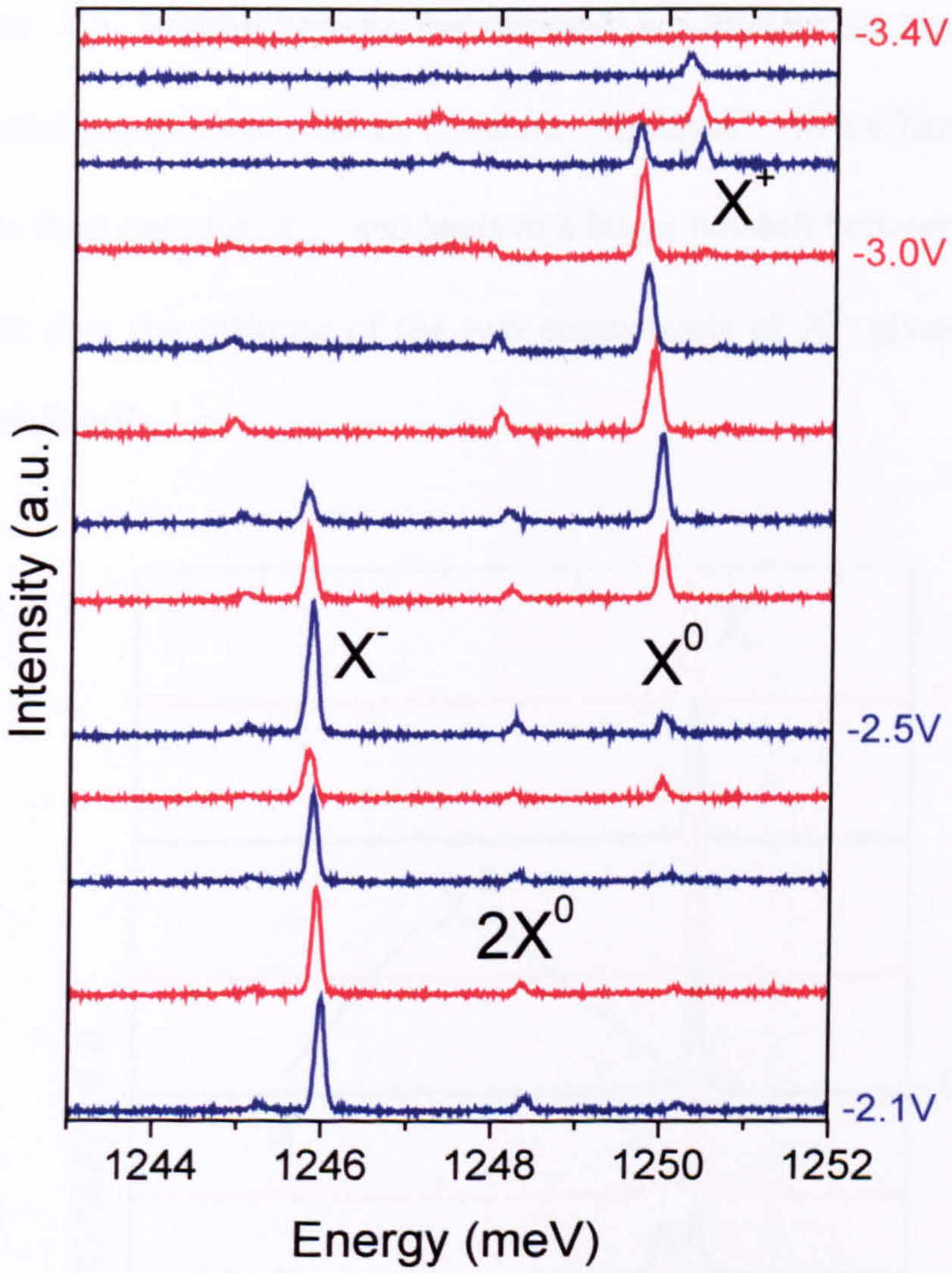

Figure 6.9 Region from Figure 6.8 showing the X^0 to X^- charging threshold in detail.

6.5.2 Exchange Interactions

The second single exciton charging threshold (Vg~0.6V) results in the emergence of two new emission lines, X_a^{2-} and X_b^{2-}, separated by 4.1±0.5meV (Figure 6.10). This doublet arises due to spin-spin exchange interaction in the final state of the doubly charged exciton, as illustrated in Figure 6.11. The two final states of X^{2-}, which have either parallel (X_a^{2-}) or antiparallel (X_b^{2-}) spins differ by twice the s-p level electron exchange energy (E_{ex}^{sp}). This situation is analogous to the He atom[14]. The shift

between X^- and X_b^{2-} is small because the attractive s-p electron exchange interaction results in a partial compensation of the Coulomb repulsion. The exchange interaction is absent in the final state for X_a^{2-} and leads to a larger redshift between X^- and X_a^{2-}. For the present dots the splitting of the two components of X^{2-} gives an exchange energy of 2.1±0.3meV.

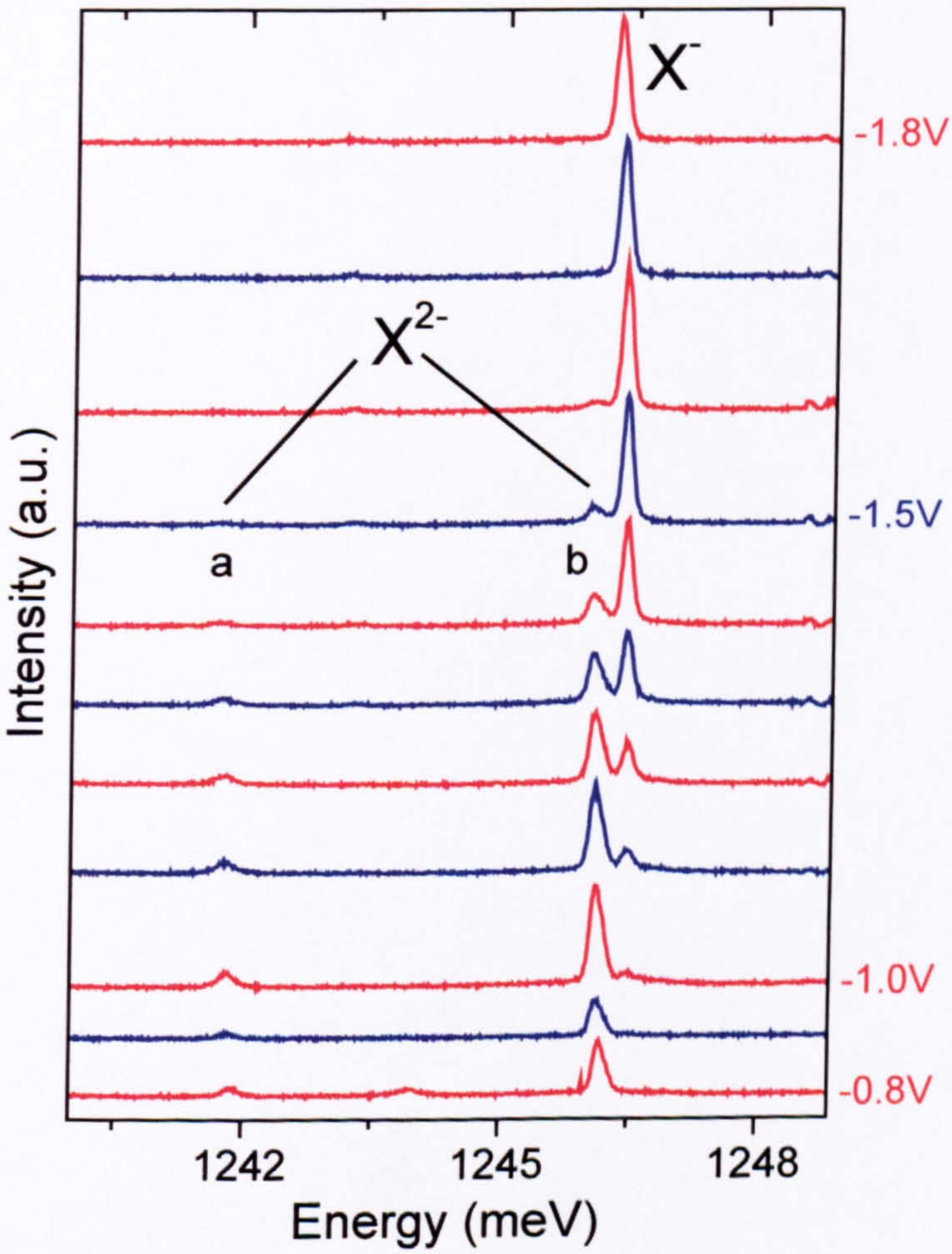

Figure 6.10 Region from Figure 6.8 showing the X^- to X^{2-} charging threshold in detail.

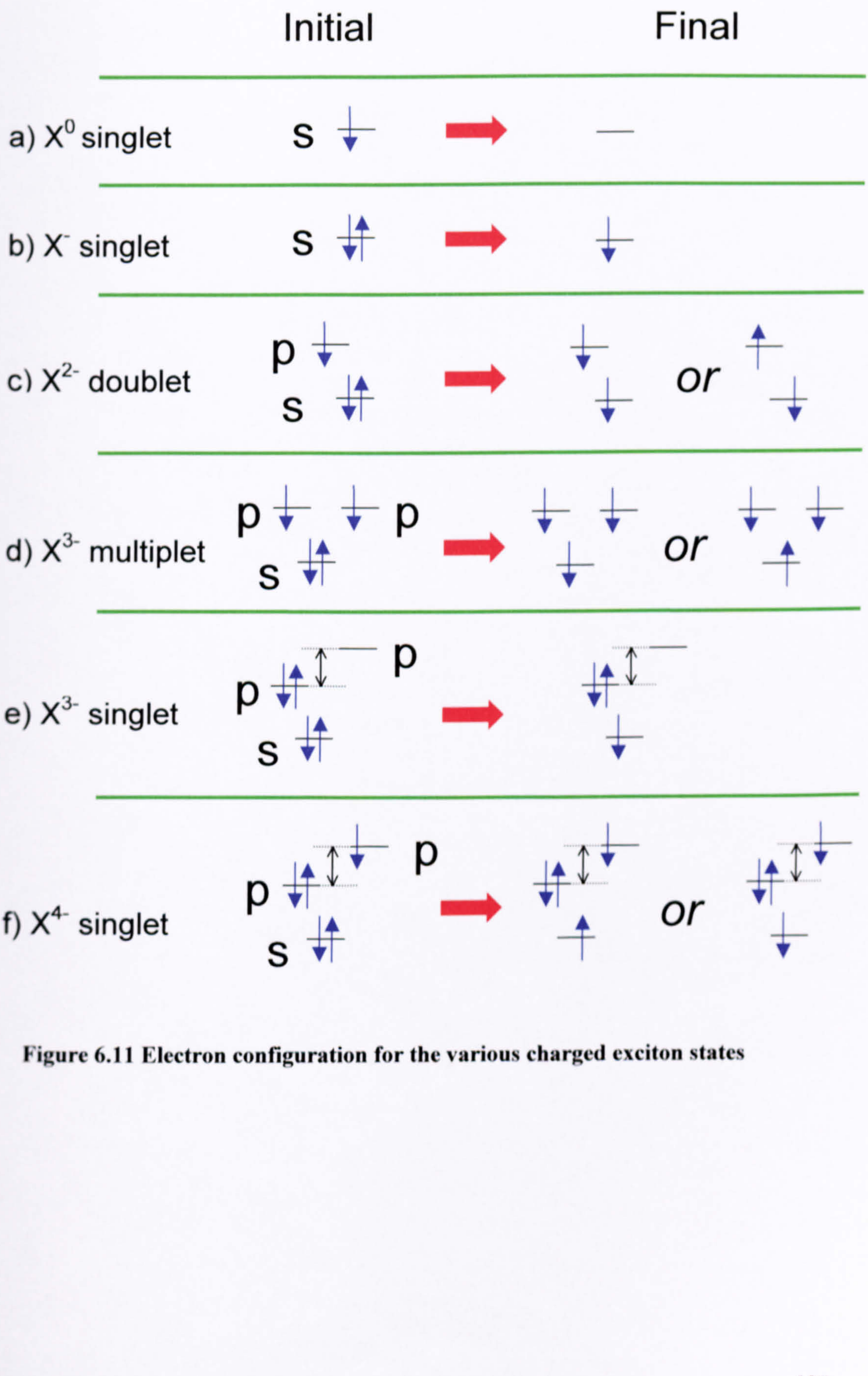

Figure 6.11 Electron configuration for the various charged exciton states

6.5.3 Highly Charged Single Exciton States

A small number of the dots investigated could be charged with more than two excess electrons (N_e>2) before electron occupation of the underlying wetting layer occured. Charging of the underlying wetting layer results in a sudden broadening of all the emission lines and the appearance of a complex band of emission features. There are many states available in the WL and this produces many different perturbations that are indistinguishable in the time averaged spectra. Before charging of the WL occurs some dots exhibit further abrupt modifications of the PL spectrum indicating the formation of highly (N_e>2) charged states.

As the N_e=3 charging threshold (V_g~-0.45V) is crossed both components of X^{2-} disappear to be replaced by a single emission line at 1244meV (X^{3-} - Figure 6.12). This observation of a single emission line for N_e=3 contrasts with theoretical predictions which indicate that X^{3-}, like X^{2-}, should generate an emission doublet resulting from the two possible final states of total spin $^3/_2$ or $^1/_2$ (Figure 6.11d). These states arise when the two p-shell sub-orbital states are degenerate and the lowest energy inital state consists of two parallel spin p-electrons, one in each sub orbital. This is a result of a Hund-like rule. The observation of only a single line for X^{3-} suggests that the orbital degeneracy of the p-levels is lifted for the present dots, with the initial state of X^{3-} corresponding to a filled sub-shell configuration (Figure 6.11e). Simiar effects, which arise from a reduction of the symmetry of the QD, have been predicted theoretically and observed experimentally[15]. The degeneracy of the p-shell may be lifted by a number of mechanisms, including an absence of four-fold

roational symmetry, interaction with the higher energy d-shell[16] or the inequivelence of the [110] and [$\bar{1}$10] directions[17].

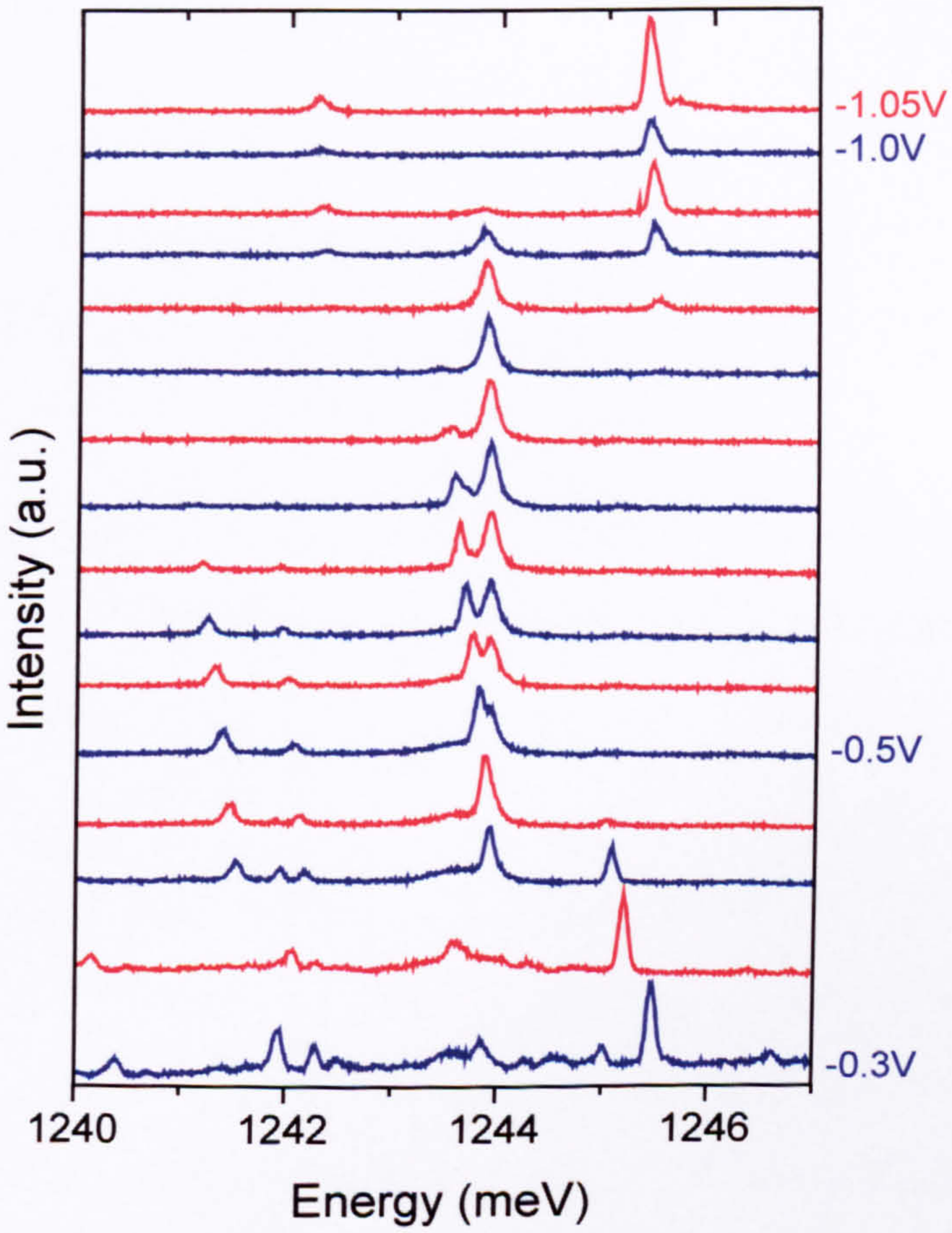

Figure 6.12 Region from Figure 6.8 showing the X^{2-} to X^{4-} charging threshold in detail. For voltages V_g<-0.3V the WL states start to be populated resulting in complex spectra with a large number of emission lines.

Following the next charging threshold of N_e=4 (X^{4-}) at V_g~-0.35V an emission multiplet reappears reflecting the s-p electron exchange interaction in the final state[18]. Beyond this point the spectra becomes highly complex making further idenification impossible. The observation of more than two components for X^{4-} in Figure 6.8 is attributed to higher order effects[19]. Shake up processes and electron-electron scattering can occur in addition to radiative recombination, resulting in lower energy

final states. Other processes, such as spin-flip and emission of an LA phonon could produce similar effects. Alternatively the additional lines could be a signature of an even higher charged state (N_e=5) as some of the lines appear at biases very close to the point where the WL begins to be populated.

6.5.4 p-shell Emission

Figure 6.13 shows a grey scale plot of the emission recorded over a spectral range which includes both the s-shell and p-shell emission. Emission from the p-shell is first observed for a bias of V_g~-0.7V, which corresponds to the bias at which the $2X^0$ to $2X^-$ charging threshold occurs. At this point an electron is injected into the p-level which may subsequently recombine with a photoexcited hole. Subsequent changes in the p-shell emission are observed at voltages corresponding to higher order s-shell charging events (e.g. N_e=2, 3, etc...) as additional electrons are added to the p-shell. However the complexity of the p-shell emission makes a detailed interpretation of the spectra difficult.

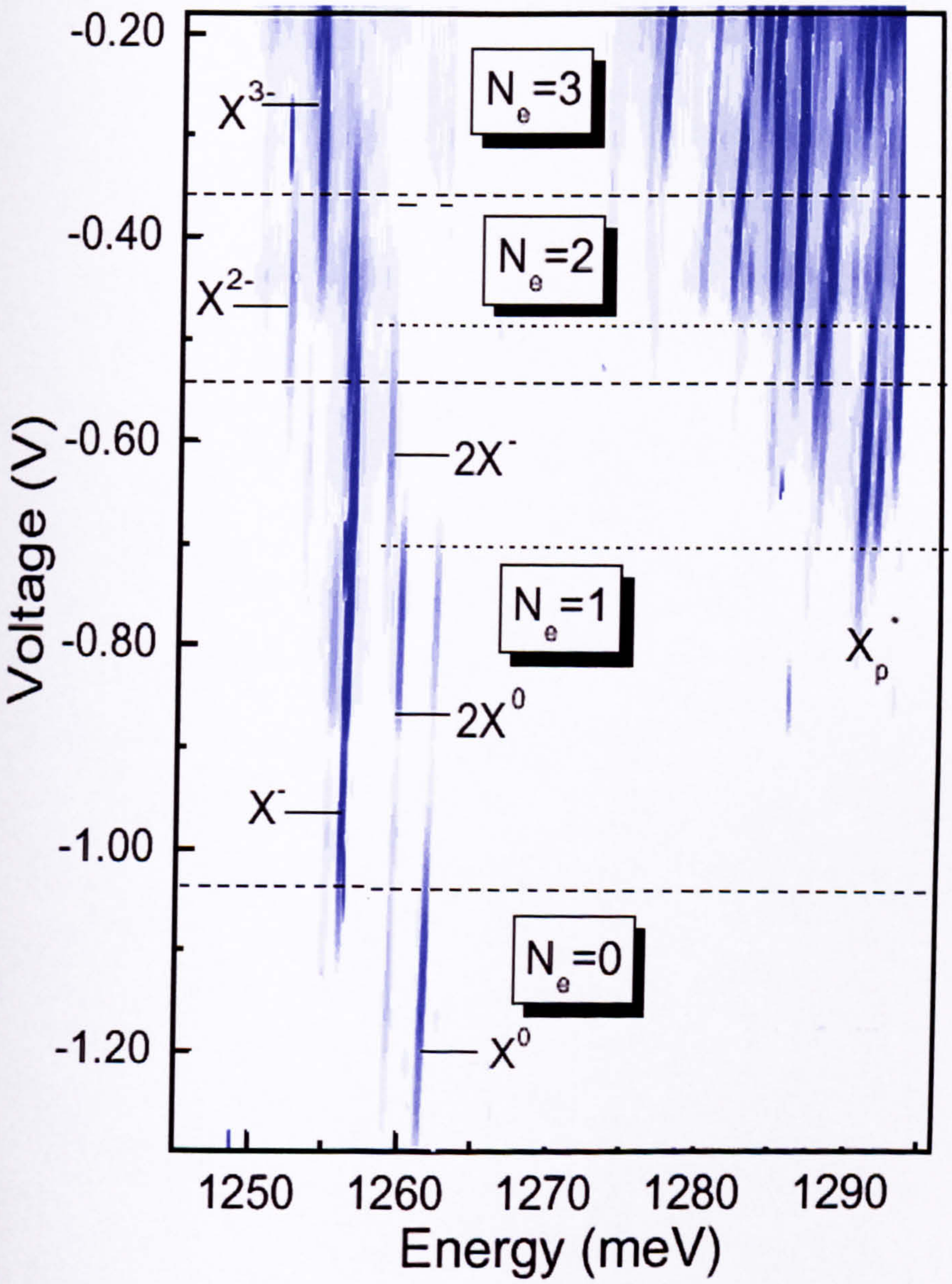

Figure 6.13 Colour plot over a broad spectral range showing the s-shell emission and, to higher energy, the p shell emission. The latter emerges as the system is filled with two or more excess electrons.

6.5.5 Intensity Variation with Bias of the Charged Exciton States.

The charging thresholds observed in the spectrum of Figure 6.8 are not totally sharp and there exist limited voltage regions where more than one charged state is observed

in the spectra. This is shown in Figure 6.14 when the intensities of the different charged emission lines are plotted as a function of gate voltage. This behaviour is a consequence of the time integrated nature of the measurements and the statistical nature of the dot carrier occupancy. In particular for a thick tunnelling barrier the electron tunnelling rate may be sufficiently low that the system spends a significant fraction of time in a non-equilibrium state. For example Baier et al.[20] found a greater overlap of the charged regions in a device with a thick (40nm) tunnelling barrier than in one with a thin barrier (20nm). Warburton et al. [11] observed no overlap in their studies of single quantum rings consistent with the very thin tunnelling barriers in their devices. The overlapping charged state regions of the present device are therefore attributed to the effects of the intermediate width (25nm) tunnelling barrier.

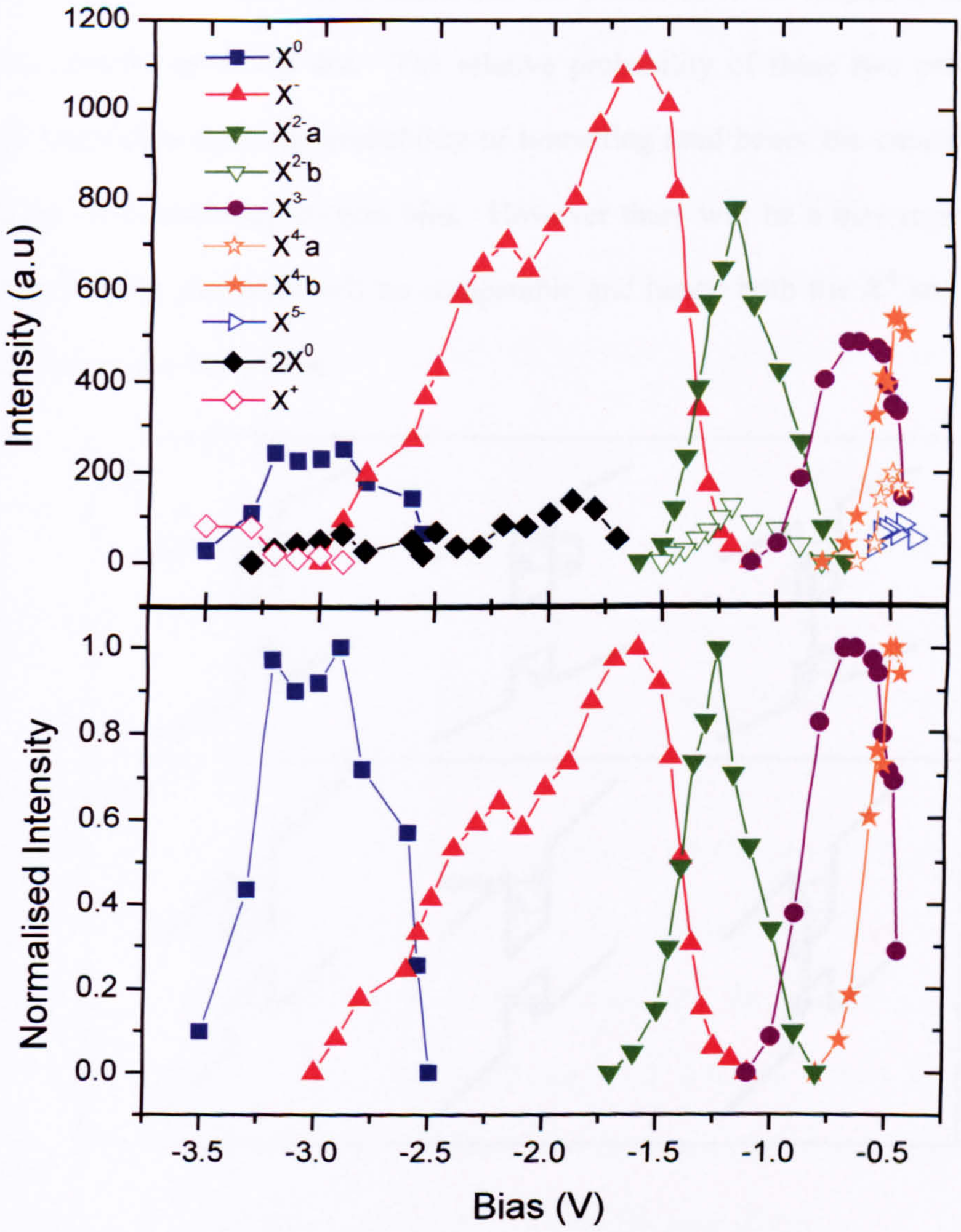

Figure 6.14 a) the intensity variation with bias of all the s-shell emission lines. b) the intensity variation of selected lines normalised to the same maximum intensity.

Another mechanism which can result in an overlap of the different charged regions is that different emission lines can be created from the same initial state. For example Figure 6.15 shows how both X^0 and X^- can result from the initial state of one single electron. Following the optical creation of an exciton (with the photoexcited electron in the p-shell and with a parallel spin to the initial electron) X^- is created if the

electron relaxes via a spin-flip process into the s-shell or X^0 is created if the p-shell electron tunnels out of the dot. The relative probability of these two processes is strongly dependent upon the probability of tunnelling (and hence the creation of X^0) increasing with increasing reverse bias. However there will be a bias region where the rates for both processes will be comparable and hence both the X^0 and X^- lines will be observed in the spectra.

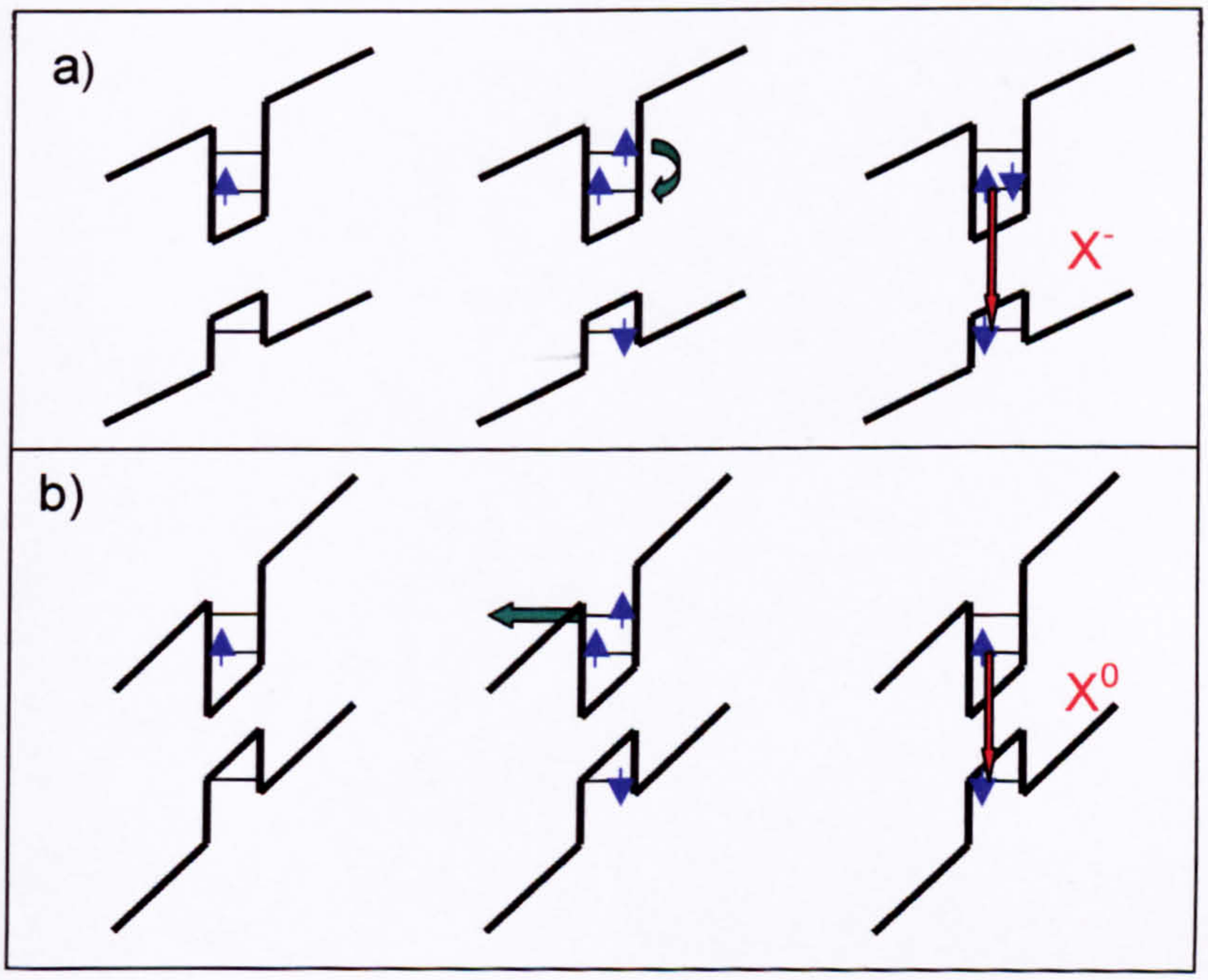

Figure 6.15 Two final outcomes from the identical initial configuration. a) Due to the small tunnelling probability the p-shell electron has time to undergo a spin flip relaxation to the s-shell producing X^-. b) a larger bias increases the tunnelling probability and the p-shell electron escapes from the dot before the system can relax. Radiative recombination occurs via the single neutral exciton, X^0.

6.6 Theoretical Modelling of the Charged Exciton State.

The effects of excess electrons on the exciton energy have been calculated by Maxsym et al.[10]. Their model used a parabolic confinement potential with different effective masses and characteristic frequencies for in-plane and normal motion,

$$V(r) = \frac{1}{2} m_{\parallel}^{*} \omega_{\parallel}^{2} (x^2 + y^2) + \frac{1}{2} m_{\perp}^{*} \omega_{\perp}^{2} z^2 \qquad \textbf{Equation 6-2}$$

The resultant many-particle states are obtained by the numerical diagonalisation of the interacting electron Hamiltonian. This model neglects sub-band mixing effects. In addition the use of the simplified harmonic oscillator potential for the single particle states gives an unrealistic calculation of correlation effects. Correlation effects result in negative energy shifts of the few-particle states and, for strongly confined systems, these effects are expected to be smaller than the Coulomb shifts, although not negligible. Thus, although the present calculations give the correct signs of the perturbations and also reproduce their magnitude well, a higher degree of accuracy will require a more sophisticated model. Similar calculations, to those described here, have been reported by Findeis et al.[13] and agree with the present ones.

Figure 6.16a), b) and c) show the calculated shift between X^0 and X^- plotted as a function of the ratio of the in-plane extents of the electron (l_e) and hole wavefunctions (l_h). Within each figure the different lines correspond to different absolute in-plane lateral extents of the electron wavefunction. The separate figures are for different spatial extents of the electron wavefunction along the growth axis. Experimentally a study of seven individual quantum dots gives an X^0 to X^- splitting of $4.9 - 5.9$meV. A red shift of this magnitude is reproduced by the calculations for $l_e > l_h$, $l_e^z > l_h^z$ and

l_e≈2-6nm. The latter range for l_e is consistent with the physical lateral extent of the dots. In addition the condition $l_e > l_h$ and $l_e^z > l_h^z$ are reasonable given that the larger hole effective mass will lead to a more compact wavefunction. A further consequence of the calculations is that the positively charged single exciton (X^+) should be blue shifted with respect to X^0. This is confirmed by studies of p-type structures which are presented below.

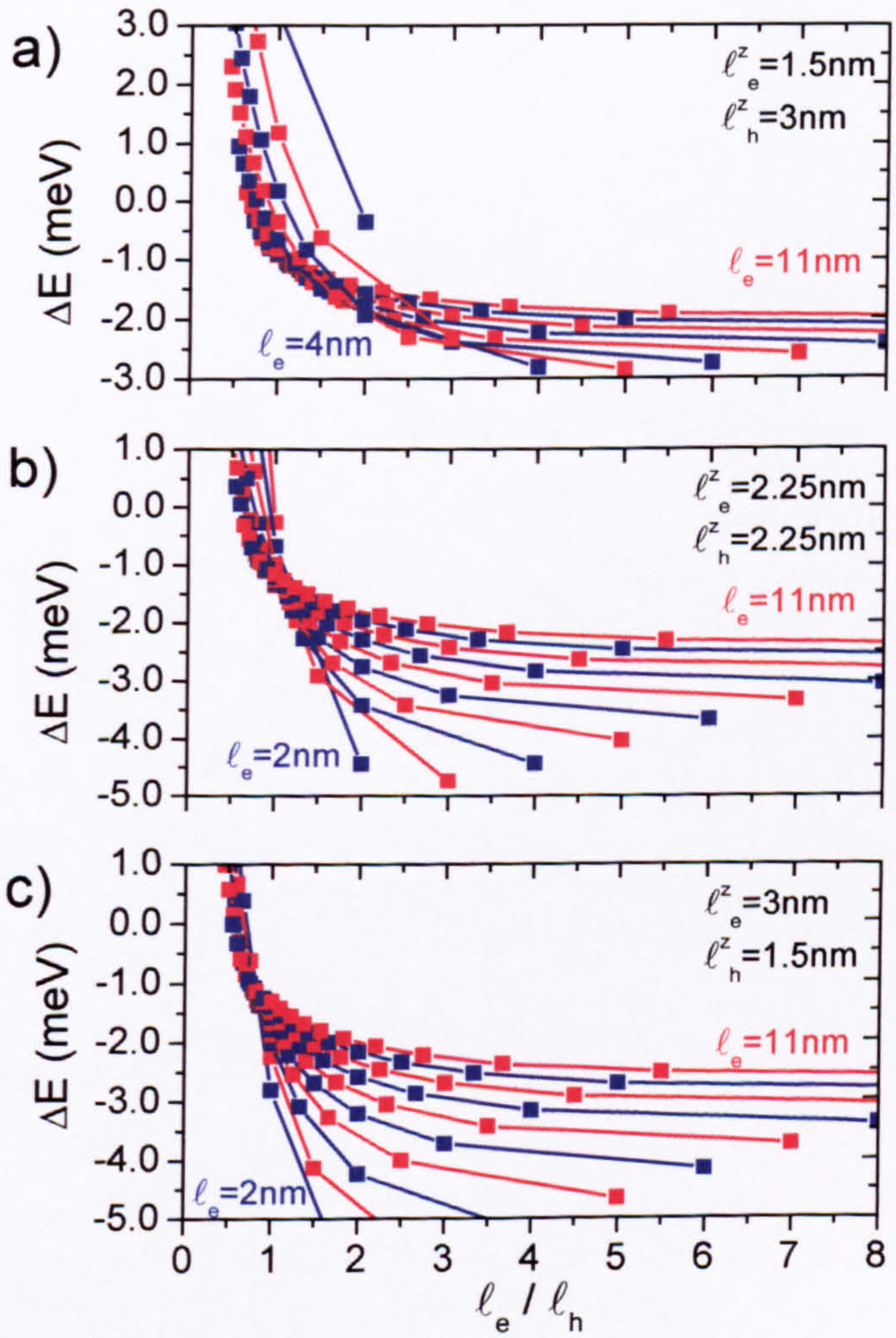

Figure 6.16 Theoretical calculations showing the perturbation of X^- from the X^0 state. The emission is perturbed more to the red as the electron to hole in plane wavefunction l_e/l_h extent is increased. The three graphs are for different wavefunction extents in the growth direction. a) l_e=1.5nm l_h=3nm b) l_e=2.25nm l_h=2.25nm c) l_e=3nm l_h=1.5nm.

6.7 Photocurrent spectroscoppy

Photocurrent (PC) spectra were recorded at low temperature (T=10K) as a function of gate bias. The excitation was provided by a tuneable Ti:Sapphire laser with very low incident power ($0.1 W.cm^{-1}$), corresponding to extremely low dot carrier occupancies (<<1).

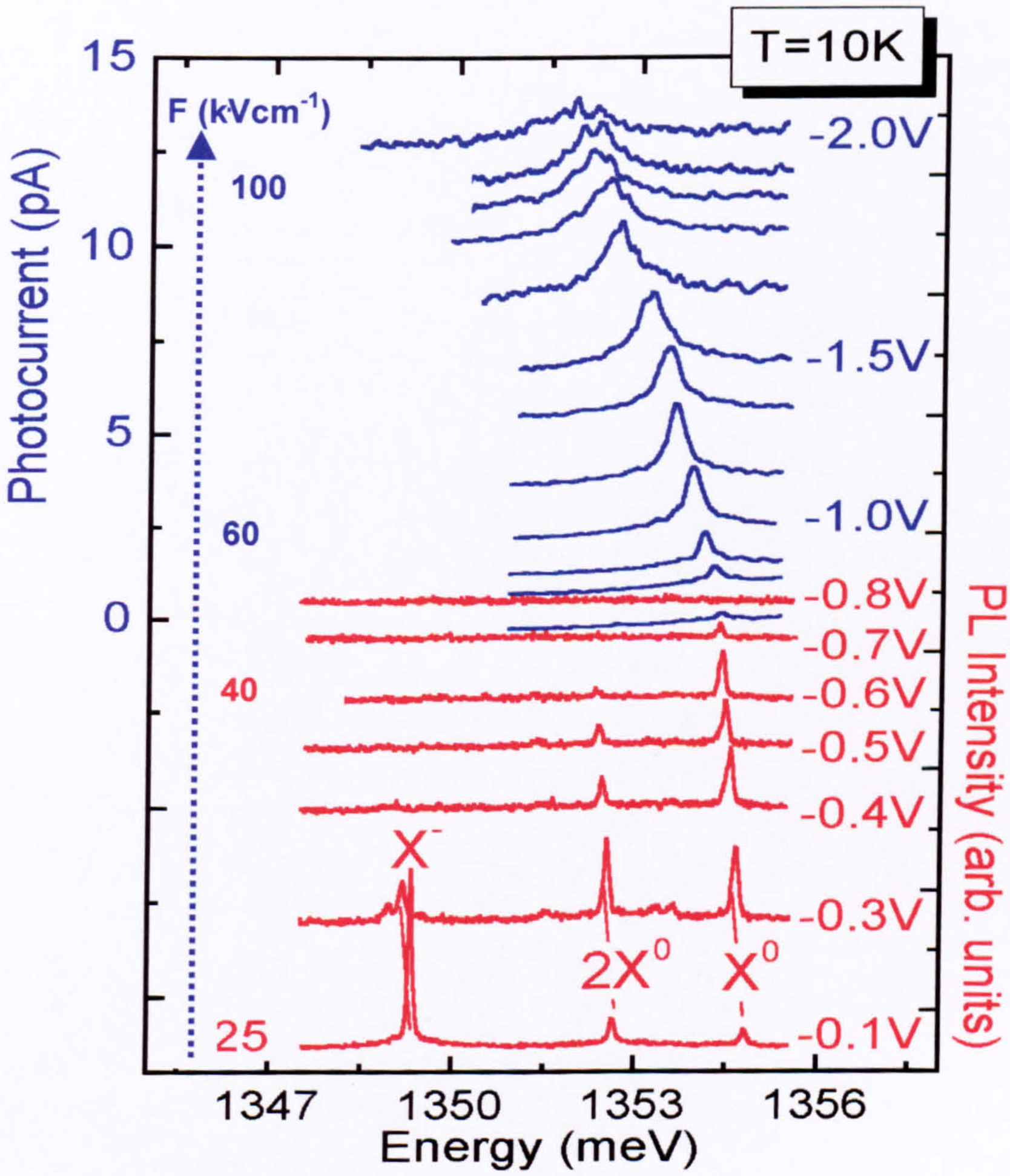

Figure 6.17 PL and PC spectra as a function of bias voltage. T=10K.

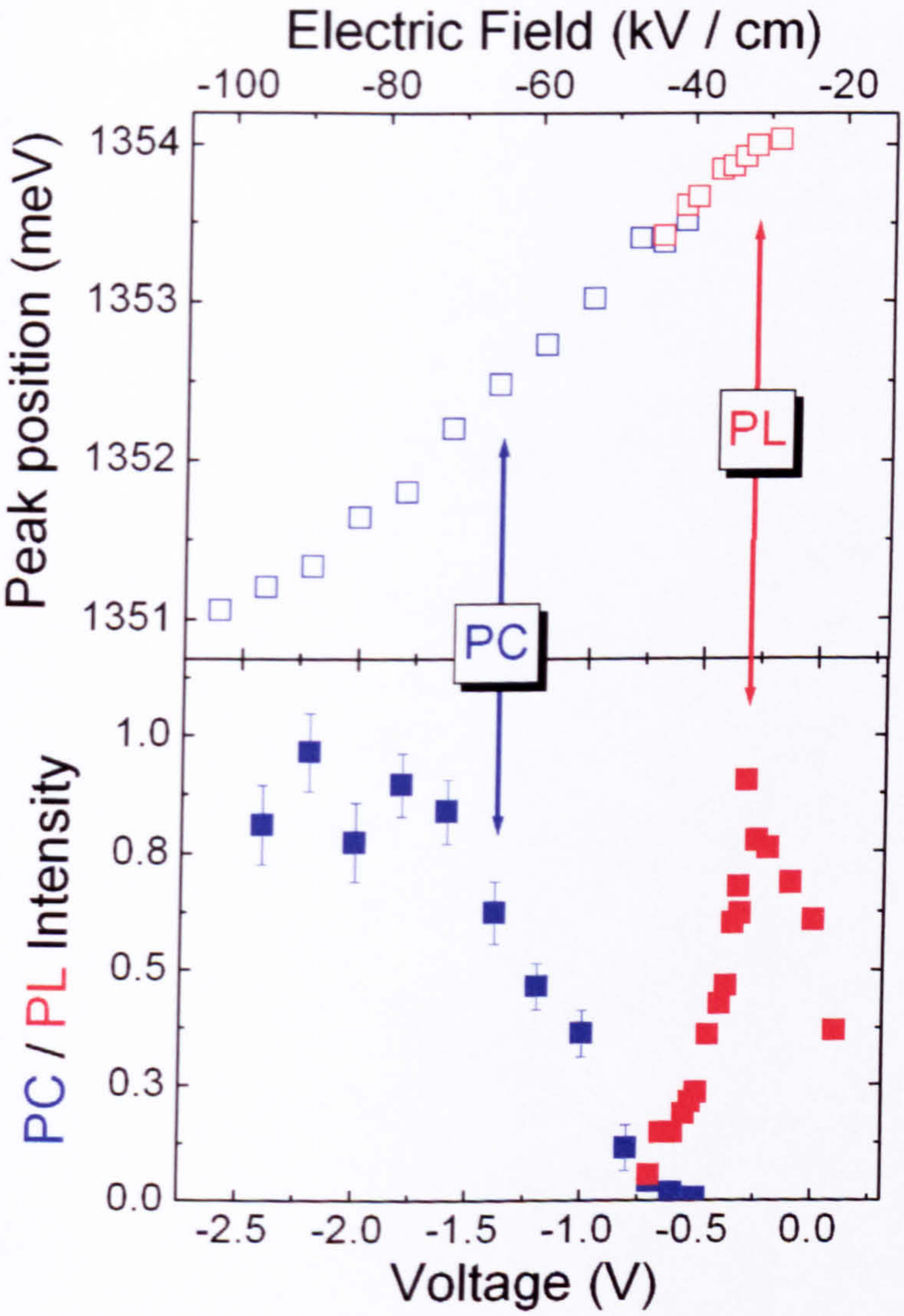

Figure 6.18 The peak position and intensity of X^0, as determined from both PC and PL, plotted as a function of bias voltage.

Figure 6.17 shows both PC and PL spectra recorded for different bias voltages. The observation of a PC signal requires that the photoexcited carriers escape from the dot before recombination occurs. At low temperatures the only possible carrier escape mechanism is tunnelling, the rate for which is a strong function of the electric field. For high electric fields (large reverse bias voltages) a PC signal is observed (Figure 6.17) but not a PL signal as the tunnelling rate considerably exceeds the

recombination rate and all the photoexcited carriers escape from the dot. As the electric field is reduced the tunneling rate is also reduced and when it becomes comparable to the radiative recombination rate ($\sim 10^{-9}s^{-1}$)[21] a PL signal starts to be observed. With further decreases in the electric field the PC signal intensity decreases whereas that of the PL rises (Figure 6.18); eventually only a PL signal is observable when the tunnelling rate becomes much smaller than the recombination rate.

In photo-current (PC) only the single, uncharged exciton can be created because the incident laser power is insufficient to excite two electron hole pairs simultaneously ($2X^0$) and the bias voltage is such that there are no additional electrons in the dot. The fact that the single line observed in PC transforms smoothly into the X^0 line observed in PL (Figure 6.18) provides conclusive evidence for the single exciton nature of the latter (the shift of the lines with bias is a result of the QCSE). At high electric fields the single exciton line, as observed in PC, broadens considerably. This is attributed to lifetime broadening as the tunnelling rate becomes very rapid.

6.8 Charging of a Single Dot with Excess Holes.

A p-type doped sample was grown to allow the effects of excess hole charging to be studied. This is similar in structure to the n-type sample, but replaces the GaAs n-type doped region with a Beryllium p-type doped region ($N=4.0x10^{18}cm^{-3}$). The valence band of the structure of this sample is shown schematically in Figure 6.19.

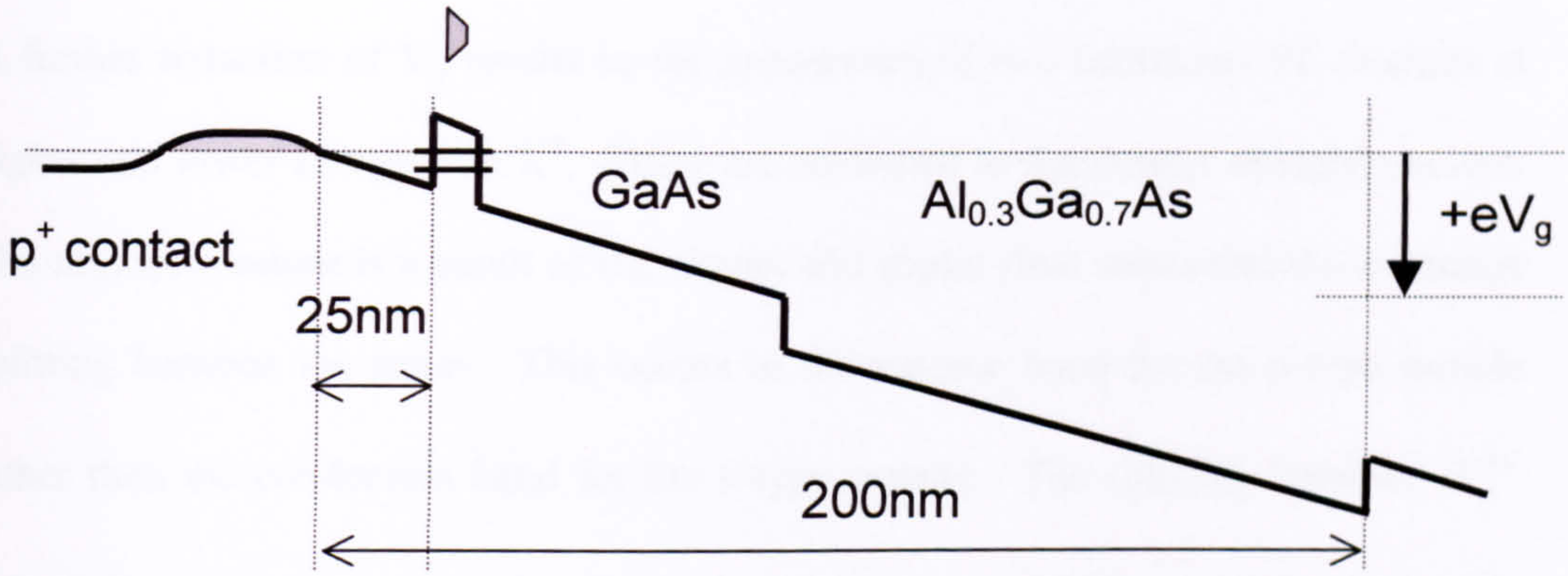

Figure 6.19 The valence band profile of the p-type structure.

For a p-type device a decreasing bias voltage produces an increasing loading of the dot with holes. Typical results for hole loading of a single QD are presented in Figure 6.20. For V_g>+0.6V a single emission line is observed, arising from the recombination of the charge neutral exciton (X^0). For V_g<0.6V an additional peak arising from the singly positively charged exciton, labelled X^+ in Figure 6.20, emerges on the high energy side of X^0. Both X^0 and X^+ exhibit a strong quantum confined Stark shift. For zero electric field the energy separation between X^+ and X^0 is +1.0±0.2meV. This observation demonstrates that, in contrast to the n-type sample discussed above, the addition of an extra hole results in a comparatively weak *blue* shift of the excitonic emission. The different signs of the energy of X^+ and X^- with respect to X^0 can be qualitatively understood in terms of the balance of the attractive and repulsive Coulomb interactions. For X^+ the hole-hole repulsion dominates due to the more localised hole wavefunction, resulting in an overall blue shift. In contrast, for X^- the electron-hole attraction outweighs the electron-electron repulsion because the larger electron wavefunction extent allows the electrons to move apart, resulting in an overall red shift (Figure 6.20).

A further reduction of V_g results in the appearance of two additional PL features at higher and lower energy than X^0. These are attributed to the doubly charged exciton. The multiplet nature is a result of the singlet and triplet final states and the exchange splitting between the states. This occurs in the valence band for the p-type sample rather than the conduction band for the n-type sample. The splitting between X_a^{2+} and X_b^{2+} is 2.4meV which implies a hole exchange splitting of 1.2meV. This compares with a value of 2.1meV for the electron exchange splitting. The present work also indicates that the charged complex, X*, observed on the high energy side of X^0 in the mesa studied in Chapters 4 and 5 (§4.2) is most likely due to a positively charged exciton.

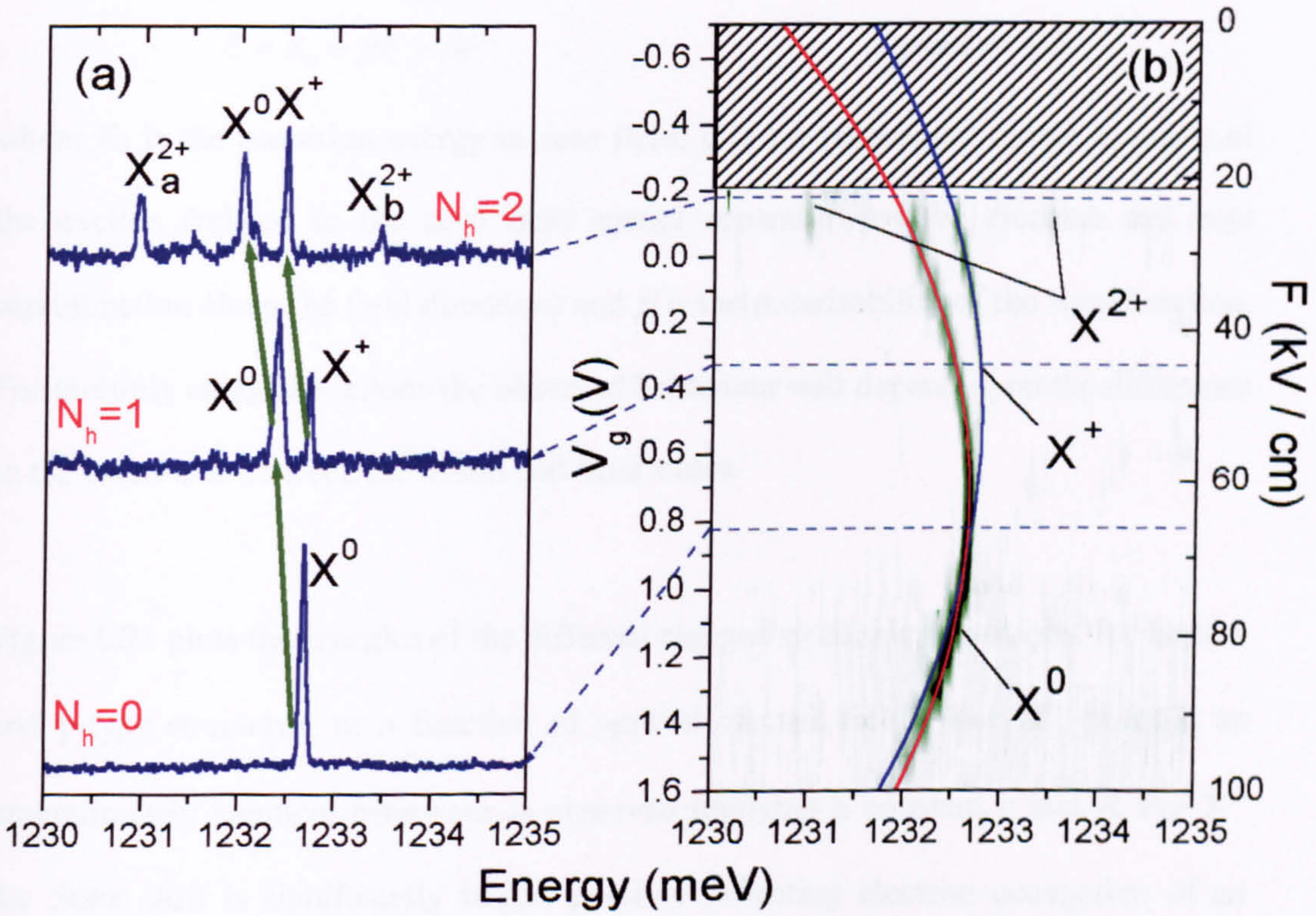

Figure 6.20 Example spectra showing the charge states for the p-type sample b) colour intensity plot showing the evolution of the ground state emission with bias and electric field.

Figure 6.20 also shows a much greater overlap of the different charged states than occurs for the n-type device (Figure 6.8). This is a further consequence of departures from equilibrium caused by the finite carrier tunnelling rates. The large effective hole mass is expected to result in much slower hole tunnelling rates compared to electrons, producing greater departures from equilibrium and hence an enhanced overlap of the different charged state.

6.9 Quantum Confined Stark Shifts of the Different Charged States.

In an applied electric field, F, the energy of an excitonic transition is given by

$$E = E_0 + pF + \beta F^2 \qquad \textbf{Equation 6-3}$$

where E_0 is the transition energy in zero field, p is the permanent dipole moment of the exciton (related to the zero field spatial separation of the electron and hole wavefunction along the field direction) and β is the polarisability of the wavefunction. For multiply charged excitons the observed behaviour will depend upon the difference in the behaviour between the initial and final states.

Figure 6.21 plots the energies of the different charged excitonic transitions, for both n- and p-type structures, as a function of applied electric field. For X^{n-} ($0 \leq n \leq 3$) an approximately identical behaviour is observed implying a constant p and β. For X^{4-} the Stark shift is significantly larger, possibly reflecting electron occupation of an excited state with a different vertical (z) quantisation. Such a state would have a larger vertical extent, giving a larger value for both p and β. In contrast to the n-type sample the behaviour of the X^{n+} ($0 \leq n \leq 2$) excitonic states is a strong function of n. In

particular the dipole moment decreases significantly with decreasing n. The reason for this behaviour is not clear but suggests very different electron and hole states. From Figure 6.21 it appears that the permanent dipole moment for the n-type and p-type samples is of opposite sign.

By fitting the X^0 peak position, as observed in the p-type sample, to equation 6-3 (blue line in Figure 6.21) values of $E_0(X^0)$ =1230.5±0.2meV, $p(X^0)$= [1.1±0.2].10^{-28} Cm and $\beta(X^0)/e$=[-8.4±0.2].10^{-36} Cm^2V^{-1} are obtained. This value for *p* corresponds to an electron-hole separation of 6.8±0.6Å (from p=er). The sign of the dipole moment indicates that the hole wavefunction is localised above that of the electron in the dot, a similar alignment to that deduced for nominally InAs dots in Fry et al.[22]. As shown in this work, this alignment requires a grading of the InGaAs composition, with a greater In content towards the top of the dot. A similar fit to the X^+ transition gives parameters of $E_0(X^+)$ =1231.53±0.2meV, $p(X^+)$=[7.5±0.5].10^{-29} Cm and $\beta(X^+)/e$=[-7.1±0.3].10^{-36} Cm^2V^{-1}.

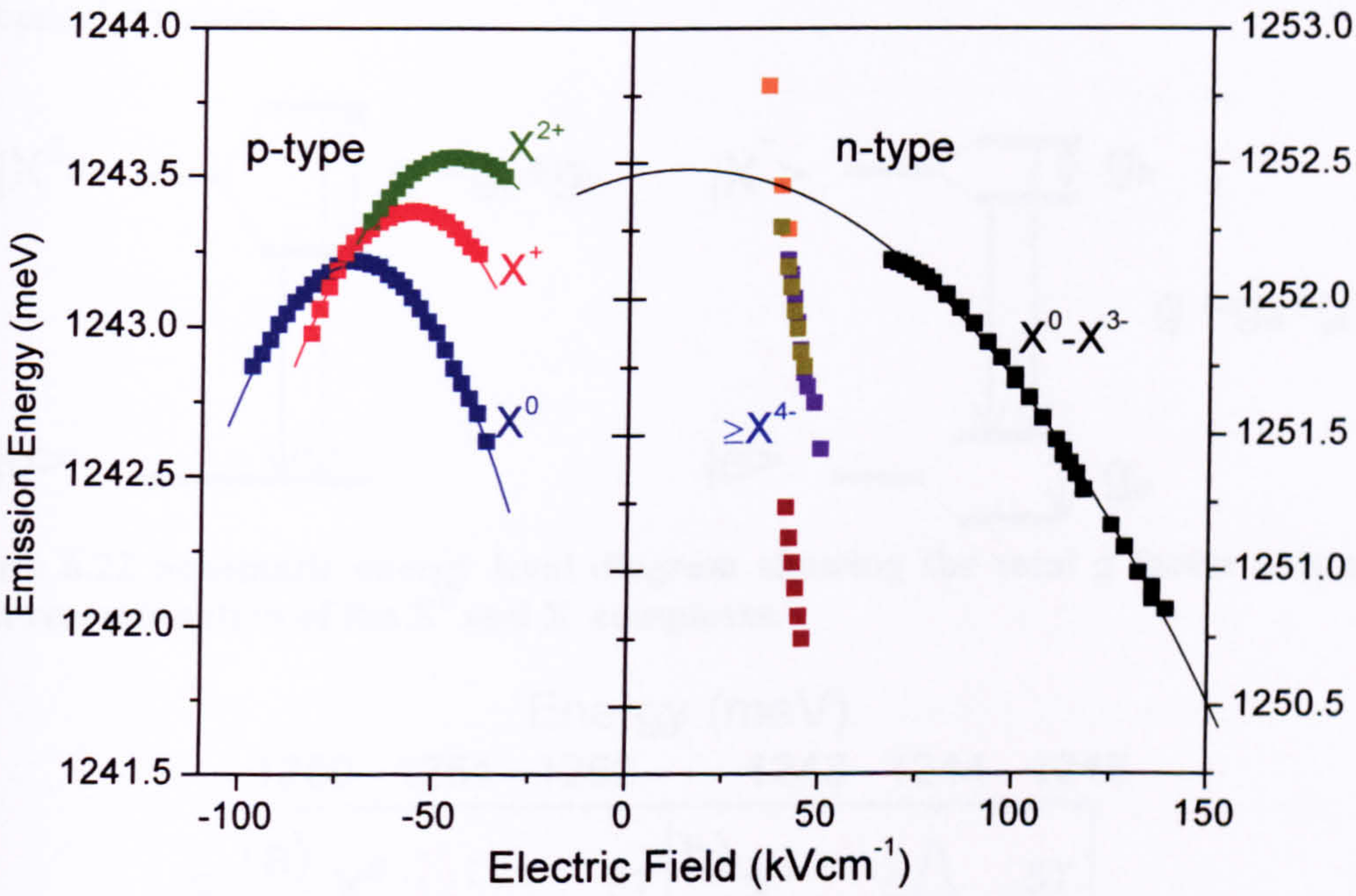

Figure 6.21 Transition energies plotted against electric field for both the n- and p-type samples. The solid lines are fits using Equation 7-3.

6.10 Magneto-Optical Study of the Charged Exciton States

To further study the nature of the different charge states X^{N_e-} ($0 \leq N_e \leq 3$), a magneto optical investigation (B||z, z-growth axis) was performed. As discussed in Chapter 4 for the fields applied the sample is in the weak field regime due to the relatively large magnetic field length. The effect of the B-field on the J=±1 s-shell exciton states consists of a linear Zeeman splitting ($\Delta E_{Zeeman} = g_X \mu_B B$) of the two spin states and a diamagnetic shift which increases their centre of gravity ($\Delta E_{dia} \approx \gamma_2 B^2$). For a few electron final state ($N_e \geq 1$) the difference between the magnetic interaction energy

($\Delta E_{Zeeman} + \Delta E_{dia}$) of the initial and final states will determine the overall behaviour of the optical transition.

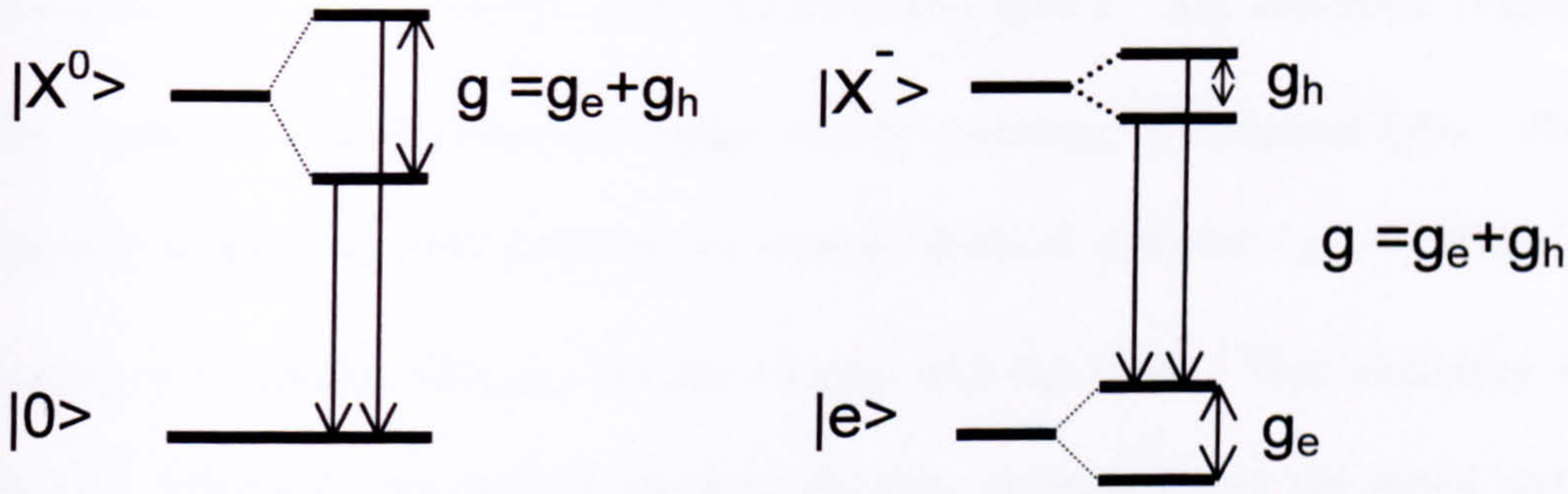

Figure 6.22 Schematic energy level diagram showing the total g factor arising from recombination of the X^0 and X^- complexes.

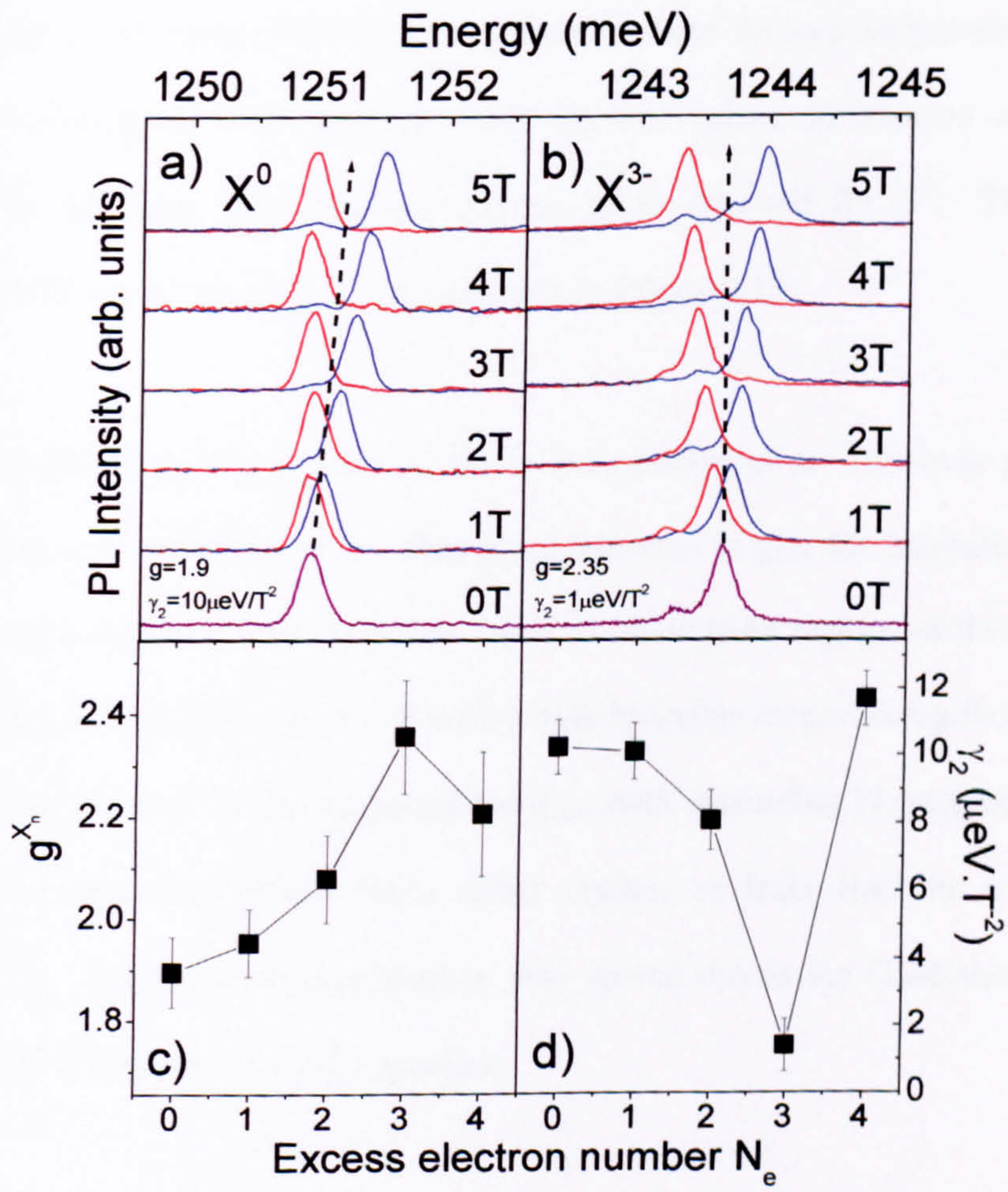

Figure 6.23 a) and b) Magnetic field dependence of the X^0 and X^{3-} emission lines. The two different coloured spectra correspond to detecting differently polarised light. The dependence of c) the g factor and d) the diamagnetic shift on excess electron number.

Figure 6.23 summarises the results of the magneto-optical investigation of the negatively charged exciton states. For X^0 a linear spin splitting and diamagnetic shift characterised by g_{X^0}=1.90±0.1 and $\gamma_2(X^0)$=10.3±0.7μeVT^{-2} are observed (Figure 6.23a, c and d). These values are typical for the presently investigated QDs. The negatively charged exciton exhibits an almost identical g-factor (g_{X^-}=1.93±0.1) reflecting very similar ΔE_{Zeeman} for the exciton and the trion. This similarity is expected. Whilst X^0 has both an electron and hole contribution in the initial state there is no splitting of the final (vacuum) state. For X^- there is only a hole contribution in the initial state as the contribution from the two antiparallel electrons cancel. However the final state (a single electron) gives an electron contribution resulting in the same total Zeeman splitting as is observed for X^0. The Zeeman splitting of X^0 and X^- are shown schematically in Figure 6.22.

Similar arguments predict a g-factor that is independent of n. However g increases from 1.9 for n=0 to 2.3 for n=3. This small increase in g_{Xn^-} for increasing n could result from the excitonic wave function "seeing" richer InAs regions of the QD. Bulk GaAs has an electron g factor of –15 whilst bulk InAs has an electron g factor of –0.4 [9]. Hence the increase in the magnitude of g_{Xn^-} with increasing N_e suggests that the excitonic wavefunction probes GaAs richer regions or leaks into the surrounding GaAs matrix. The exciton wavefunction may spread out as the Coulomb repulsion increases increasing excess carrier number.

In contrast to g, the diamagnetic coefficient, γ_2 is found to be strongly sensitive to N_e, decreasing from 10 to 6±2μeV/T^2 for $X^0 \rightarrow X^{2-}$ then dropping dramatically to ~0 for

X^{3-} before recovering to $12\pm2\mu eV/T^2$ for X^{4-}. The diamagnetic shift of an exciton is given by the formula (§4.11.1)

$$\Delta E_{dia} = \frac{e^2}{8}\left(\frac{\langle r_e^2\rangle}{m_e}+\frac{\langle r_h^2\rangle}{m_h}\right)B^2 \qquad \textbf{Equation 6-4}$$

and is hence dependent upon the spatial extent of the carrier wavefunction in the plane normal to the field direction. This extent is controlled by the combined effects of the lateral confinement potential and the Coulomb interactions between the carriers in the QD[23]. For X^-, a value of $\gamma_2(X^-)=10.1\pm0.7\mu eVT^{-2}$ is determined, identical to $\gamma_2(X^0)$ within experimental errors. This finding indicates that the Coulomb interaction and correlation effects for X^- provide only a modest perturbation of the exciton structure. This is consistent with the exciton binding energy being much larger than $\Delta E(X^0 \rightarrow X^-)\sim5meV$ and the non-interacting nature of the final state. Grundmann et al.[24] calculated the binding energy to be 20meV for a QD with base length 12nm. With further addition of electrons a very pronounced reduction of γ_2 is found (Figure 6.23d). In particular, for X^{3-} the diamagnetic shift practically vanishes ($\gamma_2=1.0\pm0.7\mu eVT^{-2}$, Figure 6.23b and d). Indicating that the diamagnetic shift for both the initial and final states are almost identical. The reason for this coincidence is not clear and a full explanation requires a detailed knowledge of the lateral extent of the multi-carrier wavefunctions.

6.11 Summary

The results of an optical spectroscopic investigation of neutral, negatively and positively charged single and multi-excitonic states in single $In_{0.5}Ga_{0.5}As$ self-assembled quantum dots (QDs) have been presented in this chapter. Both an n-type and a p-type metal-semiconductor Schottky gated structure were studied, allowing sequential charging by electrons and holes respectively. The results obtained reveal important new information regarding the influence of Coulomb interaction and correlation effects on the optical properties of QDs. Magneto-optical measurements reveal additional new information concerning the evolution of the excitonic *g*-factor and diamagnetic shift (γ_2) as electrons are controllably added to the QD.

For n-type devices with negative V_g, the dot is uncharged and recombination from the charge neutral exciton (X^0) is observed (~40μeV FWHM). As V_g is reduced, electrons are sequentially loaded into the dot and the form of the PL emission undergoes a series of pronounced transformations that reflect controlled modifications of the configuration and number of particles in the dot. For charging with a single excess electron, X^0 disappears and is replaced by the negatively charged exciton (X^-), 5.5±0.7meV to lower energy. Comparing the magnitude and sign of the $X^0 \rightarrow X^-$ energy shift with many body calculations indicates that the electron wavefunction is significantly more delocalised laterally in the QD than that of the hole.

For two excess electrons, a clear emission doublet appears (X^{2-}) reflecting the two energetically distinct (singlet and triplet) final two-electron states. However, the

emission for the triply charged state (three excess electrons) consists of only a singlet (X^{3-}). This observation suggests a pronounced departure from Aufbau-like state filling and indicates that the degeneracy of the p-levels is lifted. For four excess electrons (X^{4-}) an emission multiplet due s-p electron exchange reappears, as for X^{2-}. At V_g~-0.3V the emission spectrum suddenly broadens and sharp features are no-longer observable as charging of the underlying wetting layer occurs.

At higher optical excitation levels, neutral and charged bi-exciton recombination is observed. In contrast to X^{n-}, the energy shift between $2X^0$ and $2X^-$ is very weak (-0.8 ± 0.2 meV). This observation, which is reproduced by many body calculations, arises due to the completely filled s-shell for the $2X^0$ initial state, and is a direct optical manifestation of shell filling effects in quantum dots.

Stark shift spectroscopy of the X^{n-} lines reveals rich information regarding the form of the electron-hole wavefunctions. For X^{n-} ($0 \le n \le 3$) the observed Stark effect is weak. However, the Stark shift observed for X^{4-} is significantly larger, possibly reflecting electron occupation of an excited state corresponding to vertical (z) motion. The sign of the dipole moment for the p-type sample reveals that the hole wavefunction is localised above that of the electron, a similar alignment to that reported previously.

Magneto-optical investigations have also been performed in which the excitonic *g*-factor and diamagnetic shift γ_2 for X^{n-} ($0 \le n \le 4$) have been determined. A weak increase of the excitonic *g*-factor from 1.9 to 2.4 is observed as N_e increases from 0 to

4. In contrast, γ_2 is found to be very sensitive to N_e, decreasing from 10 to 8$\mu eV/T^2$ for $X^0 \rightarrow X^{2-}$ before reducing to $\gamma_2 \sim 0$ for X^{3-} and recovering to $12 \pm 2 \mu eV/T^2$ for X^{4-}.

[1] R.J. Warburton, C. S. Dürr, K. Karrai, J. P. Kotthaus, G. Medeiros_Ribeiro and P. M. Petroff, *Phys. Rev. Lett.* **79**,5282 (1997)
[2] K. H. Schmidt, G. Medeiros_Ribeiro and P. M. Petroff., *Phys. Rev. B.*, **58**, 3597 (1998)
[3] A Zrenner, F. Findeis, M. Baier, M. Bichler, G. Abstreiter., *Physica B* **298**, 239, (2001)
[4] F. Findeis, M. Baier, E. Beham, A. Zrenner, G. Abstreiter., *Appl. Phys. Lett* **78**, 2958, (2001)
[5] D. V. Regelman, E. Dekel, D. Gershoni, E. Ehrenfreund, W. V. Schoenfeld and P. M. Petroff, *The Physics of Semiconductors*, proceedings of the 25th International Conference on the Physics of Seminconductors (ICPS25), Osaka, Japan, 2000. Editor N. Miura, Springer Verlag (2001)
[6] E. E.Vdovin, A. Levin, A. Patané, L Eaves, P. C. Main, Yu. N. Khanin,Yu.V. Dubrovskii, M. Henini, G. Hill., *Science* **290**, 122 (2000)
[7] A. Patane, A. Levin, P.C. Main, L. Eaves, E. E. Vdovin, Yu. V. Dubrovskii M. Henini and G. Hill., *Physica* **298** 254 (2001)
[8] H.Drexler, D. Leonard, W. Hansen, J. p. Kotthaus and P. M. Petroff.,. *Phys. Rev. Lett.* **73** 2252 (1994)
[9] Landolt-Börnstein, *Numerical Data and Functional Relationships in Science and Technology,* **22a**, 83
[10] P. A. Maksym. *Unpublished work*
[11] R.J.Warburton, C.Schaflein, D. Haft, F. Bickel, A. Lorke, K. Karrai, J. M. Garcia, W. Schoenfeld, P. M. Petroff. *Nature*, **405**, 296, (2000)
[12] A. Zrenner. *J. Chem. Phys.* **112**, 7790, (2000)
[13] F. Findeis, M. Baier, A. Zrenner, M. Bichler, G. Abstreiter, U. Hohenester, E. Molinari. *Phys. Rev. B* **63**, 121309(R)
[14] T. P. Softley, *Atomic spectra.* - Oxford : Oxford University Press (1994)
[15] L. Chu, A. Zrenner, G. Bohm, G. Abstreiter. *Appl. Phys. Lett* **76**, 1944, (2000)
[16] P.Hawrylak, G A Narvaez, M Bayer, A Forchel. *Phys Rev. Lett.* **85**, 389 (2000)
[17] L. Wang, J Kim, A Zunger. Phys. Rev. B. **59**, 5678 (1999)
[18] L. Landin, M. S. Miller, M. E. Pitol, C. E. Pryor, L. Samuelson, *Science* **280**, 262 (1998)
[19] P. Hawrylak, *Optical Properties of Semiconductor Nanostructures*, Editor M.L. Sadowski. Kluwer Academic Publishers. (2000)
[20] M. Bayer, O. Stern, P. Hawrylak, S. Fafarrd, and A. Forchel, *Nature* **405** 923 (2000)
[21] R. M. Thompson, R. M. Stevenson, A. J. Shields, I. Farrer, C. J. Lobo, D. A. Ritchie, M. L. Leadbeater, and M. Pepper, *Phys. Rev. B*, **64** 201302R (2001)
[22] P.W. Fry, I. E. Itskevich, D. J. Mowbray, M. S. Skolnick, J. J. Finley, J. A. Barker, E. P. O'Reilly, L. R. Wilson, I. A. Larkin, P. A. Maksym, M. Hopkinson, M. Al-Khafaji, J. P. R. David, A. G. Cullis, G. Hill, and J. C. Clark *Phys. Rev. Lett.* **84** 733 (2000)
[23] S. N. Walck and T.L. Reinecke. *Phys. Rev. B* **57**, 9088, (1998)
[24] M. Grundmann, O. Steir and D. Bimberg *Phys. Stat. Sol. (b)* **188** 249 (1995)

Chapter 7

Characterisation of Electrically Pumped In(Ga)As/GaAs Quantum Dot Lasers

7.1 Introduction

Injection lasers with self-organised Quantum Dots (QDs) as the active region offer many potential advantages compared to more conventional lasers including low threshold currents and low temperature sensitivity and large differential gain. Carrier dynamics are also expected to be very different in comparison to the high dimensionality devices.

QD lasers emit light at wavelengths determined by the energy levels of the dots, rather than the band gap energy. Hence there is the potential for QD lasers to allow improved device performance and increased flexibility to adjust the wavelength. In addition QD lasers should possess a material gain (and differential gain) at least 2-3 orders of magnitude higher than quantum-well lasers[1]. The small active volume translates to multiple benefits, such as low power high frequency operation, large modulation bandwidth, small dynamic chirp, small linewidth enhancement factor, and low threshold current.

QD lasers also have a greatly improved threshold current temperature stability than QW lasers and an ideal QD laser, assuming infinite barriers for the carrier confinement, has a threshold current that is independent of temperature. In Arakawa and Sakaki[2] (Figure 7.1) the temperature dependence of the threshold for ideal bulk material, quantum well, wire and dot lasers is compared.

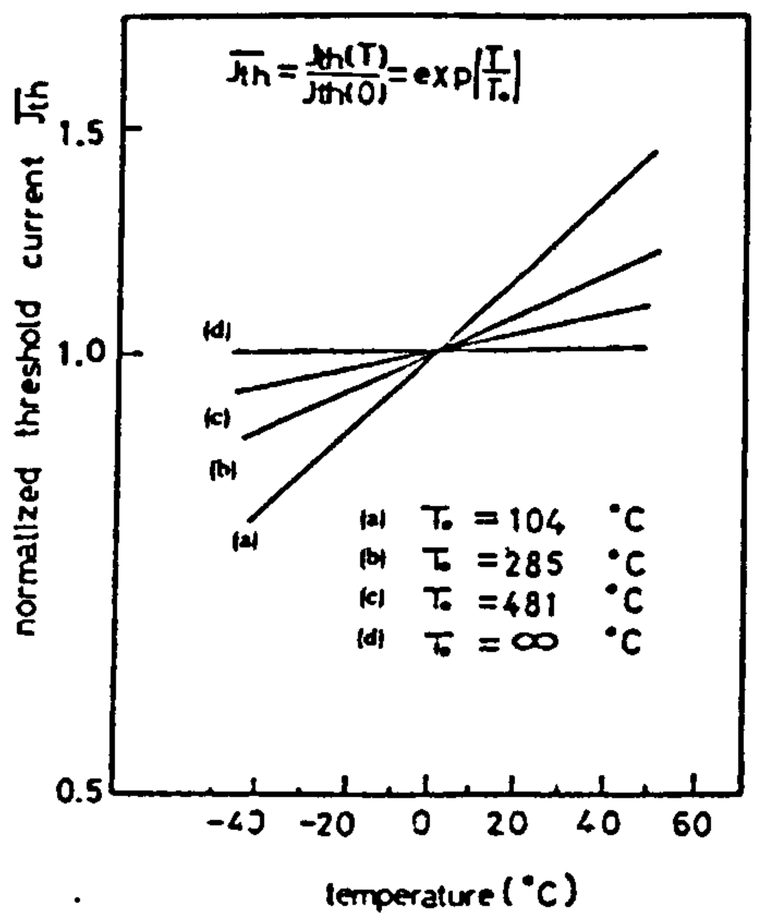

Figure 7.1 Temperature dependence of threshold current for ideal lasers based on bulk, quantum wells, quantum wires, and QDs (From Arakawa and Sakaki[2])

Carrier relaxation may be hindered by the discrete QD energy levels (the phonon bottleneck)[3] and this may limit the maximum modulation speed. In addition carriers within a given QD may be unable to directly interact with carriers in other QDs. This absence of interaction and the inhomogeneous nature of the QD ensemble, a result of size, shape and composition fluctuations, may lead to an inhomogeneously broadened gain spectrum with sub-sets of QDs lasing independently[4]. In this case the system would lack a global Fermi level[5].

In the present chapter the performance of a number of different QD laser device designs are compared. In particular the number of QDs is varied by altering the number of QD layers, the density of QDs in each layer and the device cavity length. The device performance is assessed by determining the threshold current density and its temperature dependence. In addition the form of the sub-threshold and post-threshold emission spectra are studied in detail. Finally spontaneous emission from small holes formed in the top electrical contact is used to probe carrier dynamics within the cavity.

7.1.1 Review of Related and Previously Published Quantum Dot Laser Studies

The first self-assembled QD laser[6] was reported in 1994 by Kirkstaedter et al. Lasing from an InGaAs QD laser at room temperature was demonstrated with a threshold current density of 950A.cm^{-2}. In addition a T_0 (see §7.5.1) of 350K was found at low temperatures (50K-120K) with a minimum threshold current density of 120A.cm^{-2} in this temperature range.

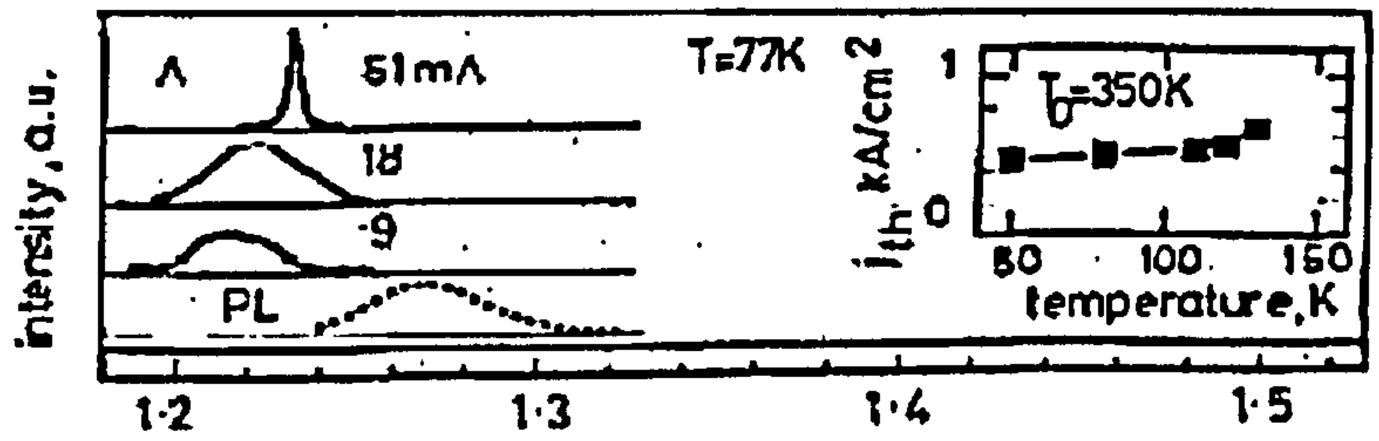

Figure 7.2 Electroluminescence spectra below and above threshold[6] for the first reported QD laser. A: Shows the development of the EL with increasing current at 77K and the inset shows the threshold current density variation with temperature.

The threshold current density was reduced in later research by increasing the number of stacked QD layers[7]. In 1996 the low value of 90A.cm^{-2} was achieved by Ledentsov *et al.*[8]. Further reductions were achieved by decreasing the mirror loss by using high reflection coating of the facets[9]. Presently, threshold currents <10A.cm^{-2} are easily obtained in a variety of structures.

Although most reports of QD lasers have concentrated on device performance there have been a limited number of reports on fundamental properties, including gain. Kirstaeder *et al.*[10] measured the gain of InGaAs/GaAs QD structures by three different means. Firstly, by converting the PL spectra at different excitation densities into material gain spectra, a saturated material gain of close to 10^5cm^{-1} is obtained for a single layer of QDs. This value is more than an order of magnitude larger than that for comparable QW lasers[11]. The second method involved are obtained using the Shaklee[12] 'stripe length method' where single-pass amplified spectra are measured for different excitation lengths from which the modal gain spectra are deduced. Finally the modal gain was determined from the dependence of the threshold gain and differential external quantum efficiency on the cavity length. This method yields values of the modal gain close to those obtained with the stripe length method.

Harris et al.[13,14] employed the Hakki-Paoli[15] technique to determine the gain spectra of a QD laser. With this technique below threshold spontaneous emission spectra are recorded. Such spectra display Fabry-Perot like oscillations as a result of either constructive or destructive interference with the cavity. From the peak-to-valley ratio of

these oscillations it is possible to extract the gain. Figure 7.3 shows the gain as a function of injection current for a 0.5mm cavity device containing five layers of QDs. The curves A, B, C and D correspond to different emission wavelengths. The inset shows the differential gain of the device extracted from the gain measurements.

Fry et al. [16] used a photocurrent technique to determine the peak ground state gain from a single layer of QDs. A typical value of 7±3cm^{-1} was found, comparable to other reports of QD lasers but much less than typical values for a QW laser (50-100cm^{-1})[1]. This low gain value, which is comparable to the internal cavity loss, leads to gain saturation problems which may prevent lasing on the ground state unless the internal loss is minimised or multiple QD layers are used. This problem may be further increased if the QD density is reduced, which may occur for certain growth conditions.

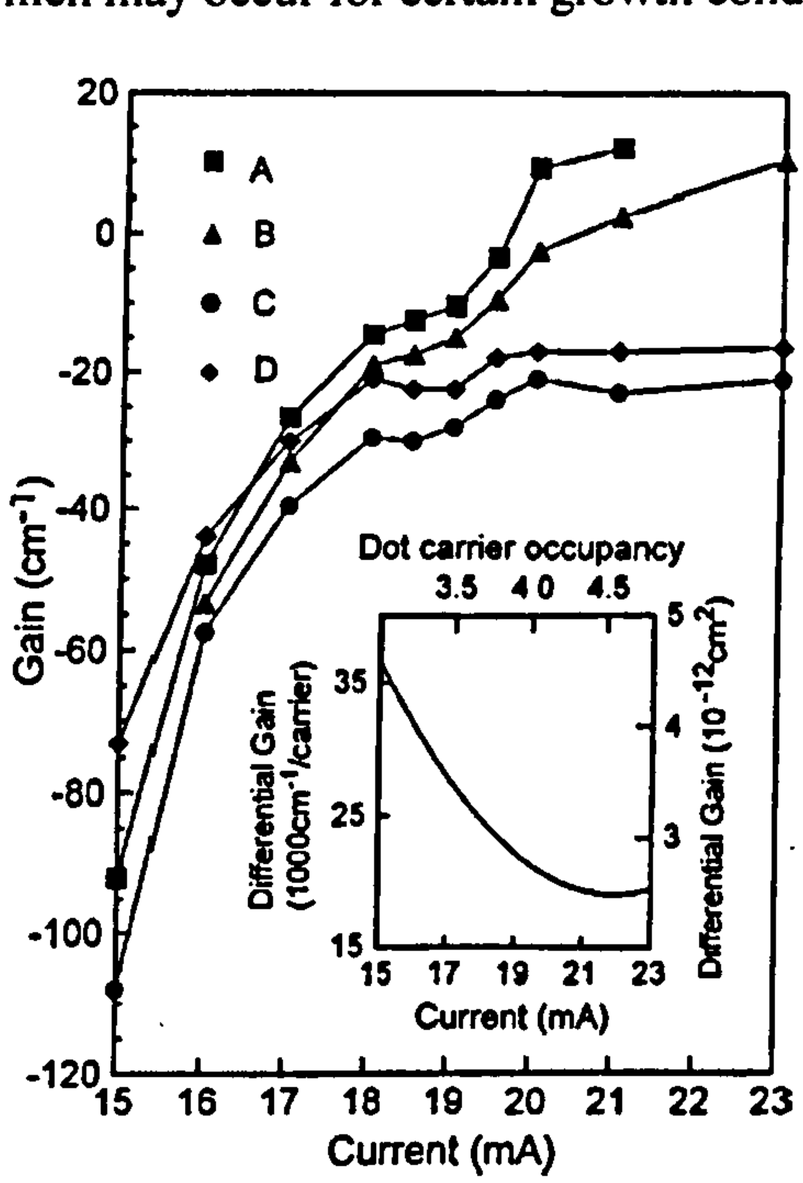

Figure 7.3 Gain variation with current at four wavlengths[14]. The insert shows the dependence of the differential gain on current and QD carrier occupancy.

Hermann et al.[17] measured the gain in a quantum dot laser using a multi-section type stripe laser. They report a similar magnitude gain as Harris et al.[14] and also observe that the modal gain per number of QD layers remains constant for one to seven layers (Figure 7.4).

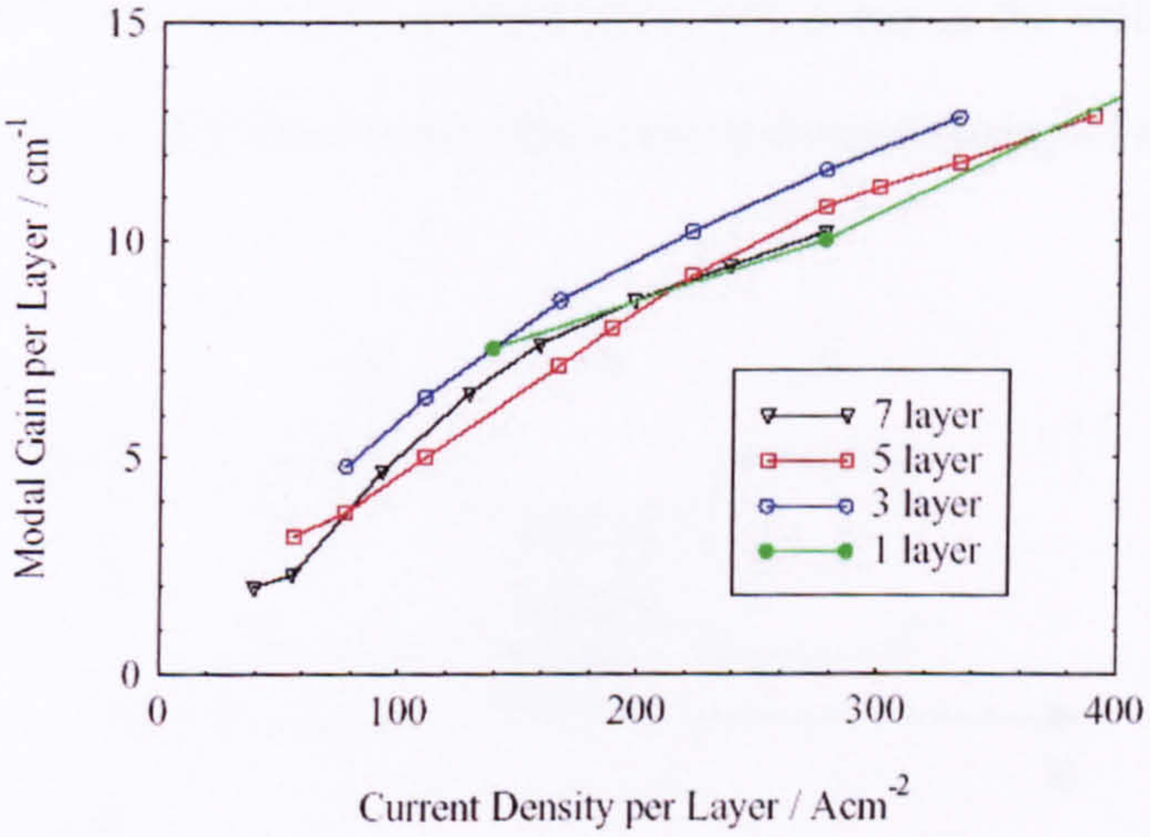

Figure 7.4 Modal Gain dependence on current density per QD layer[17]. T=293K

7.1.2 The Double-Heterostructure Injection Laser

The double-heterostructure (DH) laser was pioneered by Alferov and Kazarinov[18] and provides confinement of both carriers and photons. It forms the basis of all practical injection laser designs. The band-gap of the active region is smaller than that of the surrounding cladding material and hence provides the carrier confinement. Under forward bias electrons are injected from the *n*-type region and holes from the *p*-type region into the active region. The larger refractive index of the active region provides confinement of the photons; the transverse electric field profile is shown in Figure 7.5.

The bandgap of the cladding layers is larger than the photon energy so that photons generated in the active region are not absorbed. In the original DH laser the active region was simply a thin layer of a bulk semiconductor. However it is possible to introduce one or more quantum well, wire or dot layers within a larger band gap semiconductor to form the active region. In this case photon generation will occur in the well, wire or dot and the device performance will benefit from the reduced dimensionality of these structures.

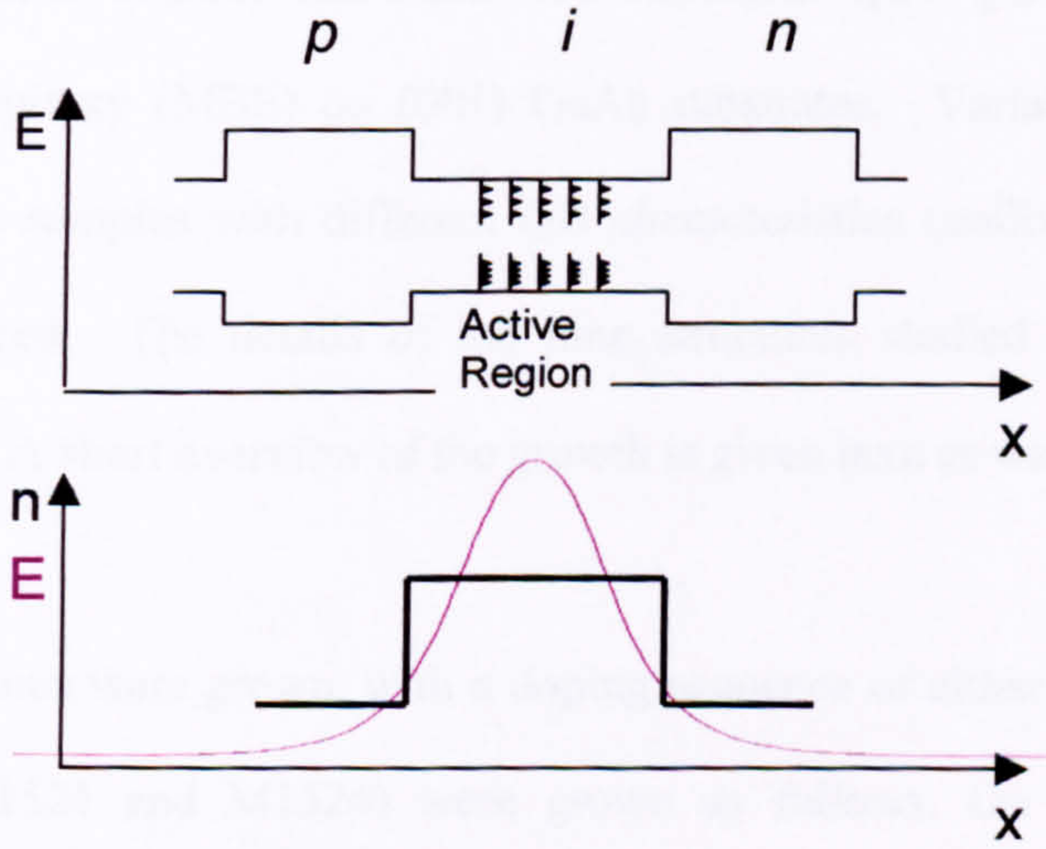

Figure 7.5 Double heterostructure diode laser. A typical quantum dot laser's energy level diagram *(top)* with the conduction and valence band at higher and lower energies respectively. The refractive index, n, profile produces an electric field profile, E, that is contained mainly in the active region.

7.2 Quantum Dot Laser Design

In this section the growth and design of the devices studied in this chapter are discussed.

7.2.1 Growth

All of the structures contain self-assembled In(Ga)As QDs grown by solid-source molecular beam epitaxy (MBE) on (001) GaAs substrates. Variations of the growth conditions enables samples with different QD characteristics (uniformity, density, size, etc.) to be produced. The details of the nine structures studied are outlined in the following section. A short overview of the growth is given here as well.

Two sets of structures were grown, with a doping sequence of either n-i-p or p-i-n. The n-i-p samples (M1521 and M1524) were grown as follows. On an undoped GaAs substrate a 100nm layer of Silicon n-doped ($1x10^{-19}cm^{-3}$) GaAs was deposited followed by a 1500nm layer of Silicon n-doped ($5x10^{-18}cm^{-3}$) $Al_{0.6}Ga_{0.4}As$ which formed the lower waveguide layer. A subsequent 100nm undoped $Al_{0.6}Ga_{0.4}As$ layer was grown to aid the quality of the device by preventing doping migration into the intrinsic active region. The intrinsic region was grown next, consisting of InAs QDs grown in a GaAs matrix. The precise details and number of QD layers is discussed in the following section. The QDs were formed by depositing a 2.4 monolayer thick InAs layer at a temperature of 500°C. The active region was followed by a 100nm layer of undoped $Al_{0.6}Ga_{0.4}As$ and 1500nm of Beryllium p-doped ($2x10^{-18}cm^{-3}$)$Al_{0.6}Ga_{0.4}As$ which formed the upper waveguide.

Finally the structure was terminated with a 100nm Beryllium p-doped ($5x10^{-18}cm^{-3}$) GaAs cap.

All the other samples are of the form p-i-n and were grown as follows. On the n-type GaAs substrate a 300nm layer of Beryllium p-doped ($1x10^{-19}cm^{-3}$) GaAs was deposited followed by a 1000nm layer Beryllium p-doped ($2x10^{-18}cm^{-3}$) $Al_{0.6}Ga_{0.4}As$ layer that formed the lower waveguide layer. A subsequent 70nm (or 90nm for M1807, 09 and 43) $Al_{0.15}Ga_{0.85}As$ layer was grown to aid device quality. The active region was grown next and consisted of InAs or nominally $In_{0.5}Ga_{0.5}As$ QDs grown in a GaAs matrix. The precise details and number of layers is outlined in the following section. The QDs were grown by depositing a 2.4 monolayer thick InAs (1.8 monolayer thick InGaAs) layer at a temperature of 500°C. The intrinsic region was capped with 70nm (or 90nm for M1807, 09 and 43) $Al_{0.15}Ga_{0.85}As$ layer and 1000nm of Silicon n-doped ($2x10^{-18}cm^{-3}$) $Al_{0.6}Ga_{0.4}As$ which formed the upper waveguide. Finally the structure was terminated by a 300nm Silicon n-doped ($2x10^{-18}cm^{-3}$) GaAs cap.

The use of either a p-i-n or n-i-p design was dictated by the availability of substrates and the ordering of the doped regions is not expected to significantly affect the device performance.

7.2.2 Sample Design

Each structure varied in the choice of the number of dot layers, the separation of the layers, the nominal composition of the QDs and the conditions used to grow the QDs. These parameters are discussed in this section.

The two n-i-p samples M1524 and M1521 contain five layers and a single layer of QDs respectively (Figure 7.6). For M1524 the separation between QD layers is 25nm which is sufficiently large to prevent any electronic coupling between QDs in differnet layers[19]. The InAs QDs were grown with a fast growth rate of $0.1MLs^{-1}$ which results in a high QD density of $2\text{-}3x10^{10}cm^{-2}$. M1807 is a repeat of M1521 although with a p-i-n structure.

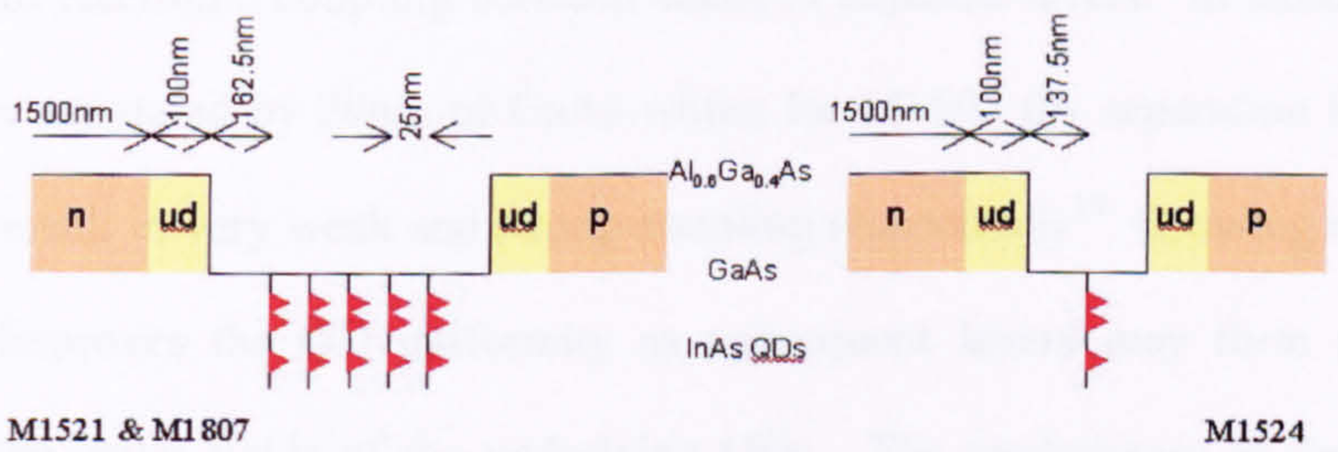

Figure 7.6 Schematic structures of samples M1521, M1524 and M1807.

Structure M1688 contains a single layer of InAs QDs (Figure 7.7) but the QDs are deposited at the low rate of $0.01ML.s^{-1}$. This low growth rate produces QDs of greater uniformity (as evidenced by a relatively narrow PL linewidth of 20meV) which emit at a lower energy than the faster growth rate QDs of samples M1521 and M1524. The greater uniformity should result in higher gain values and the deeper confinement potential

should improve the high temperature device stability by reducing carrier thermal evaporation. However the low growth rate is found to significantly reduce the QD density to 2-3x$10^9$$cm^{-2}$.

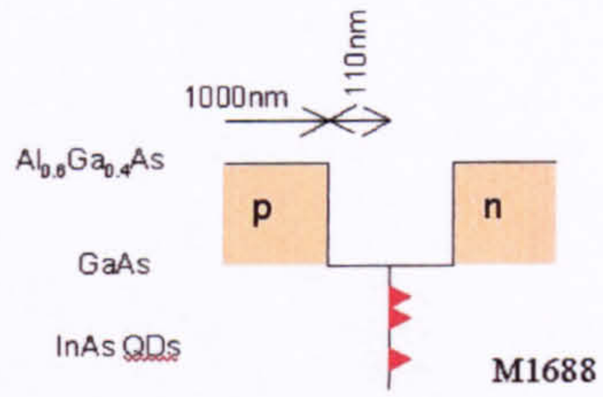

Figure 7.7 Schematic structure of sample M1688.

The QDs in structures M1691-93 are also deposited at a slow rate. Each contains five QD layers but with different separations (Figure 7.8). Structures M1691 and 92 enable a study of the effect of the separation between QD layers. A small QD layer separation should lead to electronic coupling between states in adjacent layers. In structure M1691 the layers are separated by 20nm of GaAs whilst for M1692 the separation is only 5nm. This should result in very weak and strong coupling respectively[19]. Growing multiple QD layers also improves the QD uniformity as subsequent layers may form at positions dictated by the strain fields of the underlying QDs. The randomness of the initial QD growth is hence, to some extent, reduced. The QD layers in structure M1693 are also separated by 5nm but the QD layers and immediate GaAs matrix are embedded in a 30nm $Al_{0.15}Ga_{0.85}As$/GaAs QW which should provide additional carrier confinement.

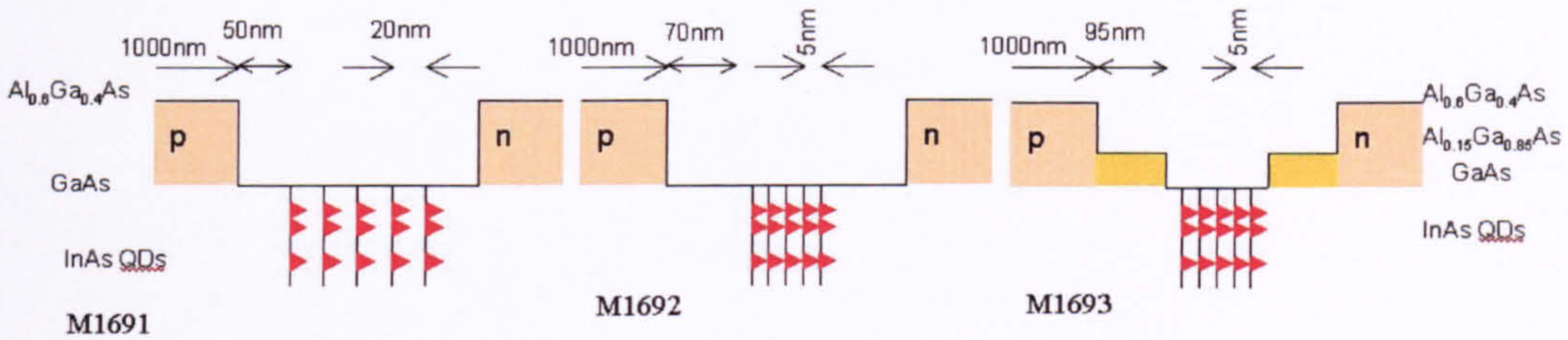

Figure 7.8 Schematic structure of samples M1691, M1692 and M1693

M1809 and M1843 are nominally identical with a single layer of either InAs or $In_{0.5}Ga_{0.5}As$ QDs respectively (Figure 7.9). The QDs in both structures are grown at a rate of $0.1MLs^{-1}$.

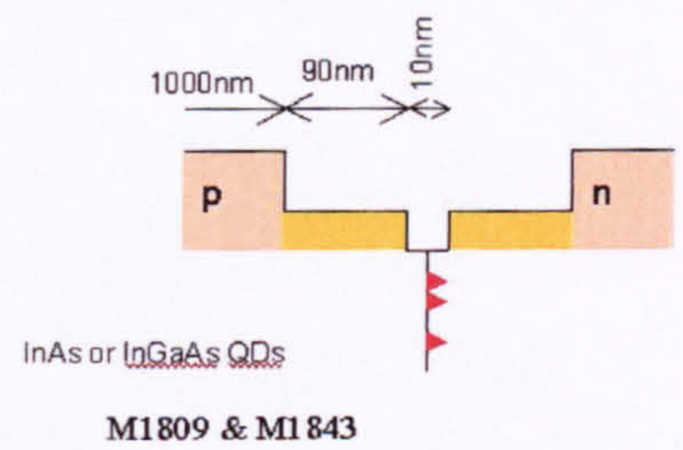

Figure 7.9 Schematic structure of samples M1809 and M1843

7.2.3 Device Fabrication

All the devices studied in this chapter were of the form of ridge waveguide structures. Photolithography is used to define the ridge and subsequent etching creates a ridge to a depth below the active region. The ridge is coated with SiN; the refractive index between the semiconductor of the active region and this SiN layer produces the lateral optical confinement. The mask set used for the photolithography produces five parallel ridges of

widths 5, 8, 10, 15 and 20μm (Figure 7.10). The final step of the process consists of cleaving the ridges into cavities of lengths 0.5 – 2mm and the bonding of the five separate devices on to a T05 header which can be easily mounted in a cryostat. Figure 7.10 shows a series of microscope images of waveguide facets.

Figure 7.10 Microscopic images of typical waveguide facets. Left: 15μm wide ridge. Despite some slight damage on the right hand edge this laser performed well. Middle: The emission from the same ridge. Right: A 20μm wide ridge.

The devices use the semiconductor-air refractive index contrast to produce the cavity mirrors, reflecting sufficient light to allow the gain in the active region to produce lasing. From Fresnel`s equations the reflectivity of the semiconductor-air interface is

$$R = \left(\frac{n_{semi} - n_{air}}{n_{semi} + n_{air}}\right)^2 \approx \left(\frac{3.6 - 1.0}{3.6 + 1.0}\right)^2 \approx 0.32 \quad \textbf{Equation 7-1}$$

Where n_{semi}=3.6 is the appropriate value for the refractive index of the active region. Because the facet reflectivity is relatively low a large gain is required which increases the threshold current density. Coating the facets with a series of dielectric layers to increase their reflectivity will reduce the threshold current density. However this would serve no purpose for the present study, as it would simply introduce another parameter to the laser design which may vary from sample to sample thus affecting the validity of any comparisons. However, in any commercial applications of QD lasers this additional

processing step could be used to reduce the operating current, albeit at the cost of a reduced external efficiency.

The non-amplified spontaneous emission from the QDs was measured in two ways. From actual cavities the emission was recorded via small 5μm holes formed in the top metal contact (§7.6). To eliminate any cavity effects the spontaneous emission was also recorded from circular mesas with anular top metal contacts, formed from the same wafers as the actual laser devices. These mesas had a diameter of 400μm.

7.3 Experimental Apparatus

The basic apparatus has been described in Chapter 2 and uses a double grating 0.85m spectrometer and a liquid cooled Germanium p-i-n photodiode. The devices were mounted in a He continuous flow cryostat which allowed their temperatures to be varied from 4-300K. The L-I characteristics described below are taken with a pulsed current source operated with a 1% duty cycle and 1ms pulse width. The spectra presented below where obtained using a CW current source

7.4 Basic characterisation

7.4.1 Threshold Current Density

InGaAs-GaAs QW lasers have threshold current densities[20] of the order of 50Acm^{-2} at room temperature. The best QD lasers already have threshold current densities[21] of 10Acm^{-2} at 77K and 100Acm^{-2} at room temperature. Groom et al have reported a current density of 47Acm^{-2} [22]. The best values achieved in the present work is for sample M1807 with values of 10.7A.cm^{-2} and 35.7A.cm^{-2} at 160K and room temperature respectively (Figure 7.11). The best threshold current density for a single layer device was 32.1Acm^{-2} at 100K for M1521.

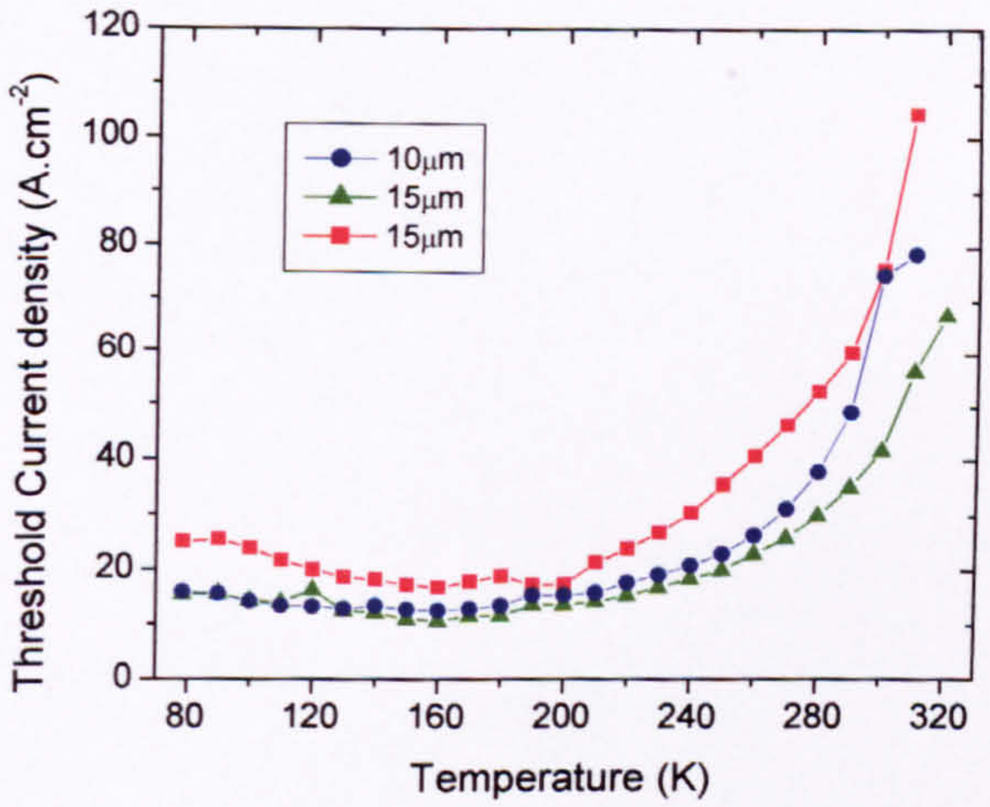

Figure 7.11 The threshold current density temperature dependence for device M1807. This device achieved the lowest threshold currents at both low and high temperatures of all the devices investigated. This is attributed to the high QD density and multiple layer structure which results in ground state lasing. Data is shown for three different cavity widths and a cavity length of 1mm.

The electrical quality of the devices can be determined by measuring the current-voltage (I-V) characteristic, which should correpsond to that of a normal diode. Any deviation will indicate problems with the growth or fabriaction. Carrier leakage, which appears as a deviation in the forward bias characteristics or a low reverse breakdown voltage may degrade the device performance if only a fraction of the injected carriers reach the active region. The characteristics shown in Figure 7.12 for structure M1807 show some leakage before forward bias turn on is reached. This current does not appear to produce an increase in the emitted light and hence represents wasted current. The reverse bias current is extremely low, showing good diode properties in this regime.

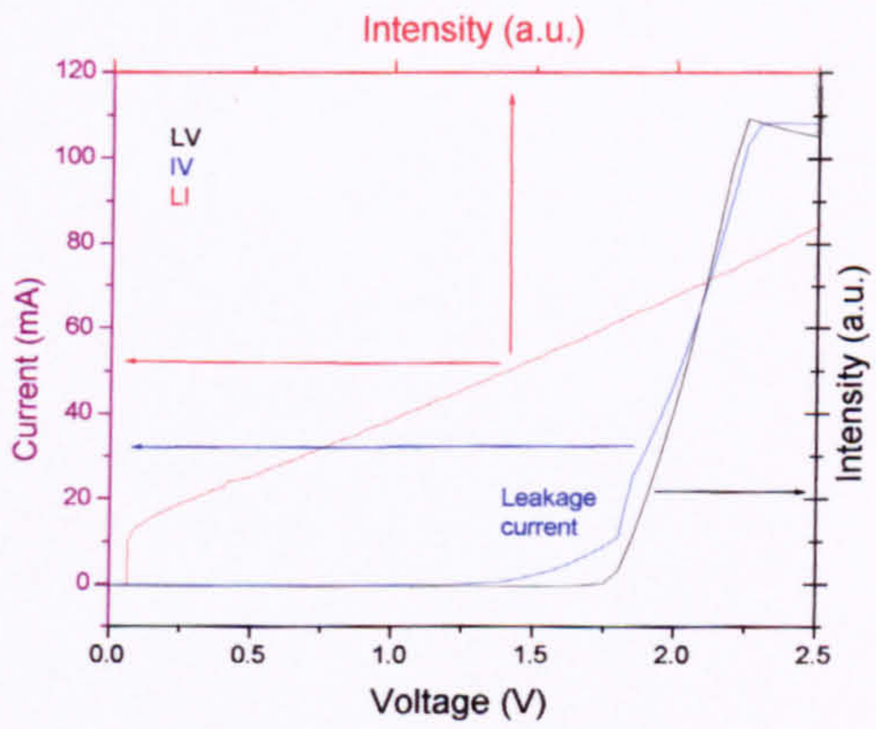

Figure 7.12 LV, IV and LI characteristics at 77K for structure M1807. This device exhibits a small leakage current.

7.4.2 Injection Current Dependence of the Emission Spectra

The spontaneous emission develops dramatically with increasing current. As more carriers are loaded into the QDs the emission becomes more intense and emission from the excited states may be observed. At low current the full-width-half-maximum

(FWHM) of the emission reflects the distribution of QD size, shape and composition in the ensemble and hence provides a measure of the QD uniformity. Figure 7.13 shows the evolution of the spectra from a mesa device, where cavity effects are removed, and in a laser device made from the same material. At low currents the average QD population is low and we see the emission is determined by the radiative recombination from the ground state (gs) transition.

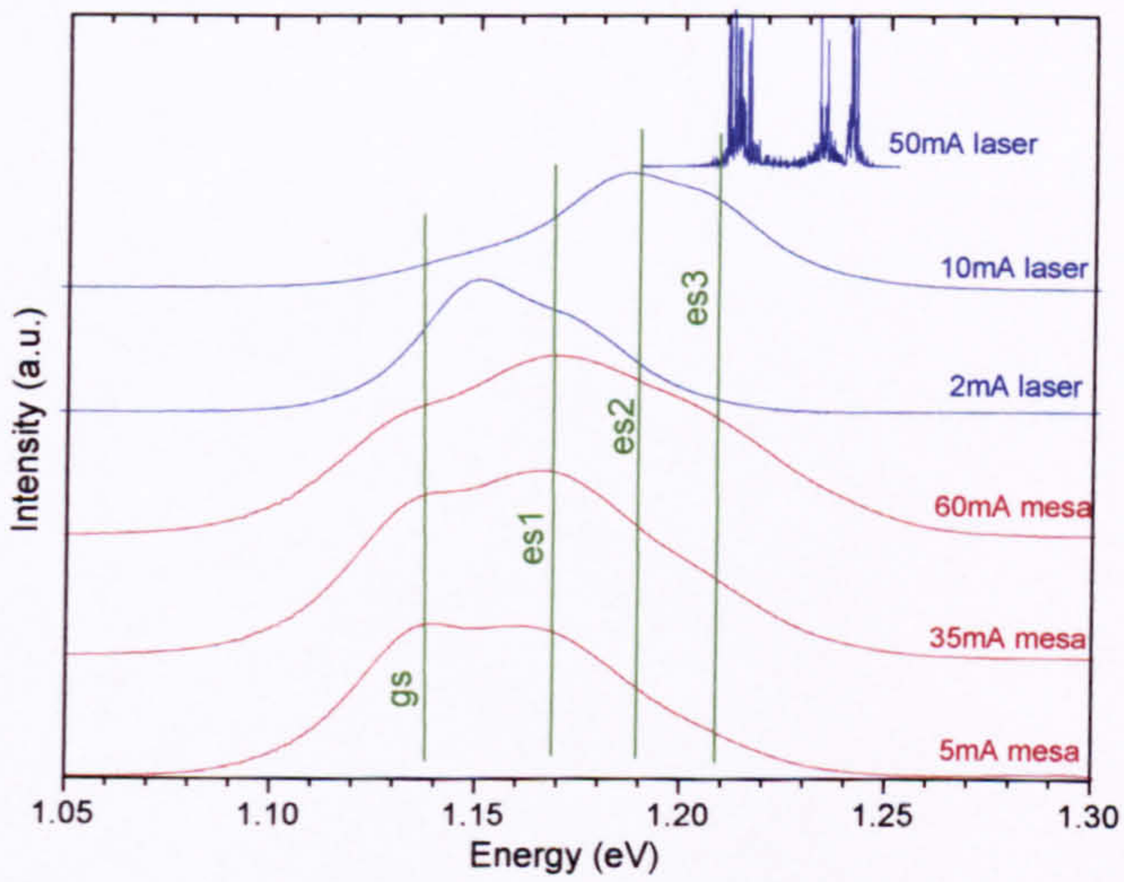

Figure 7.13 Electrical injection emission spectra for sample M1692. Shown are mesa spectra (red), spontaneous lasing spectra (blue) and stimulated laser emission (blue). The vertical green lines indicate the peak positions of the different transitions. The sample temperature is 80K.

Loading more carriers into the QDs by raising the injection current increases the intensity of the emission as seen in Figure 7.14 and Figure 7.15. The emission FWHM increases, probably reflecting the effect of emission from an excited state. Eventually a new emission peak appears that corresponds to radiative recombination from an excited state transition (es1). At even higher carrier occupation (high I) further peaks develop indicating transitions from higher electronic states (es2 and es3). Three excited state

transitions in addition to the ground state are easily identified in the present devices. For M1692 the energy separation between gs and es1, es1 and es2 and e2 and es3 is 31, 21 and 19meV respectively. For M1693 the separations are 30, 26 and 23meV respectively. These separations are significantly less than 3kT at room temperature (≡75meV). 3kT is a rule of thumb value for opto-electronic devices such that excited state populations are small compared to that of the ground state. This suggests that even in the absence of any additional carrier loss mechanisms the present devices will show significant thermal sensitivity at room temperature.

Eventually the gain in the cavity becomes large enough to support lasing. This may occur via the ground state if it has sufficient gain to overcome the cavity and mirror losses. Alternatively lasing may occur via one of the excited state transitions which appear to have a higher maximum gain than the ground state, most probably as a result of a larger degeneracy. For example, the device in Figure 7.14 lases via the second excited state transition, with possibly some contribution from a higher energy transition. The onset of lasing is also seen clearly in Figure 7.15 where a rapid narrowing of the emission occurs.

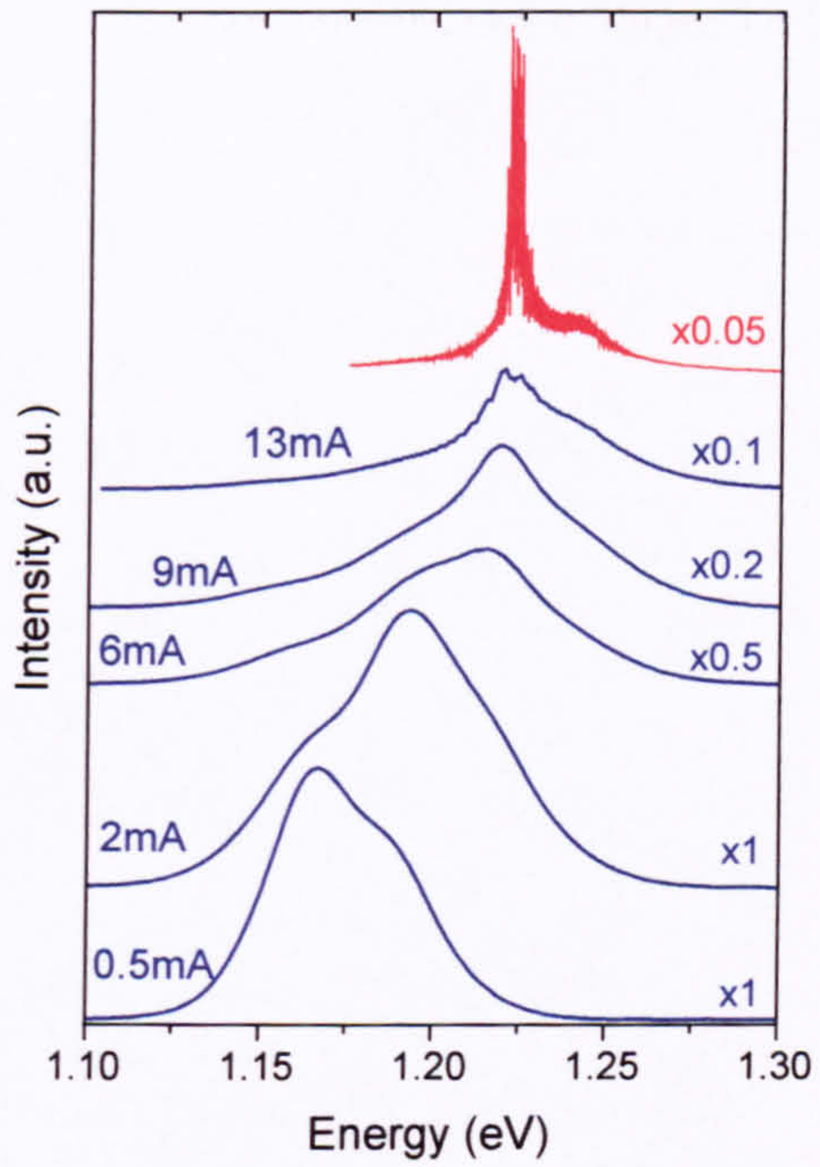

Figure 7.14 Emission spectra as a function of current for sample M1693, a coupled layer sample in which the dots are grown inside a QW. The lasing emission is shown in red, the spontaneous emission in blue. Spectra are shown for a 15μm x 1mm cavity at a temperature of 80K.

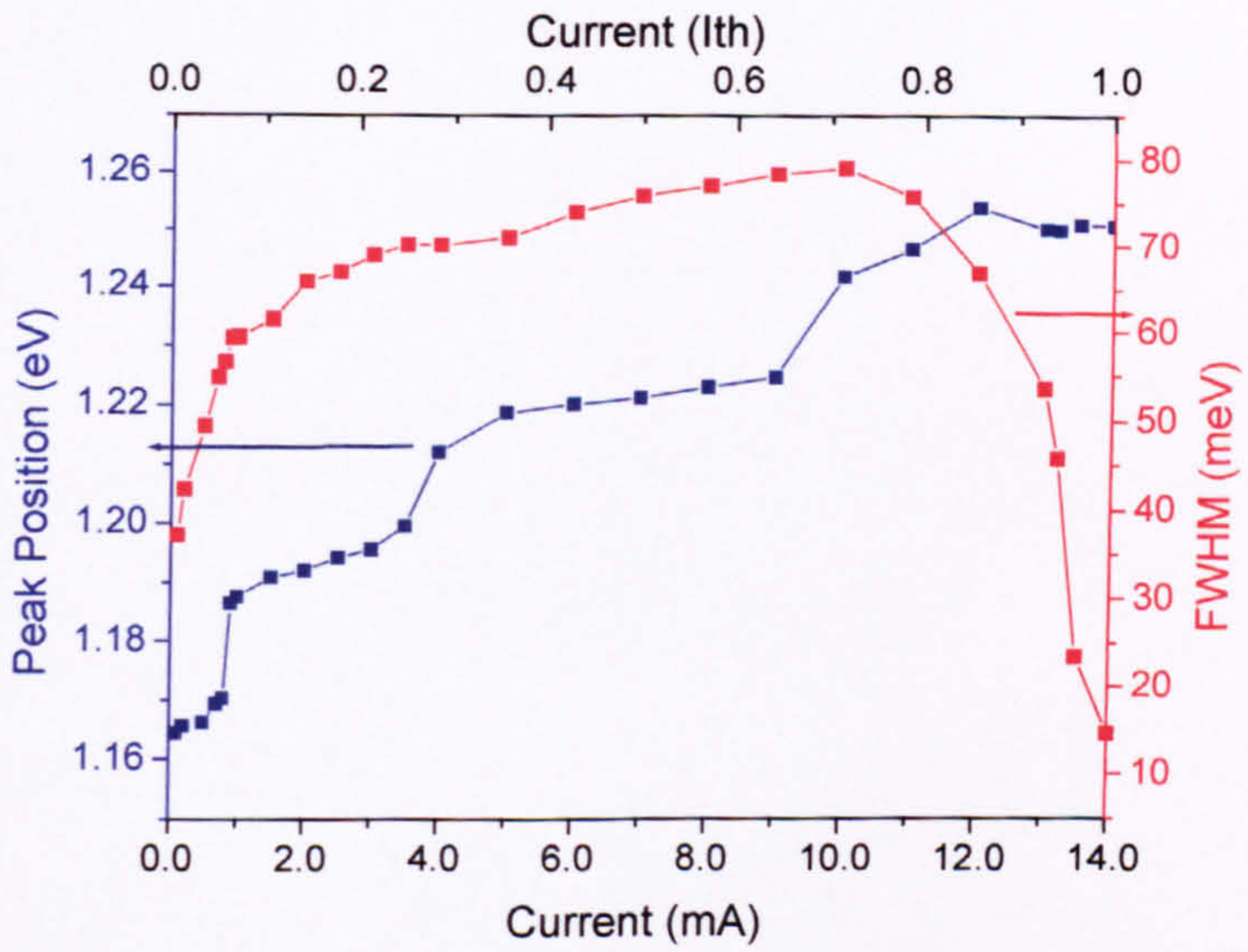

Figure 7.15 Energy of the intensity maximum and linewidth for structure M1693 as a function of current. The different QD transitions are clearly visible in the behaviour of the intensity maximum. Lasing eventually occurs on the second excited state transition with possibly some contribution from a third transition. The sample is a 15μm x 1mm cavity at a temperature of 80K.

Figure 7.16 shows a high resolution spectrum of a lasing device. The emission exhibits a spectral modulation on a number of different scales. On the small scale (~0.3meV) the spectral modulation results from the Fabrey-Perot modes of the cavity. The longitudinal mode spacing is given by the equation

$$d\upsilon = \frac{c}{2nL} \qquad \textbf{Equation 7-2}$$

where dυ is the spacing in Hz, n is the effective refractive index of the active region and L is the cavity length. From this equation the wavelength mode spacing dλ can be obtained

$$d\lambda = \frac{\lambda^2}{2nL} \qquad \textbf{Equation 7-3}$$

where λ is the emission wavelength. For a 1mm long cavity this gives a theoretical mode separation of 0.134nm at 980nm. This compares well with a measured mode spacing of 0.119nm (Figure 7.16)

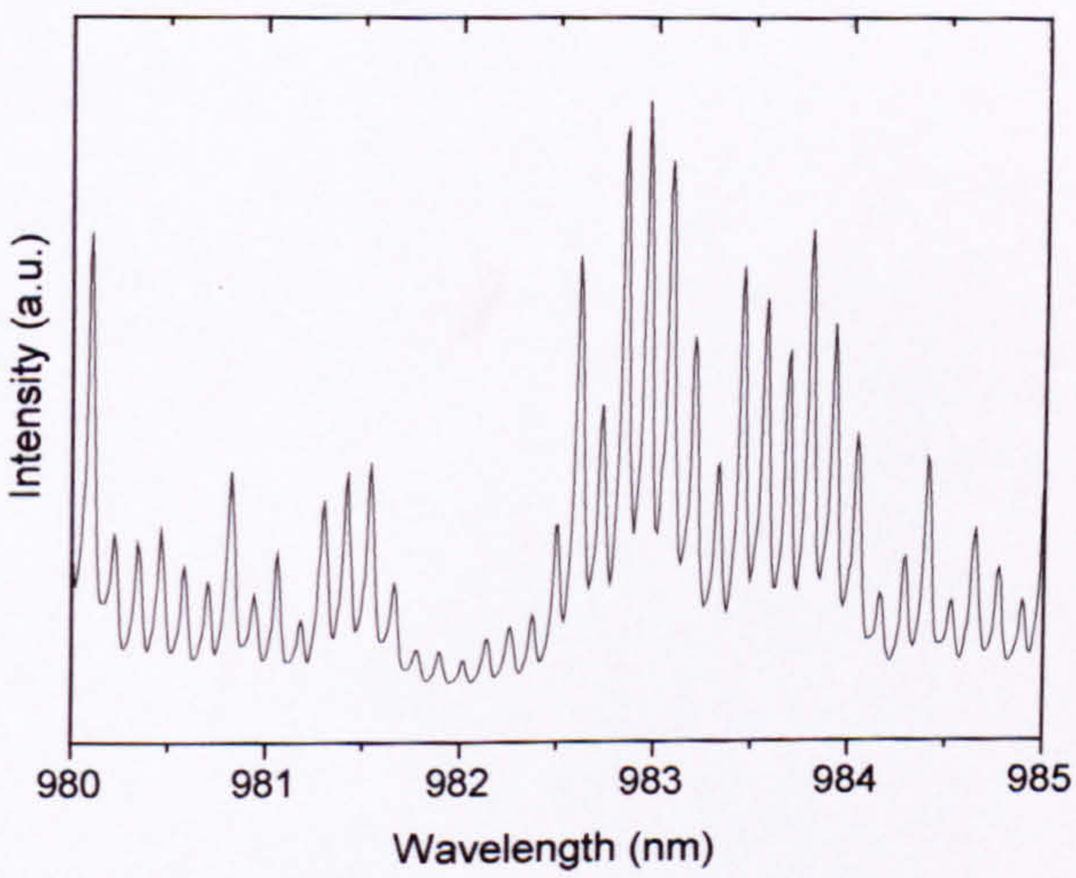

Figure 7.16 Fabry-Perot modes in a 1mm cavity. There are 42 modes visible in this spectrum.

In addition to the rapid modulation of the emission due to the cavity modes, there is a slower modulation which gives groups of cavity modes separated by non-lasing spectral regions. This behaviour is more clearly seen in the lasing spectra of Figure 7.13. This modulation, which occurs on a scale ~1-2meV, shows no systematic dependence on the structure of the active region or the cavity dimensions. It is however absent in a device identical to M1521 except that the layer of dots is replaced by a single 8nm $In_{0.26}Ga_{0.74}As$ QW (Figure 7.17). This observation indicates that the observed modulation of the lasing spectra is an intrinsic property of the QDs not the cavity[13].

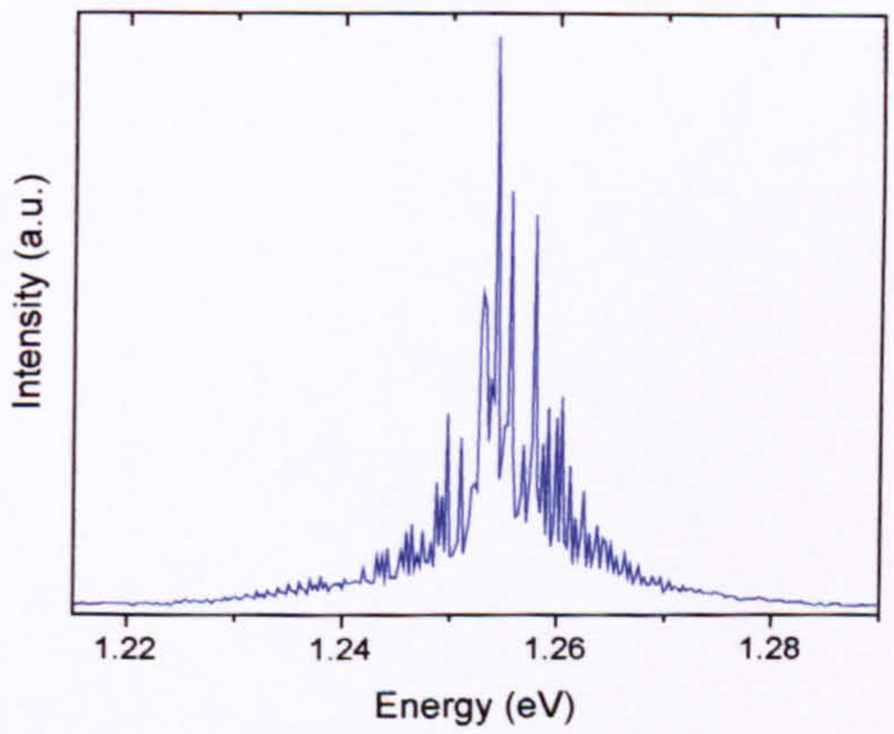

Figure 7.17 QW lasing spectrum. The Fabry-Perot modes appear under an envelope function.

A number of mechanisms have been suggested to account for this behaviour[14,16] but the most likely explanation is that of O'Reilly et al[23]. Here it is suggested that some of the confined optical mode leaks out of the active region through the finite thick lower cladding layer. Within the substrate a periodic interference occurs as this leaking mode is reflected by the air-substrate interface. The leaking mode subsequently couples back into the cavity and results in a periodic modulation of the gain and the observed spectral

modulation. However the observation of this effect requires lasing to occur over a broad spectral range, explaining why it is observed in a QD laser but never a QW laser. Confirmation of this explanation has been provided by Smowton et al[24] who studied devices with the substrate thinned to different thicknesses. A correlation was observed between the substrate thickness and the period of the modulation. However Harris et al[25] were able to directly determine the amplitude of the gain modulation using the Hakki-Paoli technique. They found that the measured modulation depth was many orders of magnitude greater than that predicted by the model of O'Reilly et al casting some doubt on this explanation.

Generally the number of lasing groups and hence total number of lasing modes increases with increasing current for a QD laser (Figure 7.18). This behaviour is very different to that observed for more conventional lasers. In bulk or QW lasers a dominant mode develops from the relatively large envelope of similar intensity modes present at threshold[26]. The number of apparent lasing modes therefore decreases as the injected current is increased above threshold. These conventional lasers have a smoothly varying, homogeneously broadened gain spectrum and the dominant mode develops at the maximum of this spectrum where the gain most closely approaches the cavity losses (although the absolute gain can never exceed the cavity losses). The homogeneously broadened gain spectrum retains the same shape and is 'clamped' once its peak reaches the threshold value. A QD laser can have the contrasting behaviour observed here if the gain spectrum is inhomogeneously broadened. This can occur when carriers in different QDs cannot interact. The initial lasing mode occurs for the subset of QDs whose number

and average population first results in a gain sufficient to overcome the cavity losses. At this point the population of these finite number of QDs, and the corresponding gain, saturates. However QDs that emit at different energies can continue to increase their population until it is sufficient to provide a gain that can overcome the device losses. These QDs will then start to lase. The number of lasing modes therefore increases with current, reflecting an increase in the number of subsets of QDs having a sufficient population to achieve the required threshold gain. This increase continues until all subsets of QDs with a high enough maximum gain achieve the required population. This behaviour is critically dependent on the absence of a global Fermi level (a consequence of an inhomogeneously broadened gain spectrum) which allows a continued gain increase at non-lasing energies even when lasing has occurred elsewhere.

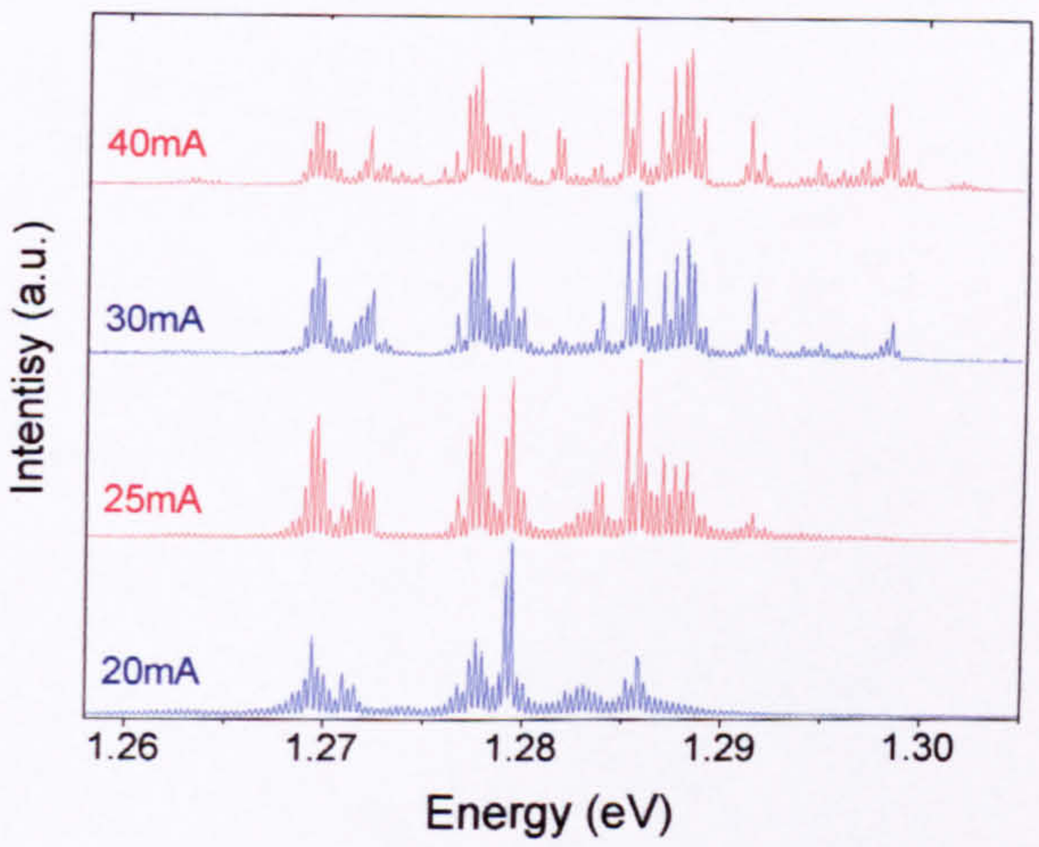

Figure 7.18 The development of the lasing spectra with current for structure M1521. The threshold current is 15mA and the device temperature is 80K.

A particularly interesting case is discussed here for structure M1693 where the lasing switches from es2 to es3. This effect is not due to device heating as this occurred over a

large range of temperatures (80-130K). The reason for this behaviour is, however, not fully clear. As the average occupation of the QDs is increased the higher degeneracy of es3 could result in a much greater gain for this transition and it will become the preferred lasing transition. In a non-interacting system it would be expected that additional lasing features would appear at higher currents, as discussed above, but this should not be at the expense of other modes. Once a subset of QDs starts to lase on es2 the carrier occupation of these QDs should clamp, preventing a further increase in occupation and hence lasing on a higher transition. Only QDs, which have not yet reached lasing, can continue to increase their carrier occupation. A possible explanation for the observed behaviour is that for the peak of the QD distribution there is sufficient QD numbers and hence gain for lasing via es2 to occur. Other subsets of QDs do not have a sufficient density to reach lasing via es2 but must increase their occupancy until the population of the es3 related states is sufficient for lasing to occur. At this point these newly lasing QDs appear to preferentially capture the injected carriers causing the QDs which lase via es2 to 'switch off'. The reason why preferential capture occurs is unclear but may simply reflect unequal capture rate of carriers from the reservoir surrounding the QDs and the different QD states.

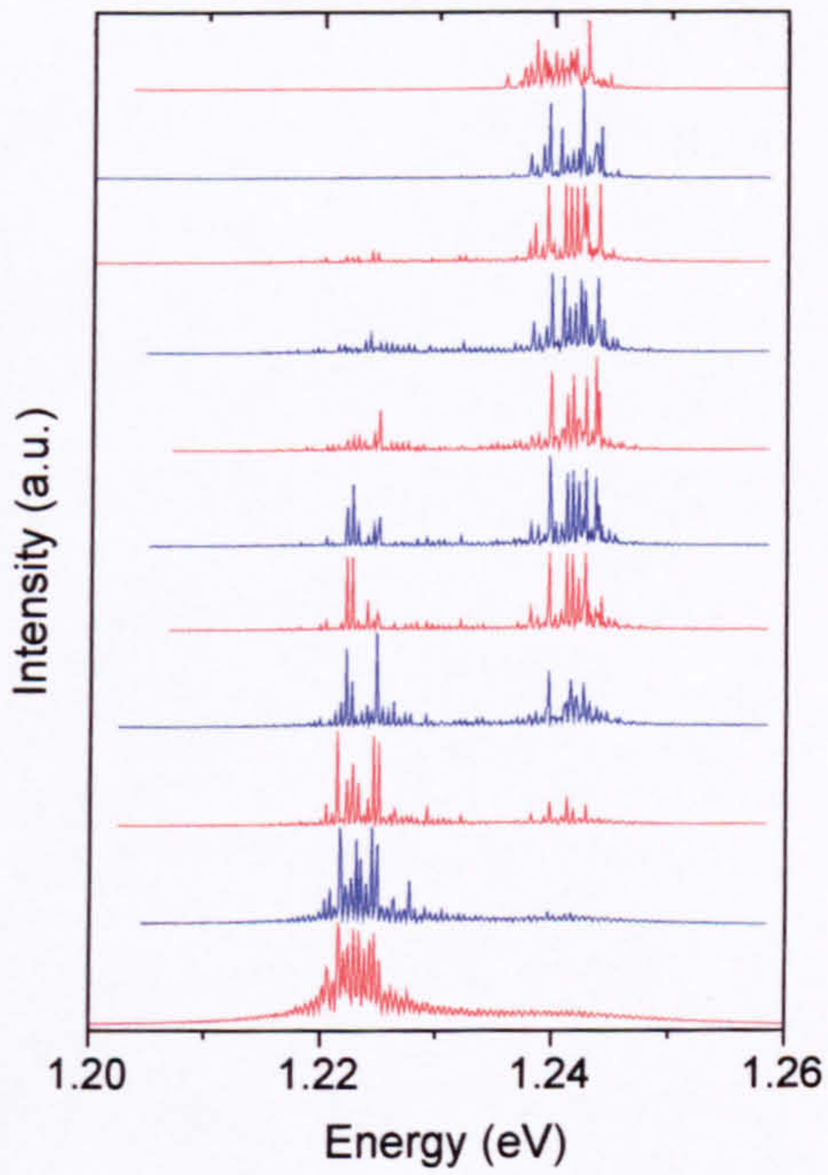

Figure 7.19 M1693 laser emission spectra. The development of a QD lasing spectrum where the lasing shifts from the 2nd to 3rd excited state.

7.4.3 Mode Intensity Fluctuations

As can be seen in Figure 7.16 adjacent longitudinal modes may vary quite dramatically in intensity. This behaviour is attributed to the relatively small number of QDs associated with each mode and the consequent large fluctuation of this number. For a 80meV FWHM Gaussian distribution for the QD emission (see Chapter 1.6 PL) and a QD density of $5x10^{10}cm^{-2}$ the number of QDs within the spectral width of each longitudinal mode is less than 5000 for a cavity of dimensions of 1mm x 20μm. This corresponds to a statistical $\sqrt{N}/N$ fluctuation of 1.5%. Although this is only a relatively small fluctuation small changes in the gain can have a disproportionate effect on the mode intensity in

common with any oscillator system[27]. The value 5000 for the number of QDs per mode is likely to reflect a lower limit if the homogeneous linewdith is greater than the longitudinal mode spacing, allowing QDs emitting at different spectral positions to contribute to a given mode. It is likely that the homogeneous linewidth will be relatively large in highly occupied QDs. The Fabry-Perot mode spacing shown in Figure 7.16 corresponds to an energy spacing of 172μeV, which is likely to be smaller than the homogeneous linewidth of a single QDs at 80K containing many carriers (see Chapter 4.8).

7.4.4 Temperature dependence of the lasing spectra

Generally the energy of the lasing emission follows the dependence of the bulk semiconductor bandgap with temperature. However a shift to higher energy may occur due to the thermal evaporation of the carriers and gain saturation[7] which may cause lasing to shift to a higher order transition. In Figure 7.21 the lasing energies of a typical laser device are plotted as a function of temperature from 4 to 250K. The temperature dependence is adequately described by the variation of the band gap of bulk GaAs given by the following expression[28]

$$E_g(eV) = 1.519 - 5.408\times10^{-4}\frac{T^2}{T+204} \qquad \textbf{Equation 7-4}$$

but shifted rigidly in energy to account for the smaller band gap of the QDs. The width of the lasing region at low temperature makes a detailed comparison with the theoretical curve difficult. The form of the lasing spectra changes dramatically with temperature

(Figure 7.20). With increasing temperature the number of lasing modes, and hence the spectral width of the lasing reign, decreases. This is caused by an increase in the carrier communication between dots. The increased thermal energy of the system allows carrier transport to occur between QDs in the ensemble via the wetting layer. Carriers can thermally escape a given QD and are subsequently recaptured by a different one[29]. In this case the system can develop a global Fermi level and in this respect act like a higher dimensionality system with a homogeneously broadened gain spectrum and a corresponding small number of lasing modes.

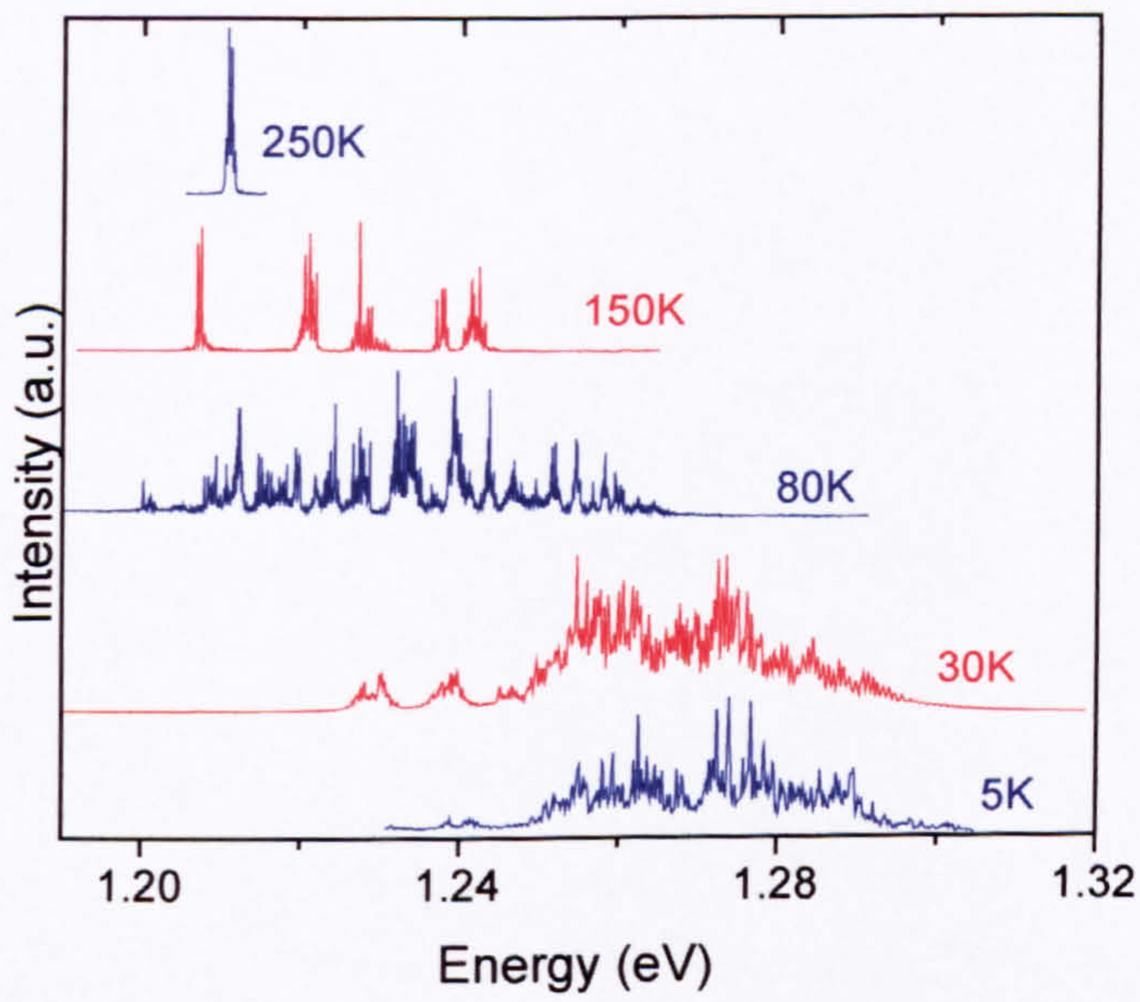

Figure 7.20 Temperature dependence of the lasing emission spectrum for sample M1521 with cavity size 1mm x 15μm. Each spectra is taken at twice threshold.

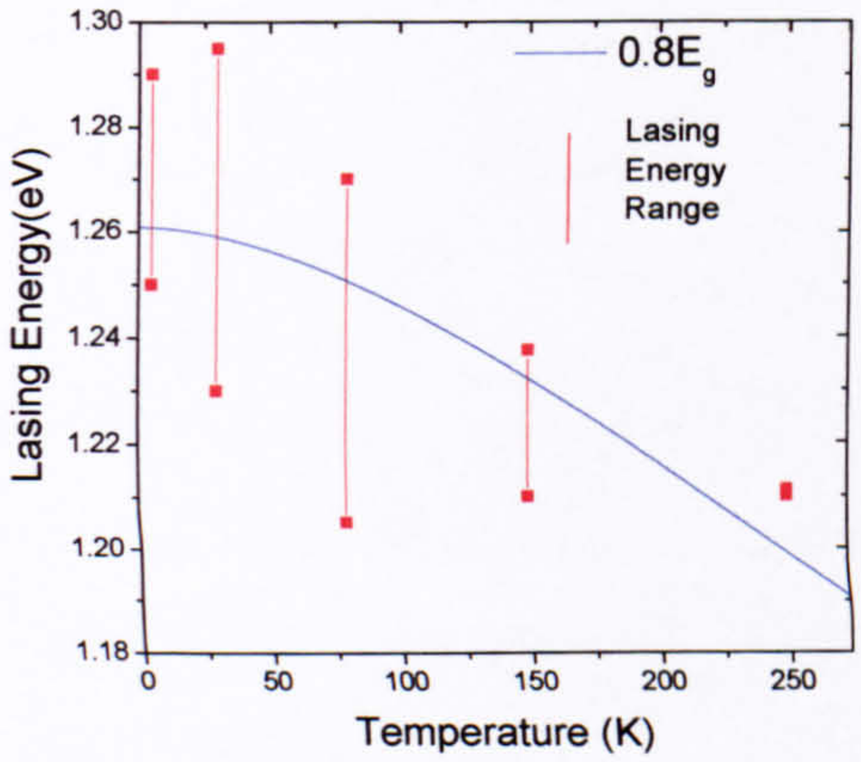

Figure 7.21 The range of lasing energies for sample M1521, plotted as a function of temperature, for the spectra shown in Figure 7.20. The solid blue line shows the bandgap variation of bulk GaAs rigidly shifted to account for the smaller QD bandgap.

7.5 Comparative Study of Different Active Region Designs

In this section the performance of different active region designs will be compared, in general by considering the temperature performance in terms of the variation of the threshold current density. Other results, such as the emission spectra will be presented where relevant.

7.5.1 Temperature Performance

It is found experimentally that the temperature dependence of the threshold current density of a semiconductor laser is described by an expression of the form

$$J(T) = J(0)e^{T/T_0} \qquad \textbf{Equation 7-5}$$

where T_0 is the characteristic temperature. A large T_0 indicates a lower degree of temperature sensitivity. The first demonstration that reducing the dimensionality of a system can increase T_0 was by Arakawa and Sakaki in 1982 who placed a QW laser in a magnetic field[2]. The additional quantisation produced by the field reduced the dimensionality from two to zero and increased T_0 from 144 to 313K. The threshold current density of a QD laser should be independent of temperature provided that the energy level spacings are >>kT. However in real QD lasers T_0 may be less than infinity when the energy level spacings are comparable to kT or if carrier loss occurs to non-radiative centres either internal or external to the QDs. The best room temperature T_0 for the QDs studied in the present work was 130K for M1807.

The data presented in Figure 7.11 shows an approximately constant J_{th} between 4 and ~240K, the behaviour expected for an ideal QD system. However above ~240K J_{th} increase relatively rapidly with temperature as carriers are thermally excited out of the lasing states to higher energy QD levels, the WL or GaAs or non-radiative states. The thermal escape of carriers from QDs has been observed directly in photocurrent measurements for temperatures above ~200K [30].

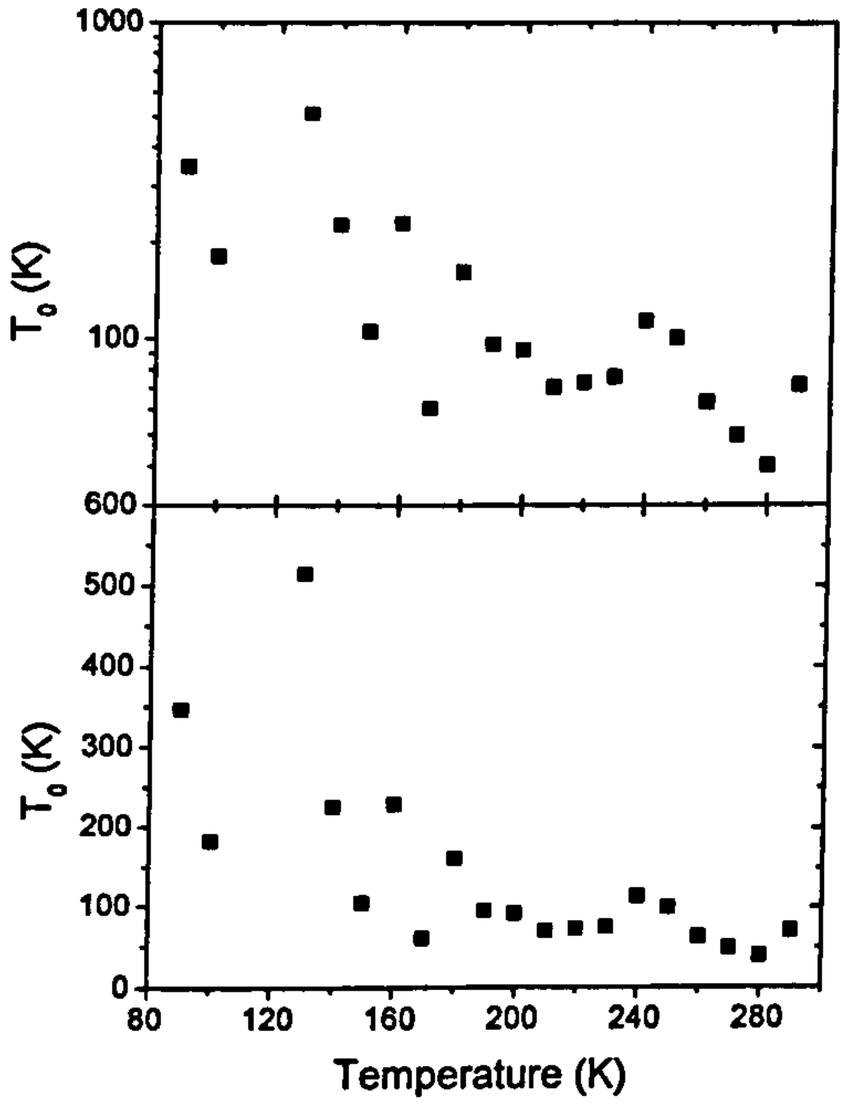

Figure 7.22 Typical variation of T_0 with temperature. Top: semi-log plot. Bottom: linear-linear plot of the same data.

Figure 7.22 shows average values of T_0 from five cavities of the structure M1807, a five layer sample of InAs QDs. The devices studied where all 2mm in length. The high values of T_0 obtained at low temperature (≤100K) fall rapidly at higher temperatures as thermal carrier escape from the QDs becomes important. No T_0 values are given for T≤80K because in this regime the threshold current decreases with temperature resulting in a negative value for T_0 (the so-called negative T_0 regime). A negative characteristic temperature in the low temperature (<130K) regime was first reported by Zhukov *et al.*[31]. This has been attributed to the transition of a nonthermal into a thermal carrier distribution with increasing temperature[4] and is discussed with reference to the PL emission in Chapter 1.

7.5.2 Cavity Length Dependence

The performance of a semiconductor laser depends critically on the cavity length, L. At threshold the modal gain $g_{mod}(J_{th})$ must equal the sum of the internal cavity loss, α_i and the end mirror loss $\frac{1}{L}\ln\left(\frac{1}{R}\right)$ where R is the reflectivity of the mirrors which are considered to be identical. Hence

$$g_{\mathrm{mod}}(J_{th}) = \alpha_i + \frac{1}{L}\ln\left(\frac{1}{R}\right) \qquad \textbf{Equation 7-6}$$

As L increases the mirror loss term decreases and the gain required for lasing (and hence also J_{th}) decreases. In the limit $L\rightarrow\infty$ $g_{mod}(J_{th}) \rightarrow\alpha_i$ and this gives the transparency condition, the point where a beam of photons propagating along the cavity is neither amplified or attenuated. For a QW laser, g_{mod}, to a good approximation may be assumed to be proportional to J_{th} ($g_{mod}=aJ_{th}$, where a is a constant). Hence a plot of J_{th} vs $1/L$ should give a straight line with an intercept equal to the transparency current density J_{trans}.

Measurement of the threshold current against 1/L is presented in Figure 7.23. This provides a transparency current density of 185A.cm^{-2} and 320A.cm^{-2} for the five layer and single layer sample respectively. The linear relationship between J_{th} and $1/L$ may break down for a QD laser at short cavity lengths, as for a given transition (gain saturation) the gain may not be sufficient to overcome the losses so the emission shifts to a higher transition where higher gain is available. This results in a higher J_{th} as more QD states have to be filled before a population inversion is achieved. This behaviour is

clearly seen for structure M1807 in Figure 7.23 and also possibly, to a lesser extent, for structure M1809. Gain saturation is a significant problem in single layer devices where the total number of QDs is relatively small[5].

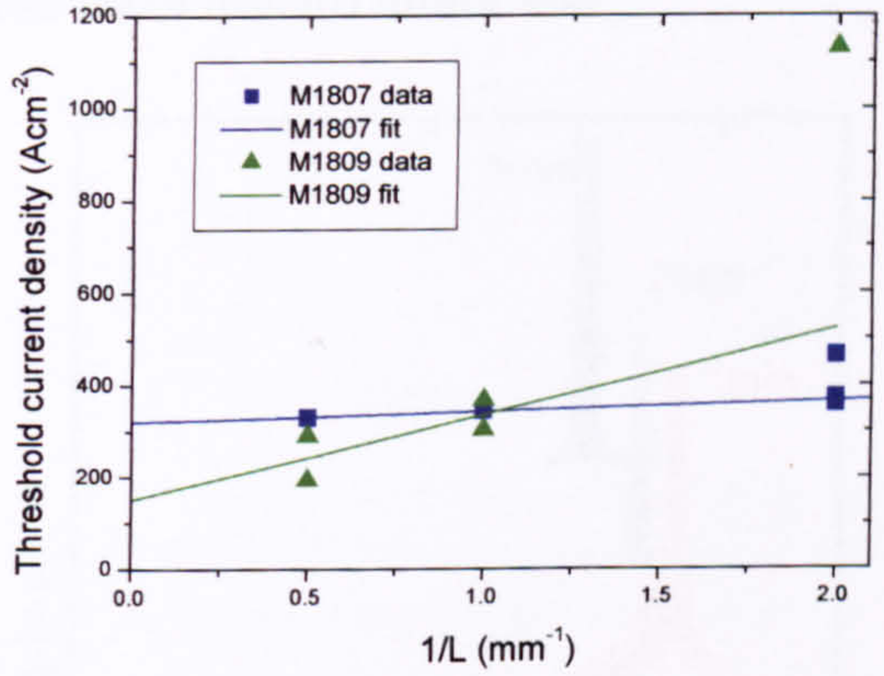

Figure 7.23 J_{th} plotted against inverse cavity length for structures M1807 (five layers) and M1809 (single layer) at 295K. At short cavity lengths the linear relationship breaks down due to gain saturation.

The lower transparency current density obtained for the five layer sample compared to that for the single layer sample arises because the multi-layer devices are able to lase via the ground state transition, and hence require relatively few carriers per QD to achieve the necessary population inversion, whilst the single layer structure always lases via an excited state[32]. This behaviour is shown clearly in Figure 7.24 and Figure 7.25 where lasing spectra for different cavity lengths are compared to the spontaneous emission spectrum. Whilst for M1807 a 2mm long cavity device lases at the peak of the ground state emission, and a 0.5mm cavity is still within the envelope of the emission, for M1524 (a single QD layer structure, equivalent to M1809) lasing occurs via the second excited state for 1mm and 2mm cavities and possibly the first excited state for a 5mm cavity. The lasing energies for M1524 as shown in Figure 7.24 are 1.30eV, 1.32eV and 1.34eV

for the 5, 2 and 1mm cavity lengths respectively. None of the single layer structures studied have exhibited ground state lasing for cavities ≤5mm. This indicates that the maximum ground state modal gain is insufficient to overcome the internal loss (which is typically ~10cm^{-1} [17]) and small residual mirror loss[33,34].

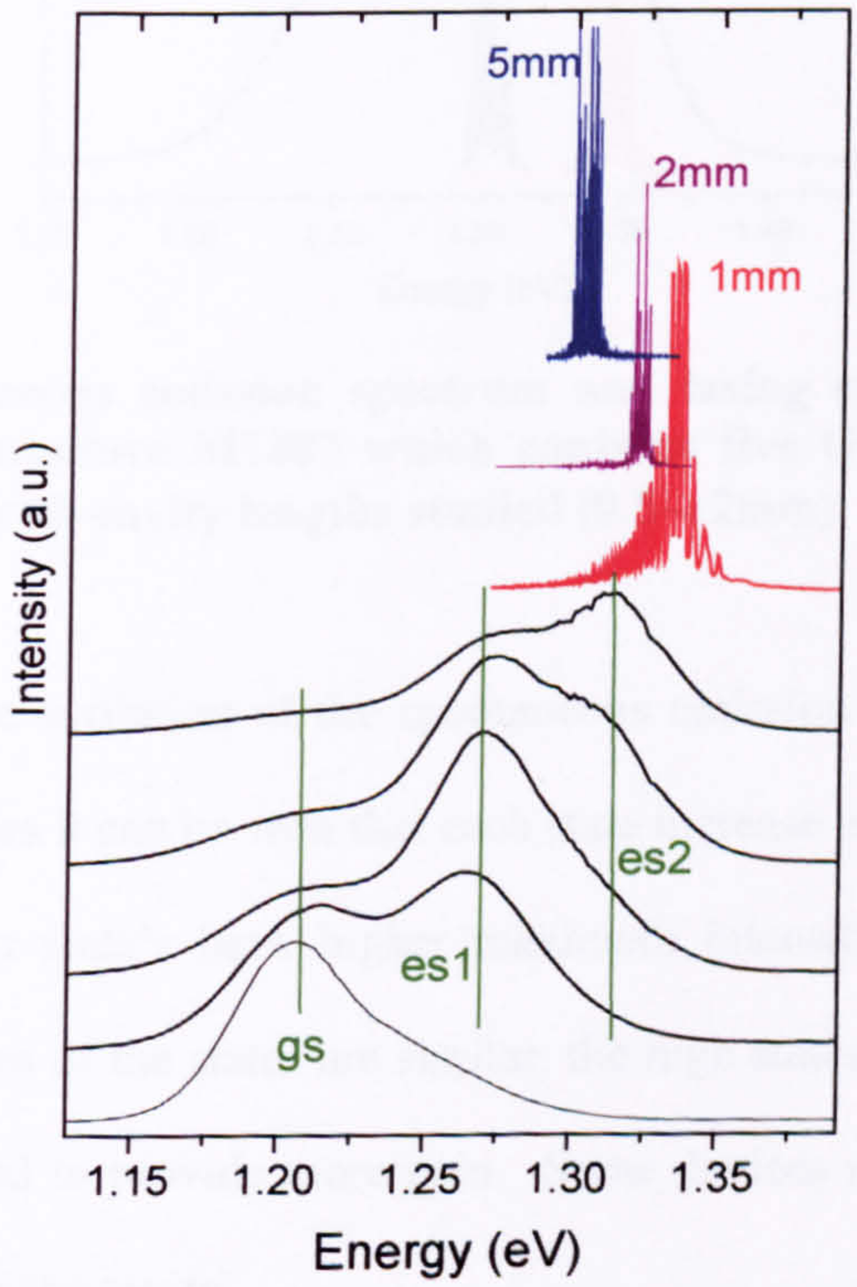

Figure 7.24 Spontaneous emission spectra and lasing spectra for different cavity lengths for structure M1524. Ground state lasing is not observed for all cavity lengths studied.

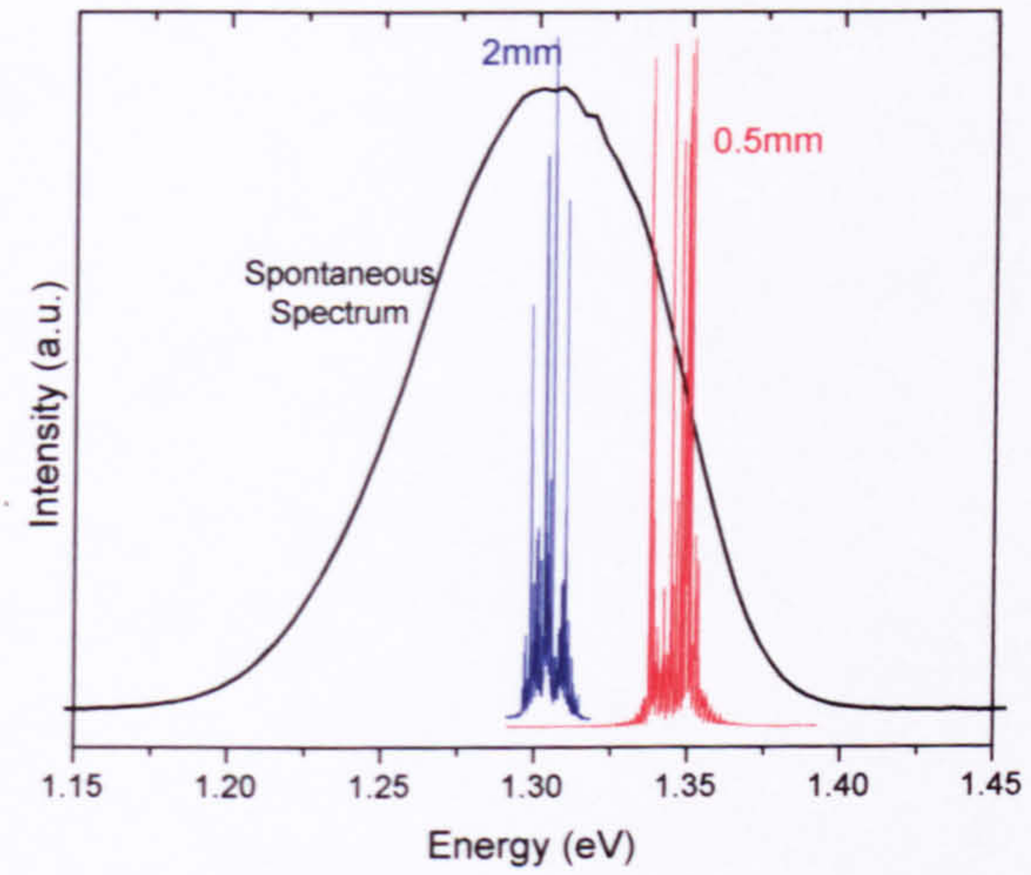

Figure 7.25 Spontaneous emission spectrum and lasing spectra for two different cavity lengths for structure M1807 which contains five QD layers. Ground state lasing is observed for all cavity lengths studied (0.5→2mm)

Figure 7.26 shows the evolution of the spontaneous emission for a single layer device.

As the current increases it can be seen that each state increase in intensity before reaching saturation. The higher state's have higher maximum intensities indicating that, if the recombination lifetimes of the states are similar, the high states have a larger degeneracy and hence the potential to provide more gain. Some devices may use this extra gain to overcome the losses of the cavity.

Not only does excited state lasing increase the threshold current density it also results in a degraded temperature performance as thermal carrier escape from excited states can occur more easily. This behaviour is clearly seen in Figure 7.27, which shows the temperature dependence of the threshold current density for three different cavity lengths. Decreasing the cavity length increases the lasing energy, increases the loss of the carriers at a given temperature and hence results in reduced temperature stability.

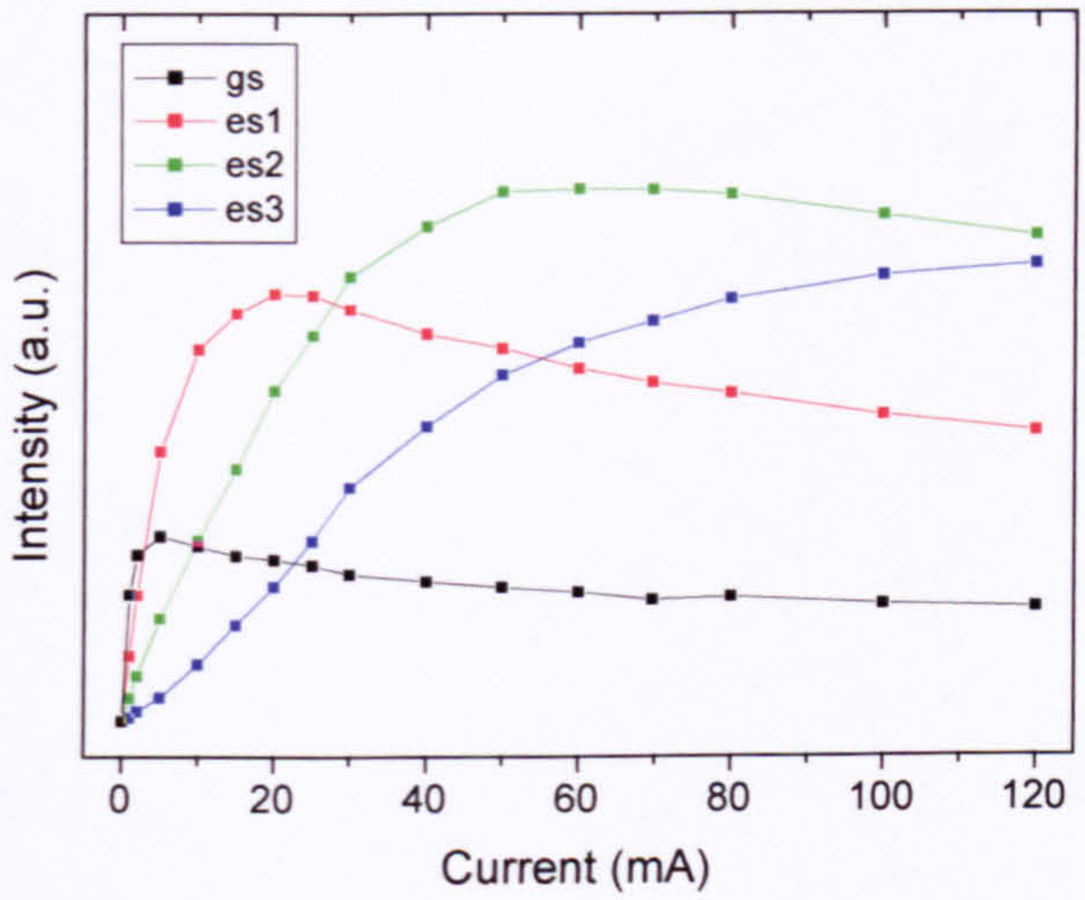

Figure 7.26 M1688. The evolution of the spontaneous emission with current for the QD transitions in a 400μm mesa.

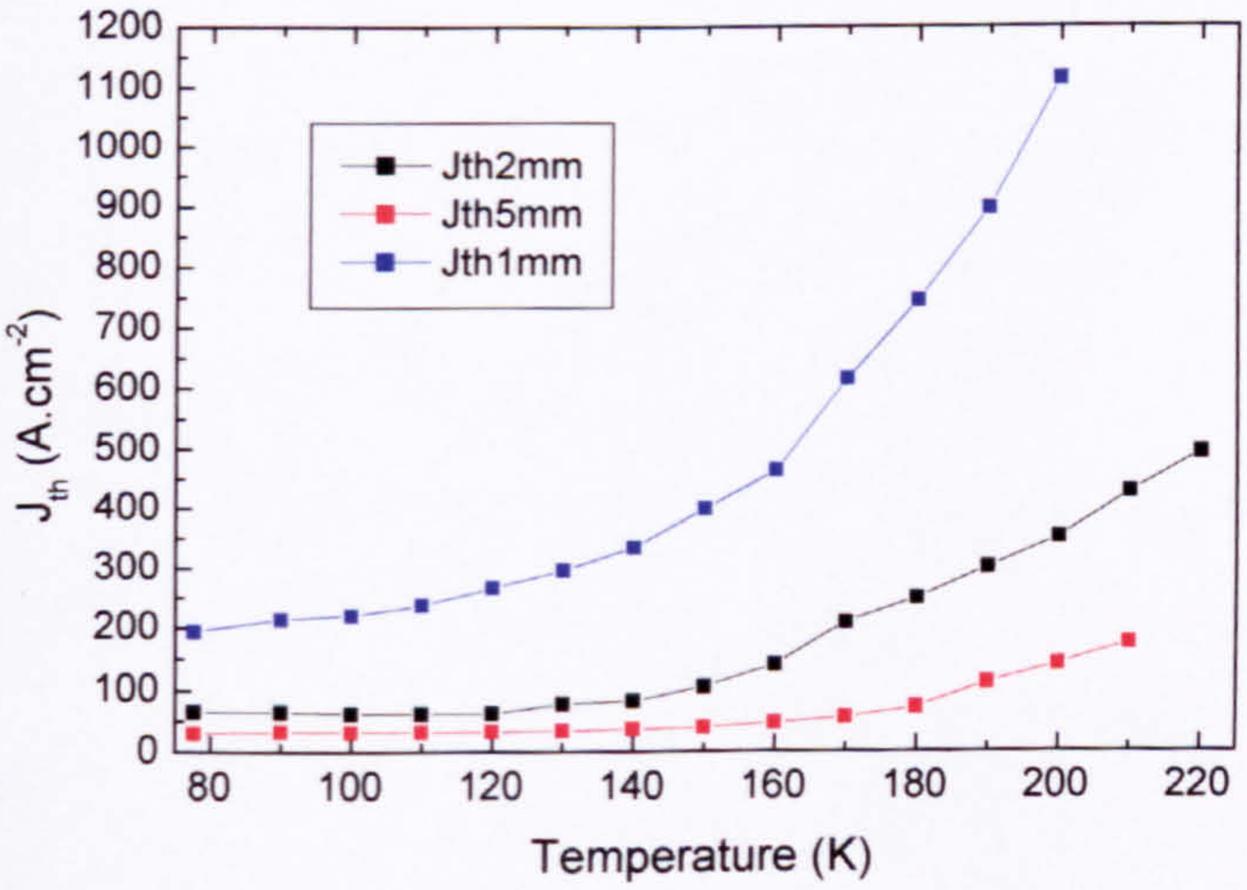

Figure 7.27 Threshold current density with temperature for 3 different cavity lengths M1524

7.5.3 Dependence of Device Performance on QD Layer Number

The maximum gain can be increased by increasing the number of QD layers. Hermann et al.[17] reported that the gain per QD layer remains constant when more layers are added (up

tp seven layers Figure 7.4). This results in a lower transition being able to produce sufficient gain to allow lasing. Ground state lasing was achieved in the five layer sample M1807 and this device exhibitted the lowest threshold currents (Figure 7.11).

7.5.4 Dependence of the Device Performance on the Dot Structure – Effect of Growth Rate

An increase in the QD uniformity should reduce the threshold current density, as less of the injected carriers will be wasted in initially non-lasing dots at energies away from the ensemble maximum. The two structures compared in this section, M1688 and M1524, are identical except for the dot density (Figure 7.6 and Figure 7.7). It is found that reducing the QD growth rate from 0.1 to 0.01MLs^{-1} results in a more uniform size, shape and composition distribution (as evidenced by the PL linewidth) and also a reduction in the emission energy. This latter effect may increase the temperature stability of a laser device as the confined carriers will require a greater thermal energy to escape from the QDs. Unfortunatly the lower growth rate also significantly reduces the QD density from 2-3x10^{10}cm^{-2} for the fast growth rate to 2-3x10^{9}cm^{-2} for the slow growth rate. These values were obtained from TEM images of uncapped structures. This reduced density results in a commensurate decrease in the gain, and ground state lasing is not possible for a single layer device containing the slow growth rate QDs, but occurs instead via an excited state transition. As a result the threshold current density is increased, outweighing any advantage of the improved QD uniformity. In addition lasing from an excited state increases the carrier thermal loss at high temperatures.

Figure 7.28 compares the performance of two devices based on fast and slow growth rate QDs. Both structures contain five QD layers and the devices have cavity dimensions of 1mm x 15μm. The performance of the device based on the fast growth rate QDs is superior to that of the slow growth rate QDs at all temperatures. For the slow growth rate devices the emission occurs via es2 and es3 (Figure 7.13). Because of the very low QD density produced by the slow growth rate it is difficult to circumvent this problem by growing multiple QD layers. It is hence concluded that the use of a slow growth rate to improve the QD uniformity offers no advantage for laser device performance.

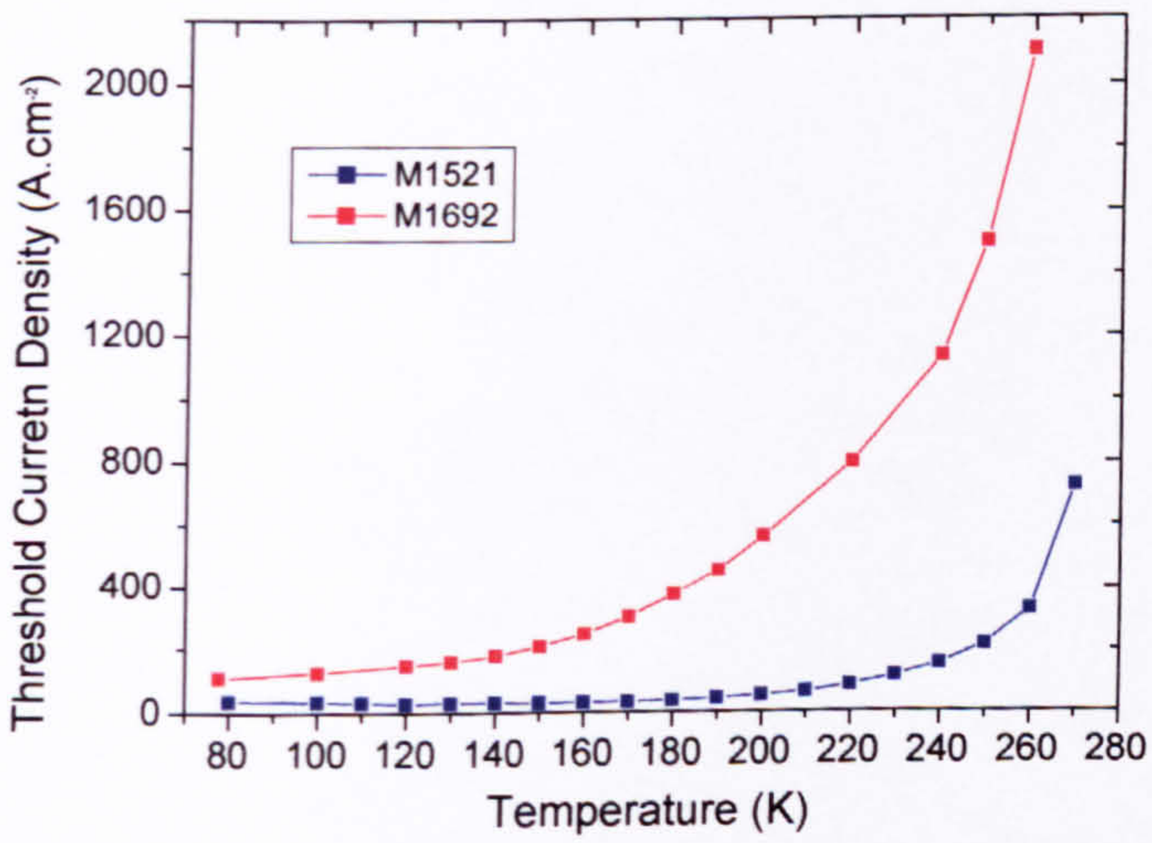

Figure 7.28 Temperature performance of two devices with five layers of QDs grown at slow rate (M1692) and a fast rate (M1521). Both devices have a 1mm long cavity.

7.5.5 Dependence of Device Performance on the QD Composition

In addition to nominally pure InAs QDs, Ga can be intentionally added during growth to give InGaAs QDs. InGaAs has a larger bandgap than InAs so InGaAs QDs may have a

reduced confinement although strain may complicate this picture. Devices based on structures M1809 (InAs) and M1843 ($In_{0.5}As_{0.5}Ga$) provide a comparison of the effect of QD composition on performance. Spectra for these one QD layer structures are shown in Figure 7.29 and Figure 7.30. Figure 7.31 compares their temperature performance. In both cases identical length (2mm) cavity devices are studied.

The low current EL linewidth for both these samples is quite large (70meV for M1809 and 100meV for M1843), indicating poor dot homogeneity. Both are single layer samples, so the seeding of subsequent layers cannot be employed to produce a more uniform sample. However it appears that the uniformity of the QDs is better in M1809. Both structures exhibit lasing that is shifted 70±10meV above the inhomogeneously broadened ground state peak.

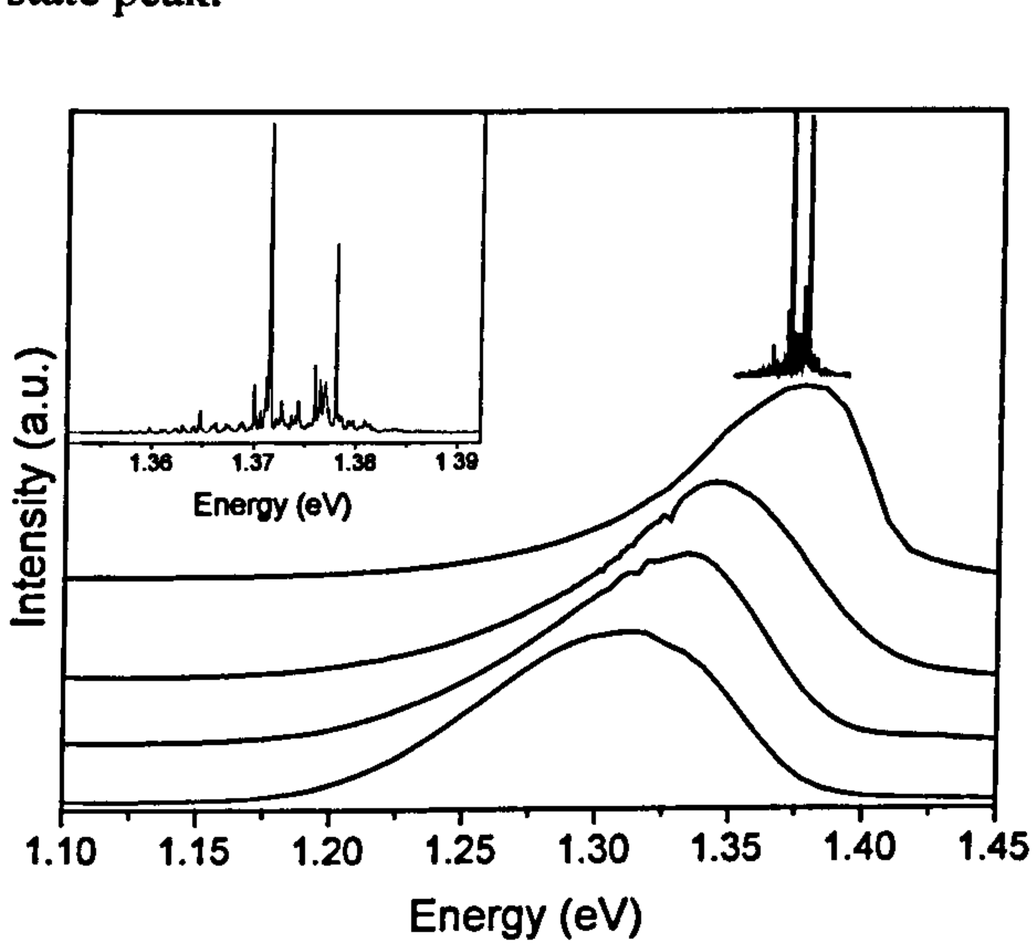

Figure 7.29 InGaAs laser spectra M1843 2mm EL Spectra at 80K

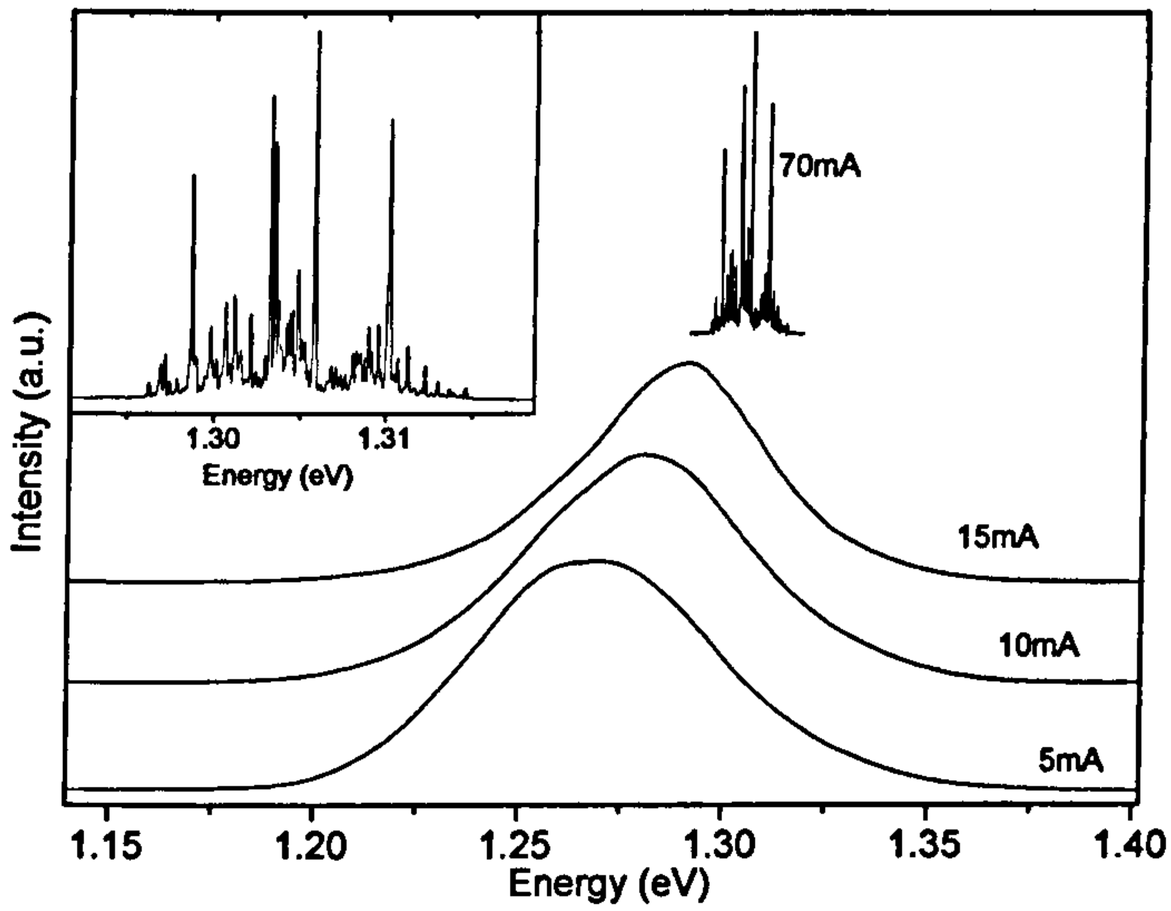

Figure 7.30 InAs laser spectra M1809 2mm EL Spectra at 80K

The InGaAs QDs exhibit not only a larger threshold current density, but also a worse temperature performance than the InAs QDs. It should be noted that many other groups have produced InGaAs QD based lasers that have excellent characteristics. The quality of growth can be the over-riding factor in determining device performance and as the inhomogeneous linewidth is larger for the InGaAs sample it appears that M1843 could be a low quality sample. More recent work by Groom et al.[22] suggests that InGaAs QD lasers (grown at the III-V Central Facility) perform better than InAs lasers, especially multiple QD layered structures. It would therefore appear that the present 'first attempt' sample is not representative of InGaAs QD based lasers in general.

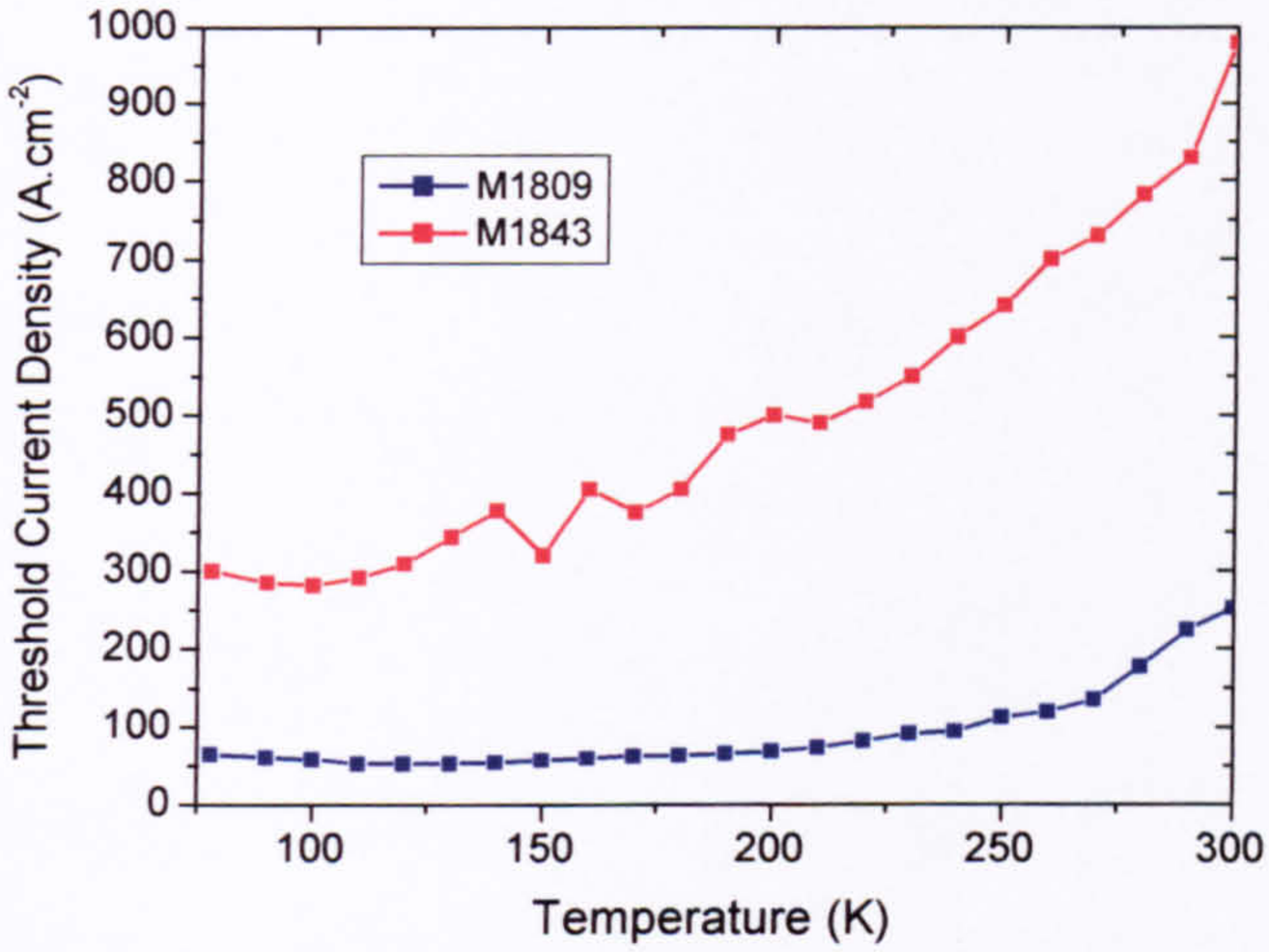

Figure 7.31 InAs and InGaAs QD laser threshold current density variations with temperature.

7.5.6 Dependence of Device Performance on the QD Layer Separation

A final parameter that can be easily varied is the separation between QD layers in a multiple layer structure. For stacked QD layers (>10nm) electronic coupling is negligible in the InAs/GaAs system and the individual QD properties are not altered. However even above 10nm separation there is an alignment of QDs in different layers (structural coupling). The structured coupling results in a narrow emission linewidth, suggesting a more uniform QD ensemble. This is believed to result from the strain fields from one QD layer acting as nucleation sites for QDs in the subsequent layer, hence removing some of the randomness of the QD formation[35]. A more uniform QD distribution should improve the device performance although the effect of any electronic coupling is unclear.

Figure 7.32 compares the performance of three devices each containing five nominal InAs QD layers. For M1691 the QD layers are separated by 20nm of GaAs and hence the QDs are expected to exhibit little or no structural and electronic coupling. For M1692 the layer separation is reduced to 5nm which should give strong structured coupling and possibly some electronic coupling. M1693 is similar to M1692 except that the QDs are grown within a 30nm GaAs/$Al_{0.15}Ga_{0.85}As$ QW to provide additional carrier confinement. At low temperature the performance of the three devices is similar although the coupled devices are slightly better. At higher temperatures it was not possible to achieve lasing with the uncoupled device beyond 250K whereas M1692 and M1693 lased up to 270K and 290K respectively. The additional confinement provided by the QW of device M1693 is demonstrated by its larger T_0 of 72K (at 260K) compared to 36K for M1692. In agreement with previously published work on QD lasers[22] there do appear to be some advantages in using coupled QDs although the reason for this is unclear.

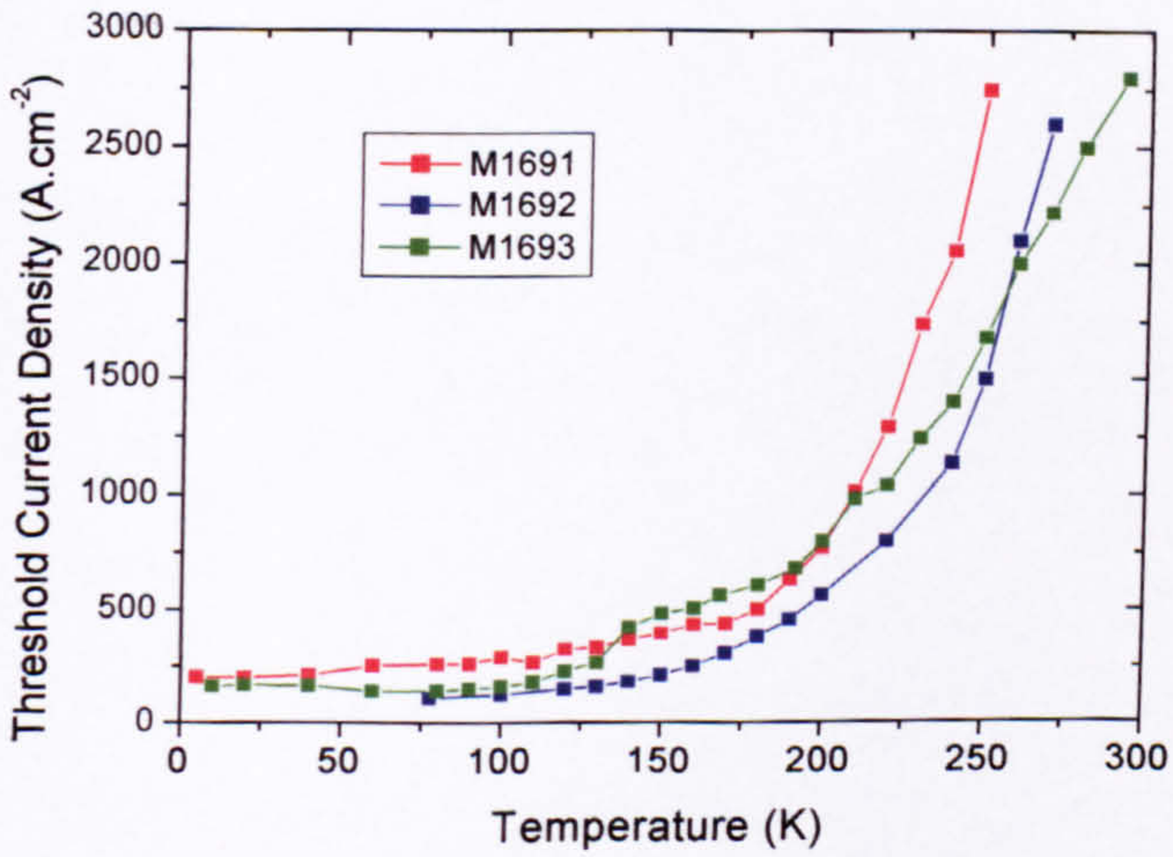

Figure 7.32 Temperature dependence of the threshold current densities of a coupled (M1692), uncoupled (M1691) and a laser where the dots are coupled inside a QW (M1693).

7.6 Spontaneous Emission Emitted Through Windows Formed in the Top Metallic Contact

Spectrally resolved spontaneous emission spectra allow the population of different QD states to be directly probed. In this section this emission is recorded from a series of windows formed in the top metal contact to eliminate any cavity amplification and to remove as much as possible of the more intense stimulated emission. Figure 7.33 shows the geometry of the holes formed in the metal contact and Figure 7.34 shows an image of an actual device.

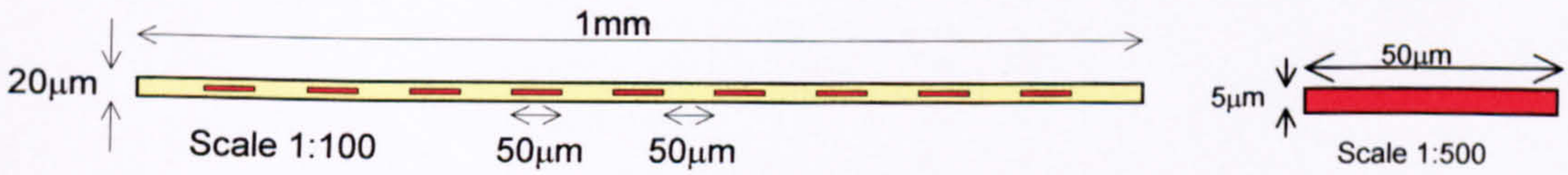

Figure 7.33 Schematic diagram showing the top window dimensions.

Figure 7.34 Top window emission viewed through the cryostat window. The TO5 header that the sample is mounted on is clearly visible.

Top contact spontaneous emission spectra are shown as a function of current at 10K in Figure 7.35 for a 1mm length laser M1693 (structure described in the previous section). For this length cavity the ground state (1.18eV) gain is insufficient to overcome the cavity losses. The first (1.21eV), second (1.23eV) and third (1.26eV) excited state

transitions are all observed, with lasing occurring on the second excited state transition. Above threshold stimulated emission is observed in the spectra, superimposed on the second excited state, as a result of scattering within the laser cavity by imperfections.

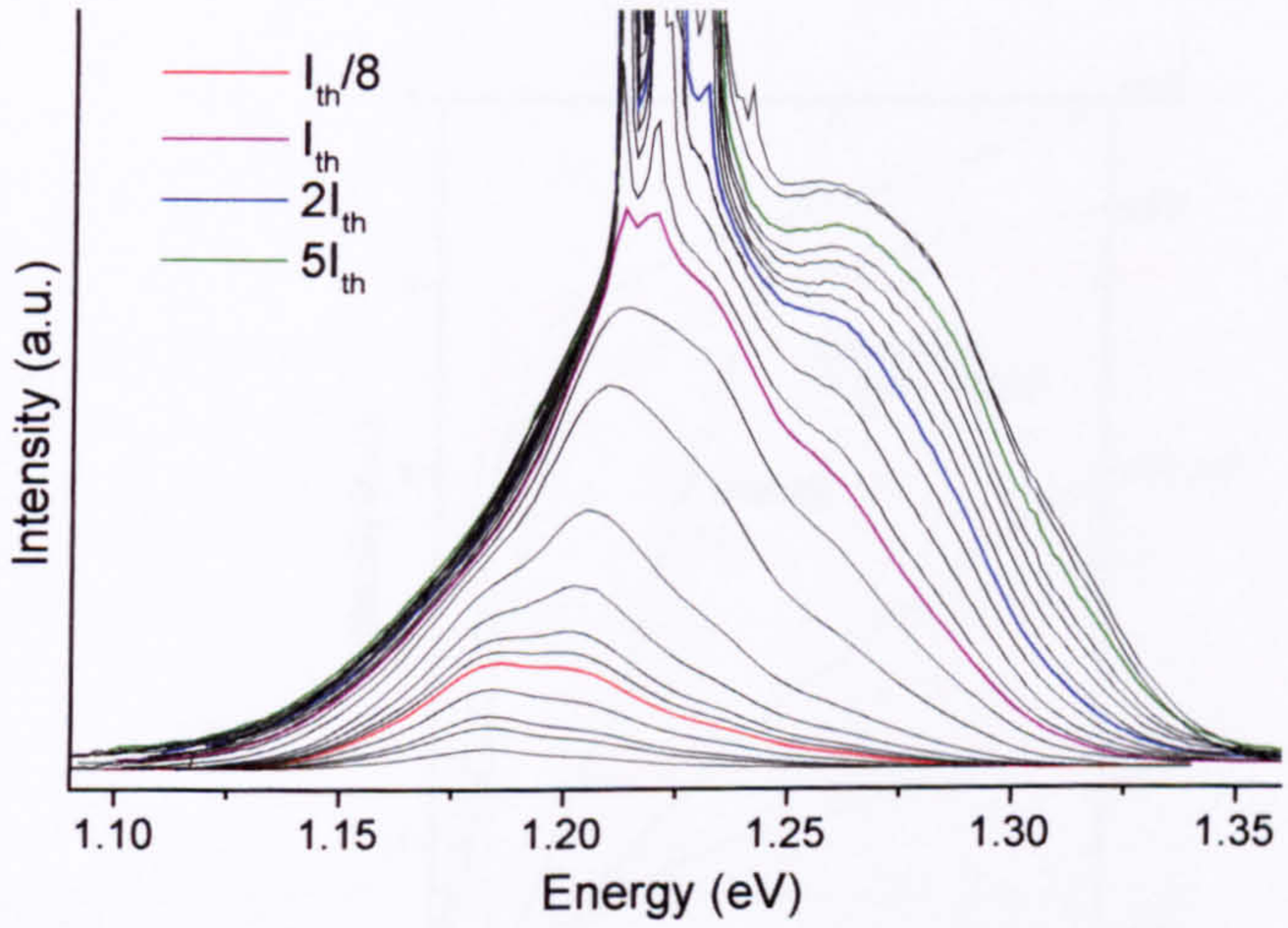

Figure 7.35 Top window measurements at T=10K Each line represents an "iso-current". The threshold current iso-current is highlighted in purple. 1mm x 20μm

The current dependence of the spontaneous emission for different QD transitions (recorded by using a spectrometer to select an appropriate energy region of the spectrum and recording the detected intensity as a function of current) is shown in Figure 7.36. Also shown is the L-I characteristic obtained from one of the end facets (green line). The spontaneous emission for each transition exhibits an initial rapid increase followed by a weaker increase at higher currents as the corresponding electronic states become fully occupied. None of the states exhibit an obvious change in slope at threshold and there is definitely no saturation of the spontaneous emission intensity at threshold. This is in contrast to the behavior observed in a QW laser where the carrier density, and hence

spontaneous emission intensity, pins at threshold due to the presence of a global Fermi level[36]. The present behaviour is therefore consistent with the absence of a global Fermi level in a QD laser at low temperatures, resulting from non-interacting carriers localised in different QD.

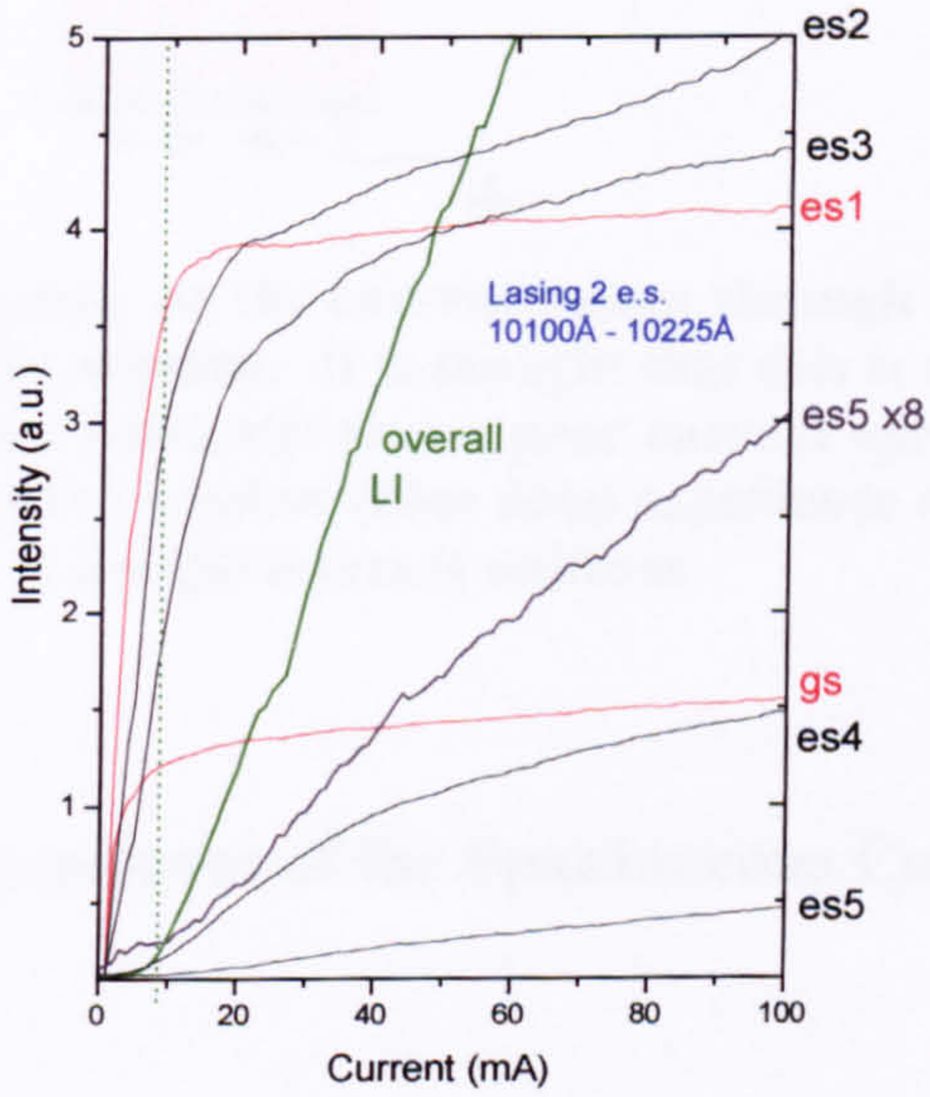

Figure 7.36 M1693 1mm x 20μm. The dependence's of the spontaneous emission on current for different QD transitions T=10K

It is possible that the observed behavior could results from insufficient current spreading in the holes formed in the contact as indicated schematically in Figure 7.37. In this case the carrier population in the QDs towards the centre of the hole would be less than that in the bulk of the laser and would continue to increase even when the majority population had reached threshold. By making the top p-type doped AlGaAs as thick as possible and as highly doped as possible ($\approx 2x10^{-18}cm^{-3}$) and by keeping the hole size relatively small it is hoped that current spreading problems can be eliminated[37]. The fact that none of the

spontaneous emission intensities exhibit obvious changes in slope at threshold, and that emission is observed from transitions above the lasing one (es3, es4 and es5 vs es2) suggests that the present evidence for a non-global Fermi level is reliable.

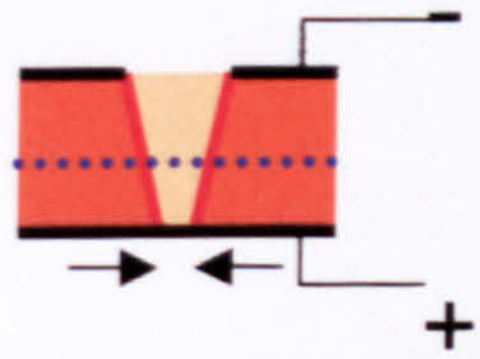

Figure 7.37 Current spreading. As the current passes through the device it spreads out into the region below the window. It is thought that this is extremely efficient in AlGaAs systems. The above schematic shows poor current spreading where not all the QDs immediately below the window (blue dots) experience the injection current. Ideally the current density at the QD layers is uniform

7.6.1 Temperature Dependence of the Spontaneous Emission Behaviour

As the device temperature is raised there is some evidence for a change in the behaviour of the spontaneous emission at threshold. This is indicated in Figure 7.38 which shows the behavior of the spontaneous emission at 80 and 150K. At the latter temperature the emission from the higher energy states (es4 and es5) shows a distinct reduction in gradient at threshold although there is still a weaker increase above threshold. Such a behavior is also seen in the total integrated spontaneous emission which is plotted as a function of current for a range of temperatures in Figure 7.39. This behavior suggest a transition to a more conventional system at high temperature where thermally activated emission allows interaction between different QDs, resulting in a system with a homogeneously broadened gain spectrum and a global Fermi level.

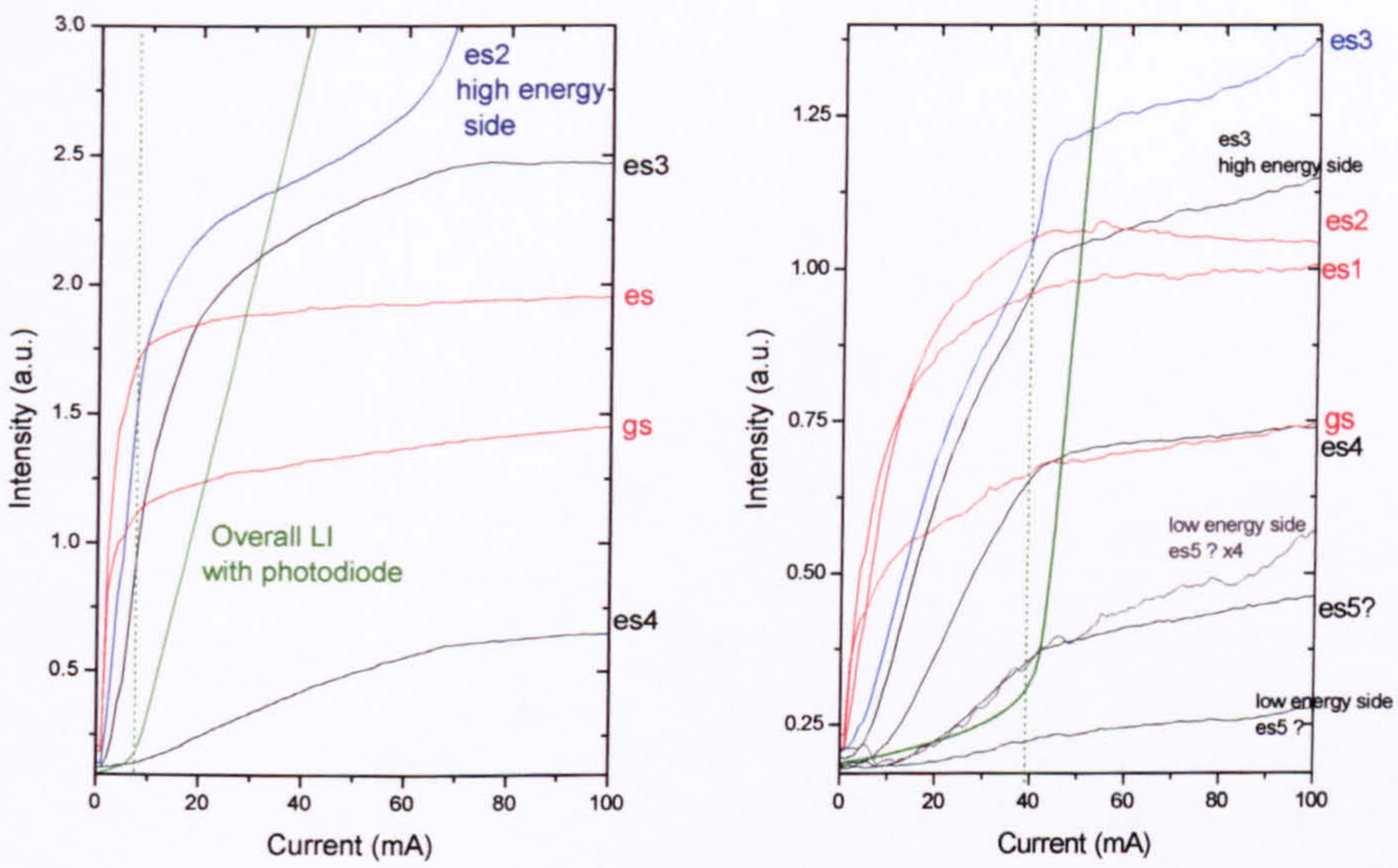

Figure 7.38 Current variation of the spontaneous emission from different transitions for T=80K and T=150K. The green line shows the L vs I characteristic recorded for emission from the end facets.

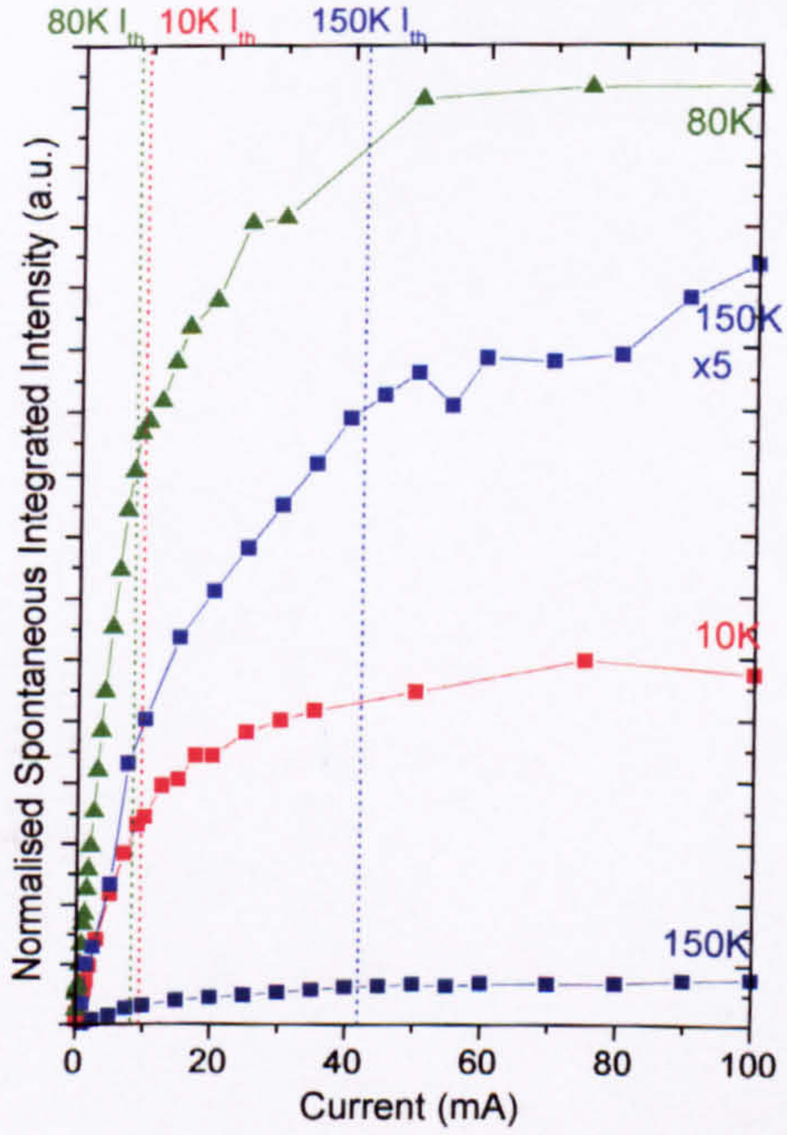

Figure 7.39 Integrated spontaneous emission as a function of current for three temperatures. The threshold current densities for each temperature are indicated by the dotted lines.

7.6.2 Carrier relaxation

For an opto-electronic device the injection current, I, is related to the carrier density n by

$$I = \left(\frac{eV}{\eta_i}\right)\left(An + Bn^2 + Cn^3\right) \quad \textbf{Equation 7-7}$$

where e is the electronic charge, V is the volume of the active region, η_i, is the internal quantum efficiency of the device and A, B and C are the rates for non-radiative recombination (via defects or impurities), spontaneous radiative recombination and non-radiative Auger recombination, respectively[38]. The spontaneous emission intensity is also related to the carrier density through

$$L = \beta n^2 \quad \textbf{Equation 7-8}$$

where β includes the coefficient B and also factors that depend on the fraction of light able to escape from the device and the efficiency of the detection system. Using Equation 7-8 to eliminate n from Equation 7-7 and taking natural logarithms gives

$$\ln(I) = \ln\left(\frac{eV}{\eta_i}\right) + \ln\left(\frac{A}{\beta^{1/2}}\left(L^{1/2}\right)^1 + \frac{B}{\beta}\left(L^{1/2}\right)^2 + \frac{C}{\beta^{13/2}}\left(L^{1/2}\right)^3\right) \quad \textbf{Equation 7-9}$$

Hence a ln(I) versus ln ($L^{1/2}$) plot will have a gradient of 1,2 or 3, respectively if defect, spontaneous or Auger recombination dominates the total carrier recombination. In this way the dominant carrier recombination mechanism can be identified and a series of measurements at different temperatures allows the temperature dependence of the recombination process to be studied.

At this point it is worth noting that Equation 7-9 is only strictly true for systems with dimensionality greater than one and for a QD system some modification may be required. For example numerical modelling suggests that for a system of non-interacting QDs the spontaneous emission should have a linear dependence on n^5. A complete analysis for a QD system requires a detailed numerical simulation. The present work is therefore limited to studying variations with temperature and not absolute values.

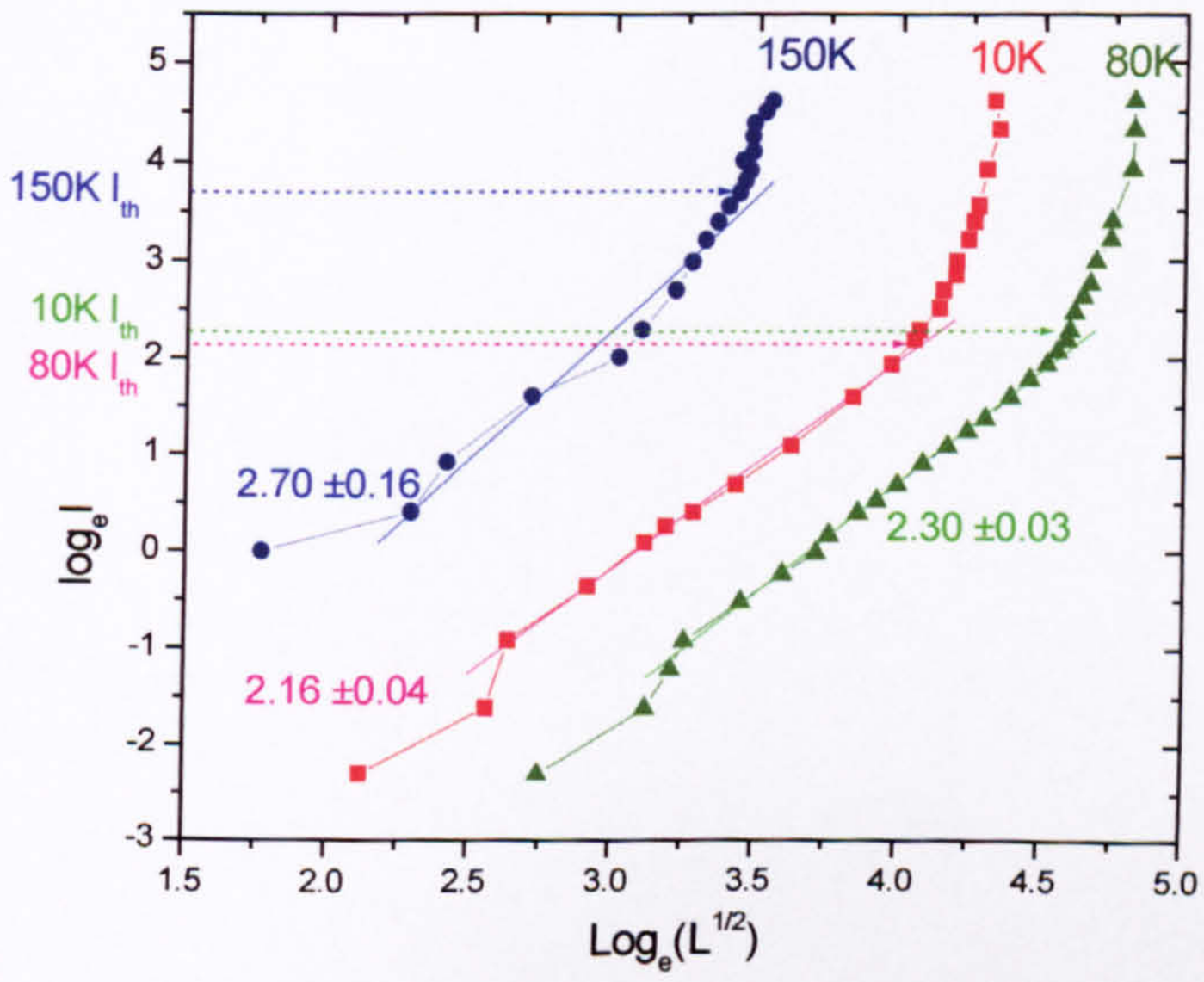

Figure 7.40 log-log plot showing the development of the spontaneous emission.

Figure 7.40 shows plots of In(I) vs ln ($L^{½}$) at three different temperatures for a QD laser device with five layers of QDs. At low temperatures the gradient is close to 2. It is expected that non-radioactive processes will be negligible at these temperatures and hence that recombination will be dominated by spontaneous emission. The observation of a gradient close to 2 therefore suggests that the above equations are valid for a QD system. With increasing temperature the gradient increases, reaching a value of 2.7±0.16

by 150K, suggesting an increasing importance of Auger recombination. This result therefore indicates that Auger recombination is the mechanism responsible for the increase in the threshold current density at high temperatures. However later and more detailed work on similar samples found a gradient which decreased above 100K to ~1 consistent with recombination via non-radiative centres[39]. However these samples contained AlGaAs layers very close to the QD layers, such layers, which are grown at low temperatures, are known to contain significant non-radiative centre densities. Additional and more detailed studies of a range of different structures appears to be needed to clarify this picture although the present results provide an indication of the usefulness of this technique to study carrier dynamics in QD lasers.

7.7 The Effect of a Strong Magnetic Field on the Characteristics on a QD Laser

The first quasi-QD laser was produced by Y.Arakawa and H.Sakaki[2], by applying a strong magnetic field to a QW laser to give full carrier confinement. The expected improvement in threshold current density and temperature stability was observed. In this section the effects of placing a QD laser, which is already zero-dimensional, in a high magnetic field is studied. The device was placed in a superconducting 14T magnet and studied in Faraday geometry with the field applied parallel to the growth direction (Figure 7.41). The experimental set-up is outlined in Chapter 2.

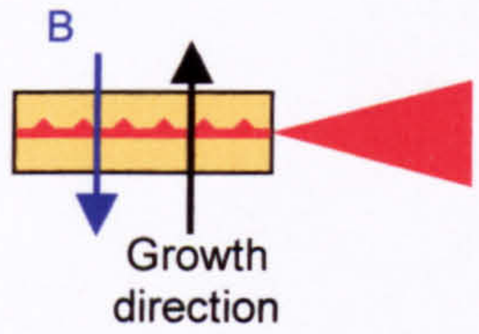

Figure 7.41 Schematic diagram showing the growth direction and magnetic field direction.

Figure 7.42 shows typical results for the effects of a magnetic field on the L vs I characteristics of a QD laser at 80K. With increasing field the threshold current density increases and the external quantum efficiency (given by the post-threshold slope of the characteristic) decreases. At high fields the L vs I curve starts to roll over at high currents. In Figure 7.43 the percentage change in the threshold current density is plotted for structure M1524 (a single QD layer device) and two five layer devices M1692 and M1807. The overall behaviour is the same, although weaker, for the multi-layer devices than the single layer one. In Figure 7.44 the percentage change in the external efficiency is plotted against field for the same three devices as for Figure 7.43. The external quantum efficiency μ_{ext} is given as a function of the cavity length L_c and mirror reflectivity R as

$$\frac{1}{\eta_{ext}} = \frac{1}{\eta_i}\left[\frac{\alpha_i L_c}{\ln(1/R)} + 1\right] \qquad \textbf{Equation 7-10}$$

where α_i is the internal cavity loss and η_i is the internal efficiency, a measure of the fraction of injected electrons entering the terminals of the device which reach the active region, in the present case the lasing QDs. It is difficult to see how a magnetic field could affect α_i and so the field induced reduction of μ_{ext} appears to arise from a reduction of η_i.

The reason for the magnetic field reduction of η_i and the increase of the threshold current density is unclear but may be related to a reduction of the in-plane mobility of the carriers. In those QDs approaching threshold the carrier lifetime will be reduced as stimulated emission becomes increasingly important. If the QD carrier capture efficiency is greater for emptier QDs (as is assumed by some dynamical models) then these QDs will be preferentially repopulated, assuming there is sufficient in-plane carrier mobility. The application of a magnetic field will reduce this mobility with the carriers forced to execute circular cyclotron orbits of radius

$$l_B = \frac{2.56}{\sqrt{B}} nm \qquad \textbf{Equation 7-11}$$

This reduced mobility would effectively reduce the internal efficiency η_i which in turn would result in an increase in the threshold current density and a reduction of the external efficiency. At 14T the cyclotron radius is 0.7nm, which is significantly smaller than the average inter-dot separation of 100nm for a QD density of $10^{10}cm^{-2}$.

Figure 7.45 shows the effect on the lasing spectra of a magnetic field for structure M1524. Figure 7.46 shows similar spectra for structure M1807. In both cases spectra are recorded at a constant multiple of the threshold (x2). For the single layer device M1524 the application of a magnetic field has a dramatic effect on the spectra, significantly reducing the number of lasing modes. A similar, but much weaker effect is observed for the five layer device M1807. The reason for this modification of the lasing spectra is unclear. Again a modification of the in-plane carrier mobility and resultant QD carrier efficiency seems likely although the explanation given previously for the decreased η_i would seem to predict an increase in the number of lasing modes as carriers injected into

lasing QDs are partially redistributed to non-lasing QDs. At present a full explanation of this behaviour is therefore not possible.

The application of a magnetic field degrades the performance of the QD lasers. Figure 7.44 shows a reduction in the internal efficiency and an increase in the threshold current. At very high fields a saturation of the L-I curve also is observed. *All of the three studied* samples show this behaviour.

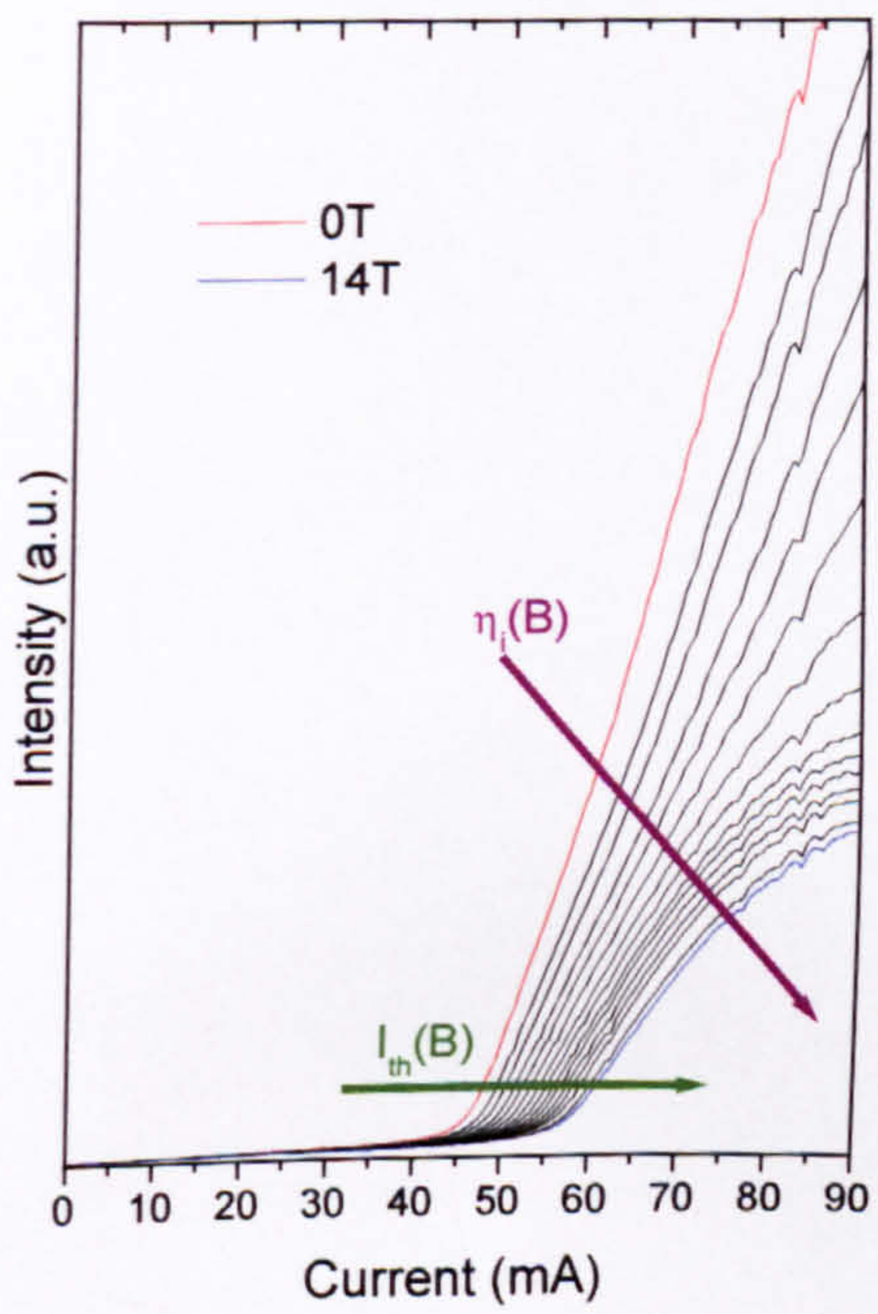

Figure 7.42 M1524 2mm x 15μm. L vs I characteristics at magnetic fields from 0 to 14T. T=80K

For M1524, the single layer sample, the fractional increase in threshold current is ~0.014T^{-1} (Figure 7.43). For the multi-layer samples (M1807 and M1692) the magnetic field dependence is not as great.

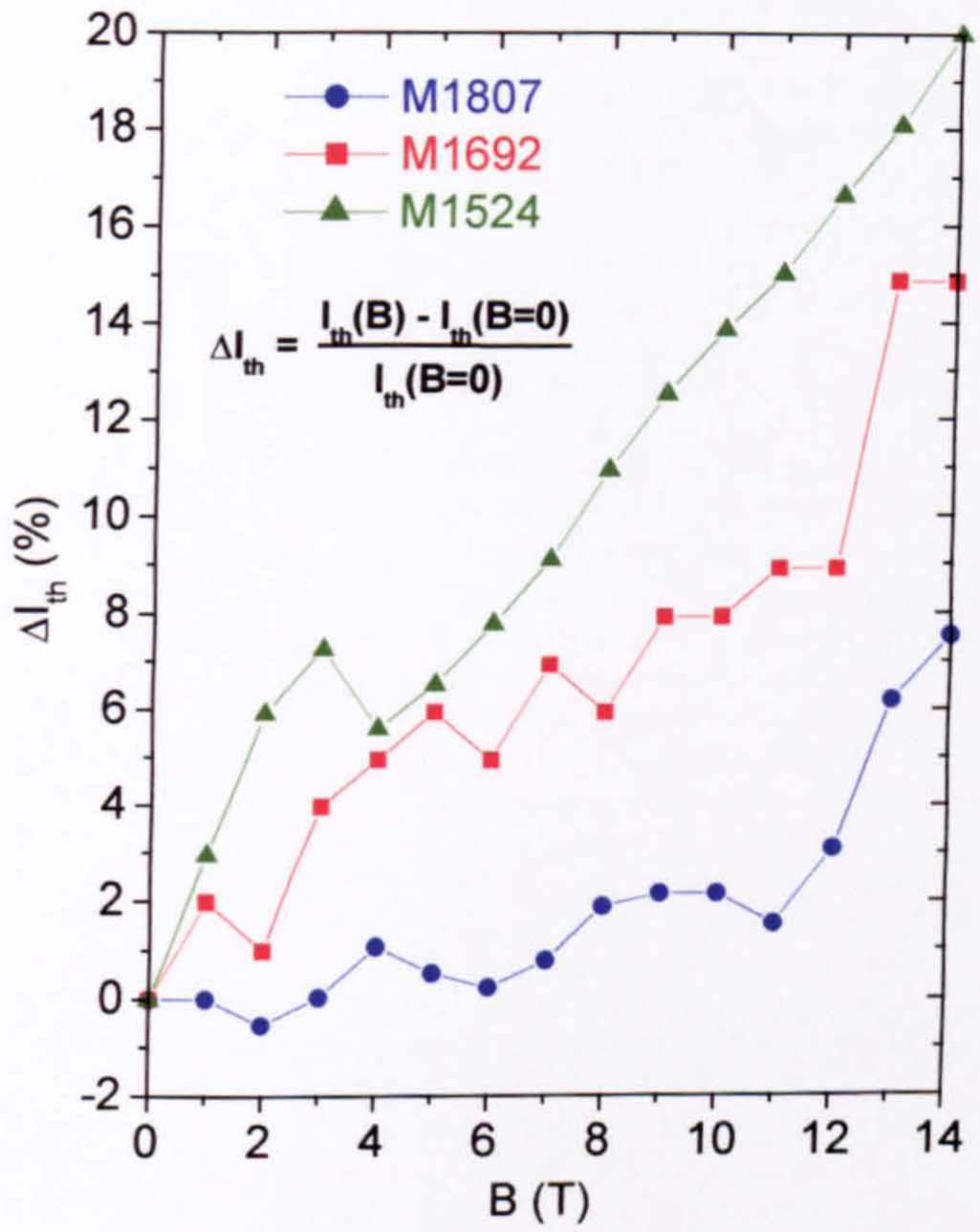

Figure 7.43 M1524 2mm x 15μm. Percentage threshold current variation with magnetic field. T=80K.

Relative changes in the internal efficiency, η_i, are easily measured as η_i is proportional to the external efficiency, η_{ext}, through the following

where α_i is the internal absorption loss, L_c is the cavity length and R is the reflection coefficient of the cavity mirrors. A 68% reduction of the internal efficiency occurs for the single layer sample M1524 in a 14T magnetic field. Reductions of 57% and 40% are observed for the multi-layer samples M1807 and M1692 respectively.

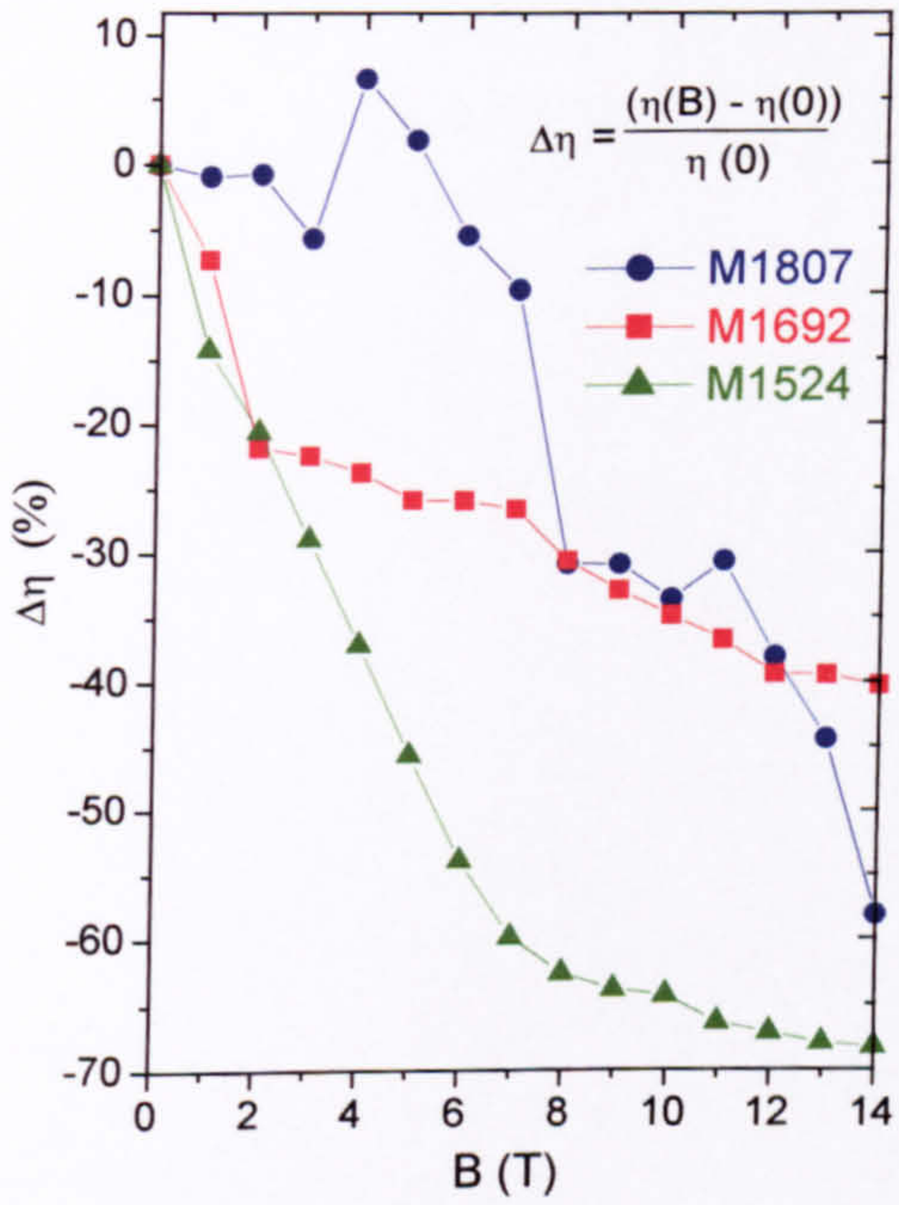

Figure 7.44 M1524 2mm x 15μm. Percentage internal efficiency change with magnetic field. T=80K.

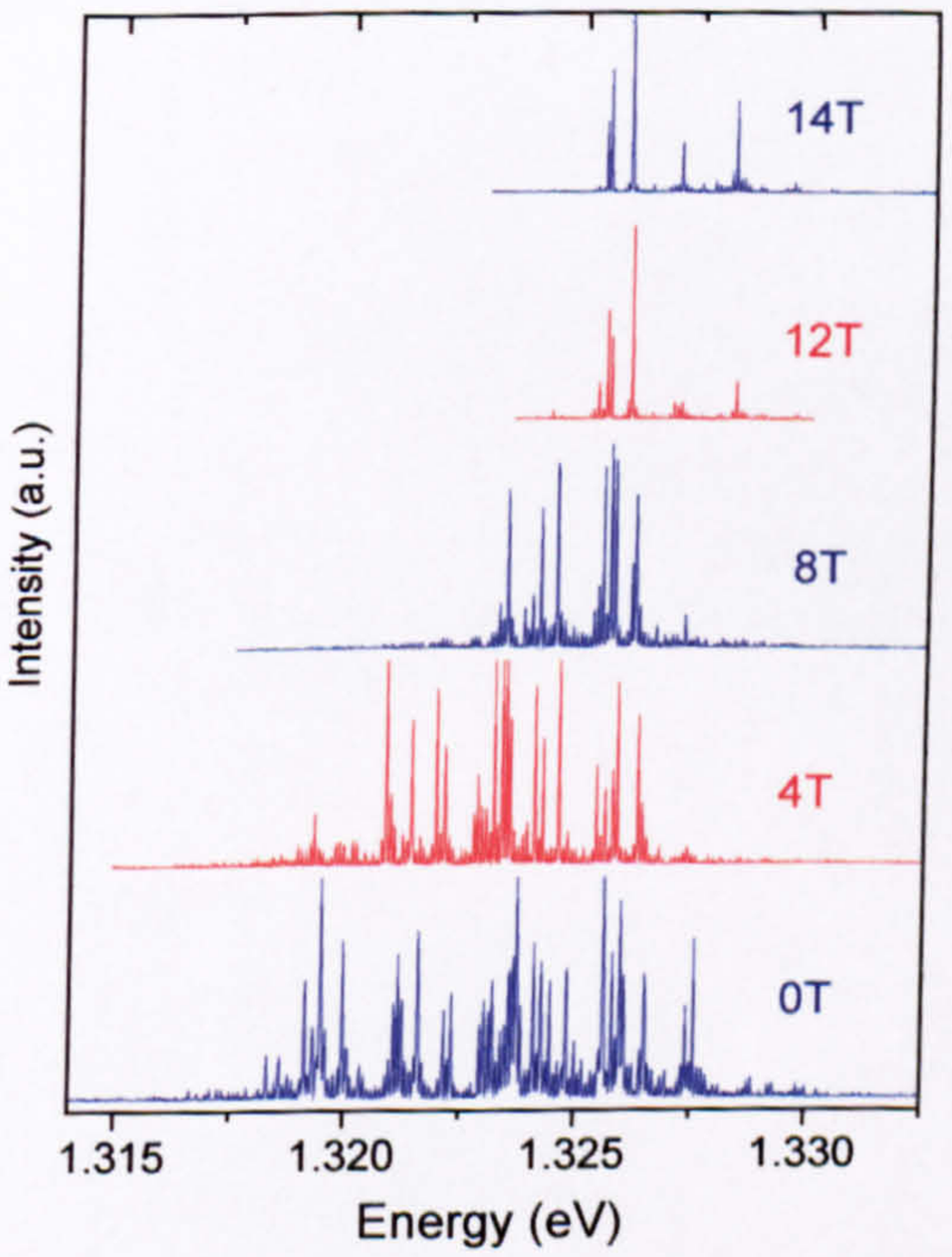

Figure 7.45 M1524 2mm x 15μm. Lasing spectra emission at $I=2I_{th}$. T=80K.

Not all the devices show a significant modification of their emission spectra. Both M1807 & M1692 do not have any strong dependence on magnetic field and the threshold current density and internal efficiency of these devices are also less dependent on magnetic field than found for other devices. Unsurprisingly, the magnetic field dependence of the lasing spectra is greatest in that sample which has the largest field dependence of the internal efficiecy.

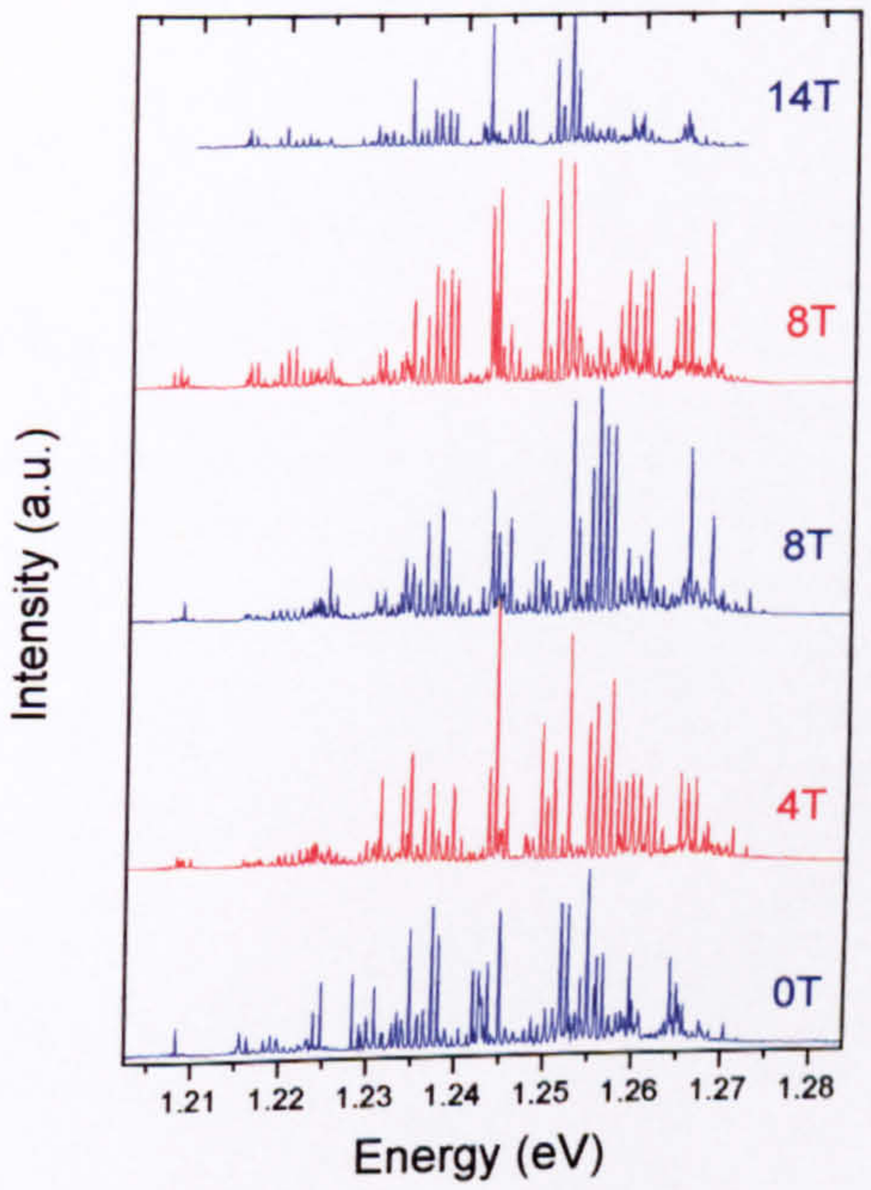

Figure 7.46 M1807 2mm x 15μm. Lasing spectra at $I=2I_{th}$ for applied fields between 0 and 14T. T=80K.

7.8 Summary

At low temperatures QD lasers exhibit temperature independent performance as expected for a 0D system. Extremely low threshold current densities of 10.7A.cm^{-2} and 35.7A.cm^{-2} at 160K and room temperature respectively are realised, with a T_0 that reaches infinity (temperature independent) at temperatures <200K and is still 130K at room temperature.

Highly multimode lasing is found, consistent with the absence of a global Fermi level which results from carriers localised in the QDs. At high temperatures the number of lasing modes decreases as inter-dot carrier transport becomes possible.

For single dot layer devices there is insufficient gain to allow lasing via the ground state transition and lasing occurs via an excited state with an inferior J_{th} and temperature stability of J_{th}.

The use of a low growth rate to achieve increased QD uniformity and longer wavelength emission is compromised by the reduced density. The use of closely separated QD layers is found to improve the device performance.

The use of a low growth rate to achieve increased QD uniformity and longer wavelength emission is compromised by the reduced density. The use of closely separated QD layers is found to improve the device performance.

Spontaneous emission recorded via a series of windows in the top metal contact reveals an absence of carrier clamping at threshold, again consistent with the absence of a global Fermi level.

Finally the application of a magnetic field, applied along the growth axis, is found to increase J_{th}, decrease the external efficiency and decrease the number of lasing modes.

[1] N. N. Ledentsov, "Quantum Dot Heterostructures: Fabrication, Properties, Lasers," *Semiconductors*, vol. **32**, pp. 343-365, 1998.
[2] Y. Arakawa and H. Sakaki, *Appl. Phys. Lett.* **40**(11), 939 (1982)
[3] D. Bimberg, M. Grundmann, N.N.Ledentsov, *Quantum Dot Heterostructurs*, (Wiley) 1999)
[4] M. Grundmann and D. Bimberg, *Jpn J. Appl Phys.*, **36**, 4181 (1997)
[5] M. Grundmann and D. Bimberg, *Phys Rev B* **55**, 9740 (1997)
[6] N. Kirstaedter, N. N. Ledentsov, M. Grundmann, D. Bimberg, V. M. Ustinov, S. S. Ruvimov, M. V. Maximov, P. S. Kop'ev, Zh. I. Alferov, U. Richter, P. Werner, U. Gösele, J. Heydenreich, *Electron. Lett.* **30** 1416 (1994)
[7] O. G. Schmidt, N. Kirstaedter, N. N. Ledentsov, M. –H. Mao, D. Bimberg, V. M. Ustinov, A. Yu Egorov, A. E. Zhukov, M. V. Maximov, P. S. Kop'ev, and Zh. I. Alferov *Electron. Lett.*, **32**, 1302 (1996)
[8] N. N. Ledentsov, V. A. Shchukin, M. Grundmann, N. Kirkstaedter, J. Böhrer, O. Schmidt, D. Bimberg, V. M. Ustinov, A. Yu Egorov, A. E. Zhukov, P. S. Kop'ev, S. V. Zaitsev, N. Yu. Gordeev, Zh. I. Alferov, A. I. Borovkov, A. O. Kosogov, S. S. Ruvimov, P. Werner, U. Gösele, and J. Heydenreich *Phys. Rev. B* **54**, 8743 (1996)
[9] H. Shoji, Y. Nakata, k. Mukai, Y. Sugiyama, m. Sugawara, N. Yokoyama and H. Ishikawa *Electron. Lett.* **32**, 2032 (1996)
[10] N. Kirstaedter, O. G. Schmidt, N. N. Ledentsov, D. Bimberg, V. M. Ustinov, A. Yu Egorov, A. E. Zhukov, M. V. Maximov, P. S. Kop'ev, and Zh. I. Alferov *Appl. Phys. Lett.* **69** 1226 (1996)
[11] Y. Z. Hu, H. Green, N. Peyghambarian, and S. W. Koch *Phys. Rev. B* **53** 4814 (1994)
[12] K. L. Shaklee, R. E. Nahory and R. F. Lahery *J. Lumin.* **7** 284 (1985)
[13] L. Harris, D. J. Mowbray, M. S. Skolnick, M. Hopkinson and G. Hill, *Appl. Phys. Lett.* **73** 969 (1998)
[14] L. Harris, A. D. Ashmore, D. J. Mowbray, M. S. Skolnick, M. Hopkinson and G. Hill, *Appl. Phys. Lett.* **75** 3512 (1999)
[15] B.W.Hakki and T.L. Paoli, *J.Appl.. Phys.* **44** 4113 (1973)
[16] P. W. Fry, L. Harris, S. R. Parnell, J. J. Finley, A. D. Ashmore, D. J. Mowbray, M. S. Skolnick, M. Hopkinson, G. Hill, and J. C. Clark, *J. Appl. Phys.* **87**, 615(2000)
[17] E. Herrmann, P. M. Smowton, H. D. Summers, J. D. Thomson, and M. Hopkinson *Appl. Phys. Lett.* Vol **77**, 163 (2000)
[18] Zh. I. Alferov, Sov. Phys. *Semicond.* **1**, 358 (1967)
[19] G. W. Bryant *Phys. Rev. B.* **47c** 1683 (1993)
[20] N.Chand et al., *Appl. Phys. Lett.*, **59** 1704 (1991)
[21] F.Heinrichsdorff et al., *Appl. Phys. Lett.*, **71**, 22 (1997)
[22] K. M. Groom, A. I. Tartakovskii, D. J. Mowbray, M. S. Skolnick, P. M. Smowton, M. Hopkinson and G. Hill, *Appl. Phys. Lett.*, **81** 1 (2002)
[23] E.P.O'Reilly, A. I. Onischenko, E. A. Avrutin, D. Bhattacharyya, J. H. Marsh, *Electron. Lett.* **34** 2035 (1998)

[24] P.M. Smowton, E.J. Johnston, S.V. Dewar, P.J. Hulyer, H.D. Summers, A. Patane, A. Polimeni, M. Henini. *Appl. Phys. Lett.*, 75, 2169 (1999)
[25] B. W. Hakki, T. L. Paoli, *J. Appl. Phys.* **44** 4113 (1973)
[26] T.-P. Le, C. A. Burrus, J. A. Copeland, A. G. Dentai and D. Marcuse, *IEEE J. Quantum Electron.* **18** 1101 (1982)
[27] G. P. Agrawal and N. K. Dutta *Semiconductor Lasers* (Van Nostrand Reinhold) (1993)
[28] O.Madleung and M.Schulz (Ed.), *Landolt-Börnstein Numerical Data and Functional Relationships in Science and Technology New Series Volume 22 Semiconductors*, Springer (1986)
[29] A.Patanè, A. Polimeni, P. C. Main, M. Henini, L. Eaves., *J. Appl. Phys.*, 85(1), 625 (1999)
[30] P.W. Fry, I. E. Itskevich, D. J. Mowbray, M. S. Skolnick, J. J. Finley, J. A. Barker, E. P. O'Reilly, L. R. Wilson, I. A. Larkin, P. A. Maksym, M. Hopkinson, M. Al-Khafaji, J. P. R. David, A. G. Cullis, G. Hill, and J. C. Clark *Phys. Rev. Lett.* **84** 733 (2000)
[31] A. E. Zhukov, V. M. Ustinov, A. Y. Egorov, A. R. Kovsh, A. F. Tsatsulnikov, N. N. Ledentsov, S. V. Zaitsev, N. Yu. Gordeev, P. S. Kop'ev, and Zh. I. Alferov, *Jpn. J. Appl. Phys.* **36** 4216 (1997)
[32] P. G. Eliseev, H. Li, A. Stintz, G. T. Liu, T. C. Newell, K. J. Malloy, and L. F. Lester *Appl. Phys. Lett.* **77**
[33] D.J.Mowbray L. Harris, P. W. Fry, A. D. Ashmore, S. R. Parnell, J. J. Finley, M. S. Skolnick, M. Hopkinson, G. Hill, J. Clark., *Physica E* **7** 489 (1999)
[34] H. Shoji, Y.Nakata, K.Mukai, y.Sugiyama, M.Sugawara, N.Yokoyama and H. Ishikawa, *IEEE J. Quantum. Electron.* **3** (1997) 188
[35] Q. M. Xie, P. Chen, N. P. Kobayashi, *Phys. Rev. Lett.* **75** 2542 (1995)
[36] P. M. Smowton and P. Blood, *Appl Phys. Lett.* **70**1073 (1997)
[37] P.M. Smowton and P. Blood, IEEE J. Sel. Top. Quant. Electr. 3, 491 (1997).
[38] A. F. Phillips, S.J. Sweeny, A. R. Adams and P. J. A. Thijs, *IEEE J. Quantum Electron* **5** 401 (1999)
[39] K. M. Groom, D.J.Mowbray, A. I. Tartakovskii, , M. S. Skolnick, P. M. Smowton, M. Hopkinson and G. Hill, *Appl. Phys. Lett.*, (to be published)